HETG Ground Calibration Report

HETG Science Team
Prof. C.R. Canizares, Instrument Principal Investigator

and the
Chandra X-Ray Observatory Center

Version 3.0

December 31, 2000

*** D R A F T ***

as of February 28, 2002

MIT Center for Space Research
70 Vassar St.
Building 37
Cambridge, MA 02139–4307
USA

Contents

List of Figures

List of Tables

Summary and Key Parameters

After a year of successful flight operation, ...

Even with flight data available, the ground calibration measurements and results described here provide unique data on:

The information and results presented here are the work of both the HETG Science Team and the ASC.

- Dan Dewey, December 31, 2000

HETG ground calibration information is available on-line at:

`http://space.mit.edu/HETG/xrcf.html` .

.

Key Parameters

Table 1: Key fabrication and ground test parameters of the HETG.

Parameter Name	Value	Unit	Comments
Grating Facet Parameters:			
Grating bar material	Gold	—	—
HEG, MEG Bar thickness	510, 360	nm	Approximate average value
HEG, MEG Bar width	120, 208	nm	”
HEG, MEG polyimide thickness	980, 550	nm	”
Plating base thicknesses	20(Au), 5.0(Cr)	nm	”
HETG Parameters:			
Rowland Diameter	8633.69	mm	HESS, as-designed
HEG average period	2000.81 ± 0.05	Å	LR, NIST referenced
MEG average period	4001.41 ± 0.22	Å	”
Vignetting, shell 1	0.937 ± 0.01	—	Inter-facet vignetting
Vignetting, shell 3	0.940 ± 0.01	—	” (from calculation)
Vignetting, shell 4	0.931 ± 0.01	—	”
Vignetting, shell 6	0.936 ± 0.01	—	”
Efficiencies (rev. N0004)	Figure 7.2	—	from X-GEF measurements and synchrotron optical constants
XRCF Measurement Results:			
XRCF Rowland Spacing	8782.8 ± 0.60	mm	as measured
HEG angle	-5.19 ± 0.05	degree	w.r.t. XRCF axes
MEG angle	4.74 ± 0.05	degree	”
HEG–MEG opening angle	9.934 ± 0.008	degree	from beam center data
HEG dp/p	146 ± 50	ppm rms	Mg-K slit scan analysis
MEG dp/p	235 ± 50	ppm rms	”
HEG roll variation	≈ 1.8	arc min. rms	2 peaks, 3 arc min. apart
MEG roll variation	≈ 1.8	arc min. rms	$\approx$ Gaussian distribution
Mis-aligned MEGs	3 – 25	arc min.	6 MEG roll outliers
HEG LRF wing	$\leq 0.013/(\Delta\lambda)^2$	%/Å	at Mg-K, 9.887 Å
MEG LRF wing	$\leq 0.020/(\Delta\lambda)^2$	%/Å	”
HEG scatter	≈ 0.2	% /Å	at 7 Å; ≤ 1 % total
MEG scatter	not seen	—	$< 1/10^{\text{th}}$ of HEG value

Section 1

Introduction

This document details the ground calibration of the HETG, including the basic models, sub-assembly ("laboratory") testing, XRCF measurements and analyses, and the resulting calibration products. Most data and software referenced in this document are available digitally through a companion HETG Calibration Archive, see Section 8.

It is assumed that the reader is familiar with Chandra (aka AXAF), the HETG, and XRCF calibration, e.g. through CXC published materials. This introductory section provides a brief overview of the HETG and summarizes basic concepts related to its calibration. The rest of the report is divided into three parts.

Part I presents the basic operating principles and models of the HETG (Sections 2 and 3) and the laboratory measurements made on the component facets of the flight HETG (section 4.)

Part II consists of an introduction to the XRCF calibration activities (Section 5) followed by XRCF analyses broken down into a set of projects (Sections 6.2 through 7.9). The status of these analysis efforts is given in Table 5.9.

Lastly, in Part III the companion HETG Calibration Archive is described, Sections 8. Data and software in the archive are described in Sections 9 and 10. Finally, in Section 11 the resulting ground calibration is captured in a set of "Calibration Interface Products" which are the starting point for the values in the CXC released ARD files which bring the calibration process to the Chandra user.

1.1 The HETG on Chandra

The High Energy Transmission Grating (HETG) is one of four Scientific Instruments (SIs) that will operate with the High Resolution Mirror Assembly (HRMA) in NASA's Chandra X-Ray Observatory (CXO), formerly the Advanced X-ray Astrophysics Facility (AXAF). Two of the Chandra SIs are imaging detectors at the HRMA focal plane: the Advanced CCD Imaging Spectrometer (ACIS) and the High Resolution Camera (HRC). These detectors each consist of two sub-imagers: an "-I" imager (ACIS-I, HRC-I) of large area and square aspect ratio for imaging applications and an "-S" imager (ACIS-S, HRC-S) with a more rectangular aspect ratio

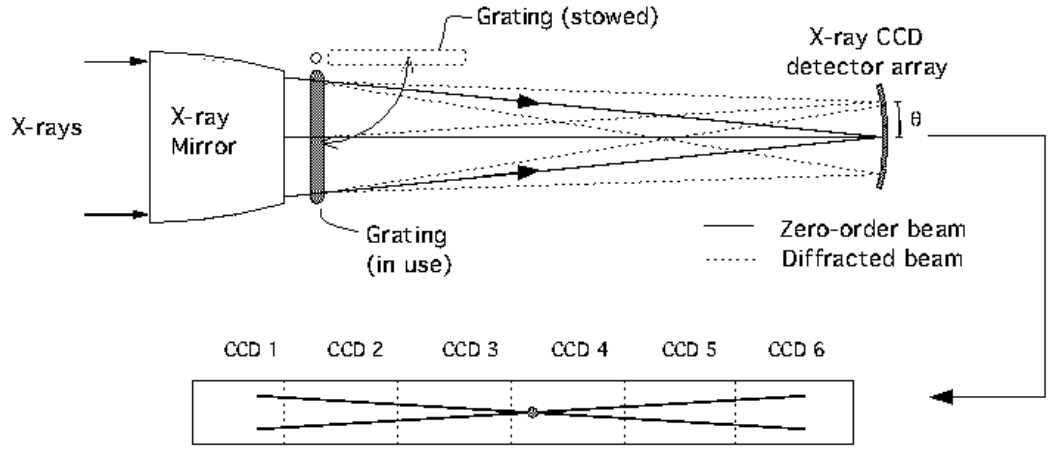

Figure 1.1: Schematic of the HETGS Configuration. The HETG can be inserted into the optical path behind the Chandra mirror (HRMA) to intercept and diffract the converging X-rays. The X-rays are diffracted by an angle β given in Equation 1.1 and are detected by the six chips of the ACIS-S CCD array. The HEG and MEG gratings have their dispersion axes oriented ± 5 degrees to the ACIS-S long axis.

designed for grating readout.

Either of the two grating SIs, HETG or LETG[15, 79], can be inserted into the optical path just behind the HRMA and, through diffraction, deflect the converging rays by angles roughly proportional to their wavelength, Figure 1.1. By combining the HRMA's high angular resolution (of order 1 arc second) and the grating's large diffraction angles (as high as 100 arc seconds/Å), the HRMA-grating-detector systems are capable of spectral resolving powers up to $E/dE \approx 1000$ in the Chandra energy band.

The prefered detector for use with the HETG is the ACIS-S array consisting of 6 imaging CCDs in a 1x6 array. An illustration of the ACIS-S focal plane layout and an HETG-diffracted spectra is shown in figure 1.2.

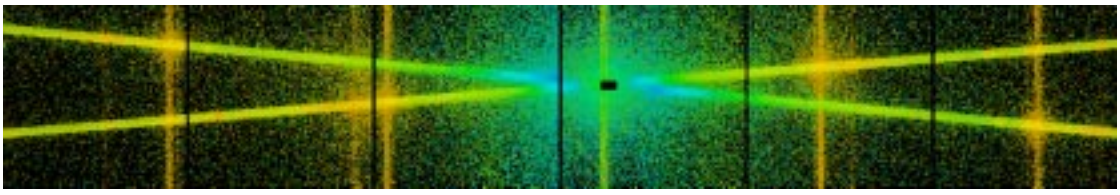

Figure 1.2: Image from the HETGS at XRCF. A unfiltered Cu-anode source produces a broadband X-ray continuum that is spread out along the HEG and MEG dispersion axes. The illustration shows the set-up of the six CCD devices, designated S0 to S5 from left to right, with the gaps between the devices. The MEG disperses into the upper right (and lower left corner), the HEG into the lower right (upper left corner). The vertical traces that appear at the 0th order image as well as at Cu-L (0.93 keV) diffracted orders are CCD-frame transfer read-out effects.

1.2 The HETG Itself

Details of the HETG have been presented previously in SPIE conferences[17, 58]. The HETG is a faceted Rowland torus design[8] that has been engineered to place each facet at its prescribed location and orientation on a Rowland torus with Rowland Diameter of 8634 mm. Specifically, in Figure 1.3 the precision, lightweight HETG Element Support Structure[77] (HESS) is populated with 336 individual grating facets. This design combined with the period and period variation properties of the facets allows high resolving powers.

The four rings of facets on the HETG are designed to intercept and diffract X-rays from the corresponding four HRMA mirror shells. Because most of the high energy area of the HRMA is due to the inner two shells, very fine period (2000 Å) "High Energy Grating" (HEG) facets are used here. The outer two shells have "Medium Energy Grating" facets ("MEG", 4000 Å period) that are efficiency-optimized below 2 keV. These two grating sets have their dispersion axes offset by 10 degrees from each other so that their spectra are spatially separated on the detector. In this way the HETG enables high-resolution spectroscopy ($E/dE > 100$) in the 0.4 keV to 9 keV band.

For reference, NASA's Level I requirements document (April 20, 1994) specifies the HETG performance requirements as follows:

> The HETG shall consist of Medium Energy Gratings and High Energy Gratings which provide dispersive spectroscopy, with minimum resolving powers (when read out with the ACIS) ranging from 700 at 0.4 keV to 90 at 4.5 keV for the medium energy grating, and from 800 at 1.0 keV to 100 at 8.0 keV for the high energy grating.
>
> The effective plus-and-minus first-order grating transmissions shall be at least 10% for energies above 1.0 keV.

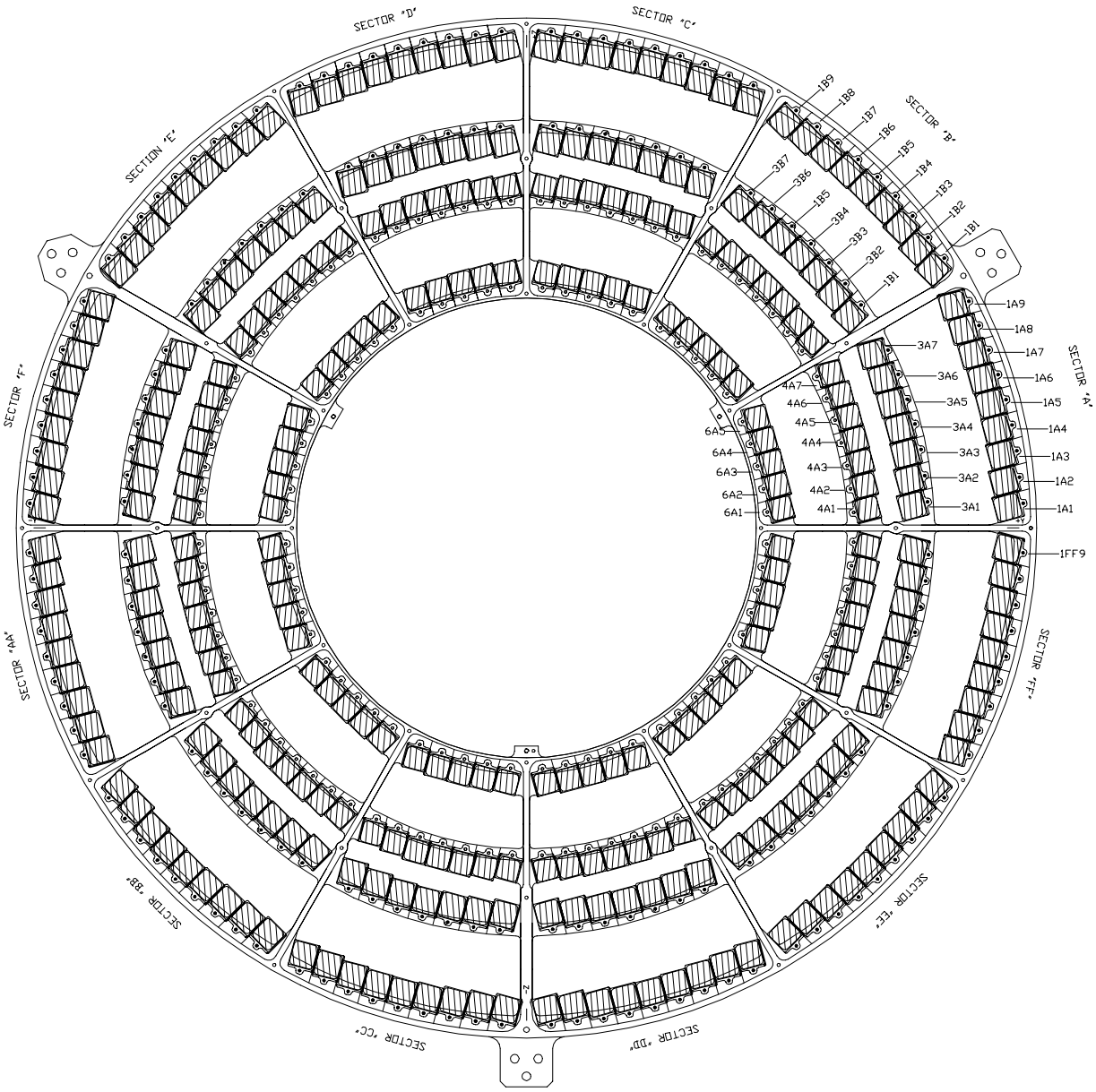

Figure 1.3: The HETG. A lightweight ($\approx$ 10 kg) aluminum structure supports 336 individual grating facets in a Rowland geometry. This view of the HETG is from the HRMA side and the facet-location identification scheme is indicated. Positive Z-axis is towards the top of the page and positive Y-axis is to the right. The HETG, as installed for ground calibration at XRCF, was rotated 180 degrees about the optical axis from this view.

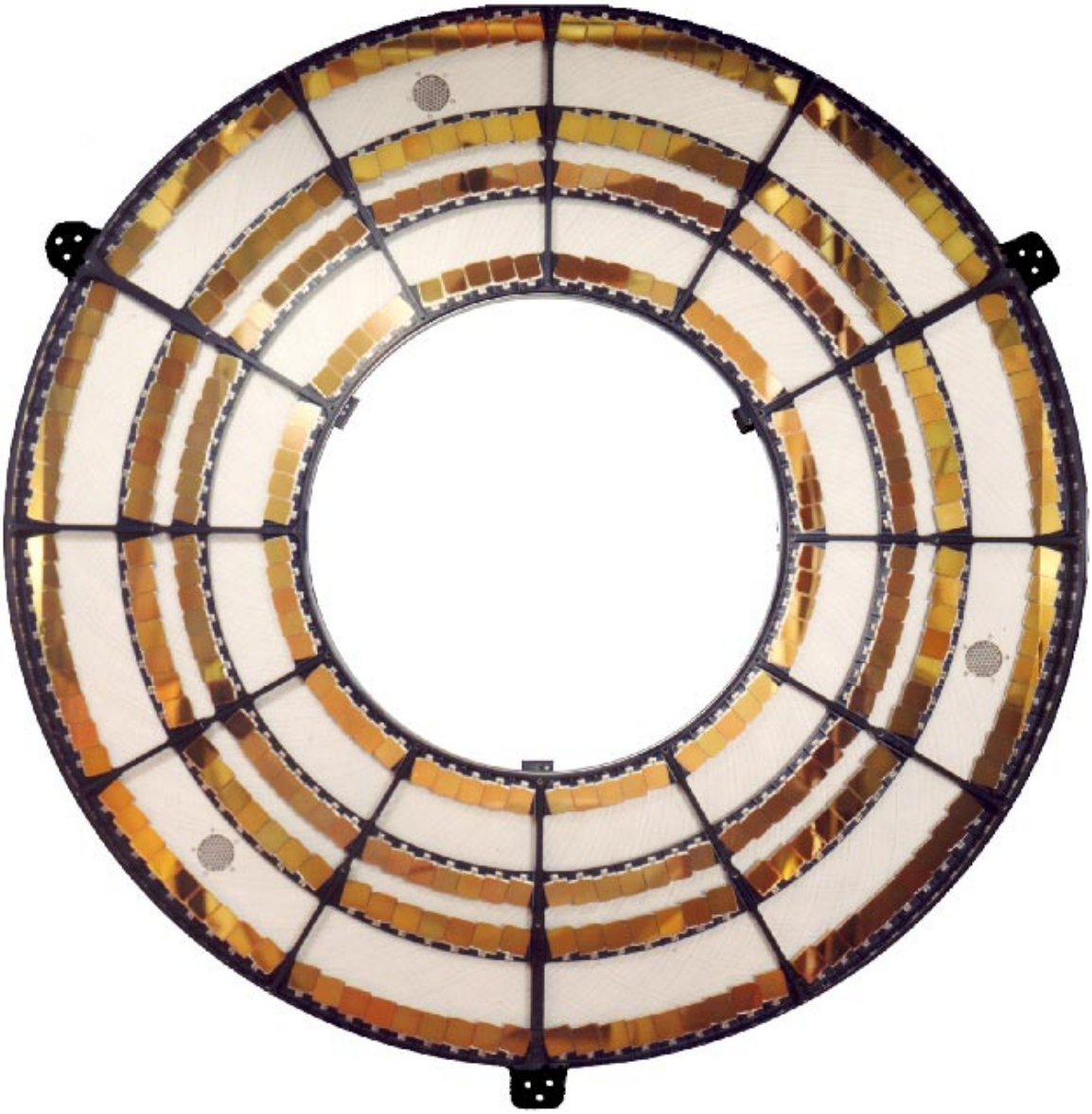

Figure 1.4: Photograph of the HETG assembly. It is made of 336 grating facets attached to a lightweight aluminum structure. The two outer rings are tiled with MEG facets, the two inner rings have HEG facets.

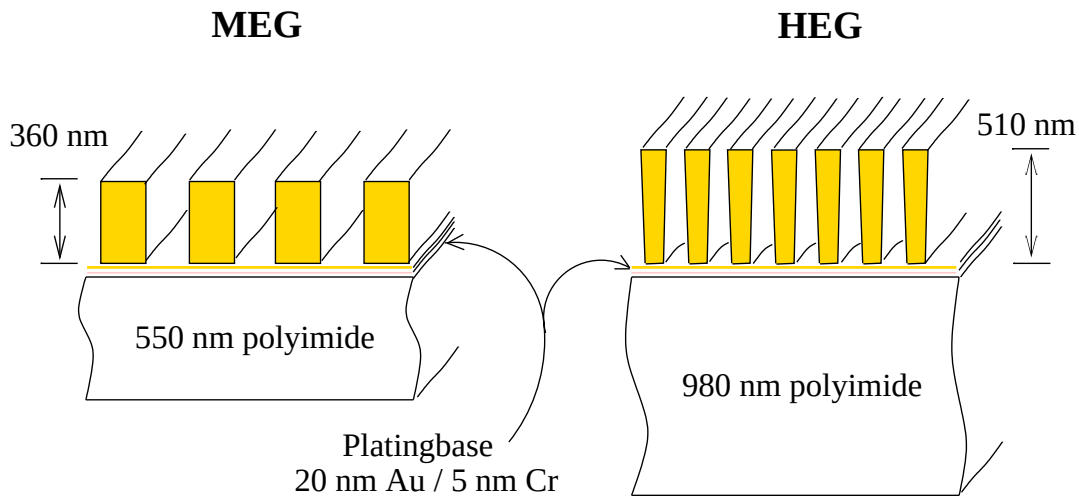

Figure 1.5: Cross-section schematic of the HETG gratings. The fine-period gold grating bars are supported on a polyimide membrane. A uniform "platingbase" layer provides adhesion of the bars to the polyimide.

1.3 Facet Fabrication Process

The 336 grating facets of the flight HETG were fabricated in-house at M.I.T. in the Space Microstructures Laboratory (SML) using state-of-the-art holographic lithography techniques[83] to create a fine period, high aspect ratio grating structures supported on a thin polyimide membranes, Figure 1.5. Each facet was then tested in-house for period and diffraction efficiency characteristics[22].

HETG grating facets were fabricated with a complicated multi-step process which is summarized here and depicted, in highly simplified form, in Fig. 1.6. Details of the fabrication process are available elsewhere [**?**].

The first step, Fig. 1.6a, is to coat 100 mm-diameter silicon wafers with six layers of polymer, metal, and dielectric, comprising either 0.5 (MEG) or 1.0 (HEG) microns of polyimide (which will later form the grating support membrane), 5 nm of chromium (for adhesion) and 20 nm of gold which serve as the plating base, ≈500 nm of anti-reflection coating (ARC) polymer, 15 nm of Ta_2O_5 interlayer (IL), and 200 nm of UV imaging photopolymer (resist).

The second step, Fig. 1.6b, is to pattern the resist layer with a grating by interference lithography with the 351.1 nm wavelength. Two essentially spherical monochromatic wavefronts interfere at a precisely repeatable angle to define the basic grating period; the radii are sufficiently large to reduce the inherent period variation across the sample to less than 50 ppm rms. A high degree of period repeatability is required from the hardware because a unique exposure is used for each grating facet of the HETG. A piggy back interferometer and active control are used to ensure that the interference pattern is stable over the of order one minute exposure time. The interlayer, ARC, and resist layers form an optically-matched stack designed to minimize the formation of planar standing waves along the surface normal which would compromise contrast and linewidth control [84].

In the third step, Fig. 1.6c, the resist pattern is transferred into the interlayer using CF_4 reactive-

ion plasma etching (RIE). In the fourth step, Fig. 1.6d, the IL pattern is transferred into the ARC using O_2 RIE. The RIE steps are designed to achieve highly directional vertical etching with minimal undercut.

The fifth step, Fig. 1.6e, is to electroplate the ARC mould with low-stress gold, which grows from the Cr/Au plating base layer. The sixth step, Fig. 1.6f, is to strip the ARC/IL plating mould using hydrofluoric (HF) acid etch, and plasma etching with CF_4 and O_2.

In the last step, Fig. 1.6g, the wafer is etched through from the backside in HF/HNO_3 acid using a spin etch process [85], stopping on the polyimide layer. The membrane is then aligned and bonded to a flight frame with a two-part, low-outgassing epoxy (Dexter Hysol A 9313) with an angular tolerance of ≤ 0.5 degree. When the epoxy has cured the excess membrane is cut away from the frame with a scalpel.

These grating frames represent a great deal of design and testing effort. The frames are black chrome plated Invar 36, chosen in order to reduce any grating period variations which might be caused by thermal variation of the HETG environment between stowed and in-use positions on **Chandra**. The frames were CNC machined to tight tolerances and the membrane bonding faces of the frames were hand lapped to remove burrs and ensure a flat, smooth surface during bonding. Mechanical details of the frame attachment to the HESS are given in the HESS section below.

As a postscript to the fabrication of the **Chandra** HETG facets, we note that even though this process represents the culmination of years of process effort, it is at the same time only a stepping stone on an advanced technology path. In particular, we have since extended our grating technology [86] to finer periods [81], mesh-supported gratings for UV/EUV and atom beam diffraction and filtering [7], and super-smooth reflection gratings [33].

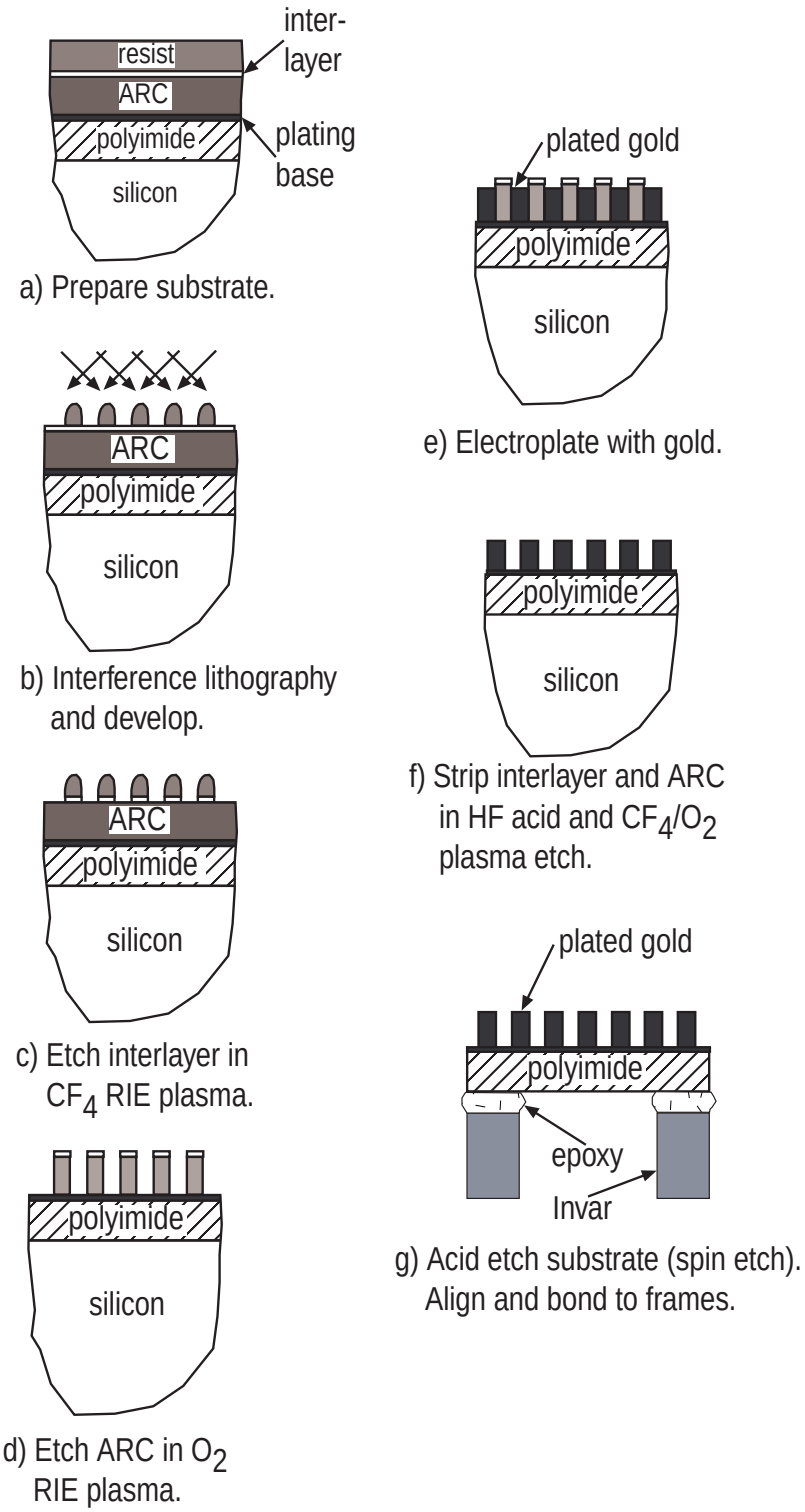

Figure 1.6: Simplified production steps for the HETG facets. The initial periodic pattern is created as the interference of two laser wave fronts. This pattern is etched into the polymer. Through electroplating gold is deposited into the spaces between polymer bars. Removal of the polymer (stripping) and Si wafer support leaves the grating membrane in the wafer center. This membrane is then aligned and bonded to the Invar frame.

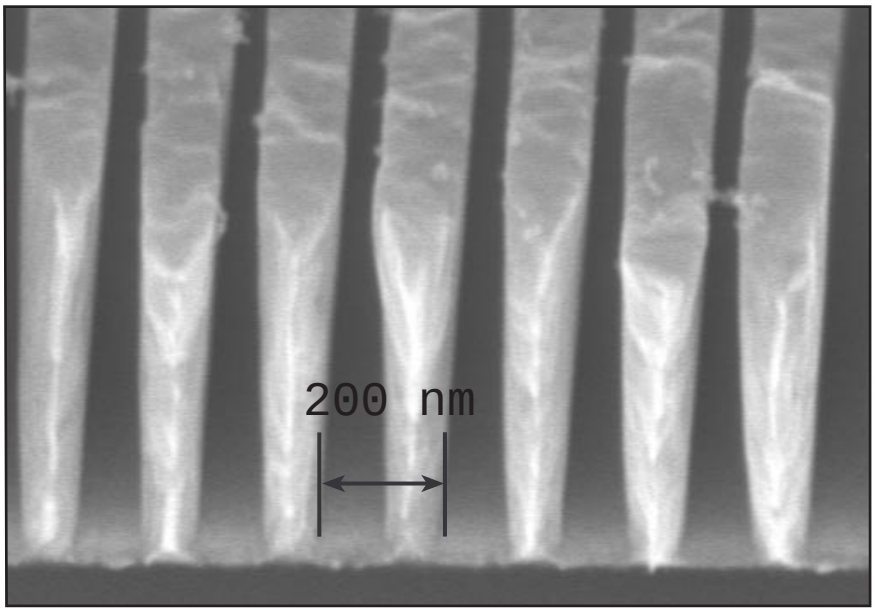

(a) High Energy Grating (HEG).

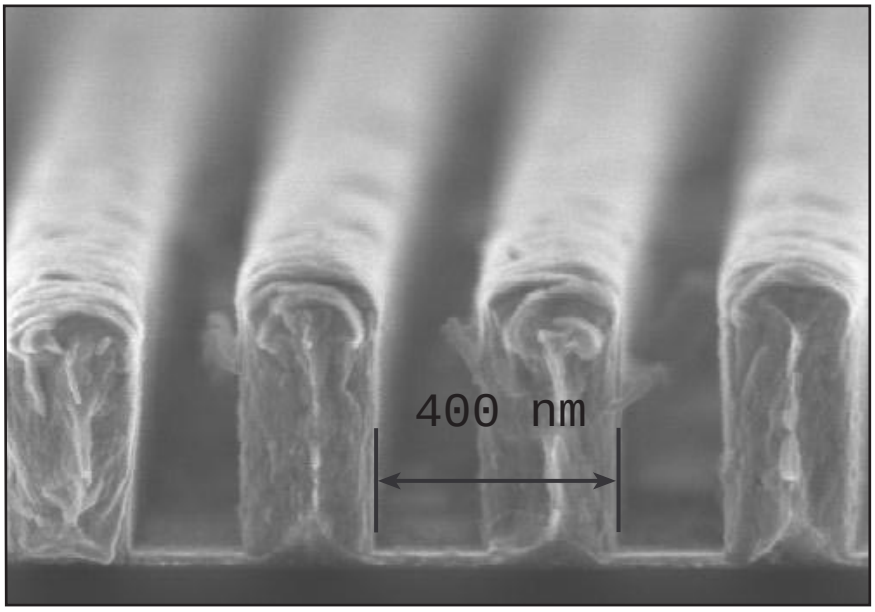

(b) Medium Energy Grating (MEG).

Figure 1.7: Electron micrographs of HEG and MEG grating bars.

1.4 HETGS Calibration Definition and Goals

The complete flight instrument that will be utilized and must be calibrated is the combination of the HRMA, HETG, and the ACIS-S—the *HETG Spectrometer (HETGS)*. The HETGS calibration requirements generally fall into two categories: calibration of the *Effective Area* and calibration of the *Line Response Function (LRF)*. Scientific goals set calibration requirements on the HETGS in these areas which are then flowed-down to requirements on the individual HEG and MEG elements themselves.

1.4.1 Effective Area and Efficiency Definitions

The HETGS response to an on-axis monochromatic point source consists of images in the various *diffracted orders* produced at locations given by the grating equation[11]:

$$sin(\beta) = \frac{m\lambda}{p} \tag{1.1}$$

where m is the order of diffraction (an integer 0, $\pm1, \pm2$, ...), p is the grating period and β is the dispersion angle. Knowledge of the dispersion axis and the grating-to-detector distance (the Rowland spacing) allows a conversion of the angle β to a physical location on the detector.

These diffracted images are, for the most part, spatially localized and so it is possible and convenient to express the system response to a monochromatic source with incident flux of 1 photon/cm^{2}s as the sum of weighted spatial functions:

$$\text{HETGS response}(E, \dots) = \sum_m SEA(E, m, \dots) \times PSF(E, m, \dots) \tag{1.2}$$

where $SEA(E, m, \dots)$ is the *system effective area*, described further below, and $PSF(E, m, \dots)$ is a unit-normalized 2-dimensional point spread function which describes the spatial distribution of the m-th order detected events, see Section 1.4.3 below. The dots $(\dots)$ in the arguments indicate that there are other dependancies, *e.g.*, off-axis angles, defocus, detector modes, etc.

The system effective area for the HETGS, in cm^{2}counts/photon, can be calculated from the following terms:

$$SEA(E, m, \dots) = \sum_{s=1,3,4,6} A_s(E, \dots)\ G_s(E, m)\ QE(E, \dots) \tag{1.3}$$

Here the sum is over the HRMA mirror shells, A_s is the *optic effective area* for HRMA shell s in cm^2, and $QE(E, \dots)$ is the detector quantum efficiency including effects of detector spatial uniformity (*e.g.*, BI/FI chips, gaps) and detection mode (*e.g.*, event grading) in counts per photon.

$G_s(E,m)$ is the average diffraction efficiency for the gratings on shell s and is calculated from the individual facet efficiencies $g_f(E,m)$:

$$G_s(E,m) = \nu_s \frac{1}{N_s} \sum_{f \in \{s\}} g_f(E,m) \tag{1.4}$$

where N_s is the number of facets on shell s and ν_s is a unitless shell-by-shell vignetting factor to account for the inter-grating gaps. Thus, the physics of $g_f(E,m)$ governs the HETG contribution to the HETGS effective area.

Finally, it is useful to define the grating "effective efficiency" for combinations of more than a single HRMA shell:

$$G_{\rm config}(E,m) = \frac{\sum_{s \in \{\rm config\}} A_s(E)\ G_s(E,m)}{\sum_{s \in \{\rm config\}} A_s(E)} \tag{1.5}$$

where "config" may usefully be the HEG (shells 4,6), MEG (shells 1,3), or HETG (shells 1,3,4,6). In practice, it is the effective efficiencies of these configurations that are measured and used.

1.4.2 Effective Area Calibration Goals

Calibration of the effective area of the HETGS is driven by the desire to extract information about the physical parameters of an emitting region (e.g., temperature, ionization age, elemental abundances) from the observed intensity of spectral lines through plasma diagnostics[19]. Analysis of the sensitivity of scientific conclusions on the calibration accuracy has led to the requirements that the HETGS effective area be known with an absolute accuracy of order 10% (1σ) at all energies, and that the relative effective area at two different energies be known to of order 3% (1σ). Note that the effective area needs to be known at least on an energy grid comparable to the coarser of the astrophysical spectrum feature scale and the instrumental response variation scale.

These requirements for HETGS calibration have implications for the calibration of the HRMA and focal plane detectors as well as the HEG/MEG elements. Ideally the effective area and/or efficiency of all components would be know accurately enough so that the composite system would be calibrated to the 3% (1σ) level on an energy scale of $\Delta E \approx E/1000$, especially around instrumental edges.

For our laboratory calibration of the HEG/MEG elements we have set a goal of 1% (1σ). This allocates most of the error to the HRMA and focal plane detector calibrations where the calibration process is inherently more difficult (i.e., measuring an effective area or an absolute detection efficiency as opposed to a transmission efficiency.)

Though not as central as the (first-order) diffraction efficiency measurements, it is important that the zero-order and higher orders be calibrated as well.

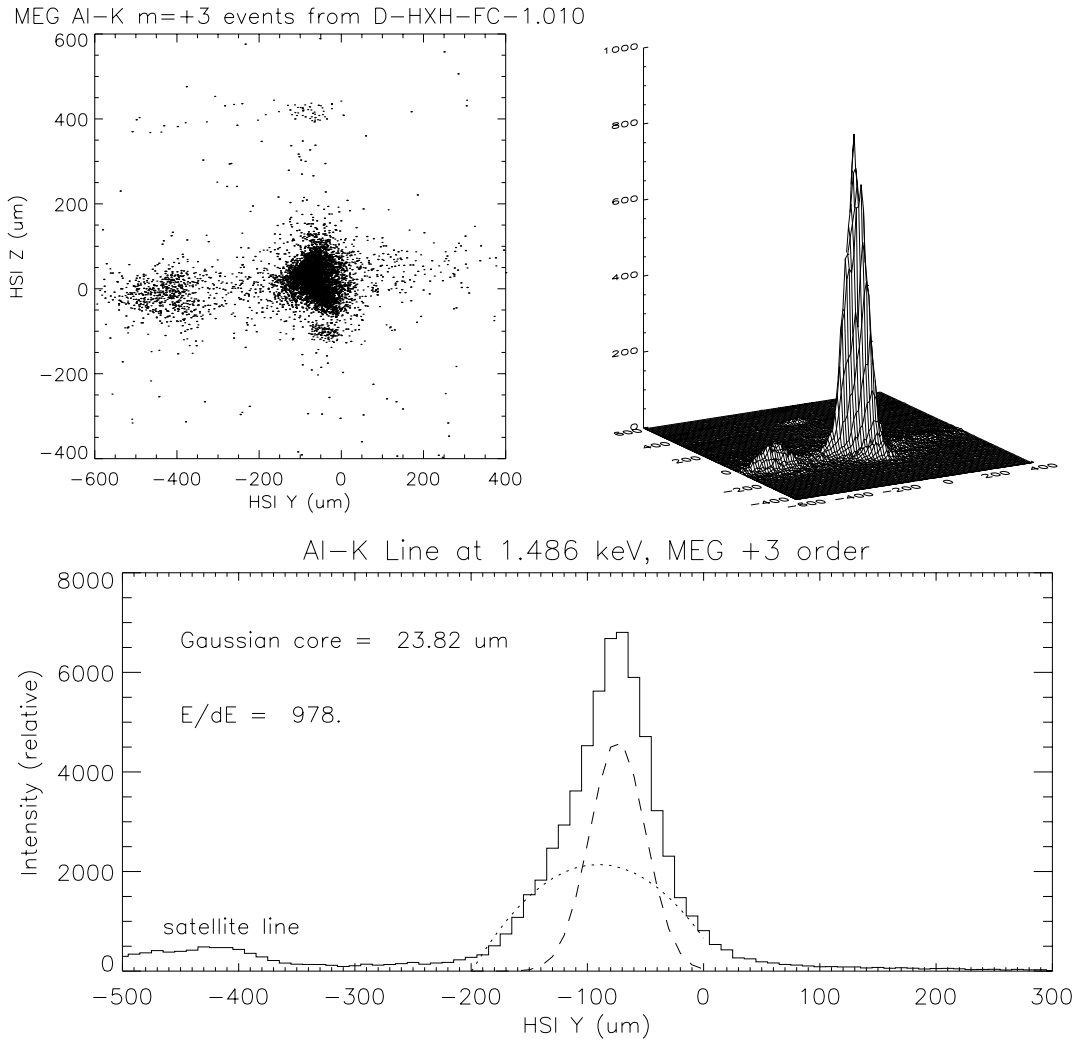

Figure 1.8: PSF and LRF example. The event distribution (top left) may be described by a 2-D point spread function PSF, $\rho(y, z)$ (top right). The resulting 1-D line response function $l(y')$ (lower plot) is shown with a Gaussian plus quadratic fit to its core.

The events are from an XRCF HSI image of the 3rd-order MEG Al-K line; the HSI is centered at HSI_Y = 54.76 mm, HSI_Z = 4.496 mm. Visible in addition to the main peak is the "satellite line" at HSI_Y = -400. PSF outliers at HSI_Z = +400 and -100 represent mis-aligned grating facets.

1.4.3 LRF Definition

As described above the focal plane image that results from a monochromatic near-axis point source can be considered as a set of images, one for each grating-order. The distribution of each of these images can be described by a *2-dimensional Point Spread Function (PSF)* which gives the normalized density of detected photons in the detector plane:

$$\rho(y,z) \Leftarrow PSF(E,m,\dots) \tag{1.6}$$

where y,z are the detector coordinates, E,m are the energy and grating-order, and "..." is again a placeholder for other dependancies, *e.g.*, the telescope defocus, location of the source with respect to the optical axis, etc. As an example, an X-ray event plot and the corresponding $\rho(y,z)$ PSF is shown in the upper plots of Figure 1.8 (these are data from XRCF and are used here for illustration purposes; they are discussed in Section 6.3.)

Because the spectroscopic information of a grating dispersive instrument is along the dispersion direction, it is useful to define the *one-dimensional Line Response Function (LRF)* to be the PSF integrated over the cross-dispersion direction:

$$L(y') = \int dz' \rho(y',z') \tag{1.7}$$

where the y',z' indicate axes aligned with the dispersion and cross-dispersion directions in the detector plane. The lower plot in Figure 1.8 gives the LRF corresponding to the example PSF. Because of the image properties of the mirror, it is generally useful to (conceptually) break the LRF into at least two regions: a core or inner LRF and the wings or outer portion of the LRF.

The *Resolving Power* of the spectrometer at energy E is defined as

$$R(E,m) \;=\; E/dE \;=\; y'_{\rm centroid}/dy'_{\rm FWHM} \tag{1.8}$$

where dE is the full-width at half-maximum (FWHM) of the LRF. Typically the LRF core can be well fit by a Gaussian profile and in this case $dE \approx 2.35\sigma$ approximates the FWHM.

1.4.4 LRF Calibration Goals

The goal of HETGS LRF calibration is to produce LRF models which are accurate (have low χ^2) when fitting a line containing of order 1000 counts. Additionaly, it is important that any "wings" or "ghosts" in the dispersed spectrum be identified and quantified. Specifically, the contribution of wings at all scales should be known or limited to 1% of the peak line flux in a resolution element.

1.5 Ground Calibration Overview

The HETG ground calibration program consists of 4 main activities:

- Creating and validating models for the HETGS LRF performance, Section 2.
- Synchrotron testing of sample and reference gratings to understand and validate the diffraction model $g_f(E, m)$, Section 3.
- Laboratory testing and assembly of all flight gratings, Section 4.
- XRCF tests of the flight hardware, Part II, Sections 5-7.

1.6 Related Documents

Table 1.1: Chandra and HETG Documents

Printed documents:		
Chandra Proposers' Observatory Guide	CXC	Dec. 2000
MARX V 2.22 Manual	CXC/MIT	Sept. 1999
Electronic documents:		
`http://asc.harvard.edu`	CXC Science	-
`http://space.mit.edu/HETG`	HETG Home Page	-
`http://space.mit.edu/ASC`	CXC/MIT home page	-
`http://space.mit.edu/ASC/MARX`	MARX	-
`http://wwwastro.msfc.nasa.gov/xray`	Project Science	-

Table 1.2: XRCF Documents

MSFC-RQMT-2229 Calibration Requirements	PS	TBD
XRCF Phase 1 Testing: Preliminary Results	MST	June 1997
Calibration of the AXAF: Project Science Analyses	Weisskopf *et al.*	October 1997

Part I

Physics, Models, and Laboratory Measurements

Section 2

LRF Physics and Model

2.1 Rowland Geometry and Astigmatism

A detailed discussion of the physics of Rowland spectrometers is beyond the scope of this report. What follows is a brief discussion of the basic principles as they apply to the HETGS. Please consult the references for more detailed accounts, including derivation of grating, astigmatism, coma, and aberration equations using Fermat's principle[89], or for specific effects of the faceted grating design.[8]

The HETGS is a simple transmission Rowland spectrometer in which the gratings and detector are located on opposite sides of a Rowland circle. It is important to emphasize that in this design the HETG serves to *deflect* the rays from the mirror while retaining the mirror's excellent focussing characteristics in the dispersion direction. The HETG does not provide focussing of the rays *per se.*

The HETG is a faceted Rowland torus design and has been engineered and built to accurately place each facet at its prescribed location and orientation. Although physical-optics analysis of the image produced by this Rowland design can be quite complex[8], the basic features can be understood through simple ray geometry.

In the "Top View" of Figure 2.1 we are looking along the cross-dispersion direction, z'. The diffraction angle is β, as defined by Equation 1.1. Through the geometric properties of the circle, rays diffracted from gratings located along the Rowland circle will all converge at the same diffracted point on the Rowland circle. The dotted lines represent zero-order ($m = 0, \beta = 0$) rays and the solid lines a set of diffracted order ($m > 0, \beta > 0$) rays. The physical distance from zero order to the $m_{\rm th}$ diffracted order, the dispersion distance $D_{\rm disp}$, is given to good approximation by:

$$D_{\rm disp} \approx (\frac{m\frac{hc}{E}}{p})(X_{\rm RS}) = (\frac{m\frac{12.3985}{E_{\rm keV}}}{p})(X_{\rm RS}) \tag{2.1}$$

The bottom panel, "Side View", looks along the dispersion direction, y', at rays from a set of gratings arranged perpendicularly to those above. The grey shaded gratings are the same gratings as visible in the Top View, located on the same Rowland circle, now seen in projection.

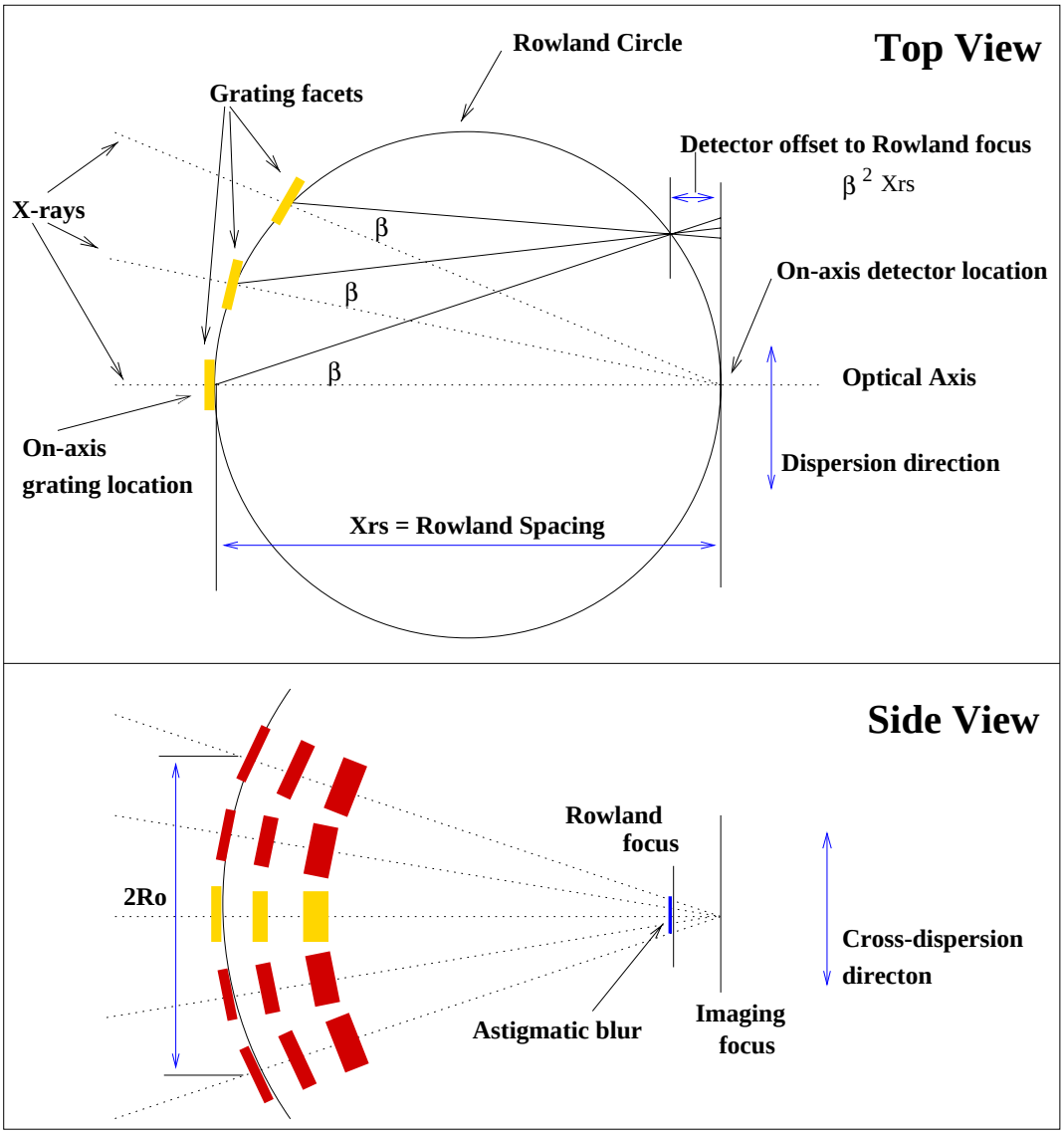

Figure 2.1: Simplified ray geometry for the Rowland torus design. The *Top View* shows the spectrometer layout viewed from +Z ("above AXAF") with the HRMA off the page to the left. X-rays reflected by the HRMA come to a focus at zero order (dotted lines). The grating facets diffract the rays into the m_{th}-order spectra at angle β with respect to the optical axis, and bring the dispersed spectrum to a focus on the Rowland circle (solid lines). The Rowland Spacing, X_{RS}, is the diameter of the Rowland circle and the distance from the gratings to the detector. In the *Side View*, we see the cross-dispersion projection of the same rays. Notice that in the cross-dispersion-direction, the diffracted rays focus behind the Rowland circle.

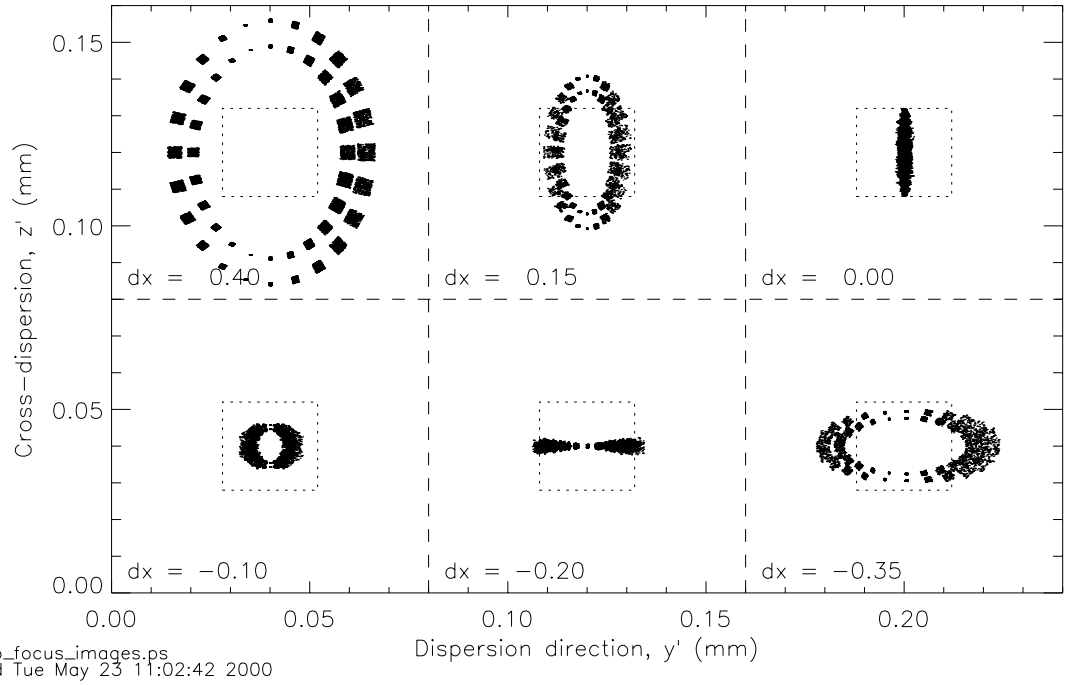

Figure 2.2: Ray-trace of Faceted Rowland Geometry, 19 Å MEG images vs defocus. The focal properties of the faceted Rowland design are demonstrated in this set of images at different defocus values, dx; positive values are a displacement of the detector towards the grating. Parameters of the simulation approximate the MEG gratings on **Chandra** at a wavelength of 19 Å. At large defocus values (dx=0.40 mm) the rays from each facet are visible, here there are 24 facets in each of two shells. The image comes to a minimum width in the dispersion direction at the Rowland focus, $dx = 0$, with a finite cross-dispersion width. At a defocus of $dx \approx -0.20$ the local detector surface is in the focal plane and the image is now best focussed in the cross-disperion direction. These spot diagrams were created by simple ray-tracing of a perfect focussing optic combined with a faceted grating set – hence, the inherent astigmatism and finite facet-size blur of the Rowland design dominate these images. For reference, the dotted square is the size of an ACIS pixel.

If the Rowland circle in the Top View is rotated about the dispersion direction axis, it will trace out the additional projected Rowland circles and grating facets shown in the Side View (black facets). The surface this rotation describes is the *Rowland torus*. Grating facets with their centers located on the torus and their surfaces normal to the converging light rays (dotted lines) will focus diffracted orders on the Rowland circle. Since the Rowland spacing is the same for all grating facets, and the zero order focus coincides for all facets, the $m_{\rm th}$ diffracted order from each facet is focussed at the same angle β, at the same place on the Rowland circle. That is, best focus for the dispersion direction projection occurs along the inner surface of the Rowland torus, which is approximately along the original (horizontal) Rowland circle.

Together, these constructions show the astigmatic nature of the spectrally focussed image: the rays come to a focus in the dispersion direction, the *Rowland focus*, at a different location from their focus in the cross-dispersion direction, the *Imaging focus*. This character is shown in the simple ray-trace example of Figure 2.2. Hence, with a detector curved to follow the Rowland focus (maintaining "$dx = 0$"), the diffracted orders of monochromatic lines are focussed and sharp in the dispersion direction, and elongated in the cross-dispersion direction.

The detector offset required to be on the Rowland circle is given by:

$$\Delta X_{\mathrm{Rowland}} = \beta^2 X_{\mathrm{RS}} \tag{2.2}$$

where X_{RS} is the Rowland spacing. In order to maintain the best spectroscopic focus the detector surface must conform to or approximate this Rowland curvature.

At the Rowland focus, *e.g.*, the $dx = 0$ case in Figure 2.2, the image is elongated (blurred) in the cross-dispersion direction, z', due to the astigmatic nature of the focus and has a peak-to-peak value given by:

$$\Delta z'_{\mathrm{astig}} = \frac{2R_0}{X_{\mathrm{RS}}} \Delta X_{\mathrm{Rowland}} \tag{2.3}$$

Here R_0 is radius of the ring of gratings around the optical axis as defined in Figure 2.1. The width of this image in the dispersion direction, y', is given by a term proportional to the size of the (planar) grating facets which tile the Rowland torus. The peak-to-peak value of this "finite-facet size" blur is given by:

$$\Delta y'_{\mathrm{ff}} = \frac{L}{X_{\mathrm{RS}}} (R_0 \beta + \frac{\Delta X_{\mathrm{Rowland}}}{2}) \tag{2.4}$$

where L is the length of a side of the square grating facet.

It is important to note (again) that in the ideal case the grating provides primarily a deflection to the rays being focussed by the HRMA. Because of this, the focus quality is not dramatically effected by perturbations of the grating geometry from the ideal Rowland Torus design. In particular, the flight HETG is built to a Rowland diameter of 8633.69 mm, yet at XRCF because of the finite source distance changes to the HRMA focal length and other considerations, the HETG Rowland spacing (on-axis grating to detector distance) was of order 8800 mm. This difference adds an insignificant additional spectral blur (of order 1 μm rms.)

2.2 LRF Approximation: Resolving Power Error Budget

For design trade-off purposes it is useful to have a simplified set of spread-sheet-like equations which calculate the monochromatic LRF blur and hence the resolving power vs energy for given parameter values. These equations are presented here relevant to the HETGS instrument design.

The LRF of the HETGS can be crudely yet usefully characterized by the location and FWHM of the LRF core in both the dispersion and cross-dispersion directions. The "resolving power" of the spectrometer is given by $E/dE = y'/dy'$ where y' is the diffraction distance and dy' is the FWHM of the resulting image projected along the dispersion axis. The design of the HETG involved the use of an error budget to sum the various contributions to the "dy'" term of the resolving power. This error budget was useful for studying the dependence of the resolving power on the variation of individual error terms. The error budget results were verified by performing simplified ray-traces of single and multiple facets.

The error budget presented in Table 2.1 includes all of the important error terms for the flight HETGS resolving power. For compactness the error equations are only referenced in the table and given, with discussion, in the following text.

The LRF of the HETGS can be crudely yet usefully characterized by the location and FWHM of the LRF core in both the dispersion and cross-dispersion directions. The "resolving power" of the spectrometer is defined by:

$$\text{ResolvingPower} = \frac{E}{dE_{\text{FWHM}}} = \frac{y'}{dy'_{\text{FWHM}}} \tag{2.5}$$

The design of the HETG involved the use of an error budget to sum the various contributions to the resolving power. This error budget was useful for studying the dependence of the resolving power on the variation of individual error terms. The error budget results were verified by performing simplified ray-traces of single and multiple facets.

The error budget presented in Table 2.1 includes all of the important error terms for the flight HETGS resolving power; a resulting range of "realistic" curves for the flight HETGS resolving power is plotted as the solid and dashed curves in Figure 2.3.

The error budget terms, their equations, and the current flight value estimates are discussed in the sections below.

Optics PSF Blur: If the optic produces a roughly symmetric Gaussian-like PSF with an rms diameter of D_{PSF} arc seconds, then the Gaussian sigma of the 1-D projection of the PSF is given, in units of mm in the focal plane, by:

$$\sigma_{y'} = \sigma_{z'} = \sigma_H = \frac{1}{2}\frac{\sqrt{2}}{2} \quad F \quad D_{\text{PSF}} \quad (\frac{1}{57.3})(\frac{1}{3600}) \tag{2.6}$$

where F is the focal length of the optic, Table 2.1. This equation is useful when specific models of the optic PSF are not available.

The above equation for σ_H could be extended in two respects given knowledge of the optic. First there is generally a dependance on energy which is slowly varying, thus σ_H can be expressed

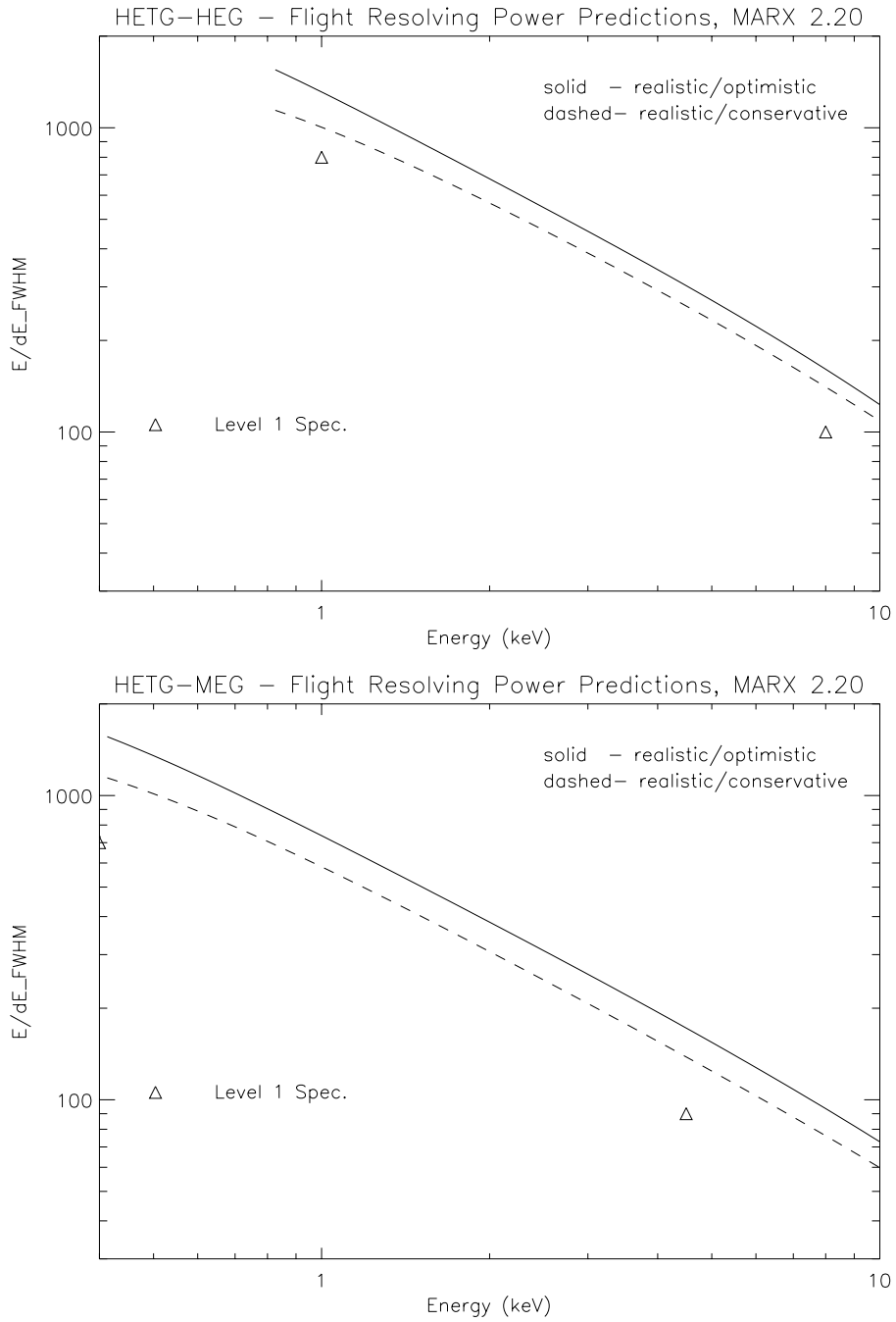

Figure 2.3: Resolving Power for the HEG and MEG spectra of the HETGS plotted vs. energy. The resolving power at high energies is dominated by the HRMA blur; at low energies the grating's effects become important.
The solid and dashed curves are the current range of realistic flight HETGS estimates. The "optimistic" solid curve is calculated from the parameters shown in Table 2.1 and related equations. The dashed curve is the same except for a (plausible) degradation in aspect, focus, and grating dp/p to: $a = 0.6, dx = 0.2, dp/p = 250 \times 10^{-6}$.

Error Description	*Error Parameter*			Blur Equations (rms μm)	
	Symbol	Key Value	Units	Dispersion Blur	Cross-Disp Blur
	Blur Sources:			$\sigma_{y',i}$	$\sigma_{z',i}$
Optics PSF	$D_{\rm PSF}$	≈ 0.6	arc sec rms dia.	Equ. 2.6, or 2.8[2.9]	Equ. 2.6, or 2.8[2.9]
Aspect	a	0.34	arc sec rms dia.	Equ. 2.10	Equ. 2.10
Detector pixel	$L_{\rm pix}$	0.024	mm	Equ. 2.11	Equ. 2.11
Dither rate	$R_{\rm dither}$	0.16	arc sec/$t_{\rm frame}$	Equ. 2.12	Equ. 2.12
Defocus w/astig.	dx	0.1	mm	Equ. 2.13	Equ. 2.14
Period variation	dp/p	162[146]	$\times 10^{-6}$ rms	Equ. 2.15	...
Roll variation	γ	1.5	arc min. rms	...	Equ. 2.16
			Total blur:	$\sigma_{y'}^{\rm tot} = \sqrt{\sum_i \sigma_{y',i}^2}$	$\sigma_{z'}^{\rm tot} = \sqrt{\sum_i \sigma_{z',i}^2}$
			Resolving power:	$E/dE = \frac{\beta X_{\rm RS}}{2.35\sigma_{y'}^{\rm tot}}$	
	Input Parameters				
Energy	E	as desired	keV		
Period	$p_{\rm MEG}$	4001.41	Å		
	$p_{\rm HEG}$	[2000.81]	Å		
Effective Radius	R_0	470.[330.]	mm		
Rowland spacing	$X_{\rm RS}$	8634.	mm		
Focal length	F	10065.5	mm		
	Derived Values:				
Rowland offset	$\Delta X_{\rm Row'd}$	$\beta^2 X_{\rm RS}$	mm		
Diffr. angle	β	$\sin^{-1}(m\lambda/p)$	radians		
Wavelength	λ	12.3985/E	Å		

Table 2.1: Simplified Resolving Power Error Budget. The major terms which contribute to the HETGS LRF blur are listed. The effective rms contributions to the dispersion and cross-dispersion blur are given by the referenced equations in the text. These blurs can be rss'ed together to arrive at the size of the Gaussian LRF core in each direction, $\sigma_{y',i}$ and $\sigma_{z',i}$. The resolving power, E/dE, can be likewise calculated. The parameter values listed here and in the equations are ground-based estimates for the HETGS. Entries that differ for MEG and HEG gratings are shown as "MEG_value[HEG_value]".

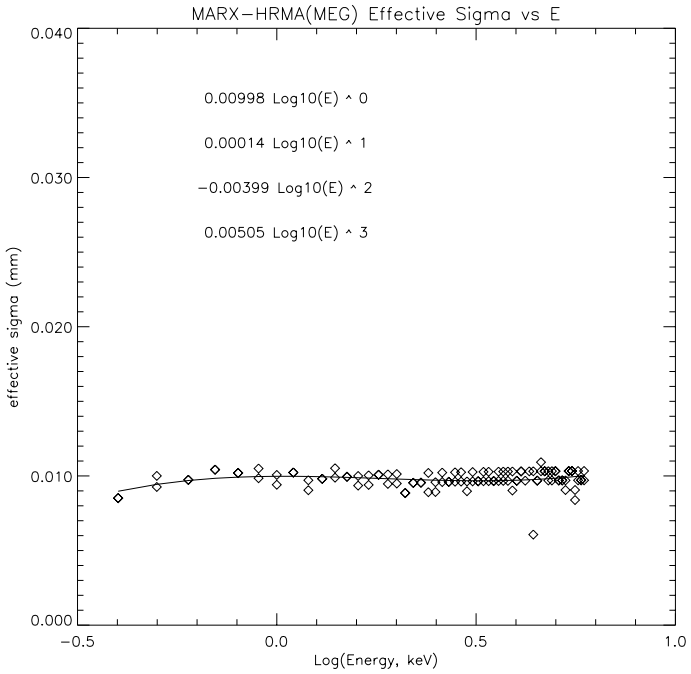

Figure 2.4: Fitting the **MARX** MEG HRMA Effective Blur

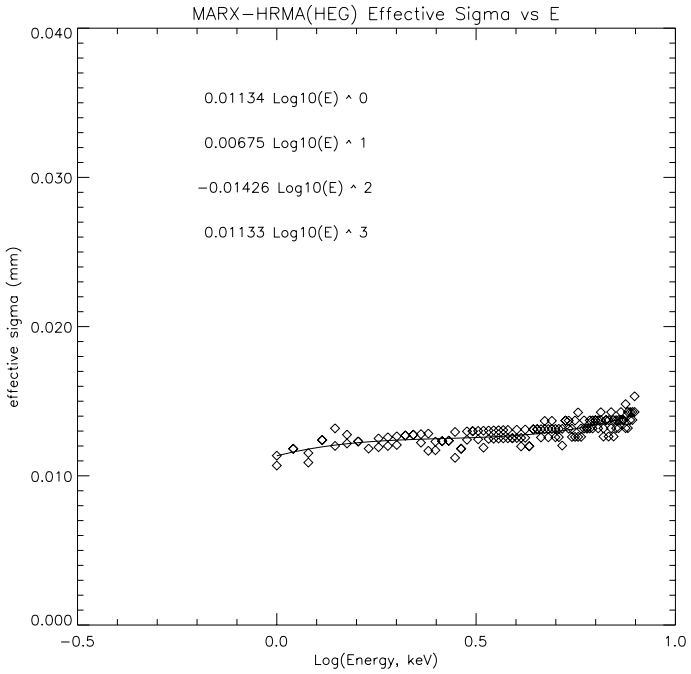

Figure 2.5: Fitting the **MARX** HEG HRMA Effective Blur

as, say, a polynomial in $\log_{10}(E)$. Second, in the case of **Chandra**, the PSF of the mirror shells is more cusp-like than Gaussian. This cusp-like PSF causes the *effective* sigma of the PSF projection to depend on the scale at which it is used, that is the size of other error terms it is convolved with.

Specifically, an effective optic blur can be determined by measuring the total resulting width, σ_T, of the convolution of the optic PSF with a Gaussian representing the other error budget terms, σ_o. The difference between these:

$$\sigma_H \equiv \sqrt{\sigma_T^2 - \sigma_o^2} \tag{2.7}$$

is the effective Gaussian sigma of the optic when used at a scale σ_o. This procedure was carried out using the approximation to the flight HRMA embodied in the MARX software, Version 2.20; plots are shown in Figures 2.4 and 2.5.

The following equations give good approximations to the value of σ_H when $\sigma_o \approx 0.0107\ mm$. Note that the HEG and MEG mirror sets are seperated here as is the case for diffracted orders; the zeroth-order is composed of all 4 HRMA shells.

$$\sigma_{H,MEG} = 0.00998 + 0.00014 \log_{10} E + -0.00399 \log_{10}^2 E + 0.000505 \log_{10}^3 E \tag{2.8}$$

$$\sigma_{H,HEG} = 0.01134 + 0.00675 \log_{10} E + -0.01426 \log_{10}^2 E + 0.01133 \log_{10}^3 E \tag{2.9}$$

Aspect Blur: Aspect reconstruction adds a blur that is expected to be of order $a = 0.34$ arc seconds rms diameter. The resulting one-dimensional rms sigma is thus:

$$\sigma_{y'}, \sigma_{z'} = \frac{1}{2}\frac{\sqrt{2}}{2} \; F \; a \; (\frac{1}{57.3})(\frac{1}{3600}) \tag{2.10}$$

where F is the HRMA focal length in mm.

Detector Pixel-size Blur: This error term is the spatial error introduced by the detector readout scheme. For a pixelated detector like ACIS we assume that the PSF drifts with respect to the detector pixels and there is a uniform distribution of the centroid location in pixel phase. In this case the reported location of an event is the center of the pixel when in fact the event may have actually arrived ± 0.5 pixel from the center. The rms value of such a uniform distribution is 0.29 times the pixel size. A further uniform blur is added to randomize the quantized pixel values and results in the factor of $\sqrt{2}$ below.

$$\sigma_{y'} = \sigma_{z'} = \sqrt{2}\ 0.29\ L_{\rm pix} \tag{2.11}$$

Dither Rate Blur: A blur is added because the arrival time of a photon at the ACIS detector is quantized in units of a frame time. The parameter $R_{\rm dither}$ is the maximum dither rate expressed in units of arc seconds per frame time and results in a blur term of:

$$\sigma_{y'}, \sigma_{z'} = 0.29 \; \frac{\sqrt{2}}{2} \; F \; R_{\rm dither} \; (\frac{1}{57.3})(\frac{1}{3600}) \tag{2.12}$$

where the factor of $\frac{\sqrt{2}}{2}$ is present because the dither pattern is sinusoidal.

Defocus and Astigmatism Blurs: Including the effect of a defocus, dx, and a factor converting the peak-to-peak blur into an rms equivalent, we get the following equations for the

Rowland astigmatism contribution to the error budget:

$$\sigma_{y'} = 0.354 \, \frac{2R_0}{X_{\rm RS}} \, dx \tag{2.13}$$

$$\sigma_{z'} = 0.354 \, \frac{2R_0}{X_{\rm RS}} \, (\Delta X_{\rm Rowland} + dx) \tag{2.14}$$

These equations assume that the detector conforms to the Rowland circle except for an overall translation by dx (positive towards the HRMA). The values of R_0 used in the error budget are effective values – weighted combinations of the relevant mirror shells.

Grating Period and Roll Variation Blurs: There are two main error terms which depend on how well the HETG is built: i) period variations within and between facets ("dp/p") and ii) alignment ("roll") variations about the normal to the facet surface within and between facets. The period variations lead to an additional blur in the dispersion direction:

$$\sigma_{y'} \approx \beta \, X_{\rm RS} \, \frac{dp}{p} \tag{2.15}$$

where dp/p is the rms period variation. The roll errors lead to additional blur in the cross-dispersion direction through the equation:

$$\sigma_{z'} \approx \beta \, X_{\rm RS} \, \gamma \, (\frac{1}{57.3})(\frac{1}{60}) \tag{2.16}$$

where γ is the rms roll variation in units of arc minutes.

2.3 Ray-trace Software: MARX

The design of the HETG has required ray-trace software in addition to simple error budgeting. Tom Markert initiated these efforts by using Webster Cash's IRT (interactive Ray-Trace) IDL package. This IRT framework was also used for the "error-budget-ray-trace" work, *e.g.*, Figure 2.2 in the previous section. In addition, IDL lookup table software (`axaf1.pro`) was developed by the HETG team for effective area studies and simulations. With the addition of ASC personel at MIT these HETG modeling efforts evolved into a pseudo ray-trace IDL code, `sim`, which was then ported to C (`csim`). Because of in-house physics/software expertise (John Davis), `csim` evolved from an error-budget-efficiency combination into a full up ray-trace code. Finally, for release as an ASC product `csim` was renamed **MARX** .

MARX , therefore, is the main HETG ray-trace code and is a joint ASC/HETG effort. It is planned that **MARX** embody all relevant effects for HETGS modeling and simulation. Please see `http://space.mit.edu/ASC/MARX` for more information on **MARX** . **MARX** version 2.22 captures the version used and referred to in this report.

2.3.1 XRCF Simulations with MARX

Custom IDL code (`marx/xrcf_sim.pro`) was produced to create modified MARX parameters for a given XRCF measurement. Some items of note in this respect are:

- The modeled spectrum is used as the SpectrumFile with SourceFlux=0.0.
- Generally the ExposureTime is set to 0.0 and the simulation controlled by the NumRays.
- The source distance is set to 537.583 meters; this is the sum of the source-to-HRMA distance, 527.522 meters, and the HRMA-to-infinite-source-focus distance in **MARX** of 10.061 meters.
- A finite source size is modeled with SourceType="DISK" and S-DiskTheta1=0.0959.
- The nominal in-focus detector position is offset to -194.872 mm.
- The MARX grating RowlandDiameter is set to the actual XRCF value minus the 194.872 mm focus offset.
- To better agree with XRCF performance, HRMABlur is set to 0.30 arc seconds.
- The effect of the HXDS axes alignment, Section 5.1.5.1, is included in FPC, SSD, and HSI simulations.
- To simulate the HXDS detectors, the HRC-I is used as the detector for its large, planar field. Additionally HRC-I-BlurSigma=0.0 and DetIdeal="yes".
- The IDL s/w post-processes the simulated events to apply the actual HXDS detector quantum efficiencies.
- The MARX coordinates are flight coordinates and hence are rotated by 180 degrees about the X-axis from the XRCF coordinate system.

Note that **MARX** version 2.22 (and 3.0X) does not include the anomalous HEG scattering seen in XRCF data; this should be a negligible effect in general.

Section 3

Efficiency Physics and Model

The key physics used to model the HETGS effective area comes in at the level of the single-grating diffraction efficiency $g_f(E, m)$ appearing in Equation 1.4. This section describes the physics of the diffraction efficiency model, the determination of the relevant optical constants used by the model, and shows the resulting level of agreement achieved. Synchrotron measurements of diffraction efficiency play a key role here.

The model, optical constants, and calibrated "reference gratings" then play a crucial role in lab measurements of the HETG gratings' diffraction efficiency; application of these results to the HETG efficiency prediction and estimates of its uncertainty is deferred to Section 4.2.

Testing at XRCF revealed anomalous scattering in the HEG, Section 6.6. The physical mechanism for this scattering appears to have been identified and its theory is presented in this section as well.

3.1 Diffraction Theory and Models

3.1.1 Scalar Diffraction Theory

The model we use is the simple scalar (Kirchhoff) diffraction theory [11]; rigorous diffraction theory, using the vector properties of the electromagnetic field and appropriate boundary conditions for the grating bars, is not required so long as the wavelength of the light being considered is much less than the period of the grating. Since we are dealing with, at most, wavelengths of 30 Å, and the grating period is no less than 2000 Å (for the HEG gratings) this condition is fulfilled fairly well. We note that the scalar model will begin to err at the lowest energies of interest, and that we will have to consider the more rigorous method (at least at the lower energies) as we continue to refine the model.

The general formula for the efficiency of a periodic transmission grating, using the Kirchhoff diffraction theory with the Fraunhofer approximation is [11, 48]:

$$\eta_{(m)}(k) = 1/p^2 \times \left| \int_0^p dx e^{ik(\nu(k)-1)z(x/p)+i2\pi mx/p} \right|^2 \tag{3.1}$$

where $\eta_{(m)}$ is the efficiency in the m^{th} order, k is the wavenumber ($2\pi/\lambda$), $\nu(k)$ is the complex index of refraction often expressed in real and imaginary parts as $\nu(k) - 1 = -(\delta(k) - i\beta(k))$, p is the grating period, and, $z(\xi)$ is the grating path-length function of the normalized coordinate $\xi = x/p$. The path-length function $z(\xi)$ may be thought of as the thickness of the grating bar versus location within the grating bar.

In addition to the parameters indicated in equation 3.1, there are other factors which effect the measured diffraction efficiencies. These are the absorptions of the support film (see Figure 1.5) and the plating base. The grating is built up onto a thin (0.98 μm for the HEGs, 0.55 μm for the MEGs) polyimide film which provides mechanical support. In addition, there are very thin metallic films ($\simeq$ 200 Å of gold and 50 Å of chromium) which are used for the electroplating process. These films are essentially uniform over the grating and serve only to absorb (and not diffract) X-rays. However, their absorption introduces edge structure which has been investigated through testing at synchrotrons (described below).

Thus, the parameters for the scalar model (with absorption) of the HETG gratings are:

$\beta(k)$ and $\delta(k)$, the components of the index of refraction for gold

$z(\xi)$, the bar shape function (note that the grating period is not an explicit parameter, but only scales the bar shape)

t_{au}, the thickness of the gold plating base

t_{cr}, the thickness of the chromium plating base

t_{poly}, the thickness of the polyimide support film

$\beta_{polyimide}(k)$ and $\beta_{cr}(k)$, the imaginary parts of the index of refraction, which give the transmission of the support film and the plating base.

The scalar model fits our data fairly well, even if a simple rectangular grating bar shape is assumed [87], [71]. However, in order to match the data at the 1 per cent level, we find in general that more complex path-length functions must be invoked. In addition, we have independent evidence, from electron microscope photographs, Figure 1.7, that the bar shapes for the HETG gratings are not simple rectangles.

The path-length function $z(\xi)$ can be reduced to a finite number of parameters. For example, if a rectangular bar shape is assumed, then z can be computed with two parameters, a bar width and a bar height. Fischbach *et al.* [28] have reported on the theory and measurements of tilted rectangular gratings which creates a trapezoidal path-length function for small incident angles.

For our modeling, the grating bar shape is parameterized as piece-wise linear, defined by the location of vertices, as shown in the insets of Figure 3.1. Each vertex is specified by its normalized location, ξ_j, and thickness, $z(\xi_j)$; fixed vertices at (0,0) and (1,0) are assumed in addition to the variable vertices. We have found in our modeling that 5 variable vertices is sufficient to broaden the space covered by the model and yet not introduce redundant parameters. Specifics of this vertex model are presented in Section 3.1.2.

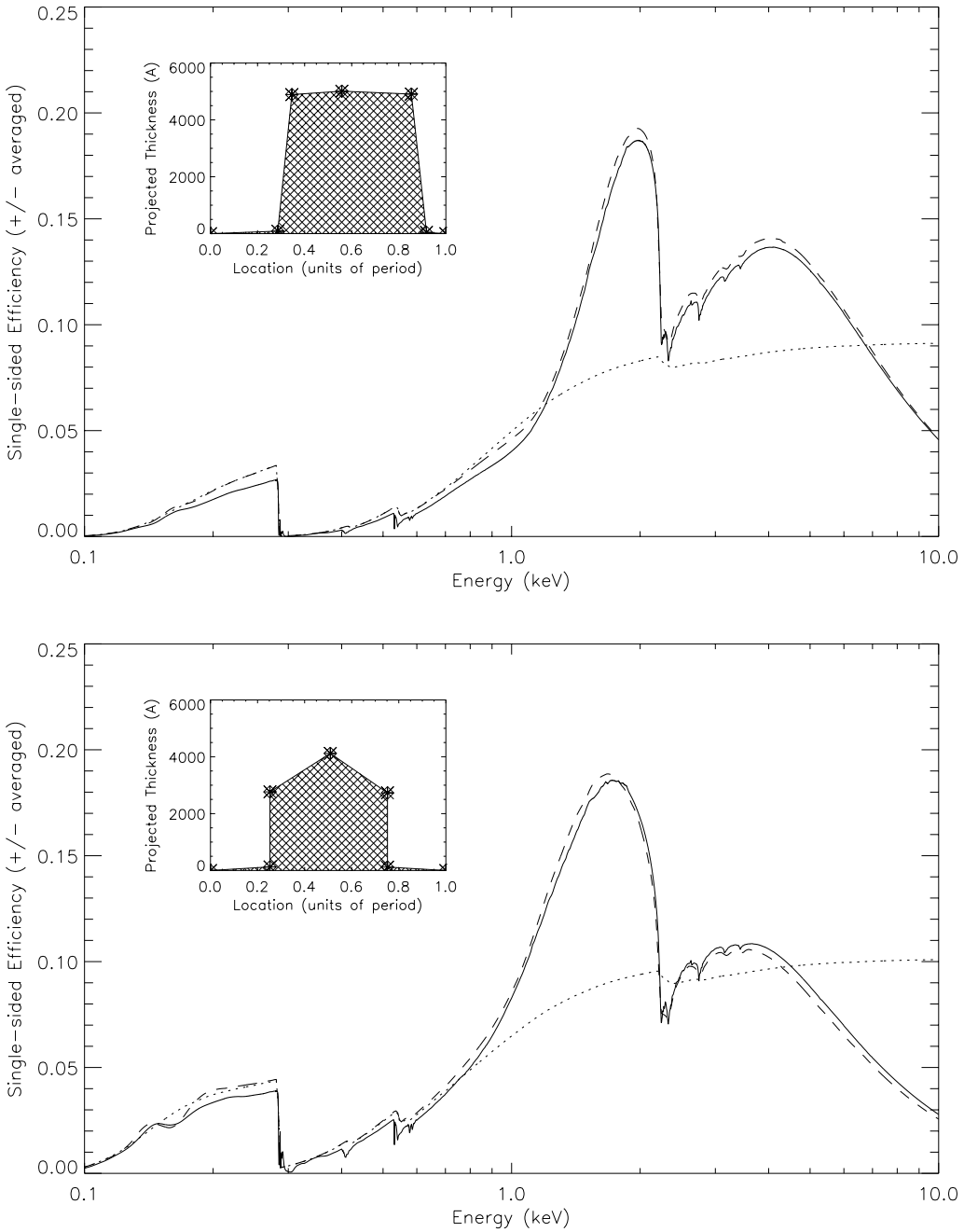

Figure 3.1: First-order diffraction efficiencies from example HEG (top) and MEG (bottom) models. The diffraction efficiency for the path-length function shown inset is plotted versus energy (solid). Effects of the polyimide and plating base layers are included and produce the falloff and Carbon, Nitrogen, Oxygen and Chromium edges seen at low energies. For reference the efficiencies from a rectangular model are shown for the cases of a constant gold thickness (dashed) and the fully opaque case (dotted). The enhancement of the diffraction efficiency due to constructive phase shift which occurs in the non-opaque cases is apparent above 1 keV. At high energies the non-opaque cases are becoming more transparent and the efficiency drops. Note also the subtle differences between the multi-vertex efficiency (solid) and that of the simple rectangular model (dashed).

3.1.2 Multi-vertex Efficiency Equations

Assuming the validity of scalar diffraction theory and ignoring reflection and refraction, the mth order grating efficiency for a perfect diffraction grating is $|F_m(k)|^2$, where the structure factor $F_m(k)$ is given by

$$F_m(k) = \frac{1}{p}\int_0^p \mathrm{d}x\; e^{i2\pi mx/p + i\phi(k,x)}. \tag{3.2}$$

Here p is the grating period, $k = 2\pi/\lambda$ is the wave-number, and $\phi(k,s)$ is a phase shift introduced by the grating bars. The phase shift is a function of energy or wave-number k and also depends upon the grating bar shape according to

$$\phi(k,x) = -k[\delta(k) - i\beta(k)]z(x), \tag{3.3}$$

where δ and β are energy dependent functions related to the dielectric constant of the grating bars. The function $z(x)$ represents the path length of the photon as it passes through a grating bar; it is sometimes called, rather loosely, the "grating bar shape", and more rigorously, the "path-length function".

It is preferable to work with the unitless quantity $\xi = x/p$ and to parametrize the path-length function in terms of it. For simplicity, we represent $z(\xi)$ as a piece-wise sum of N line segments, i.e.,

$$z(\xi) = \sum_{j=0}^{N-1}(a_j + b_j\xi)B(\xi_j \le \xi \le \xi_{j+1}), \tag{3.4}$$

where $B(X)$ is the boxcar function defined to be 1 if X is true, or zero otherwise. By demanding that the path-length function be continuous, it is easy to see that the coefficients a_j and b_j are given by

$$a_j = \frac{z_j\xi_{j+1} - z_{j+1}\xi_j}{\xi_{j+1} - \xi_j}, \tag{3.5}$$

$$b_j = \frac{z_{j+1} - z_j}{\xi_{j+1} - \xi_j}, \tag{3.6}$$

where $z_j = z(\xi_j)$. For obvious reasons, we require $z_j \ge 0$, and that the set of points $\{\xi_j\}$ be ordered according to

$$0 = \xi_0 \le \xi_1 \le \cdots \le \xi_{N-1} \le \xi_N = 1. \tag{3.7}$$

The most redeeming feature of this particular parametrization of the path-length function is that the integral appearing in Equation 3.2 may be readily evaluated with the result

$$F_m(k) = i\sum_{j=0}^{N-1} e^{-i\kappa a_j}\frac{e^{-i\xi_{j+1}(\kappa b_j + 2\pi m)} - e^{-i\xi_j(\kappa b_j + 2\pi m)}}{\kappa b_j + 2\pi m}, \tag{3.8}$$

where

$$\kappa = k[\delta(k) - i\beta(k)] \tag{3.9}$$

is complex. Although one may carry out the evaluation of $|F_m(k)|^2$ using the above expression, it is very tedious and the result is not particularly illuminating. Moreover, it computationally more efficient to evaluate the above sums numerically using complex arithmetic and then compute $|F_m(k)|^2$ by multiplying by the complex conjugate.

3.1.3 "Phased" Transmission Gratings

As shown in Figure 3.1, the efficiency for the HETG gratings (solid curves) is enhanced relative to a grating with completely opaque grating bars (dotted curve.) The HETG gratings were designed such that the grating bars are partially *transparent* at higher energies, and so the phase shift of the X-rays through the bars (the δ term) actually enhances the non-zeroth-order efficiencies for a range of energies. Gratings with this property are call *phased* transmission gratings. This section briefly summaries the considerations in selecting a grating material and thickness in the phased design.

Consider a rectangulat grating model without aborbing support layers. For a rectangular wire profile[87], *i.e*, where $z(\xi) = h$ for $0 < \xi \leq p - a$, and $z(\xi) = 0$ for $p - a < \xi \leq p$, equation **??** becomes

$$\eta_{(m)}(k) = [\frac{sin(\frac{m\pi a}{p})}{m\pi}]^2 \times [1 + e^{-2k\beta h} - 2e^{-k\beta h} cos(k\delta h)] \qquad m \neq 0 \tag{3.10}$$

and

$$\eta_{(0)}(k) = (a/p)^2 + (1 - a/p)^2 e^{-2k\beta h} + 2(a/p)(1 - a/p)e^{-k\beta h} cos(k\delta h) \qquad m = 0. \tag{3.11}$$

Here a is the width of the space between grating lines and p is the period. As before, δ and β are the complex components of the index of refraction ν. Note that ν, δ, and β are all functions of the X-ray wavelength, i.e., $\nu(k) = 1 - \delta(k) + i\beta(k)$. If βh is very large (i.e., the grating bars are opaque) then there is no wavelength dependence to the diffraction efficiency.

For a quantitative look at the higher efficiency of phased gratings as compared to opaque gratings, equations 3.12 and 3.13 below show the grating efficiencies (where η is now the sum of the grating efficiencies of the $+1$ and -1 orders):

$$\eta_{\text{opaque}} = 2 \times \frac{sin^2(\frac{\pi a}{p})}{\pi^2} \tag{3.12}$$

$$\eta_{\text{phased}} = \eta_{\text{opaque}} \times [1 + e^{-2kh\beta} - 2e^{-kh\beta} cos(kh\delta)] \tag{3.13}$$

When absorption is ignored (the fully-phased case), equation 3.13 reduces to the following[87]:

$$\eta_{\text{fully-phased}} = 4 \times sin^2(\frac{kh\delta}{2}) \times \eta_{\text{opaque}} \tag{3.14}$$

From equation 3.14, it can be seen that at an optimal wavelength ($\lambda = 2h\delta$), the fully-phased grating efficiency is four times the opaque grating efficiency. At efficiencies near this one particular wavelength, partial destructive interference of the zeroth grating diffraction order occurs and the first grating diffraction orders are enhanced. The result is a range of wavelengths for which the grating efficiency is maximized, tunable through the selection of the material (δ) and h; *e.g.*, we considered other materials, especially for the lower-energy MEG grating bars, including Carbon, Aluminum, Copper, and Silver.

3.1.4 Trapezoidal and Tilted Gratings

Another factor which makes a difference in the computed efficiencies in the various orders is the effect of tilting the grating, *i.e.*, changing the orientation of the grating surface normal with respect to the incoming X-rays. Given a grating bar cross-section, and a tilt angle (orientation of the incoming X-rays with respect to the grating plane), one can determine the grating bar shape function $z(\xi)$ from simple geometry. Since tilt and bar shape are complementary, we don't include tilt angle as a model parameter. (It is always possible to find an untilted grating with the same response as a tilted grating of an arbitrary shape. This equivalence only holds true at one specific tilt angle, however. If one studies gratings over a range of angles, then one must generally use the actual bar cross-section.)

As an example of the complementarity between tilt and bar shape, consider a rectangular cross-section: When viewed at an angle, it has a trapezoidal $z(\xi)$. Moreover, the efficiency vanishes in all orders when the the grating is tilted by an angle $\theta = tan^{-1}(h/p)$, where h is the grating bar height and p is the period. (This relationship is clear because at that angle all of the X-rays incident on the grating see the same path length through the bars, hence there can be no diffraction.) Fischbach *et al.* [28] have reported on the theory and measurements of tilted rectangular gratings.

When the path-length function is asymmetric, for example in the case of blazed transmission gratings [65], the plus and minus diffraction orders are no longer generally equal. Except for a few bar cross-sections showing great symmetry (*e.g.*, a rectangle), the efficiency in the positive and negative orders will be different at all but a few tilt angles. For example, Figure 3.2 shows the efficiency asymmetry in the plus and minus first orders for a trapezoidal grating at $E = 2.290$ keV, the energy of the Mo L α line. The asymmetry at a given tilt angle is defined as $100(I_{+1}/I_{-1} - 1)$ where I_m is the intensity in order m. There is order symmetry at *normal* orientation (zero degrees tilt), but at very few other angles.

For the HETG gratings this asymmetric-orders case arises primarilly when the (non-rectangular) HEG gratings were tilted, that is, used at non-normal incidence; they may have an asymetry of up to 30 % per degree of tilt. However, for small tilt angles from the normal the total of the plus and minus sides remains nearly constant.

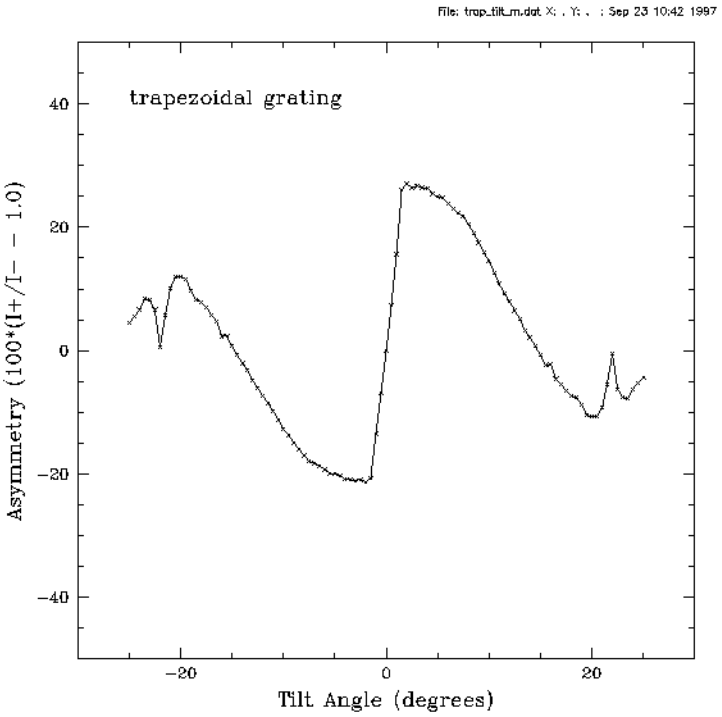

Figure 3.2: Asymetry parameter for a trapezoidal grating

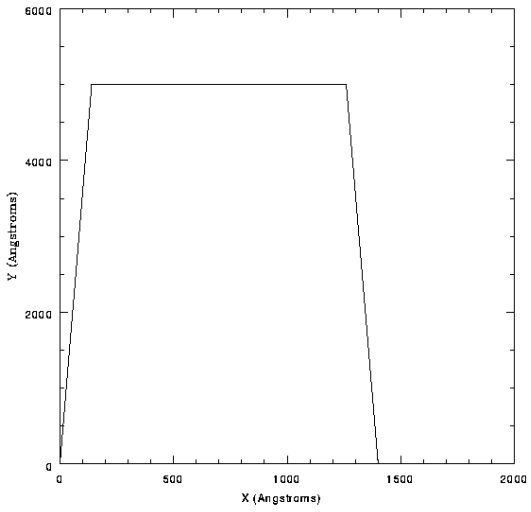

Figure 3.3: Trapezoidal bar shape assumed for the model above.

3.2 Synchrotron Measurements

The synchrotron radiation measurements serve several purposes. Transmission measurements of polyimide, plating base and gold foil samples allow the optical constants and edge structures of these materials to be determined. Absolute efficiency measurements of a few gratings serve to validate and constrain our model, and provide estimates of its intrinsic errors. Measurements of individual gratings HX220 and MX078 have enabled their use as transfer standards in laboratory tests. Finally, a comparison of synchrotron measured efficiencies of a few gratings with their predicted efficiencies based on laboratory measurements allows us to assess the limitations of our subassembly tests.

3.2.1 Synchrotron Measurements Summary

Synchrotron radiation tests for the High Energy Transmission Gratings have been performed at four facilities over a timeframe of several years. The tests are summarized in Table 1. Our earliest modeling efforts were based upon a rectangular grating bar model and employed scattering factors (f1, f2) published by Henke *et al.*[43]. (The real and imaginary parts of the index of refraction, δ and β, are obtained from the scattering factors.) However, early tests (January 1994) at the National Synchrotron Light Source (NSLS) at Brookhaven National Laboratory (BNL) indicated significant disagreement with the Henke values for the gold optical constants. The most noticeable feature was that the energies of the gold M absorption edges were shifted from the tabulated amounts by as much as 40 eV (a result obtained earlier by Blake *et al.*[10] from reflection studies of gold mirrors.) In an effort to determine more relevant optical constants, the transmission of a gold foil was measured over the range 2.03–6.04 keV, and the values of β and δ were revised[71]. (The Henke tables were modified in 1996 to reflect these results.)

Subsequent tests on gratings explored bar shape, tilt and asymmetry[59], and tests at the radiometry laboratory of the Physikalish-Technische Bundesanstalt (PTB) below 2 keV identified the need to accurately model the edge structures of the polyimide support membrane to improve the overall fit[30]. The analysis of the tests performed on gold and polyimide membranes at PTB in October 1995 has now been completed and is detailed in Sections 3.2.3 and 3.2.4. As a consequence of this analysis, our model now includes revised gold optical constants over the full energy range appropriate to HETG, and detailed structure for absorption edges of C, N, O and Cr. In addition, cross-checks of the revised gold constants (above 2 keV) and polyimide were performed (in August and November, 1996) and have confirmed our revisions. For reference, the revision date for these changes to our modeling is May 10, 1999.

While the prime use of the synchrotron data sets was to confirm our efficiency model, in particular the optical constants, a second critical use of the synchrotron measurements was to provide transfer standards for laboratory testing of the flight HETG gratings as described in Section 4.2.

3.2.2 Synchrotron Data Analysis Techniques

A complete description of the techniques employed in extracting diffraction efficiencies from synchrotron data is given in Flanagan *et al.*[30].

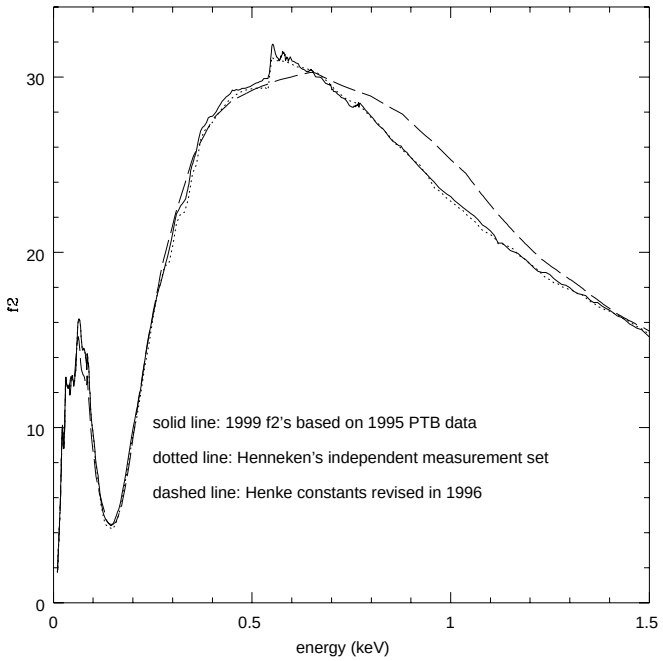

Figure 3.4: Gold scattering factor f2 obtained from independent transmission measurements by HETG team and Henneken *et al.*[**?**], compared with Henke values (updated in 1996). The optical constant β is derived directly from f2 at each energy.

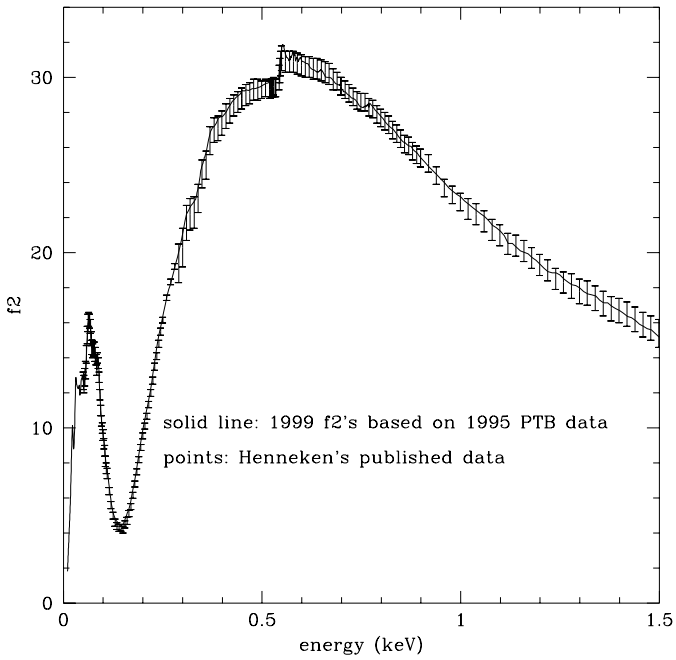

Figure 3.5: Gold scattering factor f2 obtained by HETG team overlaid with measured values and error bars from Henneken *et al.*[**?**]

Table 3.1: Summary of HETG synchrotron radiation tests

Date	Facility	Sample	Energy	Comments	First Ref.
July '93	NSLS	HX101	2.03 - 4	preliminary tests	Nelson[70]
Nov '93	Daresbury	HX101	8.442	period variations (UL)	Nelson[70]
Jan. '94	NSLS	HX101	0.7 - 6	first tests	Nelson[71]
Feb. '94	NSLS	1Au	2.03 - 6.04	gold optical constants	Nelson[71]
Jun. '94	NSLS	HA04	2.03 - 6		Nelson[71]
"	"	HX101	2 - 3.5		Nelson[71]
"	"	MA12	0.7 - 5	± 1 order assymetry	Nelson[71]
Feb. '95	NSLS	HX220	0.5 - 6.4	X-GEF reference grating	Markert[59]
"	"	MX078	0.5 - 3.5	X-GEF reference grating	Markert[59]
May '95	NSLS	HX220	1.05 - 1.95	X-GEF reference grating	Markert[59]
"	"	poly	0.4 - 1.83	poly transmission	Flanagan[32]
Oct. '95	NSLS	HA2021	2.03 - 6.5	flight lot 2, dense 0&1 orders	Flanagan[30]
"	"	MA1047	2.1 - 5.0	flight lot 3, dense 0&1 orders	Flanagan[30]
Oct. '95	PTB	HA2021	0.4 - 1.9	flight lot 2	Flanagan[30]
"	"	MA1047	0.4 - 1.5	flight lot 3	Flanagan[30]
"	"	HA2049	0.2 - 1.5	polyimide sample, flight lot 2	Flanagan[32]
"	"	MA1066	0.2 - 1.5	polyimide sample, flight lot 3	Flanagan[32]
"	"	HX507	0.05 - 1.9	gold optical constants	Flanagan[32]
Mar. '96	NSLS	HD2338	2.0 - 6.4	flight lot 4, ± 1 and higher orders	in prep
"	"	MB1148	2.1 - 4.9	flight lot 9, ± 1 and higher orders	in prep
Aug. '96	ALS	poly	0.06 - .940	polyimide transmission, R. Blake	Flanagan[32]
Nov. '96	NSLS	1Au	2.01 - 7.0	gold optical constants, R. Blake	Flanagan[32]

3.2.3 Gold Optical Constants

The optical constants for gold have been revised according to the results of three synchrotron tests: two tests (February, 1994 and November, 1996) examined the range above 2 keV, and one (October, 1995) probed energies below 2 keV.

Gold below 2 keV

In order to investigate the optical constants of gold below 2 keV, transmission tests were made on a free-standing gold sample, HX507, at the radiometry laboratory of the PTB at BESSY. Details of test procedures are given in Flanagan, *et al.*[30]. Information about the facility may be found in Scholze, *et al.*[88] and Ulm and Wende[95]. The gold foil sample contained a residual amount of Cr adhesion layer, and this needed special treatment in the analysis. We assumed Cr optical constants and edge structure as determined according to Section 3.2.4, and found a best-fit thickness for Cr of 38.7 Å by fitting near the Cr edge features. We then fixed the Cr thickness to this value and fitted over 0.2 to 0.5 keV to obtain a best-fit thickness of 1,075.53 Å for Au. Finally, from the measured transmission, we divided out the contribution due to Cr. Although this left an artifact around 580 eV and did not remove any contribution at the Cr LIII edge (near 696 eV), these effects were comparatively small. The resultant transmission was thus attributed to pure gold of thickness 1,075.53 Å and density 19.3g/cm^3. This yielded the scattering factor f2 directly.

The scattering factor for gold has been independently measured at PTB on a different gold sample by Henneken, *et al.*[**?**]. These results agree well with our measurements. This is illustrated in Figure 1, where the scattering factor f2 is plotted (from which β is directly obtained) for Henneken's data, for our measurements, and for the Henke values (as updated in 1996). Clearly, the new gold measurements represent a significant difference from earlier values in the range 0.5–1.5 keV. The close agreement between the HETG and Henneken results[**?**] is illustrated in Figure 2, where the HETG f2 curve is overlaid with Henneken's data and its associated error bars. The HETG results are in agreement with Henneken's to within the published error bars, except between .13 and .26 keV where the HETG value of f2 is slightly higher (within about 2 σ).

Our data were inadequate below 96 eV, so at this energy we have merged our f2's with those of Henneken's. A complete file of f2 was obtained by joining the measured set from PTB below 2 keV with a newly measured set from NSLS above 2 keV. From this, we generated corresponding f1's for a complete table of scattering factors. All of these revisions are incorporated in the improved grating model.

The impact of the changed gold optical constants on modeling the grating efficiency is small to moderate. Use of the new constants will result in modeled efficiencies that change by five percent or less except at the Au NIII edge near 0.55 keV, where the change is about 7%. There are larger variations at energies below 0.11 keV, but HETG is not intended for use at energies below 0.4 keV for the medium energy gratings (or 0.9 keV for the high energy gratings).

Gold above 2 keV

The gold sample (1Au) which was measured at NSLS in 1994 was remeasured above 2 keV at NSLS in November, 1996 by Richard Blake and Tony Burek. The assumed thickness was 11,304 Å and the assumed density was 19.32 g/cm^3. In this test, the experimental procedure was improved by continuous beam monitoring and normalizations taken adjacent in time to the transmission measurements. The edges were sampled in 0.5 to 1 eV step sizes. The 1996 data agree well with the 1994 measurements, and have been incorporated into revised optical constants (May 10, 1999). A comparison of the two data sets against Henke[43] values is given in Figures 3 and 4. The two data sets are virtually indistinguishable in the figures. The good agreement between the two measurements of sample 1Au serves to confirm our revisions, and allows a means of assessing some of the errors associated with these measurements.

The largest fractional differences in the two NSLS measurements of β are seen at the gold M edges (in the energy range 2.2 to 3.5 keV), but even there agreement between the two data sets is within 2% (or 4% at the MV edge around 2.2 keV). This corresponds to a 2–3% error in first order efficiency at the gold M edges. Since these two tests were performed on the same beamline, other systematic effects may not be accounted for.

3.2.4 Polyimide and Chromium Edge Structure

C, N and O Edges

Measurements of the gold optical constants have enabled the detailed gold edge structure to be well represented. A similar approach has been taken toward modeling the C, N and O edges of the polyimide. We have tested samples of polyimide from MEG and HEG flight batches at the radiometry laboratory of the PTB at BESSY[30]. These data show that there is considerable edge structure at the C, N and O edges in our polyimide. Our approach is to model the

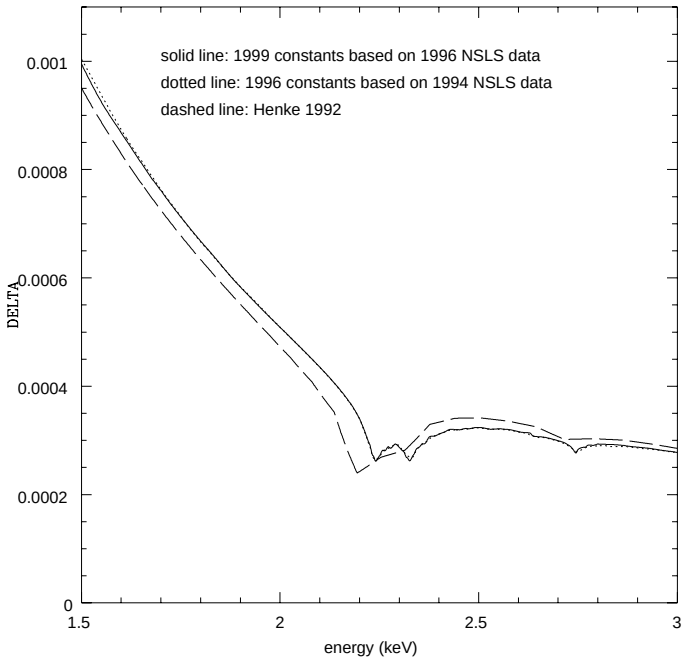

Figure 3.6: Gold optical constants were revised in May, 1999 for grating modeling. The real part of the index of refraction, δ, is shown here as determined from NSLS 1994 and 1996 measurements, along with Henke 1992 values. The two NSLS results are virtually indistinguishable.

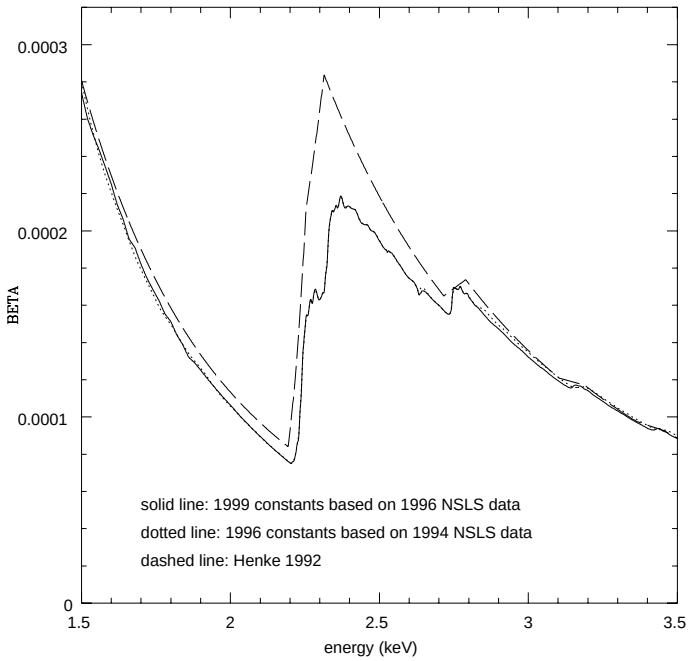

Figure 3.7: The imaginary part of the index of refraction, β, as determined from NSLS 1994 and 1996 measurements contrasts sharply with Henke 1992 values.

polyimide assuming the chemical formula ($C_{22}H_{10}O_4N_2$) and nominal density (1.45 g/cm^3) for the polyimide formulation we use (Dupont 2610). In prior modeling, the optical constants for the polyimide support film and the chromium plating base have been based on scattering factors for the constituent atoms taken from Henke, Gullikson and Davis[43]. This modeling, however, provided an unacceptable fit at the edges, with residuals up to 200% at the C and N edges in fitting polyimide transmission data. Just below 600 eV are seen edge residuals on the order of 20% from Cr L in fitting HEG grating data. Similar results have been found for the MEG grating MA1047. Taking the model as a whole, the polyimide edges have exhibited the worst discrepancies between our model and the data overall. As discussed below, synchrotron testing has allowed improvements in our modeling of these edges, although they remain the largest contributors to the errors of the model.

Nitrogen edge

In order to refine the optical constants for our polyimide at the C, N and O edges, we used the PTB data for two flight batch samples of polyimide, HA2049 and MA1066. We began by finding a best-fit thickness for each of the (MEG and HEG) polyimide samples assuming Henke optical constants and fitting over the edge-free energy range 0.6 to 1.6 keV. For each sample, an effective absorption coefficient μ was obtained assuming $T = e^{-\mu t}$ where **t** is the thickness in microns and T is the transmission through the polyimide membrane. The final value for μ was taken to be the average value of the HEG and MEG μ, between 272 eV and 875 eV, smoothly joined to the Henke values outside this region. In addition, we smoothed the derived μ in the carbon edge region between 288.8 eV and 300.99 eV because of the jittery structure there. (Although this structure might be real, the low counting statistics and limitations of the experiment discourage reliance on it.) Note that the 1982 Henke constants for carbon were employed in our initial fitting as these were found to agree better with our data and have been shown in independent tests (M. Zombeck, private communication) as the the better choice.

A different polyimide sample, manufactured with the same formulation, was tested at the Advanced Light Source (ALS) at the Lawrence Berkeley National Laboratory in 1996. We found a best-fit ρt of 124.25 μg/cm^2. Assuming a density of ρ= 1.45 g/cm^3, we derived a value for μ/ρ in a similar manner as has been described with regard to the PTB data. After conversion to comparable units, a comparison of μ/ρ from PTB, from ALS and from Henke[43] is given for the nitrogen edge in Figure 5. As seen in the figure, the Henke values represent the nitrogen edge by a single simple discontinuity, in sharp contast to the measured structure. The PTB and ALS measurements appear to be compatible if one accounts for an apparent slight energy shift (which we attribute to an energy offset in the ALS beamline.) This is shown in Figure 6, where a relative shift of 1.3 eV has been included. The two different beamlines independently trace virtually the same structure and amplitude in this region, giving confidence in the result.

Oxygen edge

Analogous plots of the absorption coefficient in the oxygen edge region are given in Figure 7, where a 1.0 eV energy offset attributed to the ALS beamline has been removed. Note that the Henke representation, which corresponds to our former modeling, cleanly misses the sharp double structure. This structure is accomodated by our updated optical constants. The close agreement generally confirms the detailed edge structure and magnitudes of the absorption coeficients we have derived.

Carbon edge

In general, there was good agreement between the two polyimide data sets (at BESSY and ALS),

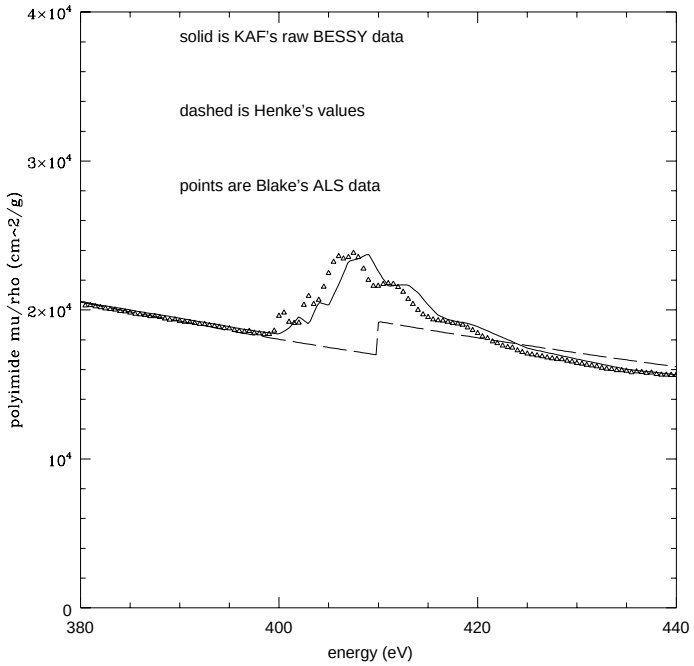

Figure 3.8: Comparison of polyimide absorption coefficients of the nitrogen edge region at PTB and ALS with Henke values (which represent the HETG model prior to the 1999 revision). The Henke values do not reproduce the complicated edge structure of the HETG polyimide.

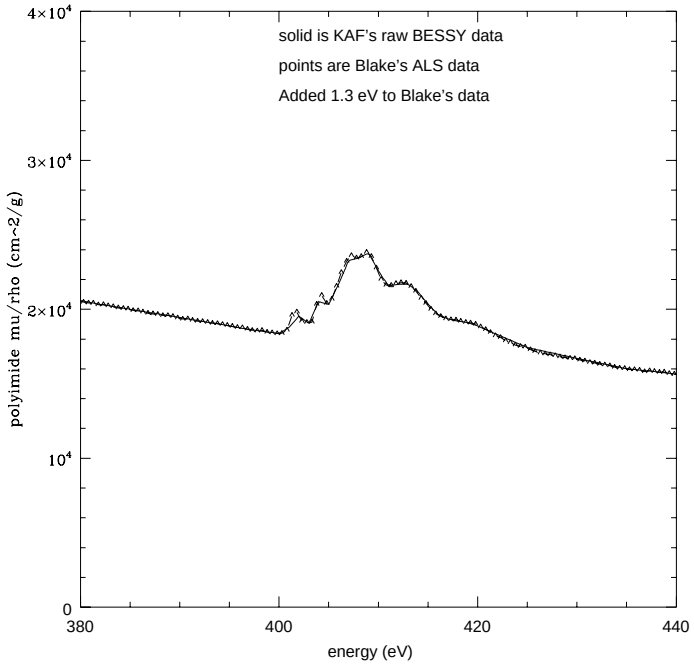

Figure 3.9: Comparison of PTB nitrogen edge data with ALS data, after an energy shift of 1.3 eV has been applied to the ALS data to accomodate a presumed beamline energy offset. Note that the structure and amplitude of the edge region is confirmed by the two independent beamline measurements.

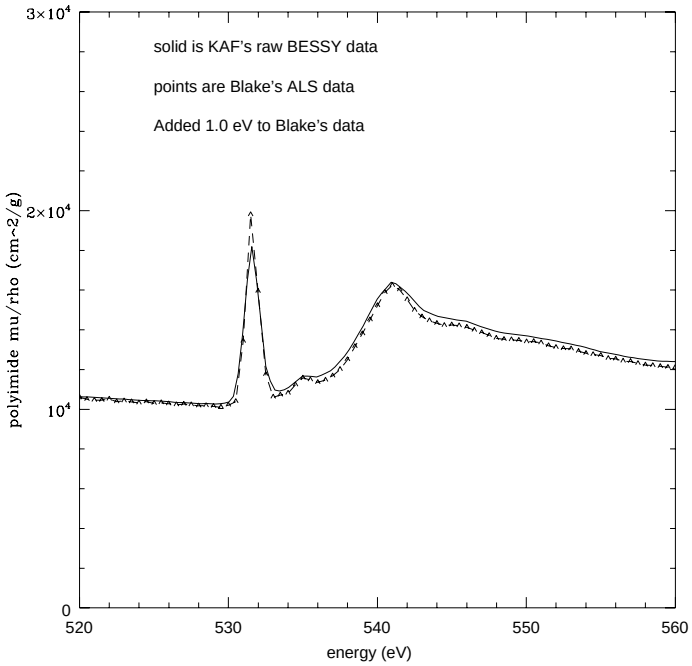

Figure 3.10: Comparison of PTB oxygen edge data with ALS data, after an energy shift of 1.0 eV has been applied to the ALS data. Note the substantial agreement of the two sets of absorption coefficients, confirming the double structure of the oxygen edge region.

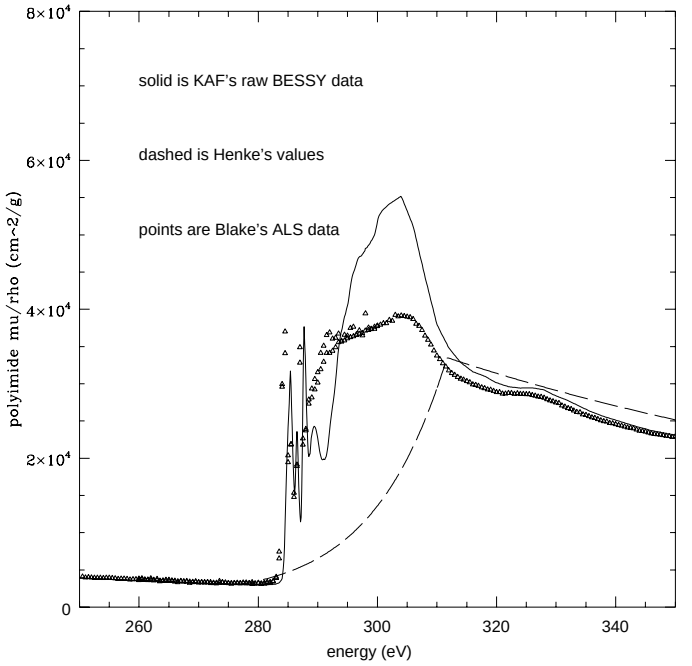

Figure 3.11: Comparison of PTB carbon edge data with ALS data and Henke values.

except at the carbon edge (see Figure 8). Synchrotron beamlines have notorious difficulty with measurements near the carbon edge. (Carbon buildup on the monochromator absorbs much of the incident flux, heightening the relative percentage of contaminant energies, and giving low overall counting statistics.) As discussed above, we take our carbon edge structure from the PTB measurements, but (arbitrarily) smoothing the data between 288.8 eV and 300.99 eV. We do not have the reassuring agreement between the ALS and PTB measurements for this region as we did for the nitrogen and oxygen edges, and model residuals remain high at the carbon edge. However, this region falls below the minimum HETG energy of 400 eV and the true edge structure does not matter for our modeling purposes.

Chromium edge

In order to accomodate the Cr edge structure below 600 eV, we employed a different approach since we do not have transmission tests of a Cr filter of known thickness. We took zero order grating data from MA1047 (measured at PTB) and fit it assuming a fixed thickness of Cr (55 Å from fabrication measurements). We assumed that the absorption features seen at 577 eV and 586 eV could be modeled as a perturbation on the absorption coefficient as derived from the Henke constants, and thereby obtained a modified absorption coefficient. This allows us to obtain a transmission for any thickness of Cr. (It is unnecessary to extract new values of f1, since the chromium absorbs but does not diffract.)

The updated grating model is evaluated in the next section. By refining our treatment of C, N, O and Cr edges, we have reduced the residuals by a factor of 2–3 relative to the former treatment.

3.2.5 Accuracy of the Grating Model

Overview

The accuracy of the phased, non-rectangular model and the effectiveness of updated optical constants for gold, polyimide and chromium can be assessed by examining how well the model fits the measured efficiencies of a well-tested grating. There are two flight-batch gratings that have been tested at synchrotrons over most of the applicable energy range. These gratings are MA1047 and HA2021, which were tested at in October, 1995 at PTB below 2 keV, and at NSLS above 2 keV. (Although other gratings have been through synchrotron testing, the experiment was limited to energies above 2 keV for these other gratings.) As discussed below, the grating model shows excellent agreement (at the level of a few percent) with synchrotron measurements of first order efficiencies, except at a limited set of energies. In particular, modeling the edges remains the largest contributor to the residuals, despite significant advances in this area. Future work on the modeling is not expected to improve the edge residuals. The second obvious energy range where the model inadequately represents the data is in the vicinity of the first order efficiency peak (or zeroth order efficiency trough). Future work on the modeling may result in improvements in this energy range.

First order fit to HA2021

The agreement between the model and the data is demonstrated in Figure 9, where first order diffraction efficiencies for flight-batch grating HA2021 have been measured at many closely-spaced energies. The residuals are shown in Figure 10, where have defined the residuals to be the fractional discrepancy between the modeled efficiency and the data (i.e. $(model-data)/data$) without consideration of the error bars on the data. To obtain the best-fit model, only the first-

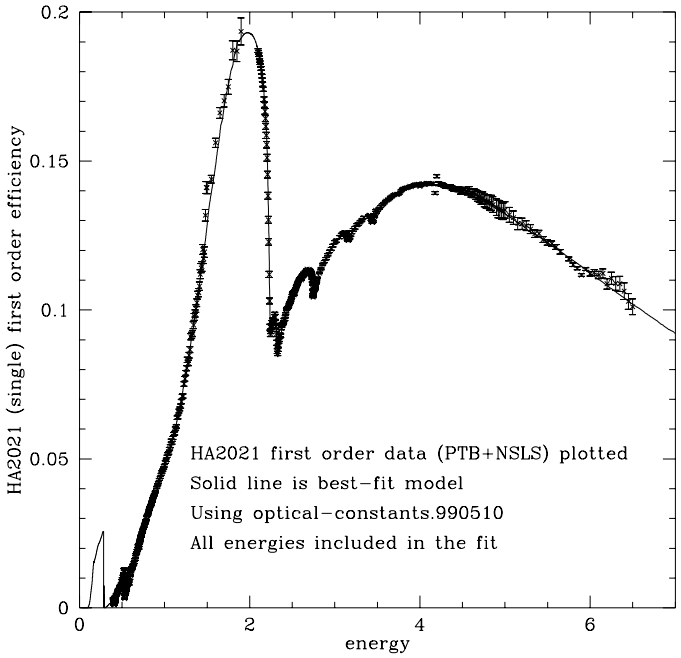

Figure 3.12: First order synchrotron data of flight batch HEG grating HA2021, overlaid with best fit model. These data come from two different synchrotrons (PTB and NSLS) to cover the full energy span. The data sets join at 2 keV.

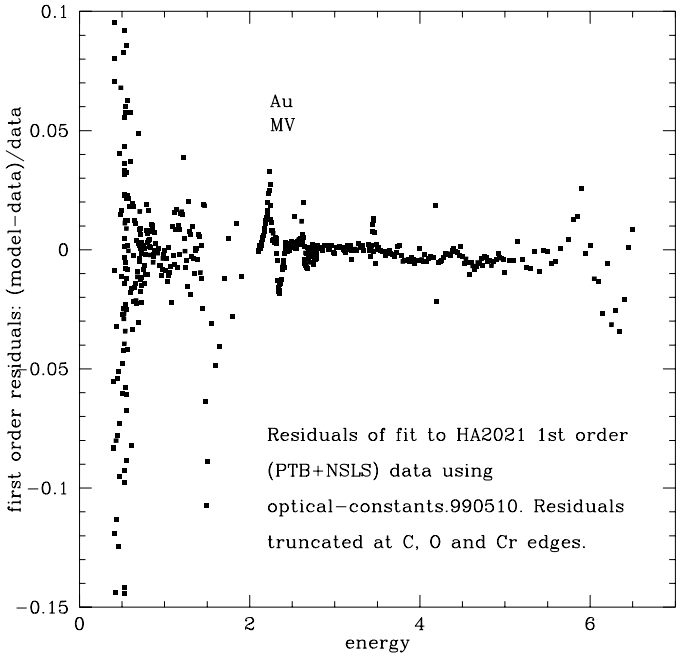

Figure 3.13: Residuals from the first order fit of grating HA2021 shown in Figure 3.2.4. The largest residuals, at the N and O edges of polyimide, have been truncated. (The region containing the N and O edges is detailed in Figures 3.2.5 and 3.14.)

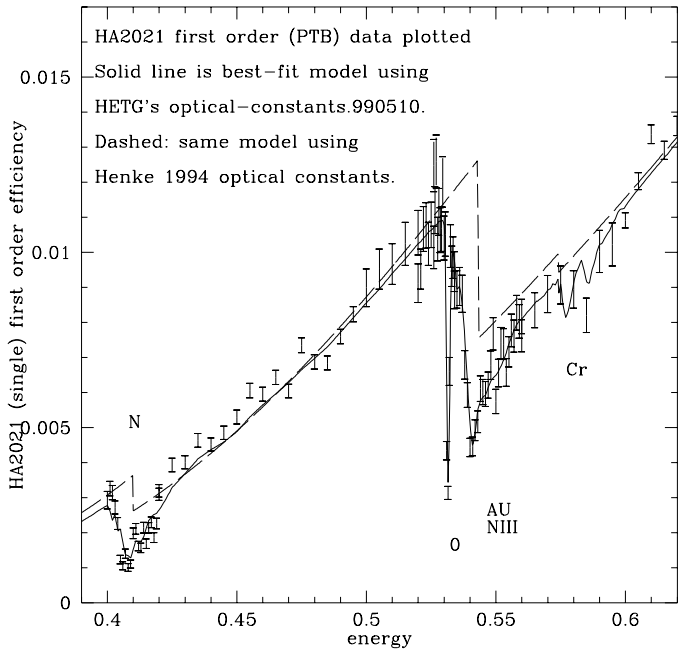

Figure 3.14: First order synchrotron data of HEG grating HA2021 overlaid with best fit model, in the polyimide and plating base edge region. The contrast between the current model (solid line) and the 1994 Henke model (dashed line) illustrates the remarkable level of improvement provided by the polyimide and gold transmission tests at the synchrotrons.

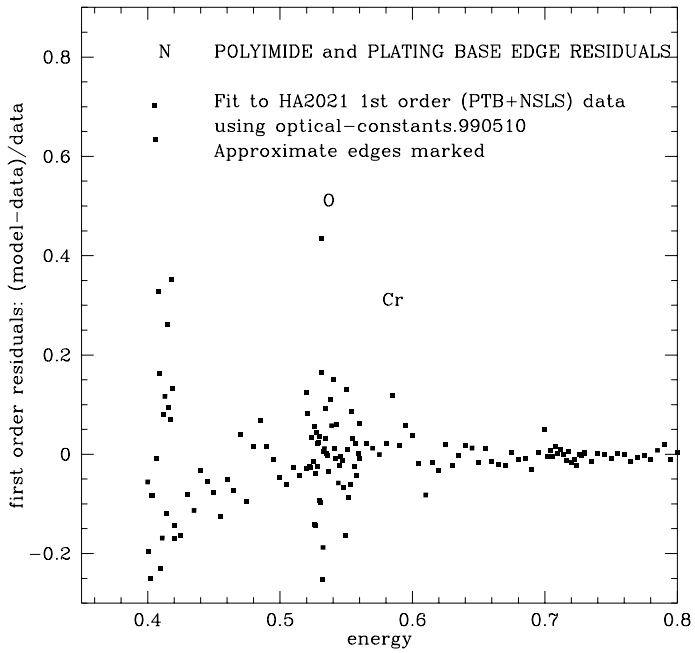

Figure 3.15: Residuals from the first order fit of grating HA2021, in the polyimide and plating base edge region. Although the residuals at the N and O edges are high, they are nevertheless significantly improved by the use of the new optical constants.

order data for HEG grating HA2021 were used in the fit. (No other orders were used, nor did we impose the constraint that the +1 and -1 orders were equal.) The largest residuals are generally due to the polyimide and plating base edges, and have been truncated in Figure 10. Detailed views of the model and the residuals in this energy region are given in Figures 11 and 12. The excellent agreement of the model with the data at the gold M edges is seen in detail in Figures 13 and 14.

By far the largest residuals (tens of percent) between the model and the data occur at the polyimide edges (N and O). (The testing range did not include the carbon edge.) Given the steep changes in response expected there and the large systematic errors found in measuring the polyimide optical constants at independent synchrotron beamlines, these residuals are perhaps not too surprising and are restricted to a relatively small region of the energy range. (Furthermore, the residuals as we have defined them do not include any impact of the error bars in evaluating the significance.) A close examination of Figure 11, in fact, shows that the model is actually quite impressive in its treatment of the complicated edge structures, despite the formal residuals.

Figure 15 summarizes the model to the first order data of HA2021. The model to which the data are fitted is a five-vertex polygon bar shape function with three absorbing layers: polyimide, chromium, and gold plating base. For HA2021, the nominal fabrication thicknesses are 0.0200 μm for the Au plating base, 0.97 μm for polyimide, and 0.005 μm for Cr. The fitted values are displayed in Figure 15, and are in the ballpark of the expected values. Also shown is the amplitude factor: it close to 1.0, as expected.

First order fit to MA1047

A fit to the first order efficiency of MEG flight batch grating MA1047 is shown in Figure 17. The residuals are shown in Figure 18, and have similar characteristic regions to those described for HA2021. In the case of the MEG, the residuals at the polyimide edges are less than for the HEG grating, as expected since the absorbing layer of polyimide is about half that of the HEG grating. Typical results for MA1047 are also given in Table 2.

Discussion

As indicated in Figure 15, the reduced chisquare of the fit shown in Figure 9 is about 3. Part of this is attributable to error bars that are too small. If the statistical errors from the synchrotron tests are increased in order to more realistically reflect systematic errors, then the reduced chisquare drops to 2.1, but not much lower. (The edge regions continue to be significant contributors.) Thus, despite improvements gained with the recent synchrotron tests, there still remain some statistically significant discrepancies between the model and the data, mostly attributable to limitations in our input data, β and δ over the edge regions.

Table 2 shows the improvement that polyimide and gold transmission tests have provided in understanding the optical constants at these edges. The improvement in the optical constants at the edges has decreased the relative residuals (improvements of a factor of 2 or 3 are typical). Note that in Table 2, most of the edges fall outside the useable energy range of the high energy grating (above 0.9 keV). Thus, from the standpoint of *Chandra* calibration, the largest applicable edge residual is 26% (i.e., the MEG grating at the oxygen edge.) Future improvements in modeling are not expected to improve the edge residuals, since these are assumed due to systematics in the synchrotron testing, location of the edge energy, variations in polyimide, and other factors outside our ability to address. Hence, further improvements in our treatment of the edges must await improved optical constants in these regions.

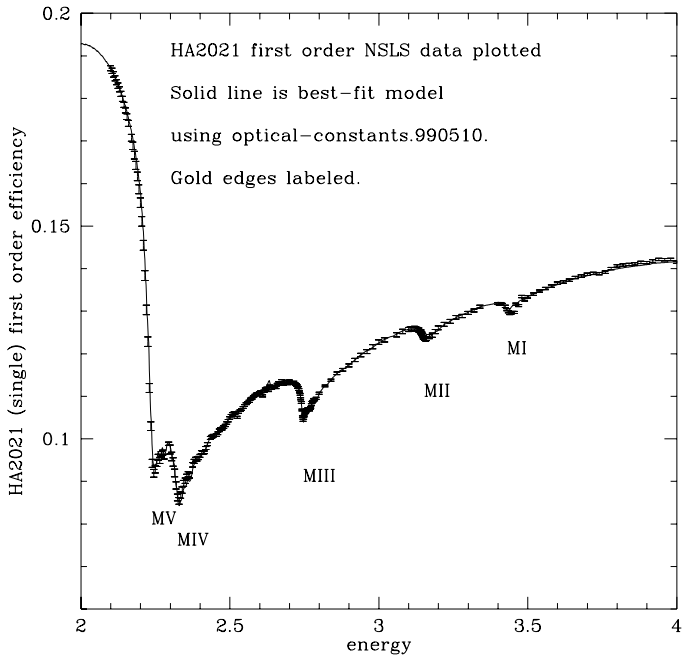

Figure 3.16: First order synchrotron data of HEG grating HA2021 overlaid with best fit model, in the gold M edge region.

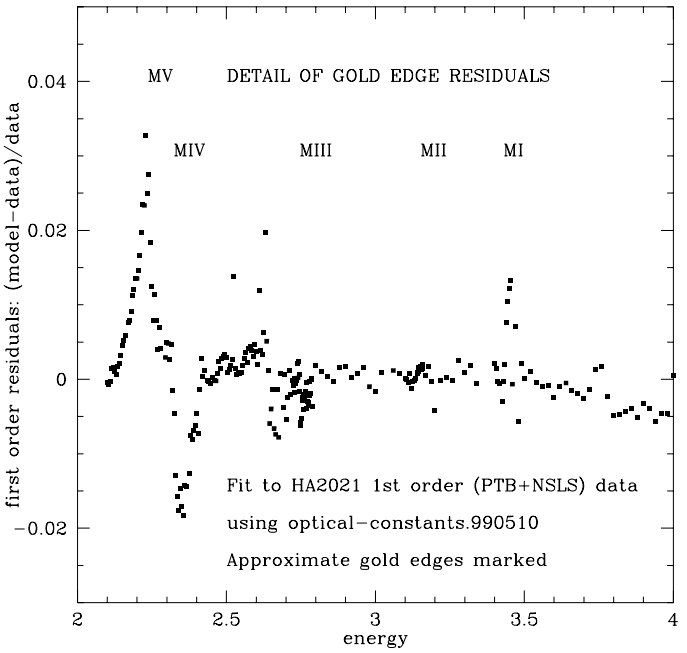

Figure 3.17: Residuals from the first order fit of grating HA2021, in the gold M edge region. Note that the residuals are small, a few percent at most.

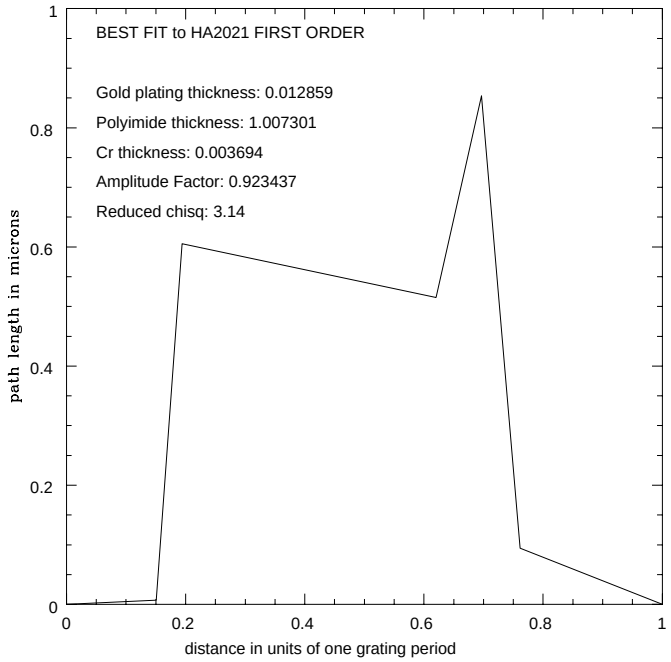

Figure 3.18: Summary of the best-fit model to the first order data of HA2021. The model includes a five-point vertex bar shape, three plating base thicknesses, and an amplitude factor.

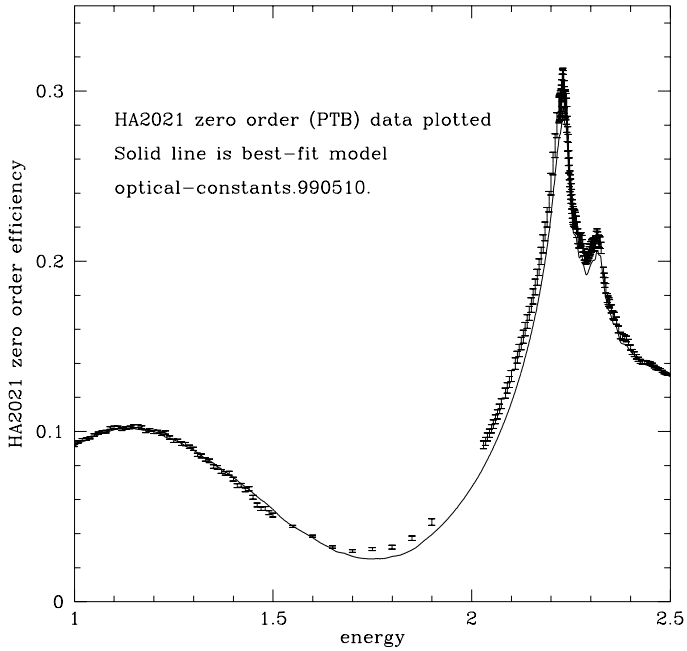

Figure 3.19: Zero order synchrotron data of flight batch HEG grating HA2021, overlaid with the best fit model. The region around the "trough" is highlighted to illustrate where conceptual improvements may be made in the grating model.

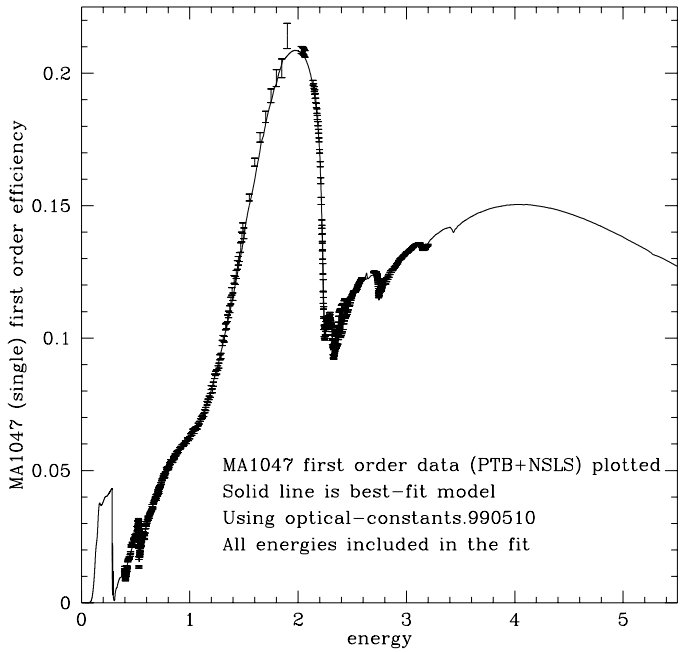

Figure 3.20: First order synchrotron data of flight batch MEG grating MA1047, overlaid with the best fit model. These data come from two different synchrotrons (PTB and NSLS) to cover the full energy span. The data sets join at 2 keV. Only first order data have been included in the fit.

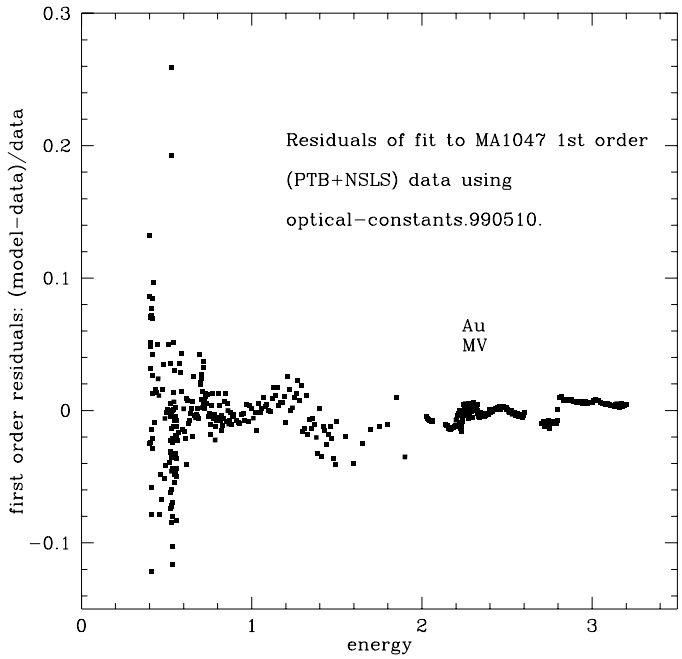

Figure 3.21: Residuals from the first order fit of grating MA1047 shown in Figure 18. Residuals have not been truncated.

Table 3.2: Typical edge residuals (percent)
Asterisk marks energies outside the applicable range for the gratings.

Model Year	Grating	N	O	Cr	MV
1999	MA1047	13	26	4.3	1.6
1996	MA1047	42	66	13	2.7
1999	HA2021	70*	43*	12*	3.3
1996	HA2021	93*	114*	28*	5.6

A perusal of Figure 9 shows two regions where the model fit does not agree well (systematically) with the data. One region is about 6 keV. This is probably due to inadequate separation of the first order from the zeroth order in the synchrotron test, and is therefore a fault of the test rather than a failure of the model. The second region is the low-energy side of the efficiency peak (about 1.5 to 2 keV). This region is also poorly fit for zeroth order, as shown in Figure 16. The reasons for the poor fit over the resonance peak (and conversely in the resonance trough of the zeroth order) are not known, although several possibilities may be considered.

The region near 2 keV corresponds to the energies in which the xray undergoes nearly a 180 degree phase shift after traversing the grating bar. This phase shift results in a near cancellation of the emerging xray wavefront in zeroth order and an enhanced first order efficiency. Hence this region is extremely sensitive to the detailed bar shapes and any attempt to model the shapes as a single shape may ultimately fall short. In fact, we believe that the unusual bar shape depicted in Figure 15 is indicative of this fact as its distorted shape will give rise to a complex pattern of phase shifts. Similarly modeling the grating efficiency as a linear combination of efficiencies from different bar shapes may also not provide an improved fit because this technique does not account for interference effects. In other words, this energy regime may be impossible to model at the desired level of accuracy using a model based upon diffraction from a periodic structure, or a superposition of periodic structures.

Other possible explanations may also be considered:

- The peak of the efficiency curve (2 keV) is also the energy where the data from the different synchrotrons meet. The actual location tested on grating HA2021 may be slightly different in the two tests, so that in effect two different gratings are being inappropriately represented by a single model. This should be easy to verify by individually modeling the two energy regions.
- The PTB beamline is known to have stray light contamination above 1500 eV, and this may affect the quality of the data being fitted in the peak.
- Since macroscopic areas of the grating are illuminated in the synchroton tests, it may be appropriate to assume more than one grating thickness. This might be expected to broaden the efficiency peak overall. Simple models with two thicknesses have *not* been found to significantly improve the model fit in this region, however.
- It may be necessary to abandon the scalar theory altogether in favor of the much more complex vector theory that includes the effects of polarization.
- The amplitude factor should probably vary with energy.

Conslusion

The grating model shows excellent agreement (at the level of a few percent) with synchrotron measurements of first order efficiencies, except at a limited set of energies. In particular, the

edges remain the largest contributor to the residuals, although our modeling of the edge structures has improved dramatically. Our measurements at PTB and NSLS have gone far to improve the optical constants β and δ which are inputs to our model. Future efforts will be directed at conceptual improvements in the model; in particular, the resonance peak around 2 keV represents one area that invites further investigation.

3.2.6 Reference Grating Measurements

Although these data provide estimates as to the validity of our grating model, synchrotron tests are impractical to use for more than a few gratings. For the full set of flight gratings, the model parameters are determined from laboratory measurements on each grating element, using a standard (electron impact) type X-ray source and a few X-ray lines in MIT's X-Ray Grating Evaluation Facility (X-GEF). Gratings that have been tested at the synchrotron are used as transfer standards in each X-GEF test, to minimize systematic errors and allow normalization against a known efficiency.

Two gratings, HX220 and MX078, were tested early in the program at a synchrotron (Markert *et al.*[59]). These are used as transfer standards in X-GEF testing; each X-GEF efficiency measurement is performed with an analogous measurement on the reference grating. Based on the assumption that the diffraction efficiency of the reference grating is correctly known at that energy, we obtain the efficiency of the test grating at the measurement energy. From measurements made at 5 or 6 energies in the laboratory, we then estimate the best-fit parameters (bar shape, gold thickness, space-to-period ratio) for the test grating and generate a model for its diffraction efficiency at all appropriate AXAF energies.

Figures 3.22 and 3.23 illustrate the quality of the model fit to the synchrotron data for the HX220 reference grating. Figures 3.24 and 3.25 show the data and fit for the reference grating MX078. These fits used both the first order and zeroth order data.

Tilt tests were performed in X-GEF on the two reference gratings. Figure 3.26 plots the asymmetry of MX078 versus angle at the Mo L line. MX078 exhibits no substantial asymmetry (confirming results found at Brookhaven). Figure 3.27 shows the asymmetry parameter found for HX220, the HEG reference grating. For reference, we have overlaid the results found in a tilt test performed at Brookhaven, which shows substantial agreement. The modeling for HX220 is discussed in Markert, *et al.*[59]

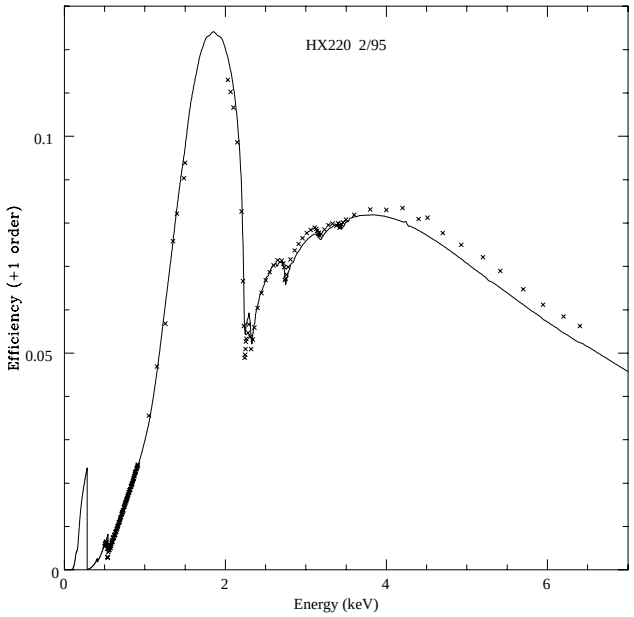

Figure 3.22: Data and best-fit model of reference grating HX220.

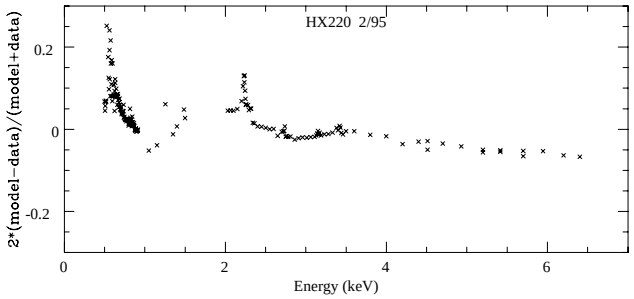

Figure 3.23: Residuals for reference grating HX220.

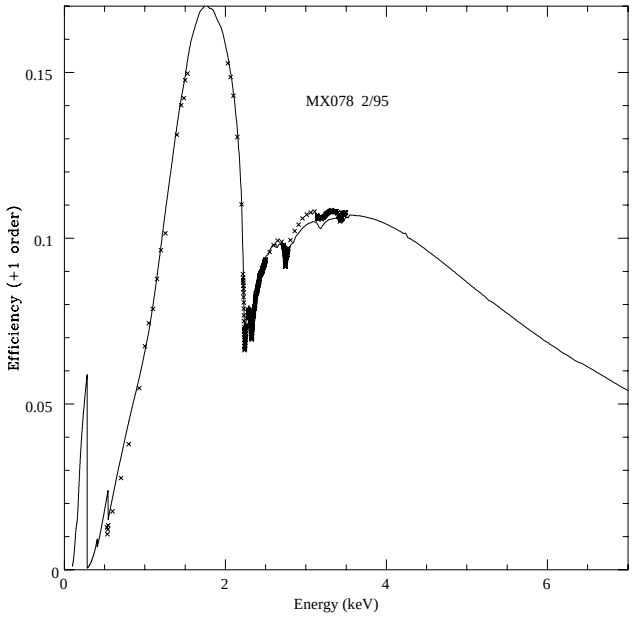

Figure 3.24: Data and best-fit model of reference grating MX078.

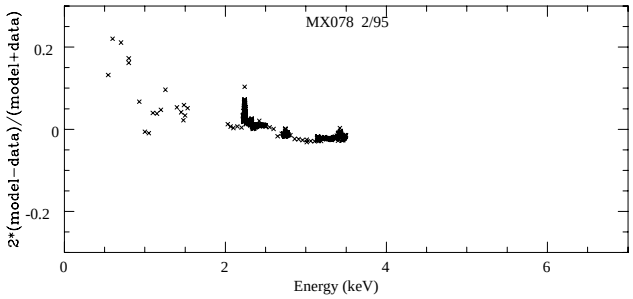

Figure 3.25: Residuals for reference grating MX078.

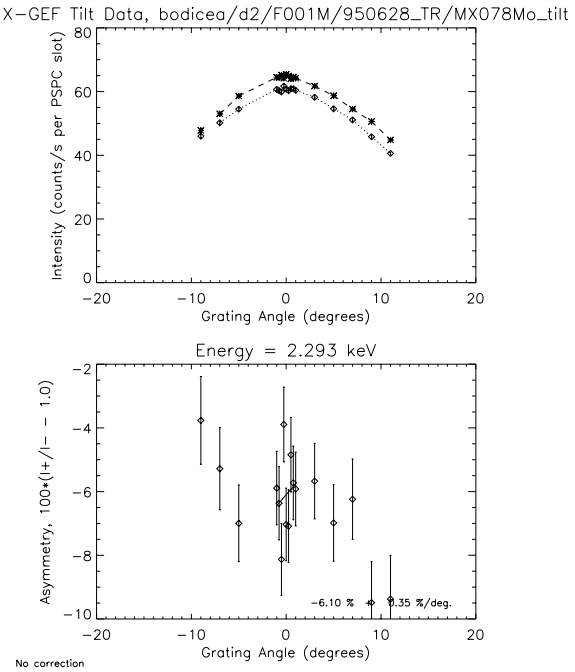

Figure 3.26: The X-GEF tilt test data for MX078 confirms the synchrtoron result of a minimal tilt-induced asymetry.

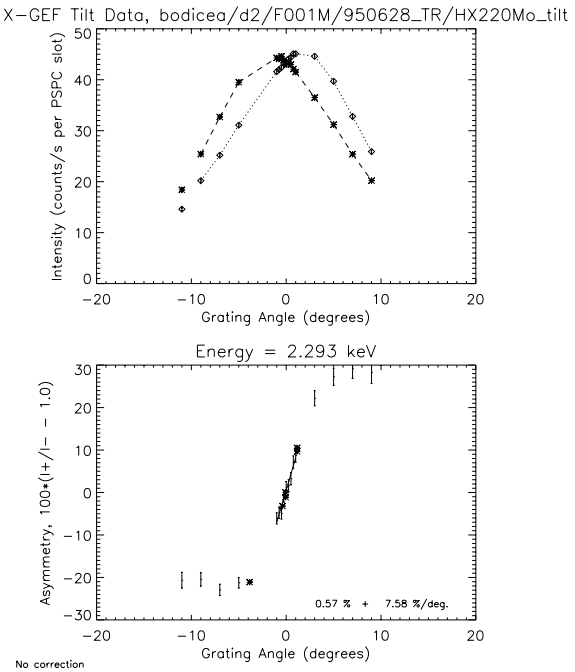

Figure 3.27: The X-GEF tilt depencance for HX220 agrees with measurements made in a tilt test at NSLS, overlaid(*). An angular offset of 1.15 degrees has been added to the NSLS measurements.

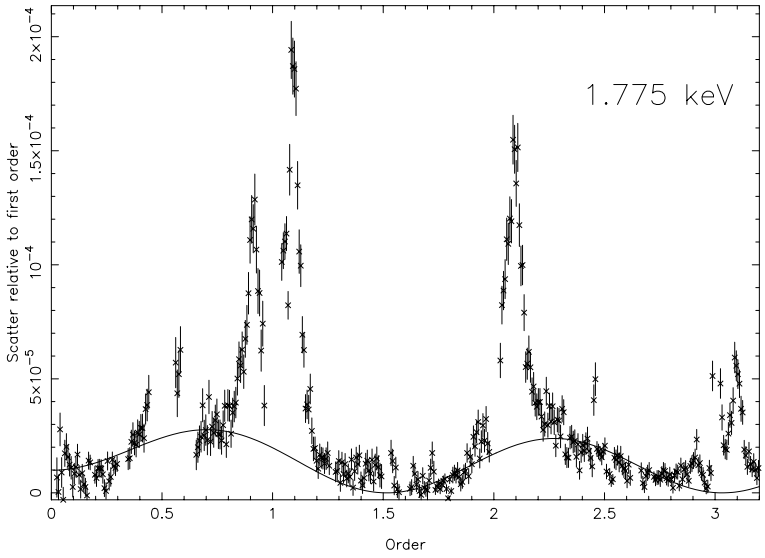

Figure 3.28: Measured HEG scatter at 1.775 keV. The scattering-per-bin normalized to the first-order intensity is plotted versus diffraction order. The solid curve is the best fit to this data using a simple rectangular grating model with no bar-to-bar correlations.

3.3 Scattering Theory

3.3.1 Introduction

In this section, based on Davis *et al.* [21], we present a general overview of grating scatter as a result of fluctuations in the grating bar geometry. This work was motivated by the XRCF tests of the HEG gratings which showed anomalous scattering of monochromatic radiation, in particular the gratings showed events with significant deviations from the integer grating orders and the events were concentrated along the dispersion direction, Section 6.6 and Marshall *et al.* [60].

The XRCF-measured HEG grating scatter is shown to be consistent with what one expects from scatter due to deviations in the grating bar geometry from perfect bars. For the purposes of this modeling, a rectangular bar model is adopted and bar parameters are deduced via fitting the model to the scattering data. The correlations deduced from this model lead to a simple physical picture of grating bar fluctuations where a small fraction of the bars, e.g., 1 in 200 are leaning.

We treat the problem of scattering from a disordered diffraction grating, and from first principles arrive at an equation for the probability distribution of scatter from such a grating. Without making any reference to a specific geometric model for the grating bar shapes, we show that the anomalous scattering observed at XRCF (e.g., see Figure 3.28) shares many of the features that one would expect to be produced as a result of grating disorder. In particular, the strong peaks that appear symmetrically about the various diffraction orders can be explained as a natural consequence of one or more correlations between neighboring bars with a correlation length that is characterized by the width of the peaks. The correlation length is estimated to be roughly three grating periods.

A more detailed description of the correlations based on a rectangular model for the bar shapes is presented in the section 3.3.5. Although the rectangular model has been shown to be inadequate for modeling the grating efficiency to the one percent calibration goal[59], it performs well at the ten to twenty percent level. Its most redeeming feature is its simplicity, which allows many of the calculations to be performed analytically. Within the context of this model, expressions for the correlations and the scattering probability are derived and then fitted to the experimental data. The resulting fit, while not perfect, does reflect many of the salient features of the data, although the resulting effective rectangular parameters are somewhat larger than the values implied by modeling of the grating efficiencies, Figure 1.5.

In the final section we present a discussion of the correlations as deduced from the modeling. Based upon the form of the correlations, a physical picture of the gratings emerge in which a small fraction (e.g., 1 in every 200) of the grating bars are leaning. Finally, the major results of this section are summarized and future modeling improvements are suggested.

3.3.2 General Formulation

Consider a diffraction grating composed of N lines, or bars, with period d, and a photon with wave number $k = 2\pi/\lambda$ incident upon the grating. It follows from Huygen's principle that the probability for scattering into an angle between θ and $\theta + \mathrm{d}\theta$ with respect to the normal of the grating is given by

$$p(k,s)\mathrm{d}s = \frac{kd}{2\pi N}\left|\sum_{j=0}^{N-1} e^{ijksd}F_j(k,s)\right|^2 \mathrm{d}s, \tag{3.15}$$

where $s = \sin\theta$ and the *structure factor* $F_j(k,s)$ is defined by

$$F_j(k,s) = \frac{1}{d}\int_0^d \mathrm{d}x e^{iksx+i\phi_j(k,x)}. \tag{3.16}$$

The shape and composition of an individual grating bar determines the complex phase shift $\phi_j(k,x)$ that, in general, depends upon energy and, possibly, the polarization of the photon. Assuming the validity of scalar diffraction theory, and neglecting reflection and refraction, the phase shift can be written in the form

$$\phi_j(k,x) = -k(\delta - i\beta)z_j(x), \tag{3.17}$$

where δ and β are energy dependent functions related to the dielectric constant of the grating bars. The function $z_j(x)$ represents the path length of the photon as it passes though the jth grating bar; it is sometimes called, rather loosely, the "grating bar shape", and more rigorously, the "path-length function".

In general, the structure factor $F_j(k,s)$ will vary with the grating bars because the "bar shape" will vary from bar to bar. Since an exact computation of the scattering probability would require complete knowledge of all the bar shapes, and since there are millions of bars that contribute to the scattering, we must resort to a statistical means of computing Eq. 3.15. This is completely analogous to the situation in statistical physics where one deals with systems that consist of large numbers of degrees of freedom, and whose complete characterization requires a knowledge of the initial conditions for each degree of freedom. These problems are treated statistically where one introduces the notion of an ensemble of macroscopically identical systems and makes an ergodic hypothesis that at any given instant the microscopic state of the system is represented by one

of the systems in the ensemble. Hence the assumption of ergodicity allows one to compute the time average of a macroscopic quantity by averaging that quantity over the ensemble. In a similar vein we shall introduce the idea of an ensemble of gratings and make the assertion that the observed scattering does not depend upon the exact "microscopic" state of the grating, but that it is an indicator of the "macroscopic" state. In other words, we shall assume that the scattering is a macroscopic property of the ensemble and may be computed via

$$p(k,s)\mathrm{d}s = \frac{kd}{2\pi N}\left\langle \left| \sum_{j=0}^{N-1} e^{ijksd} F_j(k,s) \right|^2 \right\rangle \mathrm{d}s, \tag{3.18}$$

where $\langle\cdot\rangle$ denotes averaging over the ensemble. The specification of the ensemble involves knowing the probability for a particular configuration of grating bars, denoted by the ordered set of bar shapes $\{z_j\}$. Let this probability be represented by the probability density $\mathcal{P}(z_0, z_1, \ldots, z_{N-1})$ such that the ensemble average of some function $f(z_0, \ldots z_{N-1})$ is given by [1]

$$\langle f(z_0, \ldots, z_{N-1})\rangle = \int \mathcal{D}z_0(x)\cdots\mathcal{D}z_{N-1}(x) f(z_0, \ldots, z_{N-1})\mathcal{P}(z_0, \ldots, z_{N-1}). \tag{3.19}$$

Furthermore, we shall assume that the ensemble is such that $\langle f(z_j)\rangle$ is independent of j, and that $\langle f(z_j, z_l)\rangle$ depends only upon the difference $j-l$. For obvious reasons, a probability distribution with these properties is said to be *homogeneous* or *stationary*[92].

With the assumption of a homogeneous probability distribution for bar shapes, denote the ensemble averaged structure factor by

$$\bar{F}(k,s) = \langle F_j(k,s)\rangle \tag{3.20}$$

and define $f_j(k,s)$ to be the deviation of the jth bar from this value via

$$F_j(k,s) = \bar{F}(k,s) + f_j(k,s). \tag{3.21}$$

Substituting the above definitions into Eq. 3.18 yields for the probability density

$$p(k,s) = \frac{kd\sin^2(\frac{1}{2}Nksd))}{2\pi N\sin^2(\frac{1}{2}ksd)}|\bar{F}(k,s)|^2 + \frac{kd}{2\pi N}\sum_{j,l} e^{iksd(j-l)}\langle f_j f_l^*\rangle. \tag{3.22}$$

For very large N, the first term goes to zero like $1/N$ except when ksd is a multiple of 2π where it becomes proportional to N. In fact, one can show that the factor involving N in first term is a representation of a series of delta functions:

$$\frac{kd\sin^2(\frac{1}{2}Nksd)}{2\pi N\sin^2(\frac{1}{2}ksd)} = \sum_n \delta_N(s - \frac{2\pi n}{kd}). \tag{3.23}$$

This equivalence allows the probability density to be written

$$p(k,s) = |\bar{F}(k,s)|^2\sum_n \delta_N(s - \frac{2\pi n}{kd}) + \frac{kd}{2\pi N}\sum_{j,l} e^{iksd(j-l)}\langle f_j f_l^*\rangle. \tag{3.24}$$

Thus, the first term represents the familiar interference pattern that consists of a series of sharp peaks, weighted by $|\bar{F}(k,s)|^2$, whose height varies with N. The peaks occur at values of ksd that are multiples of 2π, or equivalently when

$$n\lambda = d\sin\theta, \tag{3.25}$$

[1] Since the bar shape $z_j(x)$ is a function, the integrals in this equation are functional integrals and the symbol $\mathcal{D}z(x)$ is called the *Weiner measure*. See the book by Feynman and Hibbs[27] for a simple introduction to functional integration. Alternatively, one can view such an integral as a multiple integral over the parameters defining a shape, e.g., the bar width and height for a rectangular bar.

which is the familiar grating equation. The second term is the scattering term and is more complicated. Superficially, it appears to vanish in the limit of a large number of bars; however, owing to the double sum (hence N^2 terms), this is not necessarily true.

The quantities $\langle f_j f_l^* \rangle$ represent correlations between the various grating elements. If the shape of each grating bar element is independent of the others, then $\langle f_j f_l^* \rangle$ vanishes except when $j = l$. More explicitly, if no correlations exist between the fluctuations of the grating bars then

$$\langle f_j f_l^* \rangle = \langle |f_j|^2 \rangle \delta_{jl}. \tag{3.26}$$

If there are correlations between the various grating bars, then Eq. 3.26 is not correct. We make the assumption that if any correlations are present, then they have a short range. This is really an assumption about the fabrication method, but one could imagine the presence of long range correlations from e.g., a holographic fabrication process in which a non-monochromatic light source would create a beating effect. Similarly, for a "ruled" grating, the mechanical system could introduce periodic long range correlations. Nevertheless, we shall assume that $\langle f_j f_l^* \rangle$ is zero for $|j-l|$ greater than some number M. For example, if $M = 1$, then only nearest neighbor correlations may be present. If $M \ll N$, then one may neglect edge effects in the sum and write the scattering term in Eq. 3.24 as

$$\frac{kd}{2\pi N} \sum_{j=0}^{N-1} \sum_{m=-M}^{M} e^{imksd} \langle f_j f_{j+m}^* \rangle. \tag{3.27}$$

Since we have assumed that the ensemble governing the probability distributions is homogeneous, by definition we know that the correlations are translation invariant, i.e., $\langle f_j f_{j+m}^* \rangle$ does not depend upon j. Hence, the scattering term reduces to

$$\frac{kd}{2\pi} \sum_{m=-M}^{M} e^{imksd} c_m(k,s), \tag{3.28}$$

where c_m has been defined by

$$c_m(k,s) = \langle f_j(k,s) f_{j+m}^*(k,s) \rangle. \tag{3.29}$$

Using the property that $c_{-m} = c_m^*$, which follows from the definition of c_m, and separating out real and imaginary parts, it follows that Eq. 3.24 may be written

$$\begin{aligned} p(k,s) =& |\bar{F}(k,s)|^2 \sum_n \delta_N(s - \frac{2\pi n}{kd}) + \frac{kd}{2\pi} c_0(k,s) \\ &+ \frac{kd}{\pi} \sum_{m=1}^{M} \Big\{ \mathrm{Re}[c_m(k,s)] \cos(mksd) - \mathrm{Im}[c_m(k,s)] \sin(mksd) \Big\}. \end{aligned} \tag{3.30}$$

This equation shows that the intensity pattern will consist of sharp diffraction peaks on top of a weak but diffuse scattering background. The actual angular dependence of the diffuse scattering will depend upon the precise nature of the correlations and upon the correlation length given by M. Nevertheless, this equation permits us to make several observations about the scattering without reference to a detailed model of the grating bar shapes.

First of all, note that if the correlations $c_m(k,s)$ are slowly varying functions of s, then the scattering will be quasi-periodic with a period of $2\pi/kd$. That is, the scattering will roughly repeat itself between diffraction orders. The scattering data shown in Figure 6.20 appears to share this feature. For example, strong scattering peaks appear just to the right of the first, second, and third diffraction orders. In addition, there is a peak just to the left of first order

and there appears to be some evidence for peaks just to the left of the second and third orders, although the existence of the peak at the left of second order is questionable. On the other hand, the fact that the scattering is not strictly periodic is just an indication that $c_m(k,s)$ depends upon s.

3.3.3 Displacement Variations

One might think that since the scattering is relatively weak near zeroth order with no strong peaks in that region, the apparent quasi-periodicity reflected in the data around first, second, and third orders is coincidental. However, an important prediction of Eq. 3.30 is that for fluctuations involving simple displacements of the grating bars, there can be no scattering near zeroth order. In fact, this is a well known result from the theory of X-ray diffraction from crystals[97]. To prove this in the context of a diffraction grating, consider a model of N grating bar shapes that differ from one another only by a shift, or displacement from their ideal lattice positions. That is, the path-length function for the jth bar is assumed to be given by $z_j(x) = z(x + a_j)$ where a_j denotes the shift of the bar from its ideal position in the unit cell. Furthermore, assume that $z(x)$ is non-zero only for values of x such that $|a_j| \le x \le d - |a_j|$ for all j. Physically, this means that the center of the grating bar whose shape is described by $z(x)$ lies near middle of the cell. Then, the structure factor F_j for the jth unit cell can be written

$$\begin{aligned} F_j(k,s) &= \frac{1}{d}\int_0^d \mathrm{d}x e^{iksx+i\phi(x+a_j)} \\ &= \frac{1}{d}e^{-iksa_j}\int_{a_j}^{d+a_j} \mathrm{d}x e^{iksx+i\phi(x)} \\ &= \frac{1}{d}e^{-iksa_j}\left(\int_0^d + \int_d^{d+a_j} - \int_0^{a_j}\right)\mathrm{d}x e^{iksx+i\phi(x)}. \end{aligned} \tag{3.31}$$

With the assumption that $z(x)$, and hence $\phi(x)$, vanishes for $x < |a_j|$ or for $x \ge d - |a_j|$, the latter two integrations can be performed with the result

$$F_j(k,s) = e^{-iksa_j}F(k,s) + \frac{1}{iksd}(1 - e^{-iksa_j})(e^{iksd} - 1). \tag{3.32}$$

Here, $F(k,s)$ has been defined

$$F(k,s) = \frac{1}{d}\int_0^d \mathrm{d}x e^{iksx+i\phi(x)}. \tag{3.33}$$

From this, it trivially follows from Eq. 3.20, that

$$\bar{F}(k,s) = \langle e^{-iksa_j}\rangle F(k,s) + \frac{1}{iksd}(e^{iksd} - 1)(1 - \langle e^{-iksa_j}\rangle) \tag{3.34}$$

and we also deduce from Eq. 3.21 that

$$f_j(k,s) = \left[e^{-iksa_j} - \langle e^{-iksa_j}\rangle\right]\left[F(k,s) - \frac{1}{iksd}(e^{iksd} - 1)\right]. \tag{3.35}$$

Thus, from this equation it is immediately clear that a model of grating bar *fluctuations consisting of pure displacements produces no scattering in the immediate vicinity of zeroth order.* This result is quite general since no further assumptions were made about about the actual shape of the grating bars.

To see the impact of these fluctuations on the diffraction orders, assume that the shift parameters a_j are independently Gaussian distributed with a mean of zero and a variance of σ^2. For such a distribution, one can show that

$$\langle e^{-i2\pi n a_j/d}\rangle = e^{-\frac{1}{2}(2\pi n\sigma/d)^2} \tag{3.36}$$

from which it follows

$$|\bar{F}(k,s_n)|^2 = |F(k,s_n)|^2 e^{-(2\pi n\sigma/d)^2}, \tag{3.37}$$

where $s_n = 2n\pi/kd$ is the value of s at the nth diffraction order. This equation explicitly shows that the fluctuations reduce the power in the diffraction orders, as one would expect from considerations of flux conservation.

3.3.4 Bar Geometry Variations

The geometry of the jth grating bar may be specified by a number of geometric quantities. Let the μth such quantity for the jth bar be denoted by $\xi_\mu^{(j)}$. For example, a rectangular grating bar may be specified by three quantities: the width (ξ_1), height (ξ_2), and displacement (ξ_3). The structure factor F_j will be a function of these quantities and indicated symbolically by $F_j(k,s,\xi)$. Let $\Delta\xi_\mu^{(j)}$ be the deviation of the μth parameter from its mean, i.e.,

$$\xi_\mu^{(j)} = \langle\xi_\mu^{(j)}\rangle + \Delta\xi_\mu^{(j)}. \tag{3.38}$$

Assuming that the fluctuations $\Delta\xi_\mu^{(j)}$ are small, we can approximate the structure factor by

$$F_j(k,s,\xi) = F(k,s,\langle\xi\rangle) + \sum_\mu \frac{\partial F}{\partial\xi_\mu}\Delta\xi_\mu^{(j)}, \tag{3.39}$$

where $F(k,s,\langle\xi\rangle)$ is independent of j by virtue of the assumed homogeneity of the ensemble. It then follows from Eq. 3.21

$$f_j(k,s,\xi) = \sum_\mu \frac{\partial F}{\partial\xi_\mu}\Delta\xi_\mu^{(j)} \tag{3.40}$$

and from Eq. 3.29

$$\begin{aligned} c_m(k,s) &= \langle f_j f_{l+m}^*\rangle \\ &= \sum_{\mu\nu}\frac{\partial F}{\partial\xi_\mu}\frac{\partial F^*}{\partial\xi_\nu}\langle\Delta\xi_\mu^{(j)}\Delta\xi_\nu^{(j+m)}\rangle. \end{aligned} \tag{3.41}$$

Since the ensemble is assumed to be homogeneous, the correlations $\langle\Delta\xi_\mu^{(j)}\Delta\xi_\nu^{(j+m)}\rangle$ are independent of j, and will be denoted by $G_{\mu\nu}(m)$, i.e.,

$$G_{\mu\nu}(m) = \langle\Delta\xi_\mu^{(j)}\Delta\xi_\nu^{(j+m)}\rangle. \tag{3.42}$$

Moreover, they are independent of k and s, and assuming left-right invariance of the grating, they satisfy the symmetry relations

$$G_{\mu\nu}(m) = G_{\mu\nu}(-m) = G_{\nu\mu}(m). \tag{3.43}$$

From this symmetry it follows that $c_m(k,s)$ is real. Since $G_{\mu\nu}(m)$ is an even function of m, it may be represented as Fourier cosine series. In addition, from physical considerations the correlations

must fall off with increasing $|m|$. For simplicity, assume that the correlations $G_{\mu\nu}(m)$ may be represented in the form

$$G_{\mu\nu}(m) = \sigma_{\mu\nu} e^{-\alpha_{\mu\nu}|m|} \cos(2\pi m \Omega_{\mu\nu}). \tag{3.44}$$

In terms of these correlations, the probability density for scattering from Eq. 3.28 may be expressed as

$$\frac{kd}{2\pi} \sum_{\mu\nu} \sigma_{\mu\nu} \frac{\partial F}{\partial \xi_\mu} \frac{\partial F^*}{\partial \xi_\nu} \left[\sum_{m=-\infty}^{\infty} e^{imksd} e^{-\alpha_{\mu\nu}|m|} \cos(2\pi m \Omega_{\mu\nu}) \right]. \tag{3.45}$$

In deriving this equation, the exponential fall off of the correlations have allowed the sum to extended to all m. The sum over m may be performed by writing the cosine in its complex representation and recognizing that the resulting sum is geometric. It is left as an exercise for the reader to show that

$$\begin{aligned} \sum_{m=-\infty}^{\infty} & e^{imksd} e^{-\alpha|m|} \cos(2\pi m \Omega) \\ &= \frac{1+e^{-\alpha}}{2} \left[\frac{1-e^{-\alpha}}{(1-e^{-\alpha})^2 + 2e^{-\alpha}(1-\cos(ksd+2\pi\Omega))} \right. \\ &\qquad \left. + \frac{1-e^{-\alpha}}{(1-e^{-\alpha})^2 + 2e^{-\alpha}(1-\cos(ksd-2\pi\Omega))} \right] \end{aligned} \tag{3.46}$$

The right hand side of this equation shows that the correlations will produce peaks whenever $\cos(ksd \pm 2\pi\Omega)$ is unity, i.e., at values of s when $ksd/2\pi = n \pm \Omega$. In other words, *the scattering will consist of peaks that are symmetrically located about the diffraction orders*, although the strength of the peaks will depend upon the exact form of $c_m(k,s)$. A quick glance at Figure 6.20 shows that the peaks immediately to the left and right of first order have this property. In addition, the data has a peak just to the right of third order and it appears to have a small peak symmetrically placed at the left of third order. It is harder to make the argument about second order because if there is a peak to the left of second order then it is suppressed.

The location of the peaks and their widths provide valuable information about the parameters Ω and α. In particular the location of the peaks give information about Ω, and their widths are governed by α. To see this, suppose that α and $\theta = ksd + 2\pi\Omega$ are small. Then the first term term on the right hand side of Eq. 3.46 may be approximated by

$$\frac{\alpha}{\alpha^2 + \theta^2}. \tag{3.47}$$

This function has a maximum at $\theta = 0$ and the half-width at half-maximum is α. Hence, the width of the scattering peak provides information about α, which in turn dictates the range of the correlation responsible for the peak. Armed with this knowledge one can make a rough estimate of Ω and α for the correlation associated with the peaks closest to the diffraction orders of Figure 6.20. We estimate Ω to be around 0.1 and α to be roughly $0.05 \times 2\pi \approx 0.3$. This implies that the correlations have a length of $1/\alpha$ or about 3 grating bars.

3.3.5 Correlations in the Rectangular Model

In this section, we assume that the grating bar shapes may be represented by a simple rectangle with height h and width w. The center of the bar is assumed to offset a distance a from the center of the lattice node (see Figure 3.29).

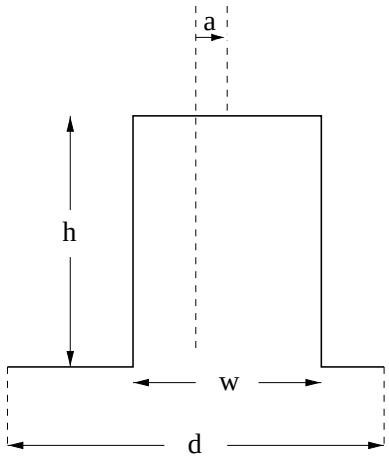

Figure 3.29: Figure showing the geometric parameters for a rectangular grating bar of width w and height h in a unit cell with period d. The displacement of the bar from the center of the unit cell is given by a.

The rectangular geometry readily permits the integral in Eq. 3.16 to computed with the result

$$F_j(k,s) = \frac{\sin(\frac{1}{2}ksd)}{\frac{1}{2}ksd} + e^{iksa_j}(e^{-kh_j\beta - ikh_j\delta} - 1)\frac{\sin(\frac{1}{2}ksw_j)}{\frac{1}{2}ksd}. \tag{3.48}$$

As in the previous section, we assume that the correlations are small so that Eq. 3.41 is valid. Expressing Eq. 3.41 in terms of h, w, and a, results in

$$\begin{aligned} c_m(k,s) =& d^2\left|\frac{\partial F}{\partial a}\right|^2 G_{aa}(m) + h^2\left|\frac{\partial F}{\partial h}\right|^2 G_{hh}(m) + d^2\left|\frac{\partial F}{\partial w}\right|^2 G_{ww}(m) \\ &+ 2hd\ \mathrm{Re}\left[\frac{\partial F}{\partial a}\frac{\partial F^*}{\partial h}\right] G_{ah}(m) + 2hd\ \mathrm{Re}\left[\frac{\partial F}{\partial w}\frac{\partial F^*}{\partial h}\right] G_{wh}(m) \\ &+ 2d^2\ \mathrm{Re}\left[\frac{\partial F}{\partial a}\frac{\partial F^*}{\partial w}\right] G_{aw}(m), \end{aligned} \tag{3.49}$$

where factors of d and h have been introduced to make the correlation functions $G_{\mu\nu}(m)$ unitless, e.g.,

$$\begin{aligned} G_{wh}(m) &= \langle \frac{\Delta w}{d}\frac{\Delta h}{h} \rangle \\ &= \sigma_{wh} e^{-\alpha_{wh}|m|}\cos(2\pi m \Omega_{wh}). \end{aligned} \tag{3.50}$$

The partial derivatives of the structure factor $F(k,s)$ are rather straightforward to carry out

h	=	0.64μm	w/d	=	0.84			
σ_{ww}	=	6.5×10^{-5}	α_{ww}	=	0.27	Ω_{ww}	=	0.092
σ_{hh}	=	5.0×10^{-5}	α_{hh}	=	0.60	Ω_{hh}	=	0.50
σ_{wh}	=	4.2×10^{-5}	α_{wh}	=	0.30	Ω_{wh}	=	0.91

Table 3.3: This table shows the best fit parameter values as deduced from fitting the scattering data at 1.384, 1.775, and 2.035 keV. Displacement variations were not considered. Figure 3.30 shows the resulting fit.

with the result:

$$\begin{aligned}
\left|\frac{\partial F}{\partial a}\right|^2 &= \frac{4}{d^2}[1 - 2e^{-kh\beta}\cos(kh\delta) + e^{-2kh\beta}]\sin^2(\frac{1}{2}ksw) \\
\left|\frac{\partial F}{\partial w}\right|^2 &= \frac{1}{d^2}[1 - 2e^{-kh\beta}\cos(kh\delta) + e^{-2kh\beta}]\cos^2(\frac{1}{2}ksw) \\
\left|\frac{\partial F}{\partial h}\right|^2 &= k^2(\delta^2 + \beta^2)e^{-2kh\beta}\left[\frac{\sin(\frac{1}{2}ksw)}{\frac{1}{2}ksd}\right]^2 \\
\mathrm{Re}\left[\frac{\partial F}{\partial w}\frac{\partial F^*}{\partial h}\right] &= \frac{k}{d}e^{-kh\beta}\left[\beta\cos(kh\delta) + \delta\sin(kh\delta) - \beta e^{-kh\beta}\right]\frac{\sin(ksw)}{ksd} \\
\mathrm{Re}\left[\frac{\partial F}{\partial a}\frac{\partial F^*}{\partial h}\right] &= \frac{4k}{d}e^{-kh\beta}\left[-\beta\sin(kh\delta) + \delta\cos(kh\delta) - \delta e^{-kh\beta}\right]\frac{\sin^2(\frac{1}{2}ksw)}{ksd} \\
\mathrm{Re}\left[\frac{\partial F}{\partial a}\frac{\partial F^*}{\partial w}\right] &= 0,
\end{aligned} \tag{3.51}$$

This model contains 17 independent parameters that include the bar width w and height h as well as the 15 parameters that define the correlation functions $G_{\mu\nu}(m)$. A χ^2 minimization procedure based upon the Marquardt algorithm[9] was used in deducing the parameters. Since the scattering contains energy-dependent terms, a global fit to the scattering data at 1.384, 1.775, and 2.035 keV was performed. These particular data were used because we feel that they have the the least experimental uncertainties and would provide the best estimates for the parameters.

We first considered the case involving no correlations. This reduced the parameter space from 17 dimensions down to 5. Figure 3.28 shows the best fit of the rectangular model with no correlations to the data 1.775 keV. From the figure, one can immediately see that the model without correlations fails to reproduce any of the rich structure seen in the data. The lack of any prominent scattering features is a strong indication that the grating scatter must be the result of correlations.

Figure 3.30 shows the result of a simultaneous fit to the 1.384, 1.775, and 2.035 keV scattering data when correlations were included. The parameters deduced from the fit are presented in Table 3.3. Fluctuations involving the bar displacement a were not included in this fit, reducing the number of free parameters down to 11 (including them did not substantially improve the fit so we felt that it was better to restrict the model to 11 parameters).

We can immediately see that including correlations results in a dramatic improvement of the fit. Although not perfect, this model shows all the main features in the scattering data at these

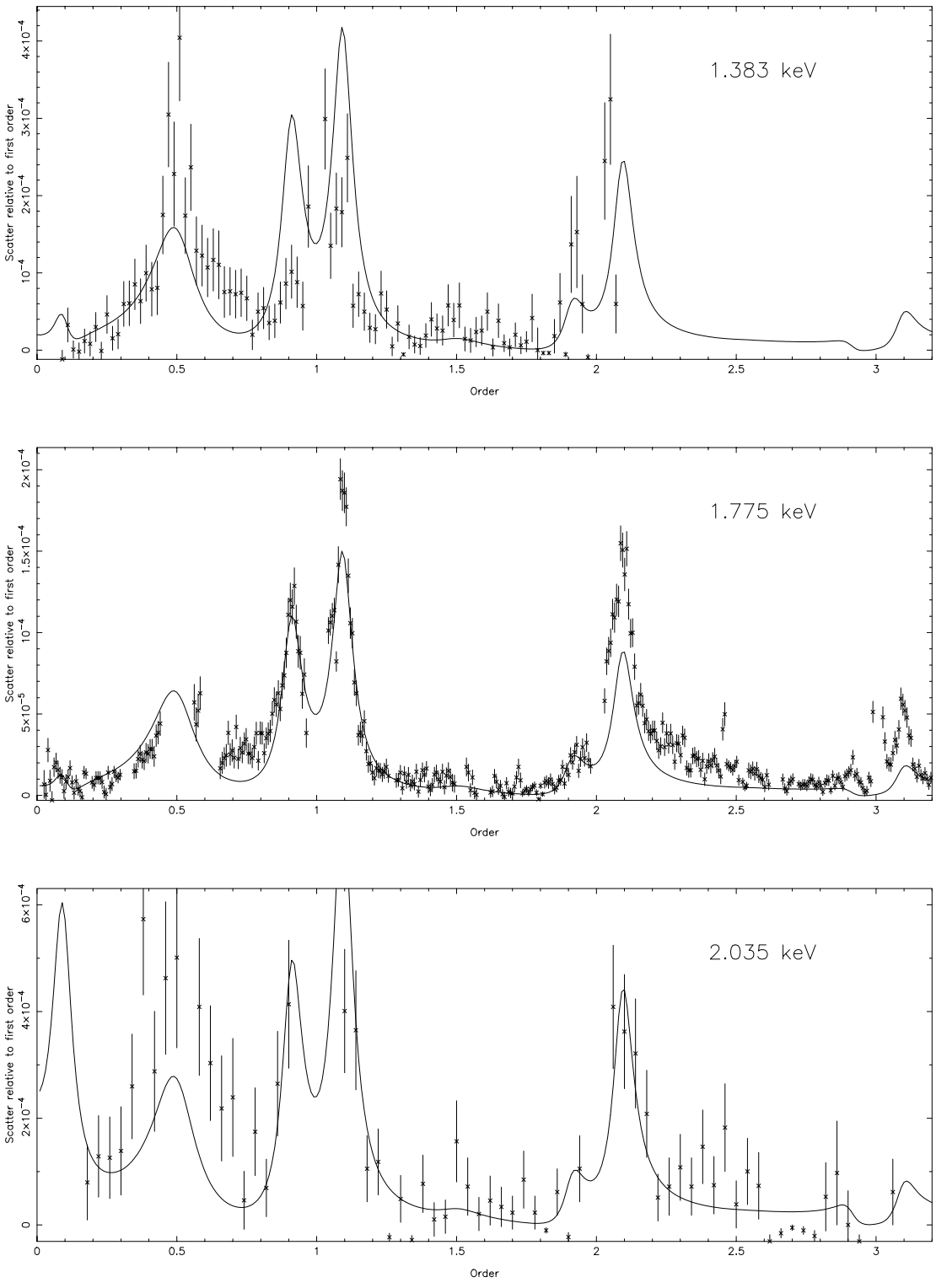

Figure 3.30: Results of a global fit to the 1.384, 1.775, and 2.035 keV scattering data. The model included width-width, height-height, and width-height correlations.

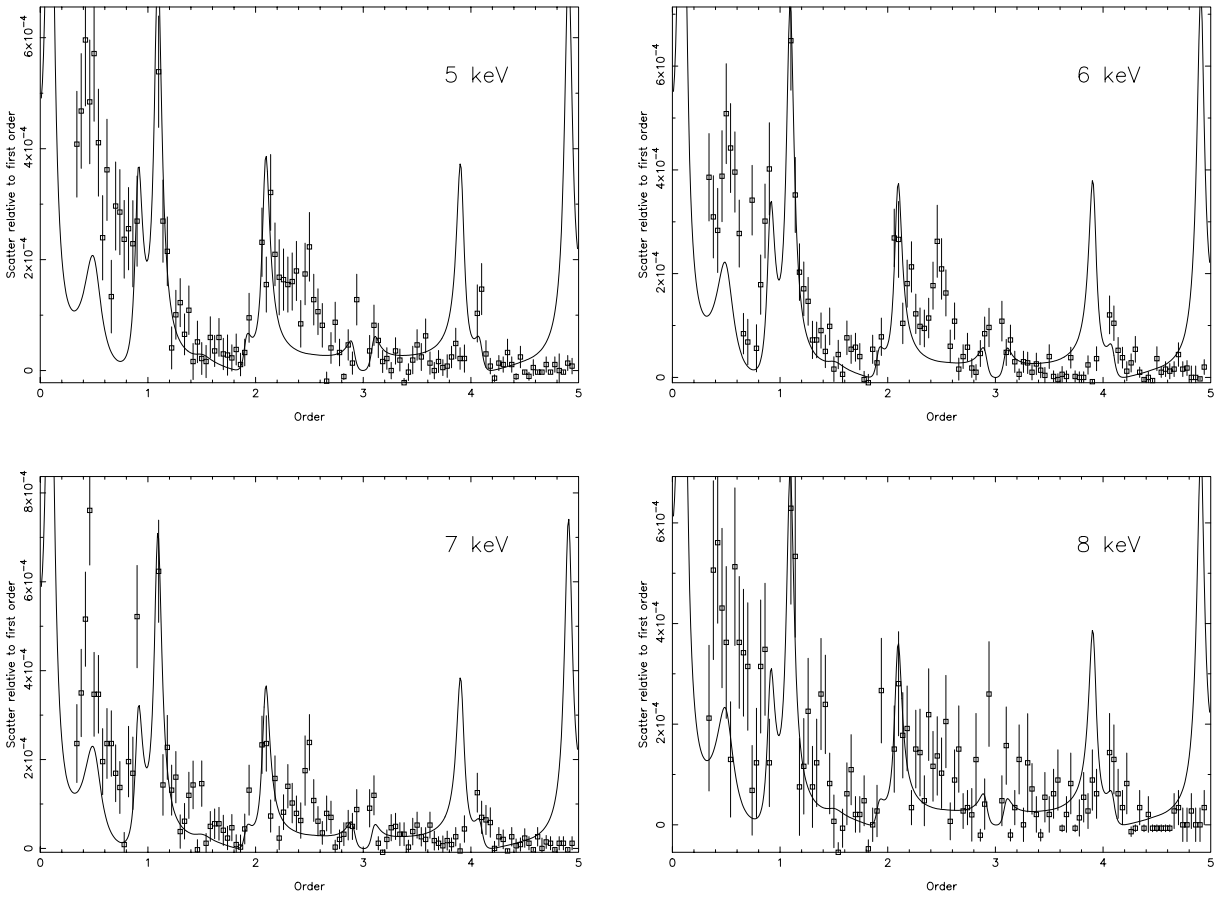

Figure 3.31: These figures show the predictions of the correlation model of Figure 3.30 evaluated at at 5, 6, 7, and 8 keV overlaid with the scattering data at these energies.

energies. This is especially true for our best data set, the data at 1.775 keV. The main areas of disagreement are near the half order locations, and at the second and third order scattering peaks where it underestimates the scattering. Also the average effective-rectangular bar width resulting from the fit is about 35 percent larger than the accepted average width: w/d is 0.84 compared to $w/d \approx 0.60$ based on detailed vertex-model fits[59] to the facet data[73]. Nevertheless, we feel that the fit is remarkable considering the simplicity and known shortcomings of the model.

Figure 3.31 shows the predictions of the model at higher energies ($5 - 8$ keV) overlaid with scattering data at those energies. The model is not too bad at predicting the scatter between the first and third orders in the high energy data, although it performs poorly when extrapolated past third order. This should not be too surprising since the data used to determine the model's parameters did not extend past third order.

3.3.6 Discussion

While the fit adequately reproduces many of the features observed in the data, the real physics lies in the form of the correlation functions deduced from the fit. A plot of the three correlation

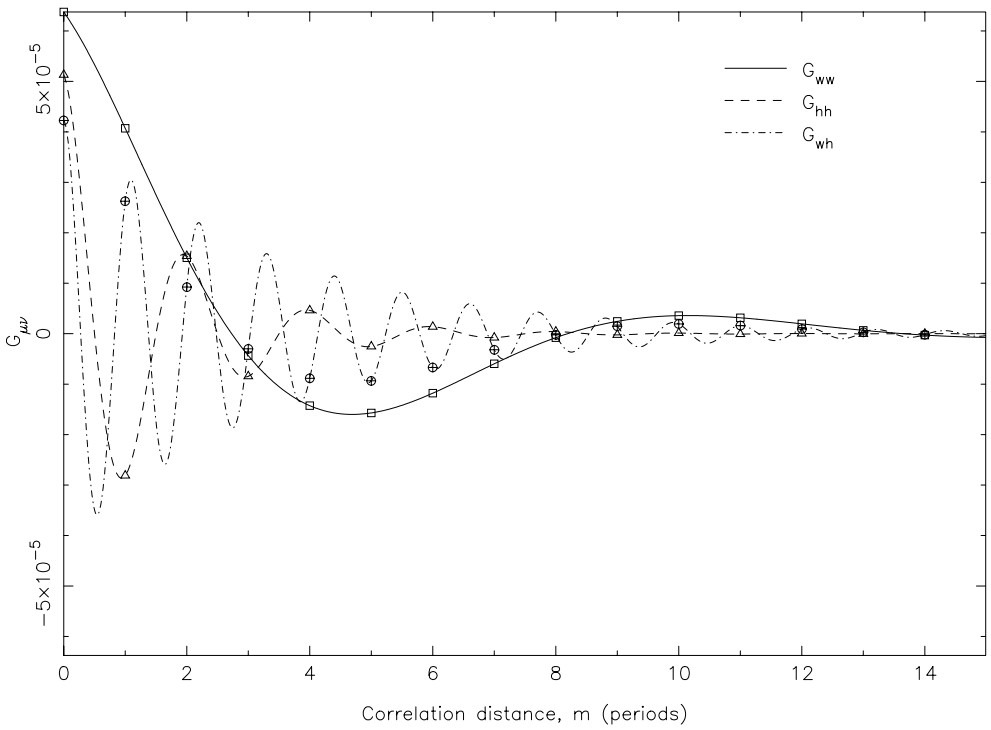

Figure 3.32: This figure shows a plot of the correlation functions parameterized in Eq. 3.44 using the parameters from Table 3.3.

functions $G_{ww}(m)$, $G_{hh}(m)$, and $G_{wh}(m)$ is shown in Figure 3.32. The dominate correlation is $G_{ww}(m)$, i.e., the width-width correlation. As can been seen from the figure, the shape of this correlation implies that the grating bar widths of the first and second nearest neighbor bars are positively correlated whereas the widths of the fourth and fifth nearest neighbors are anti-correlated. Physically, this correlation could arise by groups of two or three grating bars leaning in the same general direction. It is this correlation that appears to be responsible for the strong peaks closest to the diffraction orders.

The form of the height-height correlations, $G_{hh}(m)$, indicate that heights of nearest neighbors are anti-correlated. This has the effect of doubling the grating period and it is this correlation that contributes to the scattering near the half-orders. The simplest physical picture of this type of correlation is that of the left and right nearest neighbors leaning in the direction of the central bar.

One must not come to the conclusion that these physical pictures of the width-width and height-height correlations are mutually exclusive. Indeed there is nothing that prevents the gratings from having both types of disorder because each type may occur at disjoint parts of the grating. Thus the physical picture that emerges from these correlations is that the grating consists of localized groups of leaning bars and that the groups may be classified according to at least two varieties. The first type consists of several bars that lean in the same direction, possibly three or four together. The second type of fluctuation involves a group of three bars where the left and right bar leans on the central one. The final correlation, $G_{wh}(m)$, can be though of as the result of a combination of these two physical pictures.

If the explanation of the source of the correlations is correct, then the size of the correlations

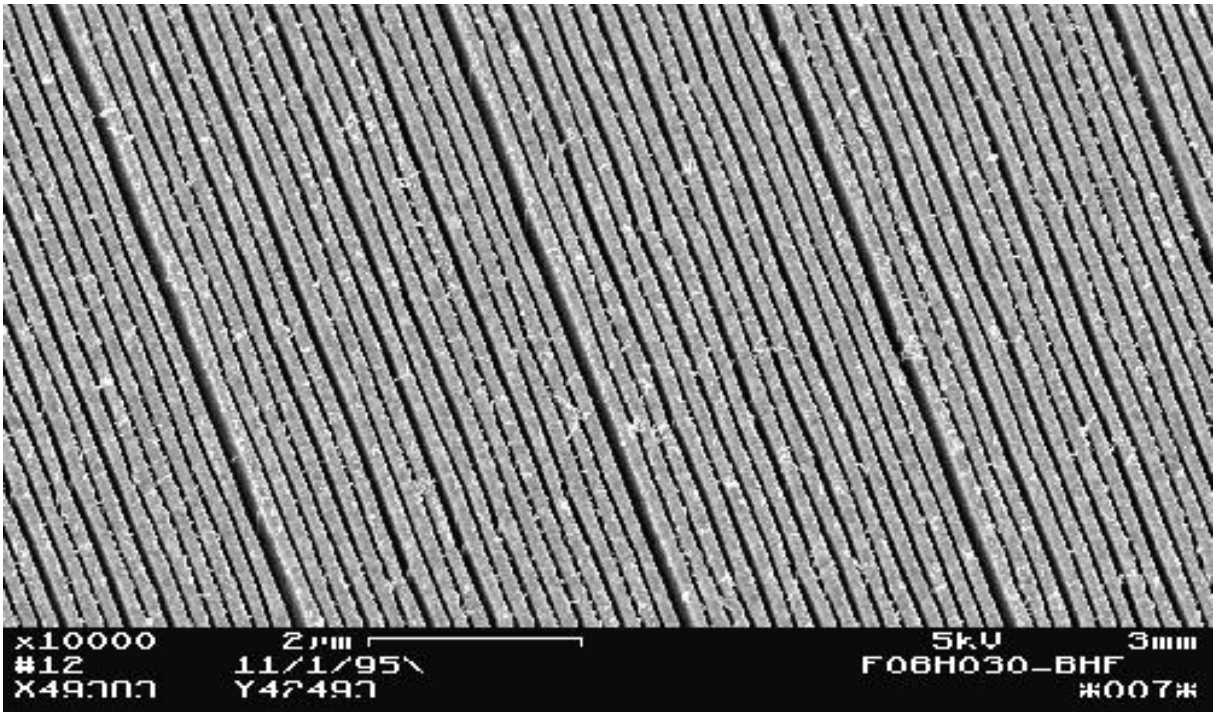

Figure 3.33: Electron micrograph of gold HEG bars on a monitor sample. The sample, F06H030b, is from flight fabrication lot 6; 6 of the 144 flight HEGs are from the same lot.

may be used to deduce the frequency of such fluctuations. For example, consider the width-width correlation, which is roughly 10^{-4} and implies that the fluctuation $\Delta w/d$ is 0.01 or about 1 percent of the period. This is consistent with 1 in 200 grating bars having a fluctuation in width by half a period, while the other 199 bars do not fluctuate at all.

Finally, if the scattering is due to the presence of leaning bars, then the absence of any detectable scattering by the MEG gratings is very easy to understand. The MEG gratings have a bar width of about 0.2 microns, and a bar height of about 0.36 microns. Hence, compared to the HEG gratings, which have a height to width ratio of about 5, the MEG gratings have a height to width ratio that is less than 2, and would be much less likely to lean.

3.3.7 Conclusion and Next Steps

Despite the apparent simplicity of both the rectangular model and the assumed form of the correlations, the resulting fits to the data are relatively good. The primary goal of this work was to demonstrate that the observed scatter could be the result of imperfections in the gratings and not to some other more exotic physical explanation. We are quite content that this goal has been achieved and we believe that the rectangular model has served us quite well in this regard.

Nevertheless, the fits are far from perfect and there are several discrepancies that should be accounted for by a more accurate and sophisticated model. Over 144 distinct grating facets contributed to the scatter and it is not inconceivable that a better fit could be achieved by using more than one set of bar parameters. This is perhaps the most trivial extension of

the simple rectangular model used here. Also, we assumed that the deviations in the bar parameters from their ideal values were small enough that only first order deviations were important. Although the average fluctuation was found to be very small, any one bar parameter could deviate significantly from its mean, with the implication that higher order terms in the expansion could be significant.

Since the actual bars have path-length functions that are more trapezoidally shaped than rectangular, it makes more sense to consider a model involving trapezoidal bars. Such a model would also permit a more direct study of leaning bars— something that is not possible within the confines of the rectangular model. Finally, there are other components of the gratings that have been totally ignored in this work, and the fluctuations in these quantities could contribute to scatter. A more complete treatment would also include these fluctuations, e.g., fluctuations in the plating base as well as in the thickness of the polyimide film.

3.4 Efficiency Software

The efficiency modeling software used to study synchrotron data, analyze laboratory data, and create the HETG efficiency values is the multi-vertex efficiency code written by John E. Davis. Key routines are written in "C" and compiled into the executable "eff". This executable can be controlled through scripts written in S-Lang, *e.g.*, `multi.sl`.

The `multi.sl` program takes a file with one or more multi-vertex-grating-parameter-sets and calculates the average efficiency at a set of energies and range of orders. Specifically, the files required for efficiency calculation are

- eff - executable containing efficiency intrinsic functions
- optical-constants.tbl - data file of material X-ray properties
- energy.dat - an ASCII list of output energies desired
- multi.sl - the S-Lang ASCII program which directs the calculation
- multi_params.txt - the model parameters of the grating(s)

The calculation is executed by typing to unix:

```
unix_prompt% /[eff_path]/eff multi.sl
```

and an output efficiency file is created.

Section 4

Laboratory Measurements and Predictions

The basic equipment for HETG laboratory testing, a Laser Reflection setup and the X-Ray Grating Evaluation Facility (X-GEF), are described in Dewey *et al.*[22] with more details of the X-GEF facility and its operation for flight testing presented in Flanagan *et al.*[29].

The gratings were mounted to the HESS at the HETG Alignment Facility where the average facet roll angle was set and measured based on the polarization alignment technique of Anderson *et al.*[4].

We have used these "sub-assembly" data (along with similar predictions for the HRMA and ACIS-S) to produce predicted curves as a baseline for comparison with the XRCF measurement results and an initial flight prediction.

Table 4.1: HETG laboratory setups and the parameters measured

Parameter	Lab Setup
Period	LR
Period variation	LR
Roll	Alignment
Roll variation	LR
Efficiency	X-GEF

4.1 LR Measurements

4.1.1 LR Period and Roll Variations

The key facet-level parameters that appear in the error budget of Section 2.2 are the grating period variations dp/p (both within and between facets) and the grating alignment, or "roll", variations γ (again within and between facets). The facet period, period variations, and roll variations were measured using the Laser Reflection setup [22].

In the Laser Reflection test the grating facet is moved under computer control so that a laser beam (HeNe 632.8 nm for MEGs and HeCd 325.0 nm for HEGs) illuminates sequentially ≈ 1 mm diameter locations on each grating facet in a 10x11 or 11x12 rectangular grid. At each location the centroid of the reflected and diffracted beams from the grating, Figure 4.1, are measured using CCD imagers. From these values variations in the reflected and diffracted angles are computed and a local grating period is determined. The test setup also includes MEG and HEG period references which are measured along with the sample and ensure the stability of the measurements.

Each execution of the LR test creates an ASCII data file (13Kb or 16Kb) which can be analyzed to create a period contour map, Figure 4.2, and estimates of the grating average period, P, and period variations, "dp/p". The data can be re-analyzed limited to the "active" region that is expected to be illuminated by the HRMA to get a more accurate estimate of the grating's effect on performace.

Note that this measurement scheme assumes that the only deviations from perfect periodicity of the grating are slow large-spatial scale changes in the average period; this assumption is warranted by the interferometric formation of the grating lines. The expected HETG equivalent dp/p is expected to be less than 130 ppm rms for both HEG and MEG gratings based on the data summarized in Figures 4.3-4.5.

4.1.2 LR Calibration using NIST Samples

As mentioned, the LR system includes HEG and MEG period-reference gratings which are measured along with the sample and ensure an absolute period stability of the measurements. The nominal periods of these reference gratings were assigned based on the laser wavelengths and the absolute diffraction angles measured by the encoded rotation stage.

For higher absolute period accuracy, we sent HEG and MEG calibration samples on Silicon wafers to John Kramar et al. at NIST (jkramar@NIST.GOV). They measured these HEG and MEG samples with the results shown in the table below.

These samples were then measured by Dick Elder in the LR setup. From these measurements a *calibration factor* establishing the absolute period of our LR period scale is obtained, Table 4.2. Note that the MEG calibration sample period ($\approx$ 4008 Å) is significantly different from the average of the flight gratings ($\approx$ 4001 Å); to cover this a 3 % 1-sigma term was also included in the scale factor error. These calibration factors and errors are then applied to the measured average periods of the flight HETG and TOGA gratings yielding the final "LR-NIST" periods of Table 4.3.

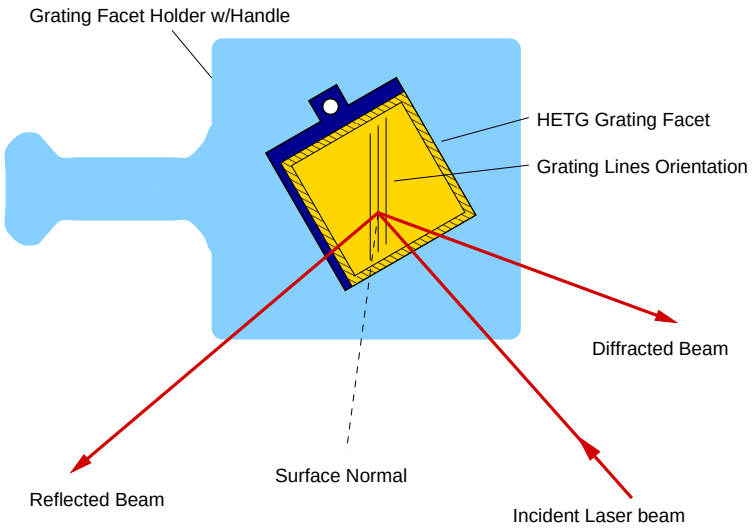

Figure 4.1: Operation of the Laser Reflection test setup. The period and its variations over the facets were tested using the Laser Reflection setup. The angles of reflected and diffracted laser beams, 628 nm for MEG and 325 nm for HEG, are recorded from a grid of locations on the facet. Note that here the grating facet is installed in a "holder" via a single mounting screw. The holder provides convenient handling of the facet as it is variously tested and stored awaiting flight installation. The facets are mounted in the holder at an angle such that the grating lines are perpendicular to the axis of the holder handle.

Sample	NIST Period nm	NIST Error (1 σ) nm	LR Period Å[LR]	Calibration Factor Å/Å[LR]	Error ppm
NIST MEG	400.800	0.010	4007.74	1.00006	56.
NIST HEG	200.011	0.005	2001.43	0.999340	27.

Table 4.2: NIST samples for LR calibration

Grating	LR Average Period Å[LR]	LR-NIST Period Å	LR-NIST Error Å
Flight MEG	4001.17	4001.41	0.22
Flight HEG	2002.13	2000.81	0.05
TOGA MEG	4000.72	4000.96	0.22
TOGA HEG	2002.36	2001.04	0.05

Table 4.3: Correction of the LR Period Measurements

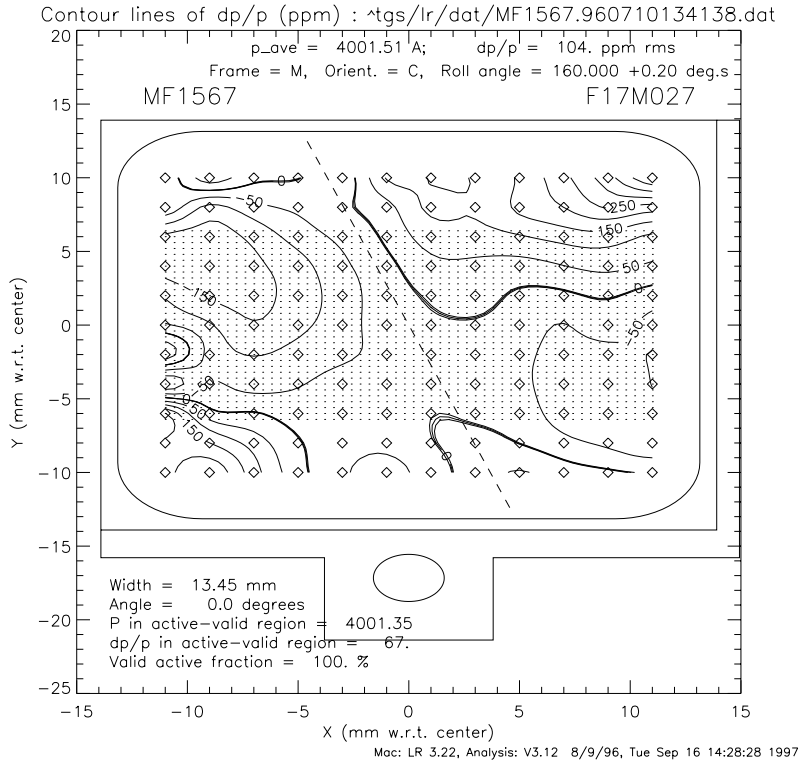

Figure 4.2: Period contour plot of MEG grating MF1567 from LR test data. Each diamond represents a measurement point. The dotted region is the "active" region that will be illuminated by X-rays from the HRMA. The period variation in the active region, dp/p = 67 ppm, is well below the required instrument variation of 250 ppm.

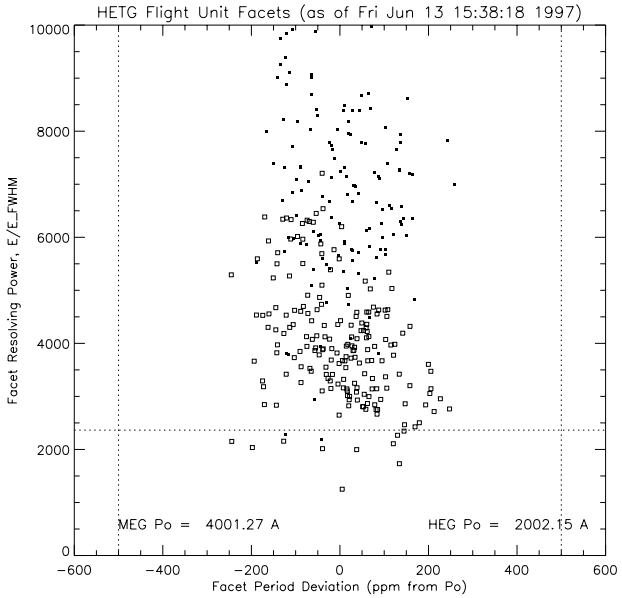

Figure 4.3: Period-dp/p scatter plot for the 336 HETG flight grating facets. The X-axis is each grating's departure from the average period for its type. The Y-axis is the inherent resolving power limit for the grating, that is: $(p/dp)(1/2.35)$. The horizontal dashed line at $E/dE \approx 2400$ corresponds to $dp/p = 180$ ppm.

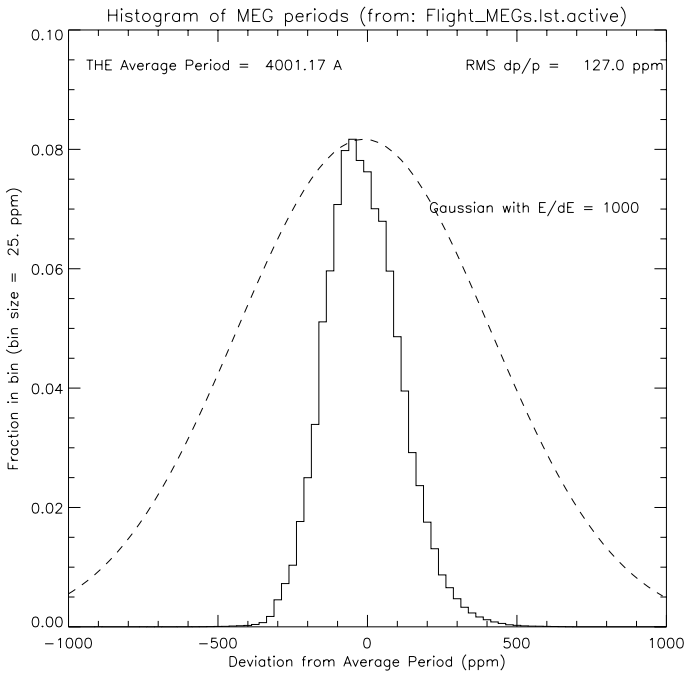

Figure 4.4: Period Histogram of the MEG Flight Gratings. The histogram and average period indicated here are based on the approximate "active" region of each facet. The rms dp/p value of 127 ppm corresponds to an E/dE limit of 3350. Note that the average period indicated here is in "LR-Å"; see Table 4.3 for the grating absolute periods.

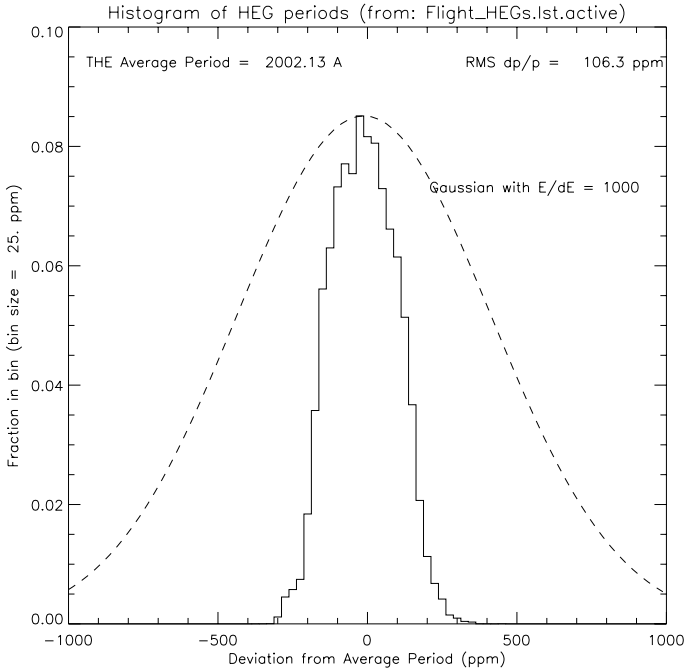

Figure 4.5: Period Histogram of the HEG Flight Gratings. The histogram and average period indicated here are based on the approximate "active" region of each facet. The rms dp/p value of 106.3 ppm corresponds to an E/dE limit of 4000. Note that the average period indicated here is in "LR-Å"; see Table 4.3 for the grating absolute periods.

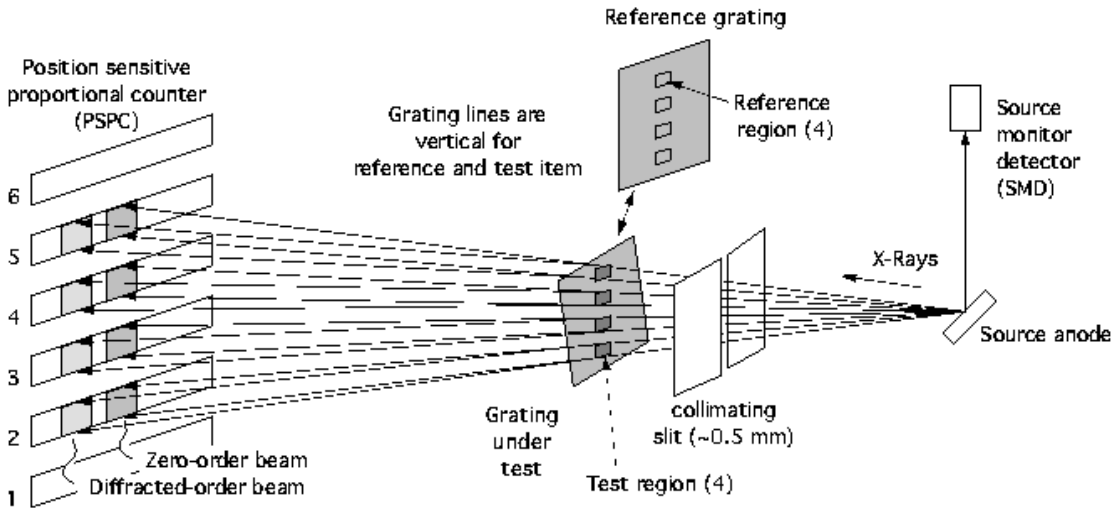

Figure 4.6: Simplified schematic of the X-ray Grating Evaluation Facility, X-GEF. X-rays from an electron impact source are slit-collimated and diffracted by the illuminated region on the under-test grating. The diffracted events are detected by a multi-wire position-sensitive proportional counter, PSPC. The intensity of X-rays diffracted by the under-test grating are ratioed to the intensity from a reference grating of known efficiency. This schematic is not to scale: the gratings are $\approx$ 20 mm square, the source-grating and grating-detector distances are $\approx$ 8.5 m, and the PSPC operates over a 120 mm range in the dispersion direction.

4.2 X-GEF Measurements

With the X-Ray Grating Evaluation Facility, X-GEF, at M.I.T. we have measured the diffraction efficiency of each flight grating at several energies and orders and fit these measurements to determine the physical-model parameters for each grating. From these best-fit parameters we can generate $g_f(E, m)$ for each grating on a fine energy scale.

The basic X-GEF test configuration is shown in Figure 4.6. The source of X-rays is an electron-impact source (Manson multi-anode) which has an X-ray spectrum that is made up of a continuum plus one or more discrete lines. The incoming X-ray beam, collimated by either a slit or 1-D optic, illuminates a grating. X-rays emerge from the grating into various diffraction orders and are detected by a position sensitive proportional counter, PSPC, which has a spatial range of +/- 60 mm. The goal of the measurement is to measure the fraction of the incoming beam (at the line energy) that is diffracted into the combined first-orders of the grating.

Because of the presence of continuum and other lines in the source and the poor energy resolution of the PSPC, there are many error sources that can foil a straight-forward measurement of the efficiency based only on with-grating/with-out-grating PSPC measurements. To avoid these pitfalls we have installed in X-GEF two gratings which serve as efficiency references, Section 3.2.6. During flight testing, measurements are also taken with the reference grating in the beam. The ratio of grating-under-test diffracted count rate to reference-grating diffracted count rate can then be made directly and with a much reduced sensitivity to systematic errors. In this way the known reference-grating efficiencies are transferred to the grating-under-test efficiencies.

Two gratings are tested in each unattended overnight X-GEF run. The ≈ 300 Mb of data collected are written to two DAT tapes (one stays at MIT and one goes to the ASC.) Figure 4.7 shows an example of the results of X-GEF data analysis[30] for an MEG grating. The measured plus and minus first order efficiencies at five energies (Cu-L 0.930 keV, Mg-K 1.254 keV, Al-K 1.486 keV, Mo-L 2.293 keV, and Ti-K 4.511 keV) are shown along with a model fit which uses a 5-vertex bar shape, Figure 4.9. For HEGs a measurement is additionally made at Fe-K 6.400 keV, Figures 4.8 and 4.10.

These X-GEF model parameters and resulting model fits are the laboratory measure of $g_f(E, m)$ of Equation 1.4.

To-do:
Need a .ps version of the X-GEF schematic.
Add more details about the different regions tested.
Update X-GEF analysis and predictions when more accurate reference grating efficiencies are available.
Create table of measured asymmetry slopes for each grating-region to estimate HEG and MEG asymmetry slopes.

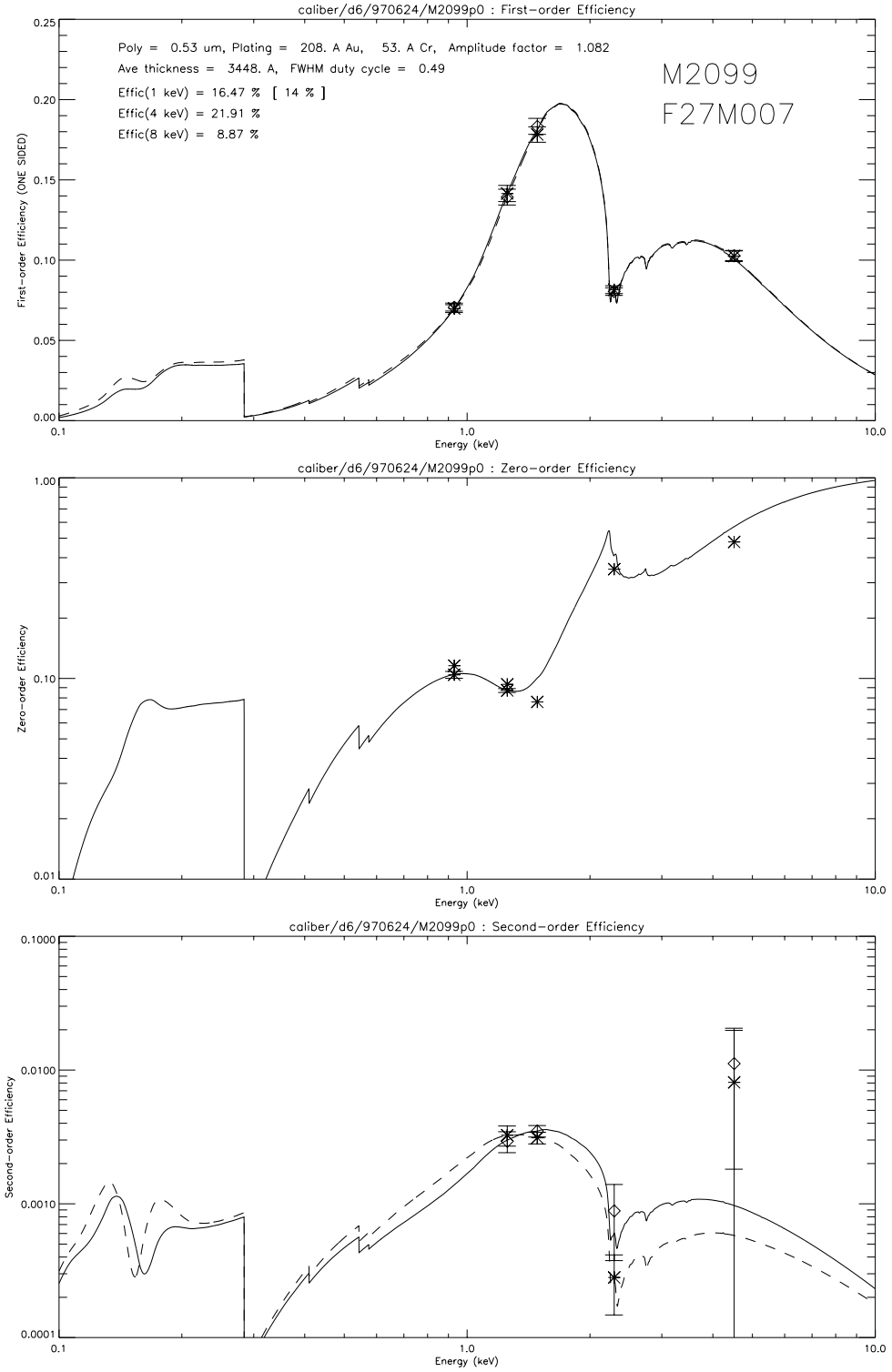

Figure 4.7: Measured and modeled first-order efficiency of the central region of MEG grating M2099. The model is simultaneously fit to +/- 1st-order, zero-order, and 2nd-order data. The interpolated combined efficiency at 1 keV of 16.47% exceeds the specification-required average of 14% .

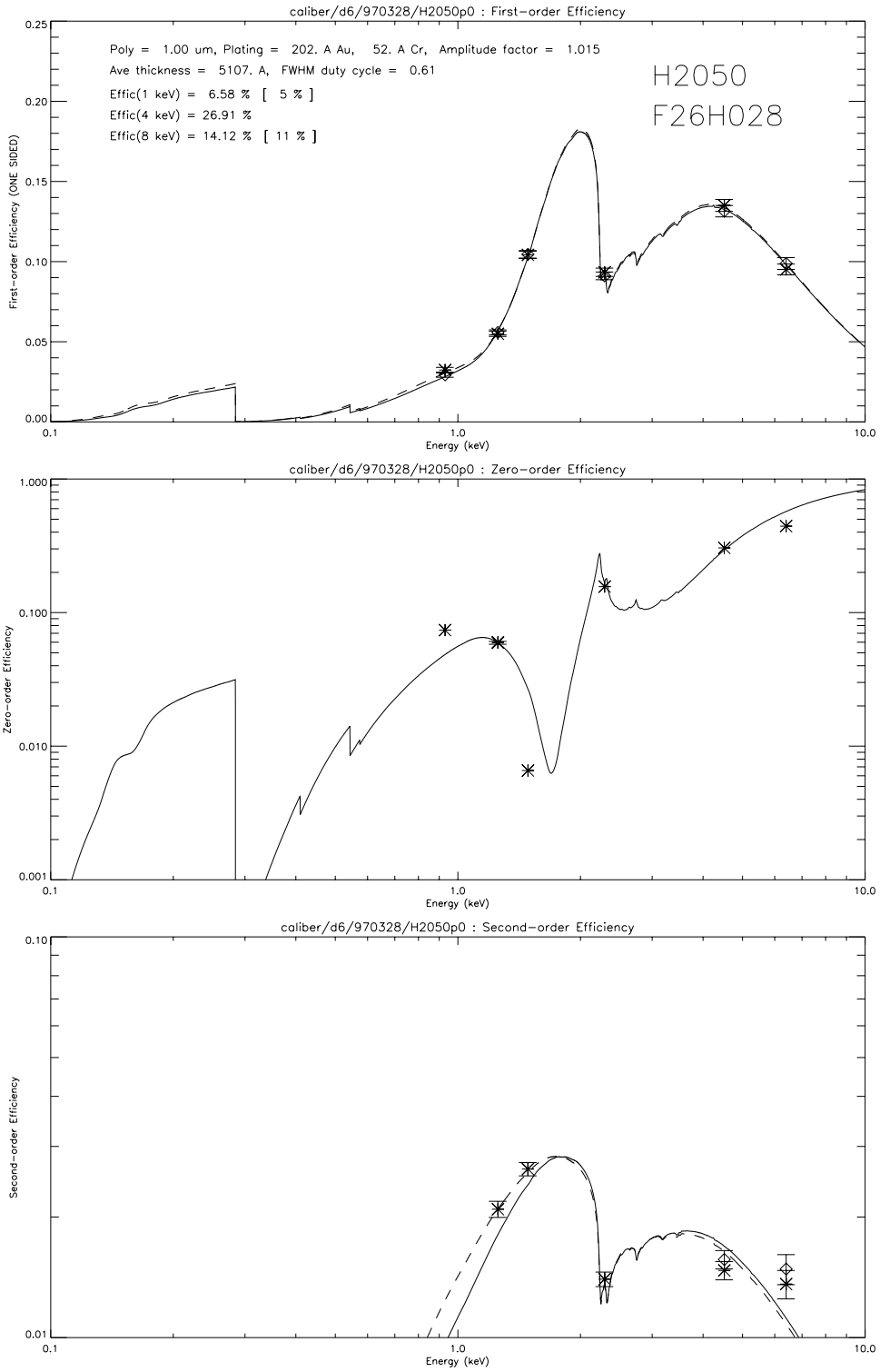

Figure 4.8: Measured and modeled first-order efficiency of the central region of HEG grating H2050. The model is simultaneously fit to +/- 1st-order, zero-order, and 2nd-order data. The interpolated combined efficiency at 8 keV of 14.1% exceeds the specification-required average of 11% .

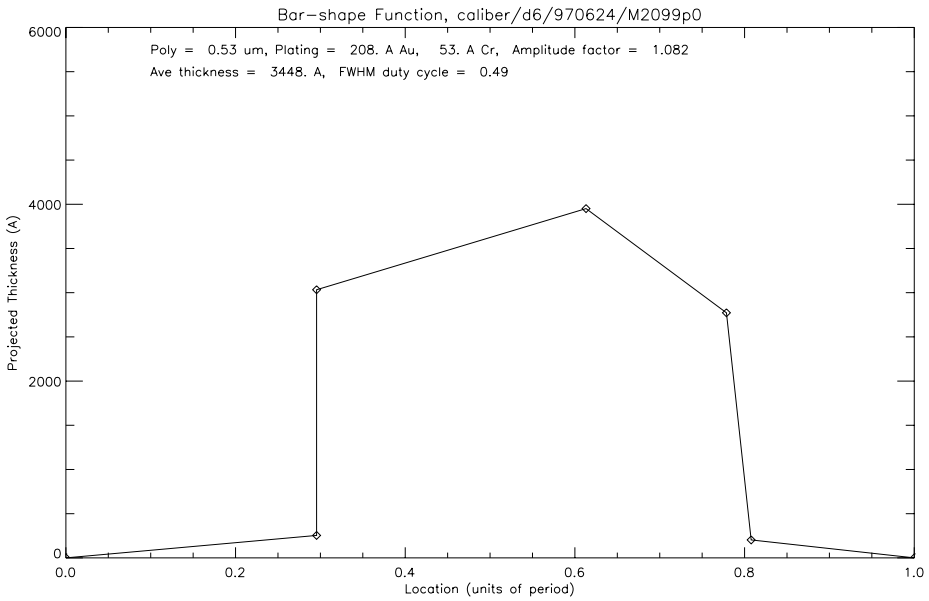

Figure 4.9: The 5-vertex bar shape used in the MEG model of Figure 4.7. The use of 5 adjustable vertices ensures a good fit of the model to the measured first-order efficiencies.

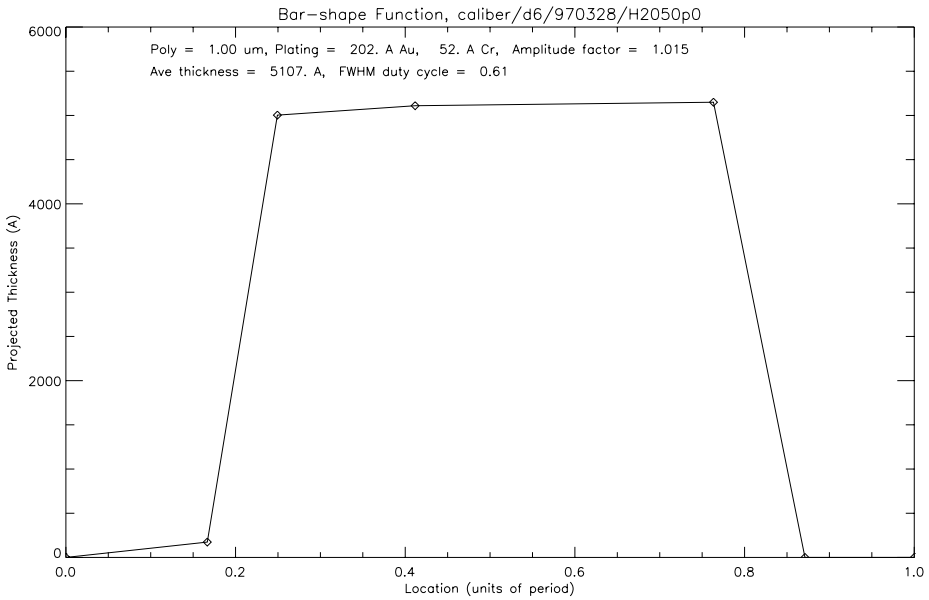

Figure 4.10: The vertex bar shape used in HEG the model of Figure 4.8. Note that the HEG shape here is thicker, wider, and more trapezoidal than the MEG example of Figure 4.9.

4.2.1 Order Assymmetry and Tilt

As expected by the diffraction theory, the trapezoidal profile of the gratings, when operated away from normal incidence, will produce an asymmetry in the intensity of the plus and minus diffracted orders. This asymmetry is measured routinely in X-GEF flight testing at the Al-K line, 1.486 keV. Figures 4.11 and 4.12 show the tilt test results for the example MEG and HEG gratings M2099 and H2050. Note the higher tilt sensitivity (steeper asymetry slope) of the HEG due to its more trapezoidal bar shape.

Because of the Rowland design of the HETG, the grating facets in use "see" X-rays arriving at normal incidence. For off-axis sources (due to multiple sources in the field or offset pointing of a desired source) the HETG may be called on to operate at angles of incidence of order 0.05 degrees (3 arc minutes or 9 mm off-axis.) Even for the HEG gratings this would result in an asymmetry of less than 2% between the plus and minus orders.

Note that the tilt curves are very linear within a degree of normal incidence (Grating Angle = 0). This means that the *total* first-order diffraction efficiency is very insensitive to small tilts. For this reason the primary efficiency calibration is the combined first-order values.

4.2.2 Laboratory Efficiency Predictions

MORE HERE ABOUT MAKING THE 'N0004 EFFICIENCIES!!!

The full set of model parameters derived from the X-GEF data are then used to create the shell-averaged efficiencies $G_s(E, m)$ for the full HETG. Coming into XRCF testing these represent out best estimate of expected HETG efficiency performance, Figures 7.13 and 7.14, and efficiency product, Section 11.3.4.

4.2.3 Error Estimates for X-GEF Grating Efficiency

Four gratings have been cross-tested both at X-GEF (using standard flight testing and analysis prodecures including the reference gratings to normalize their efficiencies) and at the synchrotron. By comparing the X-GEF derived efficiency model with the synchrotron measurements, we have an estimate of the errors implicit in using X-GEF to predict the efficiencies for each grating facet. The residuals between the X-GEF generated model and the synchrotron data are shown in Figure 4.13 and 4.14. In effect, this provides an *upper limit to the errors of our subassemby efficiency predictions*, because a large strip of the reference grating is in fact illuminated in each X-GEF test, and the diffraction efficiency of this strip is (incorrectly) assumed to have the synchrotron reference efficiency. Only a small portion of the reference grating was actually tested at the synchrotron and it is only this small portion which should actually be assigned the reference efficiency. Therefore, the assignment of this fixed efficiency to a much larger area of the reference grating is incorrect. Tests have been done to cross-normalize the strip efficiency in comparison to the confined area for each grating, but the results have not been included yet.

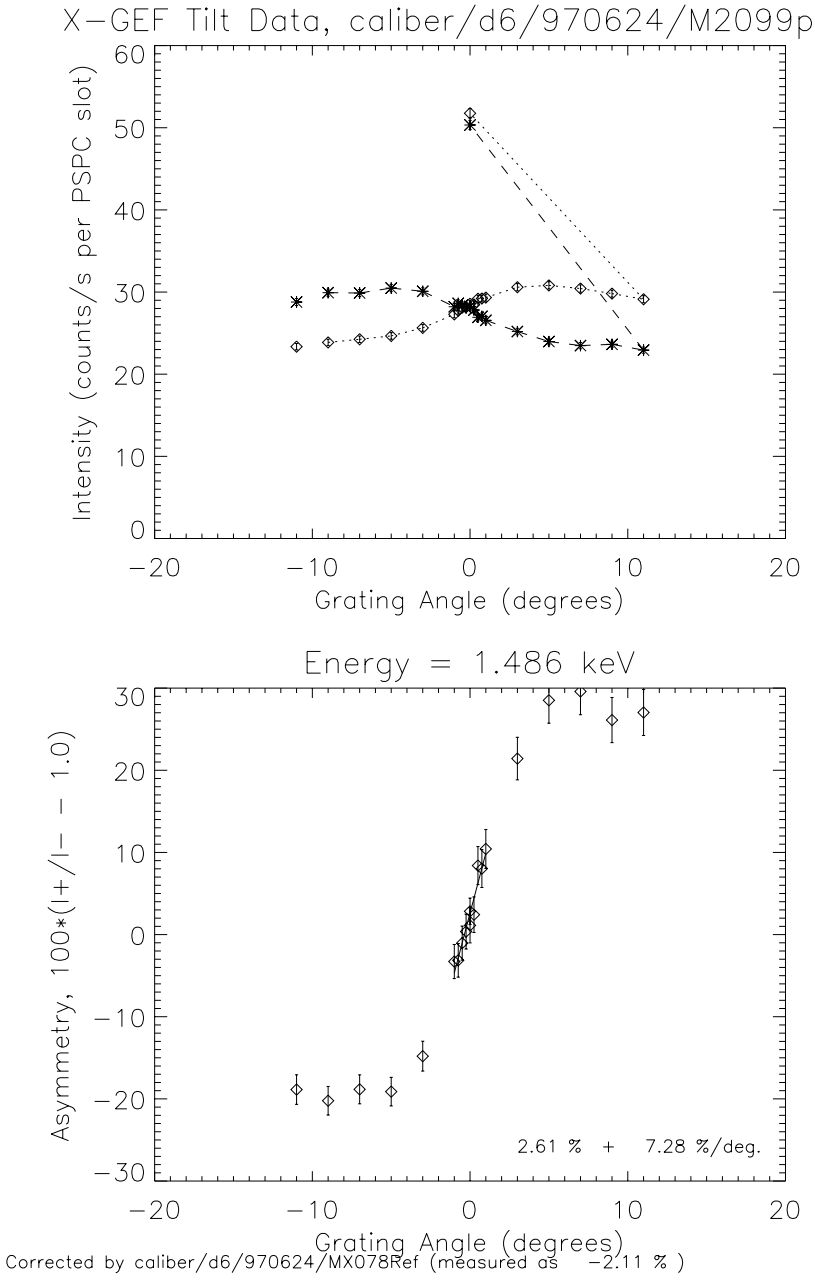

Figure 4.11: X-GEF Tilt Plots for an MEG. The top plot shows the plus and minus first-order Al-K count rates as a function of incidence angle. The bottom plot shows the "asymmetry" plotted versus angle. The normal-incidence asymmetry is only 2.6% with a slope of 7.3% per degree.

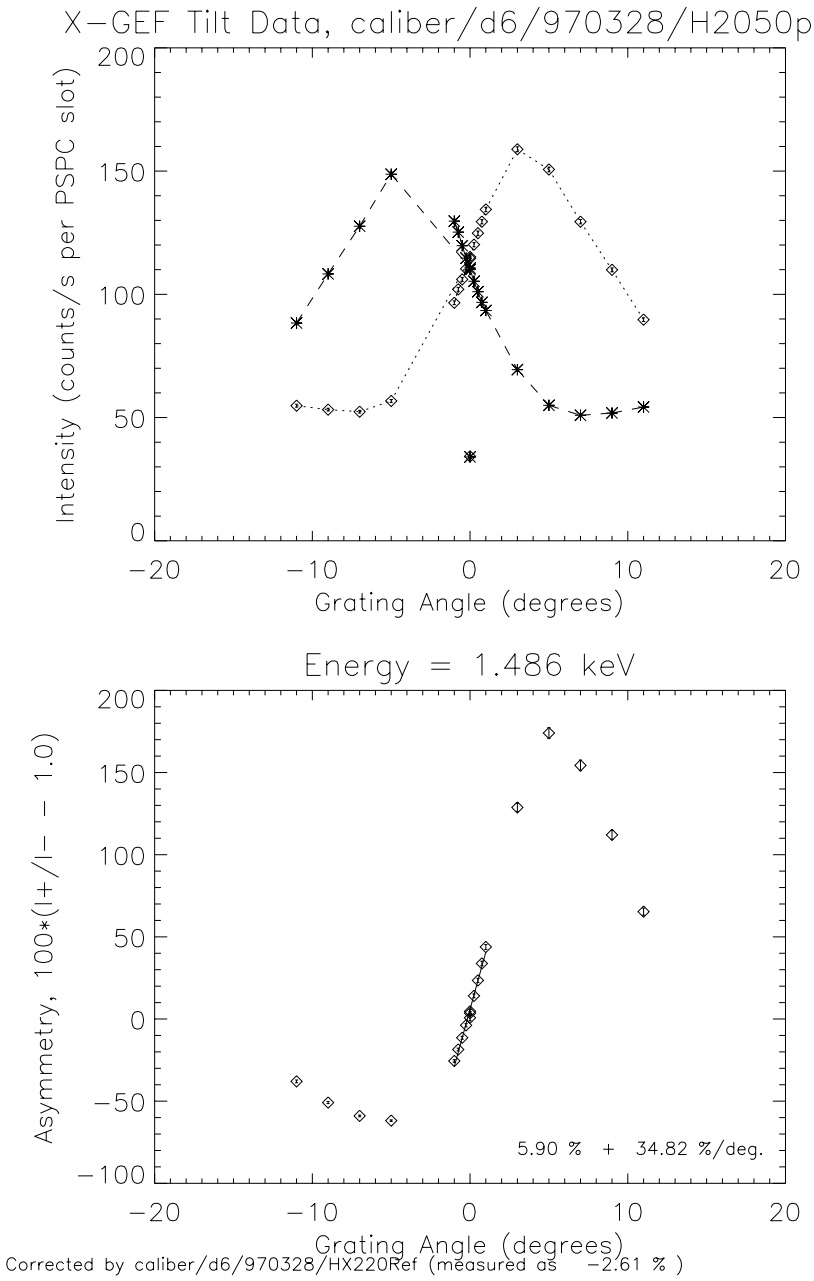

Figure 4.12: X-GEF Tilt Plots for an HEG. The top plot shows the plus and minus first-order Al-K count rates as a function of incidence angle. The bottom plot shows the "asymmetry" plotted versus angle. The normal-incidence asymmetry is 5.9% with a slope of almost 35% per degree. This strong asymmetry with angle is the result of the trapezoidal shape of the grating bar, Figure 4.10.

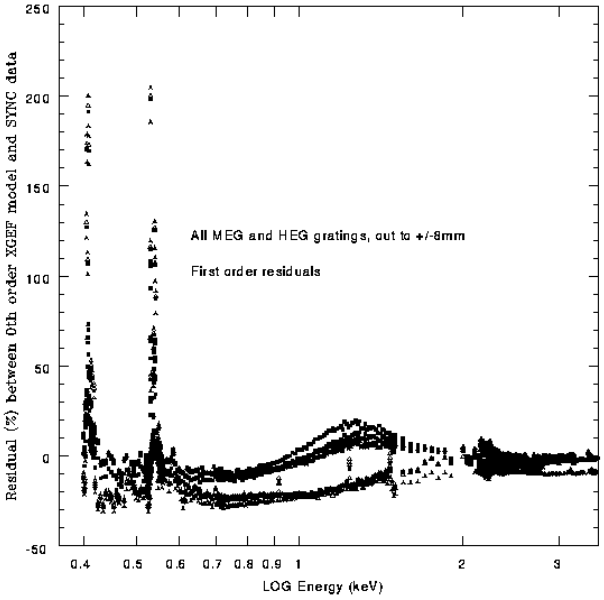

Figure 4.13: Residuals between first order X-GEF predictions and synchrotron data. The large residuals at the N and O edges should be reduced when new X-GEF predictions are generated assuming updated (October, 1998) optical constants.

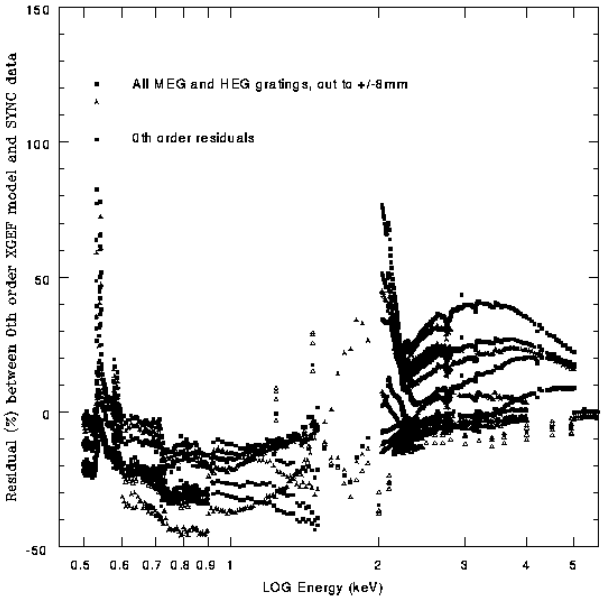

Figure 4.14: Residuals between 0th order X-GEF predictions and synchrotron data. Edge residuals between 0.5 and 0.6 keV should be reduced when predictions are generated assuming updated (October, 1998) optical constants.

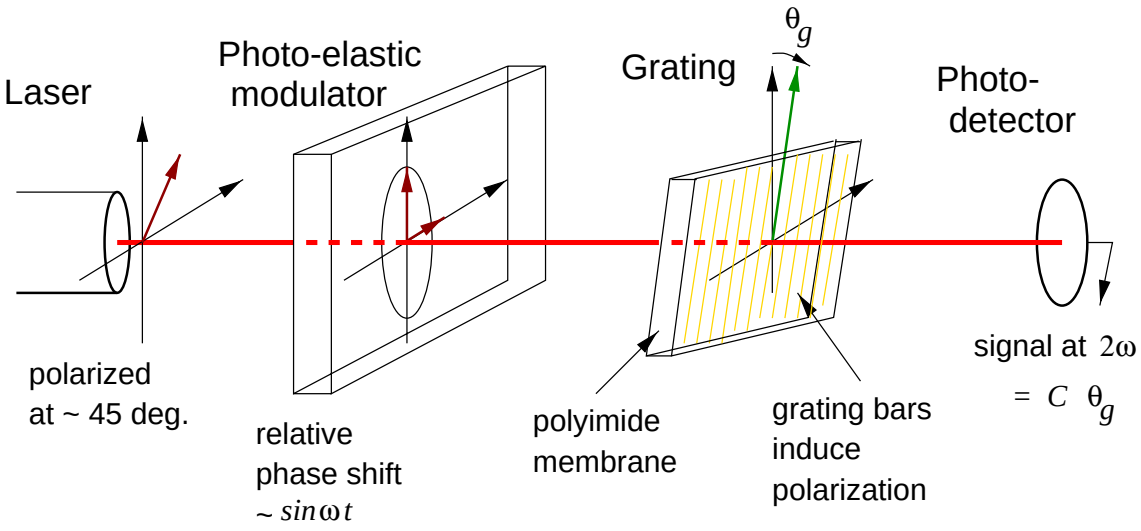

Figure 4.15: Schematic of the polarization modulation alignment setup. A polarization-modulated laser beam is sent from the nominal focal plane location through the grating to be aligned. A signal at twice the modulation frequency is detected by the photodetector. The amplitude of this signal is proportional to the angle the grating bars make with respect to the axes of the modulator. Note that the grating's polyimide membrane is located between the modulator and the grating bars; stress birefringence in the membrane can thus modify the detected signal.

4.3 Alignment Measurements

A single-screw mounting scheme was used to attached the facets to the HESS and fixes all degrees of freedom of the facet except for rotation around the screw axis, *i.e.*, the "roll" angle of the facet. To install the HEG and MEG facets on the HESS with the desired roll angles a polarization modulation alignment scheme and special purpose tooling were used; the system allowed each facet to be aligned to its desired angular orientation to an accuracy better than 1 arc minute.

The HESS was supported vertically by a test stand and one each HEG and MEG roll-angle reference gratings were mounted on ground support equipment (GSE) attached to the HESS. These gratings defined the roll angles of the HEG and MEG grating sets by serving as transfer standards.

The ability of these fine period gratings to act as optical polarizers was used to measure the facets' roll angle [4]. As schematically shown in Fig. 4.15, a photo-elastic modulator is used to create a beam having a modulated relative phase shift between two orthogonal axes. The grating when not aligned to these axes mixes the two axes producing an interference signal at twice the modulation frequency. The amplitude of this signal when demodulated at a fixed phase, is linear in the error angle, the angle betweent the PEM axis and the grating lines.

The same kind of epoxy that was used to bond the membranes to the frames was then applied to permanently secure the facets to the HESS, and the flight HETG was born. The HETG was vibration tested and a final lab measurement of the facet angles was carried out. The final measurements indicated an rms roll variation less than 1 arc minute for both the HEG and MEG grating sets and with less than a dozen facets having angular errors greater than 1 arc minute.

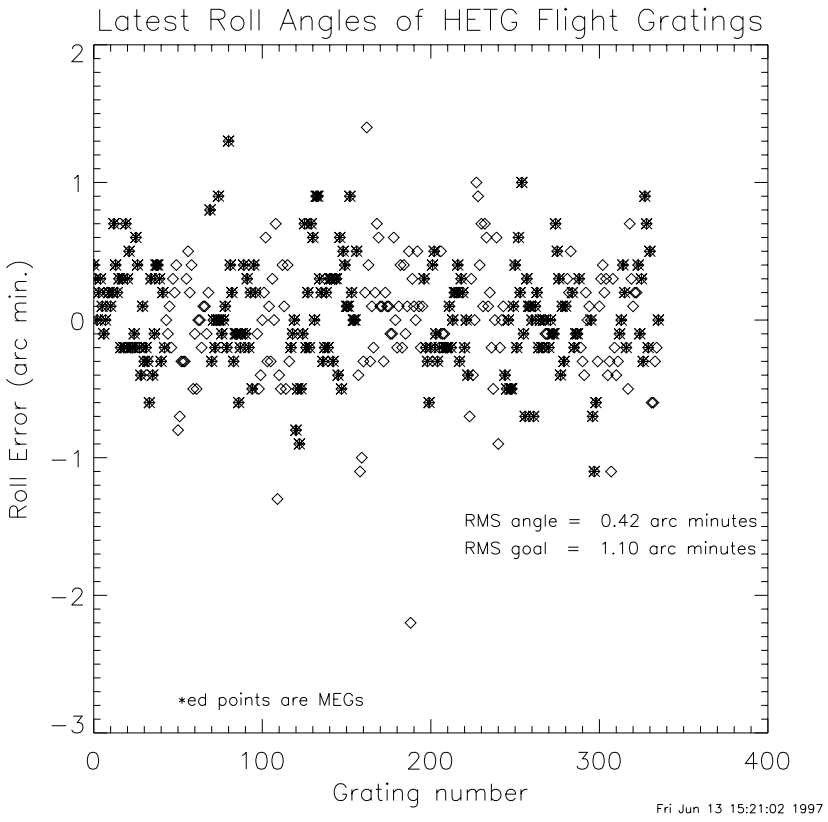

Figure 4.16: Measured roll errors for the 336 flight gratings. The rms value $\gamma = 0.42$ arc minutes is well below the specification of 1.1 arc minutes.

In spite of these lab results, system ground testing, described below, revealed that 6 of the MEG facets actually have roll errors in the range of 3 to 25 arc minutes! All of these facets were identified as coming from fabrication lot #7. Lot #7 was produced with prototype fabrication tooling, not used with other lots, in the membrane mounting step (Fig. 1.6g) which introduced large non-uniform stress in the polyimide support membrane. Through stress birefringence [12] the polyimide layer, which is between the PEM and grating bars in the alignment optical path, introduced errors between the polarization measurent angle and the actual grating bar angle. This same effect acting at a lower level is likely responsible for the slightly larger than 1 arc minute rms roll variation measured for both the HEG and MEG facets in the system tests.

4.4 Long-term: Vacuum Storage Gratings

A sample of HETG gratings has been aged in a laboratory high vacuum environment and measured in the LR and X-GEF setups periodically since late 1996, see Figure 4.17, to determine if there are any changes ("aging") in the performance parameters. The following is from the summary of a November 1998 VSG status report; for more and up-to-date information see `http://space.mit.edu/HETG/vsg/vsg.html`.

Period Properties Summary: All grating periods and period variations appear stable (periods within 20 ppm and dp/p within 20 %); the only unexplained exception is grating HA2003 which varied by -110 ppm but has returned to its original period.

HEG Efficiencies The HEG efficiencies appear stable or reasons have been found for the several anomalies seen.

MEG Efficiencies The MEG efficiencies show a drift with time. At 4 keV at least three of the six gratings show a trend towards lower efficiency with time at a rate of roughly -3 % per year. At 1 keV, the MEGs show an increase in efficiency with time at a rate of about $+4$ % per year.

Investigating the "MEG drift with time" has lead to clear evidence that the X-GEF system detectors were being very slowly coated with a contamination layer, changing their detection efficiency properties. The detector "contamination rate" is ≈ 1 micron of polyimide-equivalent per year for the SSD, ≈ 0.4 microns/year for the PSPC and negligible accumulation on the SMD. Analysis and re-analysis of data-in-hand is on-going to assess the effects on the VSG X-GEF measurements. Future testing will monitor and decontaminate the SSD and PSPC windows.

Finally, while the details and effects of the detector changes are under study, we consider the possibility that the observed MEG efficiency drift is a real sample change. Assuming as a worst case that all of the drift seen is due to real sample changes, the MEG 4 keV efficiency will remain above the Level 1 requirement for over 10 years and the 1 keV efficiency is actually improving with time!

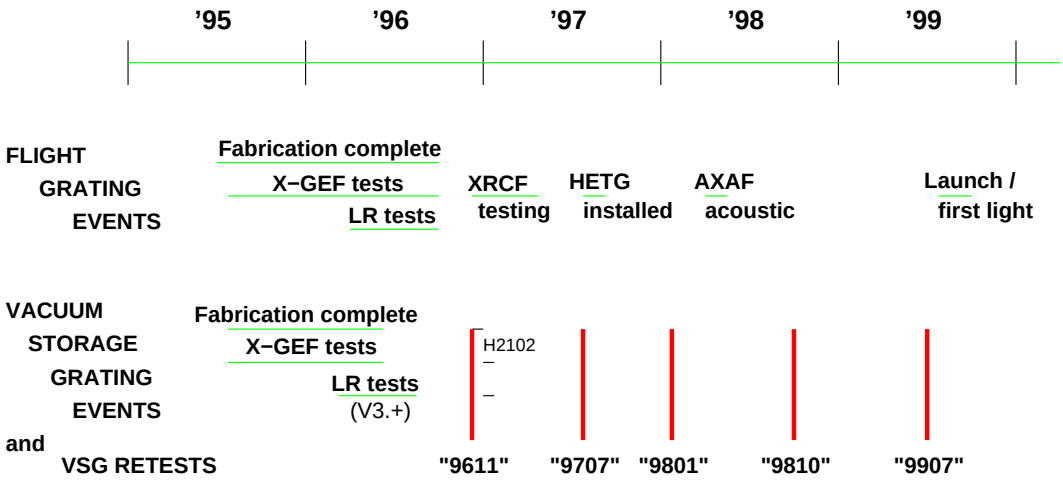

Figure 4.17: Vacuum storage grating (VSG) timeline is shown here with relevant events for the flight gratings and the storage gratings indicated. Five VSG re-tests are shown and indicated by a date code: 9611, 9707, 9801, 9810, and 9907.

4.5 Optical Transmission of the Gratings

Gratings MA1046, HA2044, HA2031, and M2214 were provided to Prof. Gordon Garmire of PSU for optical transmission measurements.

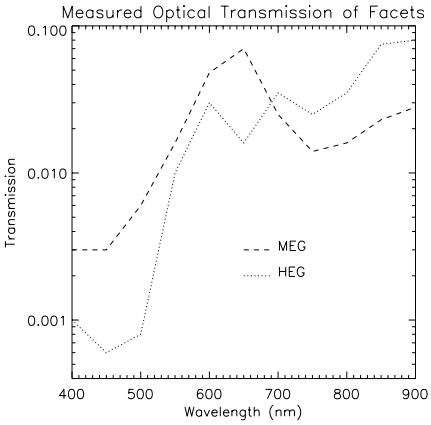

Figure 4.18: Measure transmission of two grating facets in the optical range. Data taken from Garmire *et al.*[36].

4.6 Radiation Tests and Effects

The main radiation concern for the HETG is effects to the polyimide support material. When this material was considered in another context, as windows for proportional counters, tests were carried out and no increase in (low) leak rate was seen at a dosage of 9 kRad. For the HETG, the main concern is loss of mechanical integrity. Such effects are reported in the literature to occur at levels of order 1000 MRads [47].

At the time of this writing (Dec. 2000) plans are underway to make X-GEF measurements on HETG grating samples before and after exposure to a proton flux. Results of these tests will be available at `http://space.mit.edu/HETG/rad/rad.html`

Part II

X-Ray Calibration Facility Measurements and Analysis

Section 5

XRCF and the HETG

5.1 XRCF Harware Introduction

During December 1996 through April 1997 all three key components of the HETGS, HRMA-HETG-ACIS-S, were integrated for test at NASA's Marshall Space Flight Center (MSFC) in their X-Ray Calibration Facility (XRCF). The XRCF and related hardware are described in great depth in the documents listed in Table 1.2, however some key concepts are presented here for completeness and to support the grating analysis discussion.

The general layout of XRCF hardware is shown in Figures 5.1 and 5.2 and specifics of the key subsystems are presented in the sections below.

Calibration was divided into two main calibration phases, Phase 1 and Phase 2, defined physically by differences in the focal plane detectors; the Beam normalization detectors (BND) were present in both Phases. Each of these major phases had subphases designated sequentially by letter, see Table 5.1.

Table 5.1: XRCF Phases and Detectors

Phase	Desig.	Focal Plane	Comments
Rehearsal 1	A	FPC, SSD, HSI	TMA and TOGA
Rehearsal 2	B	FPC, SSD, HSI	"
Phase 1.1	C	FPC, SSD, HSI	HXDA translation system
Phase 1.2	D	FPC, SSD, HSI	"
Phase 1.3	E	FPC, SSD, HSI	"
Phase 2.1	F	ACIS-2C	detector on FAM
Phase 2.2	G	HRC and '2C	"
Phase 2.3	H	ACIS	"
Cross-cal 1	I	ACIS	Flat fields, no HRMA
Cross-cal 2	J	FPC, SSD, HSI	HXDS detector cross-calibrations

In Phase 1 the non-flight detectors, FPC_X2 (Flow Proportional Counter), SSD_X (Solid State Detector), and HSI (micro-channel plate High Speed Imager), were in the focal plane. The philosophy of Phase 1 is that the detectors are (or will be) well characterized and of proven

and understood technology so that measurements are performed to understand the HRMA and gratings. Grating-in grating-out measurements were performed to measure grating Efficiency; images and scans were obtained to verify the grating LRF model.

In Phase 2 a "two-chip ACIS" (ACIS-2C) and the flight ACIS and HRC detectors were variously present. Here the philosophy is that the HRMA and gratings are understood and the flight detectors and/or the HRMA-(grating-)detector interaction is being studied. For this reason, the HETG tests were primarily related to Effective Area. Because LRF tests generally require well focussed beams and given the HRC pore extraction limits and the ACIS telemetry limits, extensive LRF studies were not in general carried out with the HETG in Phase 2 – the exception being enough data with ACIS-S to allow us to verify the Rowland curvature of the CCDs.

5.1.1 XSS

Details of the X-Ray Source System (XSS) are presented in Kolodziejczak *et al.* [54].

5.1.2 Double Crystal Monochromator (DCM)

The DCM is part of the X-ray Source System (XSS) used at XRCF [93, 54]. It offered three 3 different crystals for these tests, of which we only used the Thallium Acis Phthlate (TAP) between 0.9 and 2.5 keV and the germanium (Ge111) between 2.5 and 8.7 keV. The source is a rotating-anode tungsten source, which operates at a high voltage to generate a strong continuum, however it also produces several bright W lines at 1.38, 1.78, and 1.84 keV. Those lines actually proved quite useful for tests of HETG scattering, Sections 6.6 and 3.3. The DCM has an energy gradient in dispersion direction, which results in a non-negligible beam non-uniformity when tuned near the the W lines. Another source of non-uniformity is introduced while using the TAP crystal due to some waviness on the crystals surface.

5.1.3 BNDs

The beam normalization detectors (BNDs) monitor the source flux without the effects of the HRMA or HETG. There are six BND detectors: two, a Flow Proportional Counter (FPC) and a Ge solid state detector (SSD), are located 37.43 and 38.20 meters from the source in "Building 500", and four FPCs surround the HRMA entrance, see Figure 5.2. To ensure some BND data is available over a wide range of source flux, apertures can be selected on the FPC_5, SSD_5, and FPC_HN BNDs.

5.1.4 HRMA, Gratings, and Shutters

The HRMA, gratings and shutters were all mounted to a common platform at XRCF. The status of the shutters was recorded in a shutter log with the format:

```
    Shell      1     3     4     6
 quadrant    tnbs  tnbs  tnbs  tnbs
             cccc  ooeo  cccc  cccc
```

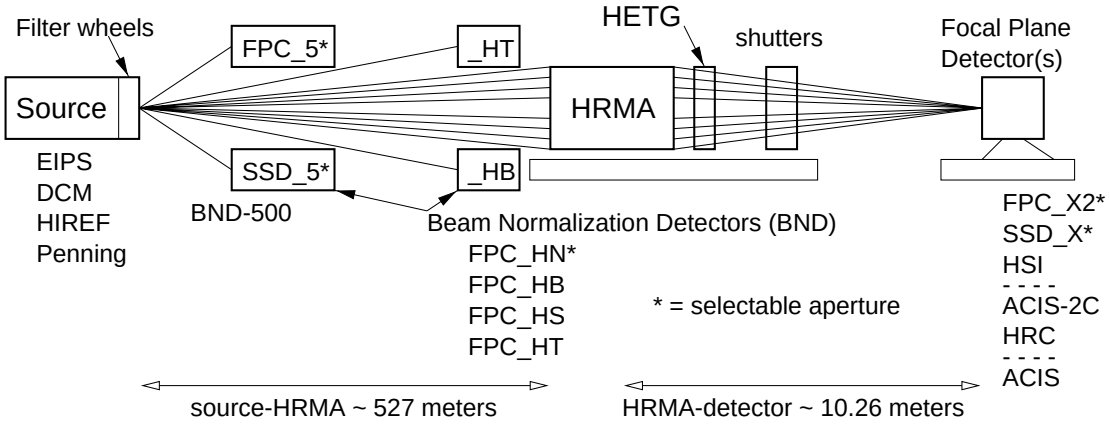

Figure 5.1: XRCF hardware schematic. The XRCF HETG configurations include i) X-ray source and filters, ii) Beam normalization detectors (BNDs), iii) AXAF optics (HRMA, HETG), iv) shutter assembly, and v) focal plane detectors.

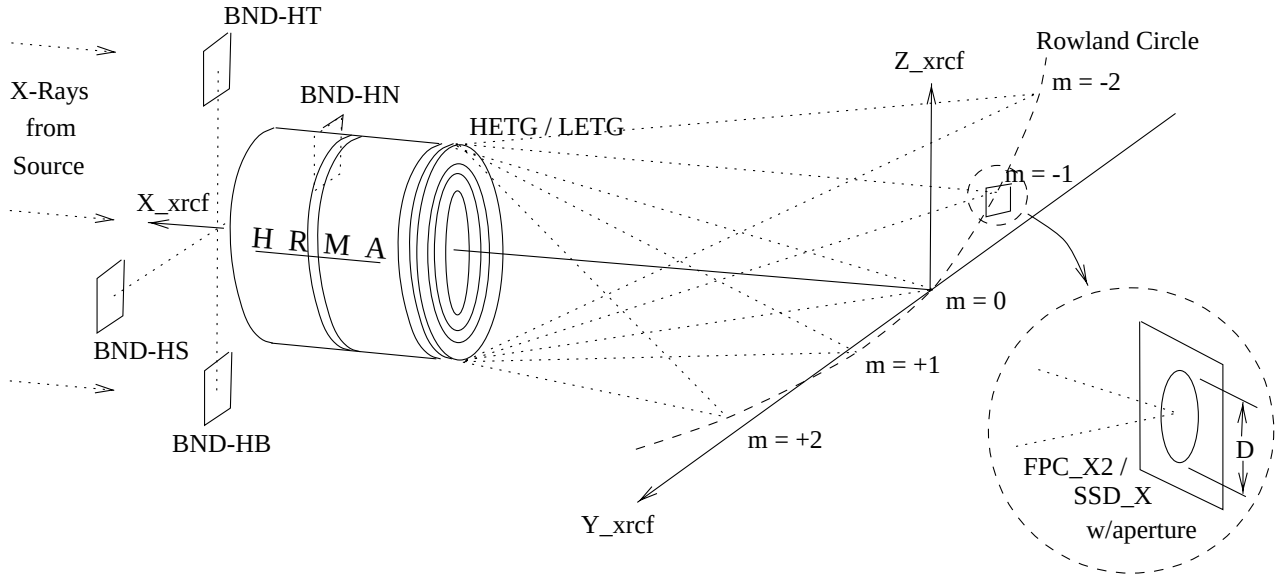

Figure 5.2: Phase 1 Hardware Schematic. In all phases the incident source flux is monitored by a set of beam monitor detectors (BNDs), four of which are located around the HRMA entrance aperture, shown at left. One or the other of the AXAF gratings, HETG or LETG, may be inserted into the converging HRMA beam. The HXDS detectors, of similar design to the BNDs, are located in the focal plane and can be positioned through 3-axes of motorized stages. For example, the FPC with aperture can be moved along the curved, inclined HEG Rowland circle (dashed curve) in order to intercept the diffracted beam.

where the letter codes corespond to "open", "closed", and "error".

Some useful XRCF HETG parameters are tabulated in Table 5.2 for reference.

Table 5.2: Table of useful XRCF HETG parameters. These preliminary values are based on subassembly and XRCF testing, from Calibration Products, Section 11.3.

Description	value	error	units	comments
Rowland distance	8782.8	0.5	mm	see Section 5.2.1
MEG average period	4001.41	≈ 0.10	$\mathring{A}$	based on lab measurement
HEG average period	2000.81	≈ 0.05	$\mathring{A}$	LR/NIST: based on lab measurement
MEG angle	4.74	0.05	deg.s	
HEG angle	-5.19	0.05	deg.s	
MEG-HEG angle	9.934	0.008	deg.s	
(MEG+HEG)/2 angle	-0.225	0.01	deg.s	(-0.275 in Phase C)

5.1.5 HXDS Focal Plane System

In Phase 1 the non-flight detectors, FPC_X2 (Flow Proportional Counter), SSD_X (Solid State Detector), and HSI (micro-channel plate High Speed Imager), were in the focal plane.

5.1.5.1 HXDS Axes

The HXDS axes are nominally along the XRCF coordinates, Figure 5.2. The HXDS primeY axis, however, was determined after-the-fact to have had its axis rotated by an angle of 0.0058 radians about $+Z_{\rm xrcf}$. Thus a commanded motion in the $+Y_{\rm xrcf}$ direction resulted as well in a motion of $0.0058 \times \Delta Y$ in the $-X_{\rm xrcf}$ direction. **MARX** simulations of XRCF measurements must take this into account.

5.1.5.2 HSI in the Focal Plane

During Phase 1 calibration the HSI detector[26] provided imaging capability at high event rates, for example the image in Figure 1.8. The HSI also was fitted with a mask with a "cusp" to allow the bright PSF core to be occulted while the surrounding wings of the PSF were observed. For HETG purposes, the HSI was used for PSF imaging and to record the spectral images of the various line sources used in efficiency testing. The quantum efficiency of the HSI, Figure 5.3, was used to convert the observed counts spectrum to flux units for the observed source spectra.

Two other effects of the HSI are a variation of QE with incident angle and a gain/QE depression near the center of the imager. The QE variation shows up clearly in ring focus images as non-uniform illumination around the mirror shell's rings. Data at two of these tests (hsi108944 and hsi106856) have been analyzed to produce the plots of Figure 5.4 which show relative QE vs azimuth for the cone of rays from each mirror shell. The central region of the HSI, centered at (y,z) = (2046.7, 2045.5) with one-sigma radius of 17.5 pixels, was used extensively at XRCF, its gain/QE degraded with the total exposure received. Plots related to this effect are given in Figure 5.4 and this effect was compensated for by randomly adding duplicate events in the region (`xrcf/xrcf_hsi_read.pro`).

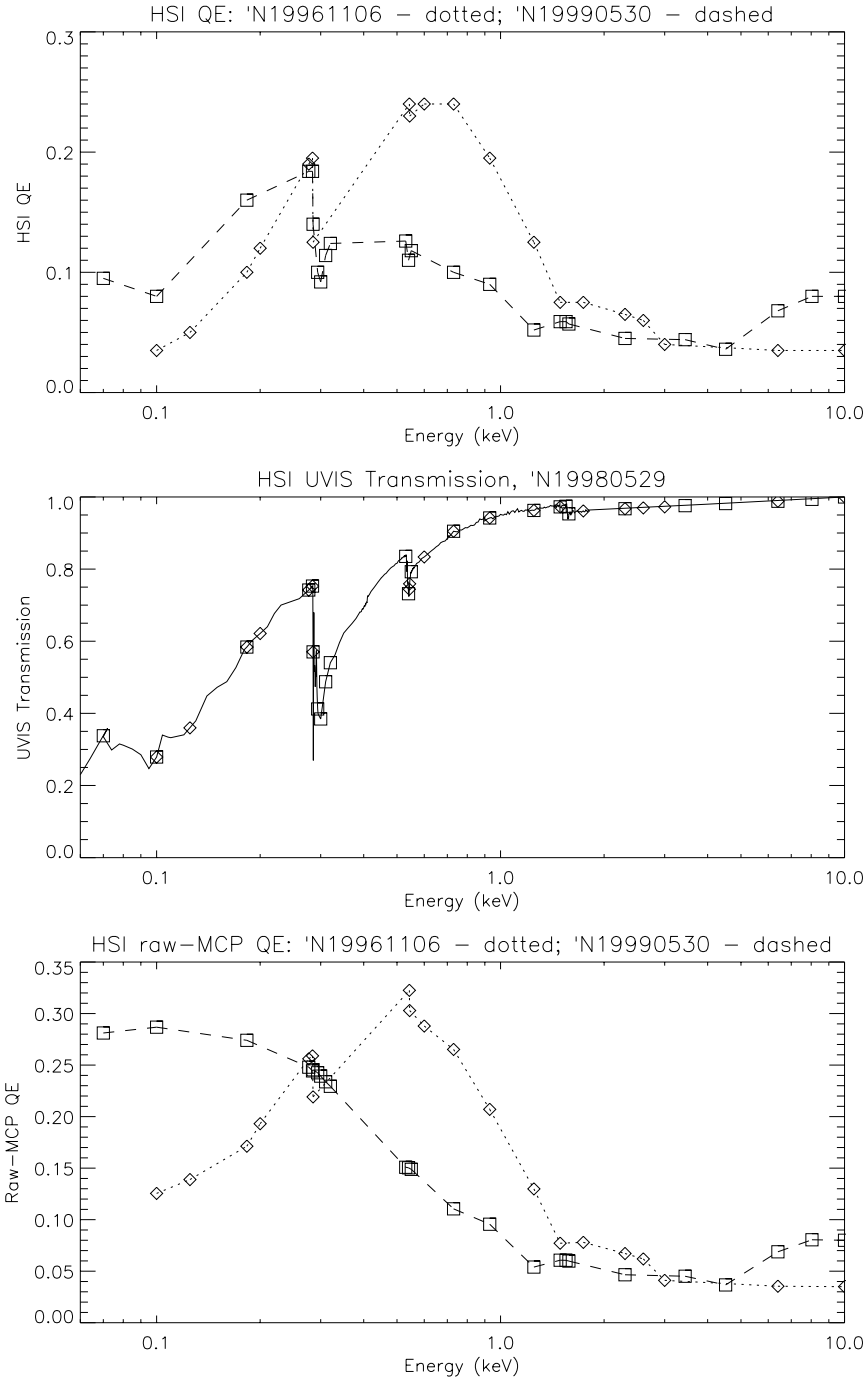

Figure 5.3: High speed imager (HSI) quantum efficiency.

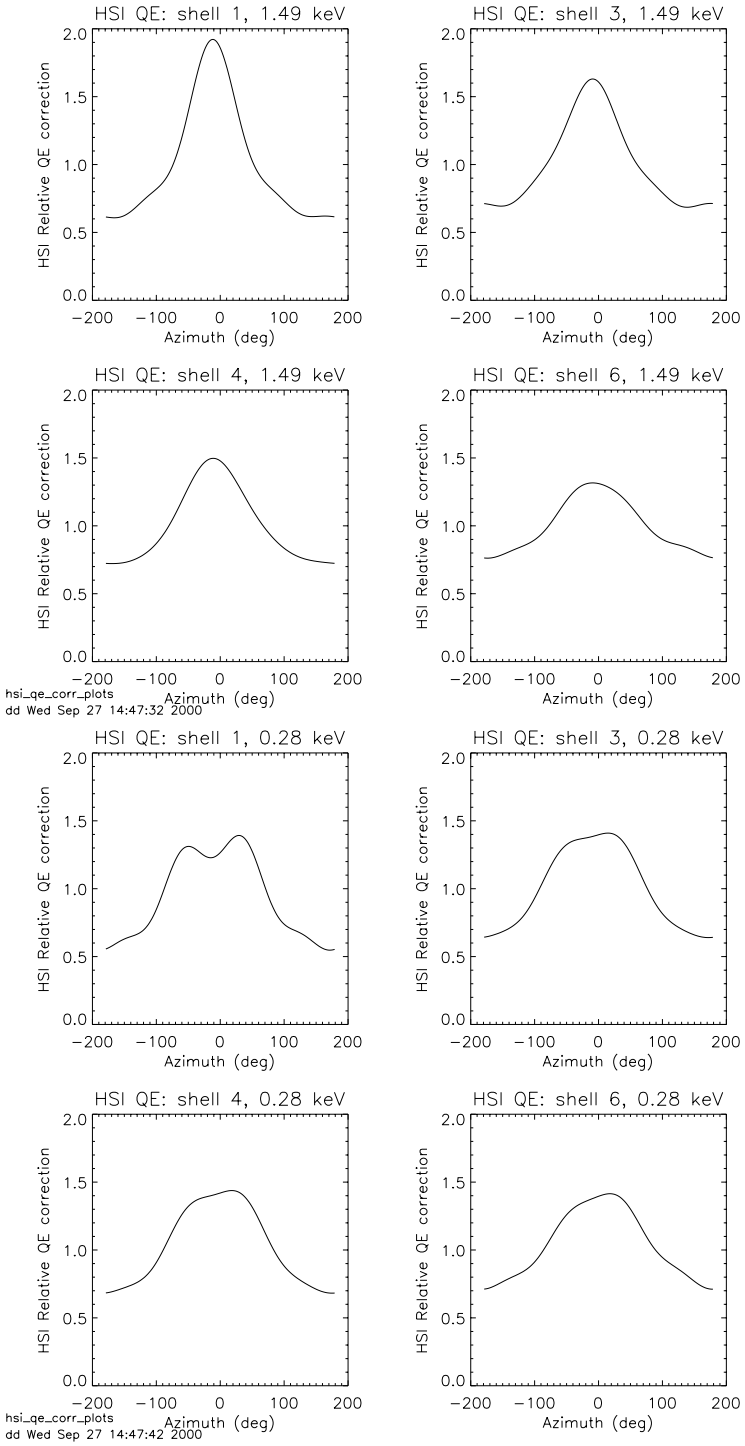

Figure 5.4: HSI QE correction vs azimuth.

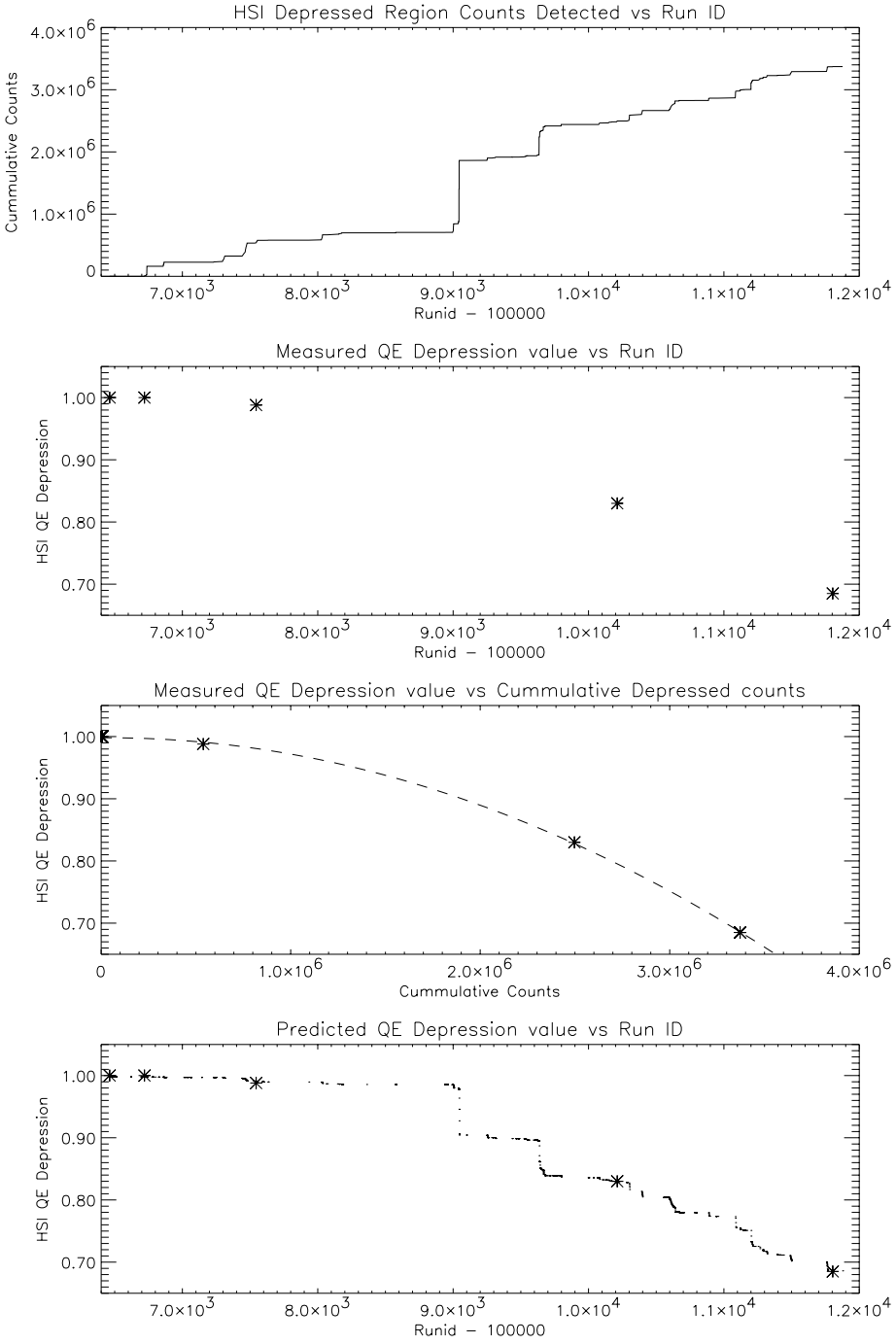

Figure 5.5: HSI QE depression plots.

5.1.5.3 FPC and SSD in the Focal Plane

The FPC and SSD are non-imaging detectors with moderate energy resolution and have a variety of apertures used to isolate and measure grating-dispersed spectral features in the focal plane, *e.g.*, the aperture of diameter D in Figure 5.2. These detectors have well studied characteristics[96, 64], are similar to the BNDs, and provide some of the fundamental data for characterizing the efficiencies and effective area of the system without the novelty and complication of the flight-detectors and their $QE(E, \dots)$ terms.

The FPC and SSD detectors could have a slit aperture selected for use - in this way a direct measurement of the 1D LRF was possible, Section 6.3

5.1.6 ACIS-2C

Extensive LRF tests could be performed with the ACIS-2C detector given its (non-flight) high event-rate readout.

5.1.7 ACIS

ACIS was installed in XRCF with its $+Z$ axis pointing in the $-Z_{\rm xrcf}$ direction.

5.2 Differences between XRCF and Flight

The arrangement and operation of the components at XRCF are flight-like with the following differences:

- The source is not infinitely far away and so i) the HRMA focal length is greater than the flight value and ii) the HRMA reflection angles and optic illumination are different from flight.
- The HRMA is in a "1-g off-loaded" condition approximating the 0-g flight configuration, so flight PSFs will be slightly different.
- The $+Z$ axis of the HRMA, gratings, and flight detectors pointed "down" at XRCF, (*i.e.*, aligned to XRCF $-Z$).
- The gratings are designed to operate at a Rowland distance of 8633.69 mm but because of the HRMA focal length change they are placed $\approx$ 8800 mm from the focus; this introduces negligible LRF effects and some slight additional vignetting, primarily for the LETG ($< 5\%$).

5.2.1 HETG Location at XRCF

The Rowland spacing of the grating is the on-axis Rowland circle intercept to focal plane distance. This spacing must be inferred from measurements between the HETG and HRMA as well as assumed/measured location of the HRMA focus w.r.t. the HRMA fiducial location, *e.g.*, CAP center line.

In order to put measured values into context it is important to have various axial reference points of the HRMA and gratings well defined and specified relative to each other; these references are tabulated in Table 5.2.1.

HETG Axial References	X_g
$X_g = 0$	0.0
HESS/GESS surface (metrology reference)	0.800 inches
ARM reflective surface	1.500 inches
OTG Datum -D- alignment pad surface	1.670 inches
Rowland intercept	2.500 inches
HRMA Axial References	**X w.r.t. CAP CL**
CAP CL (midplane)	0.0
HRMA node	0.371 inches
CAP Datum -A-	0.9825 inches
XRCF ARM	2.846 inches

Table 5.3: Axial references for HETG and HRMA.

The following equation gives the Rowland spacing in terms of other measurable values:

$$\text{(RC spacing)} = \text{(Focus to CAP CL)} - \text{(CAP CL to OTGorg)} + \text{(OTGorg to RC)} \quad (5.1)$$

Values for these quantities are tabulated, Table 5.2.1, for three cases:

- (i) XRCF design drawing (301331)

- (ii) drawing plus a 0.392 inch shim designed to improve the vignetting performance of the gratings designed to improve the vignetting performance of the gratings
- (iii) post-XRCF values inferred from HRMA ARM to OTG ARM laser ranger measurements and improved HRMA focal length value

The later of these is TRW's best value for the as-used spacing at XRCF. The error on the Rowland Spacing at XRCF is at least 0.5 mm due to error in determining the "Focus to CAP CL" distance. Additionally, the "CAP CL to OTGorigin" distances were measured with a laser ranger, measuring the distance between the grating ARM reflective surface and the HRMA "XRCF ARM" surface. This measurement requires compensation for traversing the HRMA XRCF ARM glass substrate - systematics here could allow a common axial shift of both the HETG and LETG.

RC spacing		Focus to CAP CL	CAP CL to OTGorg	OTGorg to RC
mm	inches	inches	inches	inches
		(i) Drawing 301331:		
8772.83 mm	345.387	403.5	60.613	2.5
		(ii) Drawing 301331 with 0.392 shim:		
8782.79 mm	345.779	403.5	60.221	2.5
		(iii) Measurements with laser ranger:		
8787.99 mm	345.984	403.512	60.028	2.5

5.2.2 Rowland Spacing Mystery

X-ray measurements at XRCF, Section 6.2, have been used to verify the grating periods and Rowland spacing. Fits to the XRCF data using a Rowland spacing of 8788.04 mm (the mean of the HETG and LETG spacings of type (iii) above) show a discrepancy between the HEG/MEG sub-assembly periods and the X-ray derived periods; the results agree with the LETG subassembly period value. Because *both* the HEG and MEG periods appear in error by the same fraction, an HETG Rowland spacing error is a more simple explanation than coincident period errors. The Rowland spacing which agrees with the data is close to the expected design value given by case (ii) above. To minimize the number of Rowland spacing values kicking around, the current working hypothesis is that the HETG was installed at XRCF with a Rowland Spacing of 8782.8 mm. The origin of the difference between HETG and LETG XRCF Rowland spacings remains a mystery.

5.2.3 HETG Orientation at XRCF

The drawing of Figure 1.3 **when turned upside down** shows the HETG as oriented at XRCF. The view will then be from the HRMA towards the HETG with the +Z_facility (Up) at the top of the (flipped) page and +Y_facility (South) is to the right. This orientation is rotated 180 degrees about X from the Lab and Flight orientations.

Grating facet locations are given by a code such as 6EE3 where:

The leading digit is the shell number (1,3,4,6).

The next one or two letters specify the sector
(designated A, B,..., F, AA, BB,..., FF).
For the **XRCF orientation**:

sector A is between 9 and 8 o'clock
sector B is between 8 and 7 o'clock
...
sector F is between 4 and 3 o'clock
sector AA is between 3 and 2 o'clock
sector BB is between 2 and 1 o'clock
...
sector FF is between 10 and 9 o'clock.

The final number gives the grating location within
the sector (numbered 1,2,... increasing in CCW direction,
i.e., grating 1 is the most clockwise in a given sector.)

When used with the XRCF shutters the following HETG sectors are illuminated:

Shutter	Illuminated Sectors
Top	BB high-numbered half, CC, DD, EE low-numbered half
North	EE high-numbered half, FF, A, B low-numbered half
Bottom	B high-numbered half, C, D, E low-numbered half
South	E high-numbered half, F, AA, BB low-numbered half

5.3 Overview of HETG XRCF Measurements

5.3.1 Measurements and the CMDB

To support semi-automated test operation, the measurements to be made at XRCF were specified as rows in a 92 column tab-delimited ASCII file. These 92 columns specified nearly completely the desired state of the source, filters, HRMA, gratings, shutters, normalization detectors, and focal plane detectors. Testing proceeded through sequentially "executing" lines of this Calibration Measurement Data Base (CMDB). An as-run (or at least "as-requested"—modifications could be made manually in real time) version of the CMDB is now a useful starting point in understanding what data were taken.

Each measurement is labeled by a "TRW ID". The format of this label was created by TRW systems engineers (*e.g.*, the wild-man trio: Arenberg, Carlson, and Texter) as a convenient way to "name" the measurements. The format is given by:

`[Phase]-[Grating][FP Detector]-[Meas Type]-[Suite].[Number][char]`

Examples: `D-HXD-3D-11.020` or `H-HAS-EA-8.001`

where

`[Phase]` is the letter designation of the XRCF phase found in Table 5.1.

`[Grating]` indicates if a grating is inserted in the beam and takes on the values `I`, `H`, or `L` coresponding to the cases of no-grating, HETG, or LETG.

`[FP Detector]` indicates the focal plane detector through a two letter designation. The HXDA detectors (FPC, SSD, HSI) are specified by `XF`, `XS`, or `XH`; the ACIS-2C by `2C` and the ACIS and HRC detectors are specified with: `AI`, `AS`, `HI`, or `HS`.

`[Meas Type]` is a two character code used to indicate the general scientific purpose of the measurement being carried out. Valid types include `AL BG BU CR dF EA EE FA FC FM GI HF KF MC PI PO PW P1 P2 RC RF SC SF SG SL SM` and `3D !`

`[Suite]` is an integer used to group similar tests of a given type (a "suite" of tests).

`[Number]` is a three-digit integer to label a specific test within a suite.

`[char]` is an infrequent and optional additional character, *e.g.*, "`a`", to indicate a repeat of a measurement.

Tables 5.4 and 5.5 provide a summary of all data taken at XRCF with the HETG inserted in the optical path. The complete set of measurements is thus broken down by focal plane detector and measurement type. Reference to relevant sections of this report are given as well as the number of relevant measurements in brackets. These measurements, with hyper-links to CMDB summaries, are available on the web at:

`http://space.mit.edu/HETG/mtab/meas_table.html`

5.3.2 Efficiency Measurements

The measurement types related to effective area break into three main divisions based on source type: (*i*) quasi-monochromatic measurements using the EIPS sources: types EE (encircled energy), EA (effective area), and 3D(an automated version of EA); (*ii*) measurements using the DCM or HIREFS monochromators; and (*iii*) Molecular Contamination (MC) measurements where the broad-band continuum produced by the source is utilized, *e.g.*, Section 7.8).

The distinctions between EE, 3D, and EA are primarily in Phase 1 and represent different methods of placing the focal plane hardware at the desired location: in EE a beam-center is performed to set the aperture(s) precisely on the image center, using the starting location specified in the CMDB; in 3D measurements, one or more locations are sampled in the focal plane at coordinates specified by a locations file; and in EA the location is specified in the CMDB.

A valuable fraction of the data were taken using the XRCF monochromators, sometimes these were scanned in energy. These tests are all of type EA. Although scientifically similar to EIPS data, these data are more difficult to analyze because of the fundamental complication of the non-uniformity of the monochromators' beam. For scanned data there is the additional irritation that there was no direct synchronization between the source energy scan and the data collection.

In addition to these tests, the Alignment test was designed to set limits on vignetting due to (unplanned) decentering of the HETG at XRCF.

A large number of HETG-ACIS-2C data sets were taken that should allow grating-in/grating-out efficiency measurements to be made similar to the Phase 1 FPC/SSD measurements. These '2C analyses have not been carried out as of this writing, however.

In Phase 2, important effective area tests were carried out in the flight configuration, HRMA-HETG-ACIS-S, using the EIPS, monochromators, and continuum sources. Similar HRMA-HETG-HRC-I tests allow the untangling of grating and detector effects.

5.3.3 LRF Measurements

Phase 1 LRF measurements were generally performed with the HSI to obtain images. However, the FPC fitted with slits was used to scan the diffracted Mg-K line (PSF/1-D) and the beam center results of EE tests served to measure precisely the location of the diffracted images to determine grating periods and diffraction angles. The Alignment test performed on the MEG 3rd order was used to identify the specific mis-aligned gratings and in this context was a tool for LRF diagnosis.

Only a limited set of LRF related data were taken with the ACIS-S and HRC-I due to ACIS pileup (and hence time) limits, and HRC dose limits. The ACIS-2C LRF data is generally unanalyzed with the very notable exception of the scattering tests at 1.775 keV.

Table 5.4: Summary of HETG XRCF Measurements in Phase 1. The relevant report section is shown in **bold** and the number of measurements is shown in brackets.

Type	Detector	
	FPC/SSD	HSI
LRF-related . . .		
EE	Order locations: **6.2** [33]	-
FC, SF	-	Verify focus, check PSF, Mis-aligned gratings: **6.3**, **6.4** [16]
Alignment	-	Mis-aligned gratings: **6.4** [2]
dFocus	-	Defocus set of images: **N/A** [2]
PSF/1D	LRF core, wings: **6.3, 6.5** [21]	-
3D	-	MEG-Penning PSF: **6.3** [1]
PSF/Outer	-	Wings, scatter: **6.6** [8]
3D (Offaxis)	-	Offaxis images: **N/A** [6]
Eff.area-related . . .		
Alignment	-	Gross vignetting: **7.2** [1]
EE (EIPS)	Eff. area: **7.4** [*33*]	-
3D,EA (EIPS)	Eff. area: **7.4** [56]	Source spectra: **7.3** [32]
EA (MonoC)	Eff. area: **N/A** [29]	Source spectra (DCM, HIREFS): **7.3** [8]
3D (Molecular Contamination)	-	Identify and search for edges, etc.: **7.8** [6]

Table 5.5: Summary of HETG XRCF Measurements in Phase 2. The relevant report section is shown in **bold** and the number of measurements is shown in brackets.

Type	Detector		
	ACIS-2C	HRC-I	ACIS-S
LRF-related . . .			
FC, SF	Verify focus: **N/A** [7]	Verify focus: **TBD** [1]	Rowland geom.: **6.8** [2] Core, wings: **6.3** [1]
dFocus	Find best focus: **N/A** [10]	-	-
PSF/Inner	Core, wings: **N/A** [14] Offaxis images: **N/A** [9]	-	Offaxis images: **N/A** [4]
Scattering	Wings, scatter: **6.6** [5]	-	Grating scatter: **6.6** [6]
Eff.area-related . . .			
EA (EIPS)	Eff. area: **N/A** [126]	Eff. area: **7.9** [6]	Eff. area: **7.7** [7]
EA (MonoC)	Eff. area: **N/A** [36]	Eff. area: **7.9** [28]	Eff. area: **7.7** [15]
MC (Molecular Contamination)	Identify and search for edges, etc.: **N/A** [53]	- -	Identify and search for edges, etc.: **7.8** [5]

5.4 HETG-ACIS-S Data at XRCF

The measurements carried out at XRCF with the HETGS flight configuraion, HRMA-HETG-ACIS-S, are explicitly listed here because of their importance. This represents a diverse set of data both in terms of source/instrument modes as well as possibilities for analysis. References to the XRCF data analysis sections where the measurements are treated are given.

To-do:
Get actual defocus values for EA tests

Table 5.6: HETG-ACIS-S LRF Measurements at XRCF. All LRF measurements here were made with ACIS-S at nominal focus. All data are taken in TE mode unless noted.

TRW ID	run id	day	Source	Off-axis?	Comments
Rowland Geometry			EIPS:		Analysis Section 6.8
H-HAS-SF-1.001	115167	112	Al-K	-	scanned quadrants
H-HAS-SF-1.003	115168	112	Al-K	-	“
a.k.a. 'PI-1.001,3					
PSF Inner			EIPS:		Analysis Section 6.3
H-HAS-SF-18.001	115177-80	113	Al-K	-	TE alt. frame mode,
a.k.a. 'PI-18.001					scanned quadrants
Off-axis			EIPS:		
H-HAS-PI-1.011	115170	112	Al-K	0,3'	
H-HAS-PI-1.012	115171	112	Al-K	-4.2',-4.2'	
H-HAS-PI-19.001	115301	114	Si-K	-4.2',-4.2'	
H-HAS-PI-19.002	115302	114	Si-K	0,-10'	
Scattering			DCM:		Analysis Section 6.6
H-HAS-SC-7.001	115037	109	1.38	-	
H-HAS-SC-7.002	115038	109	1.38	-	
H-HAS-SC-7.003	115039	109	2.02	-	
H-HAS-SC-7.004	115040	109	2.02	-	
H-HAS-SC-7.005	115041	109	4-9	-	
H-HAS-SC-17.006	115113,4	111	4-9	-	TE alt. frame mode

Table 5.7: HETG-ACIS-S Effective Area Measurements at XRCF. All effective area measurements here are made on-axis. All data are taken in TE mode unless noted.

TRW ID	run id	day	Source	Defocus?	Comments
Effective Area			EIPS:		Analysis Section 7.7
H-HAS-EA-2.001	115169	112	Al-K		
H-HAS-EA-6.001	115310	114	O-K		
H-HAS-EA-6.002	115443,4	115	Fe-L		TE alt. frame mode
H-HAS-EA-6.003	115373	115	Cu-L		TE alt. frame mode
H-HAS-EA-6.004	115303	114	Si-K		
H-HAS-EA-6.005	115451	115	Fe-K		TE alt. frame mode
H-HAS-EA-6.006	115366	115	Cu-K		TE alt. frame mode
Effective Area			DCM:		Analysis Section 7.7
H-HAS-EA-8.001	115026	109	0.95-1.15		
H-HAS-EA-8.002	115027	109	1.2-1.4		
H-HAS-EA-8.003	115028	109	1.4-1.7		
H-HAS-EA-8.004	115029	109	1.86-2.00		
H-HAS-EA-8.005	115030	109	2.05-2.35		
H-HAS-EA-8.006	115032	109	2.5-4		
H-HAS-EA-8.007	115033	109	4-5		
H-HAS-EA-8.008	115034	109	5-7		
H-HAS-EA-8.009	115035	109	7.2-8.7		
Effective Area			HIREFS:		Analysis Section 7.7
H-HAS-EA-10.001	115488	116	0.392		
H-HAS-EA-10.002	115489	116	0.486		
H-HAS-EA-10.003	115490	116	0.577		
H-HAS-EA-10.004	115491	116	0.642		
H-HAS-EA-10.005	115492	116	0.751		
H-HAS-EA-10.006	115493	116	0.800		
Molecular Contamination			EIPS:		Analysis Section 7.8
H-HAS-MC-3.001	115360	115	Cu	0.0	CC mode, HEG only
H-HAS-MC-3.005	115362	115	Cu	0.0	CC mode, MEG only
H-HAS-MC-3.010	115264	113	C	0.0	CC mode, HEG only
H-HAS-MC-3.011	115265	114	C	0.0	CC mode, MEG only
H-HAS-MC-20.001	115359	115	Cu	0.0	TE alt. frame mode

5.5 Examples of XRCF Data

With complicated data it is best to start with an image—and so in Phase 1 we generally took images of the diffracted X-rays with the High Speed Imager (HSI). Figure 5.6 shows the HSI image of the Al-K line in the MEG 3rd order—deflected 55 mm from the zero-order (HRMA focus) location. These are the "raw" HSI data and show the instrumental "gaps"[26], *e.g.*, one goes through the K-β peak. Note that the "line" in fact consists of several discrete lines as well as continuum. The "satellite" line just shortward of the K-α peak has been previously observed during XMM grating testing[76]; we also observe a second, weaker satellite line at 8.22Å.

To accurately measure the intensity of the line in Phase 1, the FPC_X2 (or SSD_X) with selected aperture could be moved to the line center and the pulse-height histogram of events through the aperture measured. An example of the acquired focal-plane and BND histograms is shown in Figure 5.7 for the MEG first order of Al-K and a 500 μm diameter aperture. Note that while the BNDs are able to resolve an Al-K peak and broadband continuum, the detailed spectral structure of the Al-K line is unresolved. The 500 μm first-order aperture size corresponds spectrally to the region within the 1500 μm circle shown in Figure 5.6—thus the FPC_X2 is detecting the K-α and satellite lines and some continuum, but is excluding other continuun and the K-β peak.

In Phase 2 the focal plane detectors were all imaging instruments (ACIS-2C, ACIS, and HRC) and so provide their own source spectral diagnostics. Effective area measurements generally did not required precise positioning; in fact, because of per-pixel count-rate limits (set generally by pile-up for ACIS and dose limits for HRC) the measurements were performed with a large defocus. Figure 5.8 shows an ACIS-2C image of the HEG first-order of Al-K. The defocussed images of the HRMA shells 4 and 6 are modulated by the individual grating facets. Because of the defocus, extraction of the K-α events will necessarily be contaminated by the existence of the other lines and continuum. HRC and ACIS effective area data are very similar to this ACIS-2C example as the ACIS-S event plot of Figure 5.9 demonstrates.

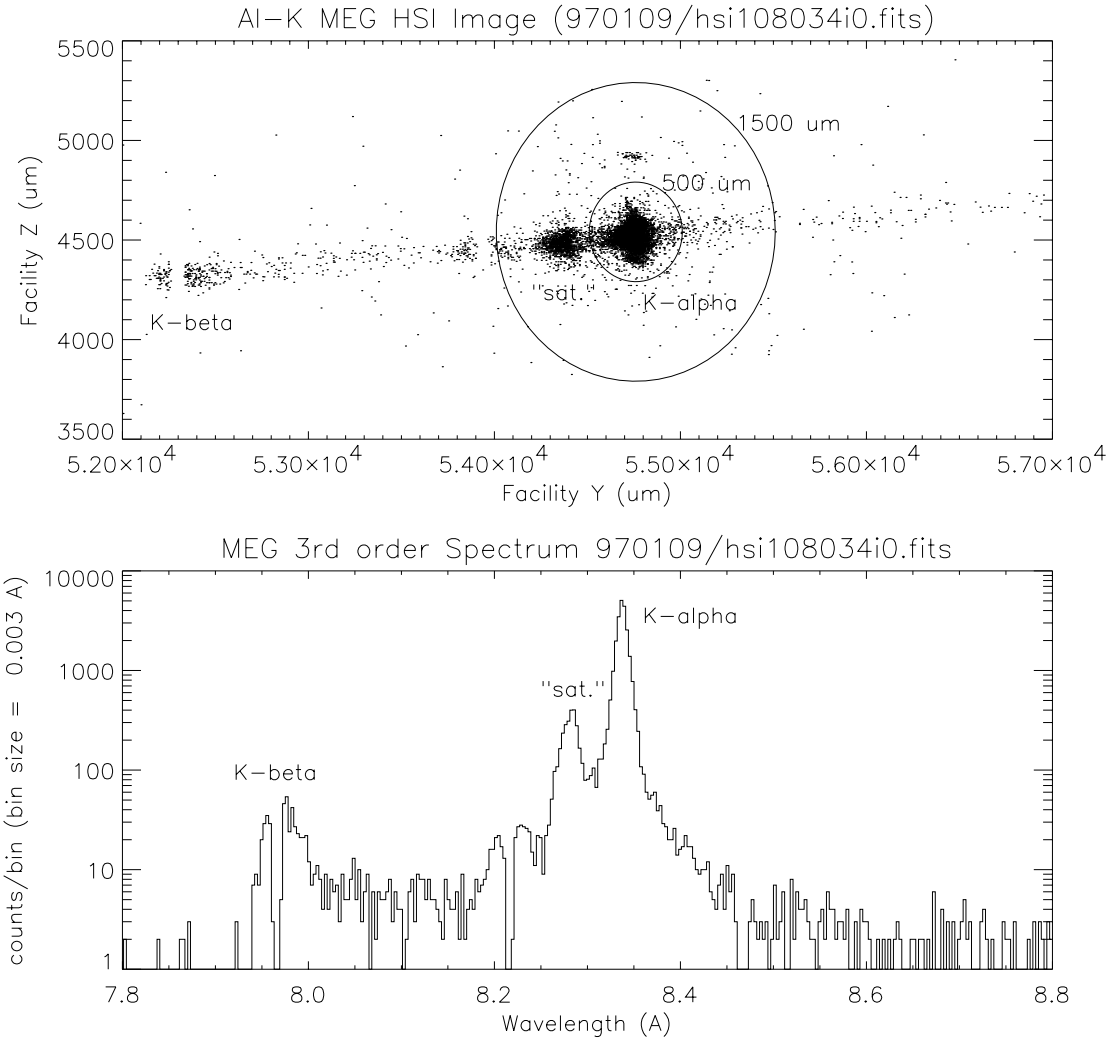

Figure 5.6: HSI image of 3rd-order MEG Al-K line (top) and the resulting grating-produced spectrum (bottom). Note that all of this spectral structure is unresolved by the FPC and SSD detectors, Figure 5.7. A strong "satellite" line is clearly visible near the K-α peak. HSI instrumental gaps have not been removed, *e.g.*, at the K-β line.

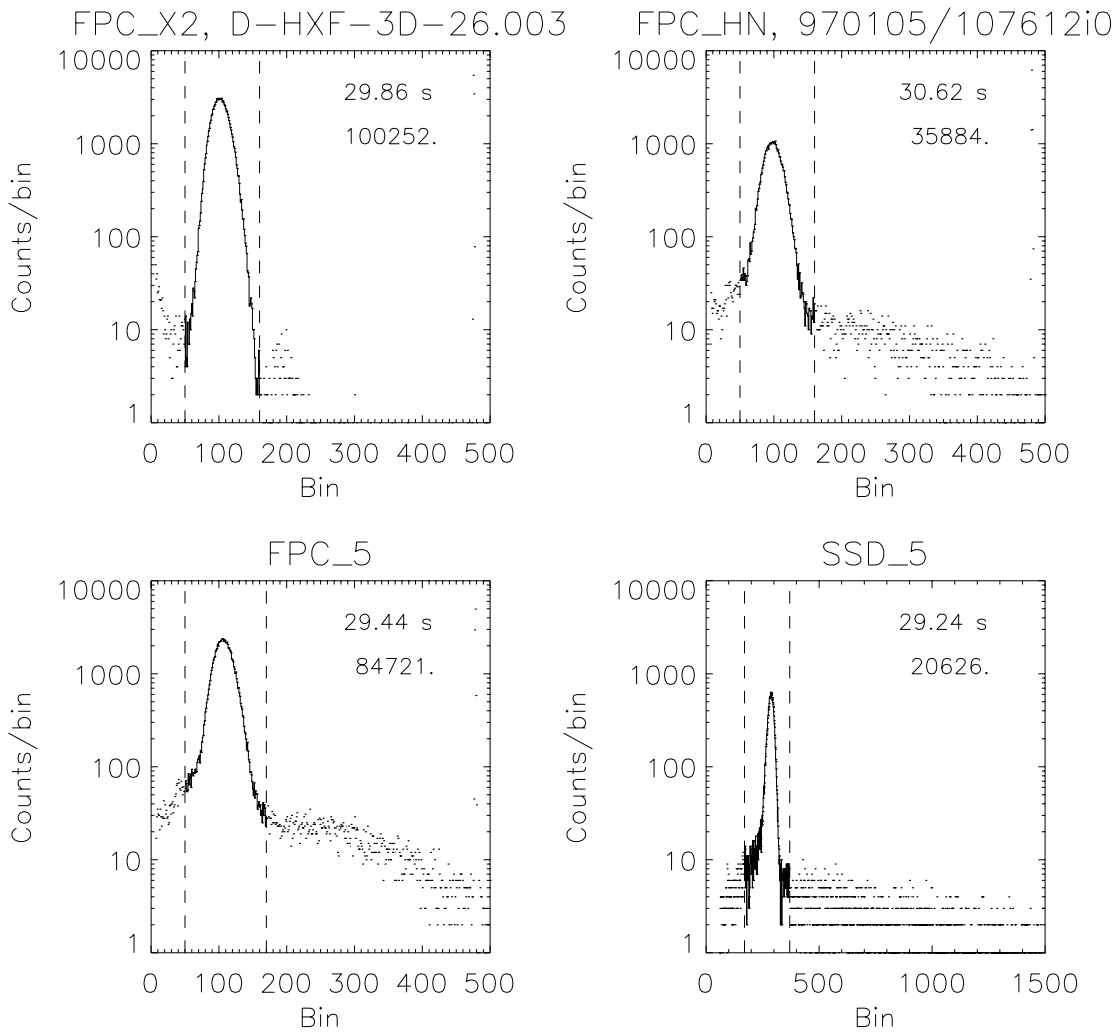

Figure 5.7: PHA spectra from Al-K MEG +1 order measurement. The focal plane FPC_X2 shows only a monochromatic response (with a slight pile-up peak at $2E$) while the beam normalization detectors (FPC_HN, FPC_5, and SSD_5) show both the Al-K "line" and broad-band (unfiltered) continuum.

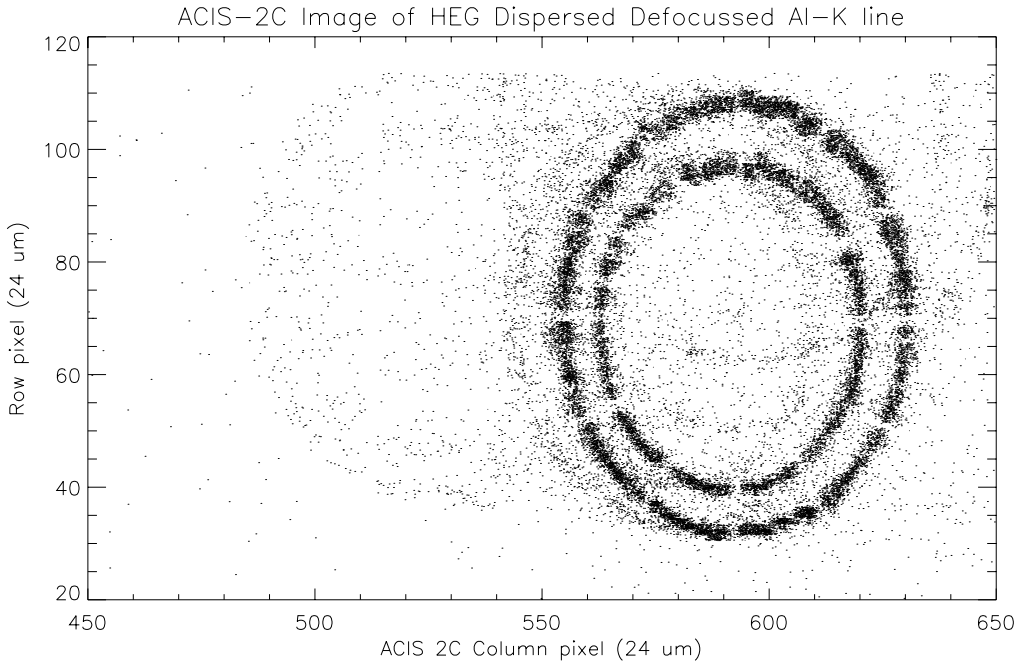

Figure 5.8: ACIS-2C defocussed image of HEG dispersed Al-K line. Note that the same line components as in Figure 5.6 are present.

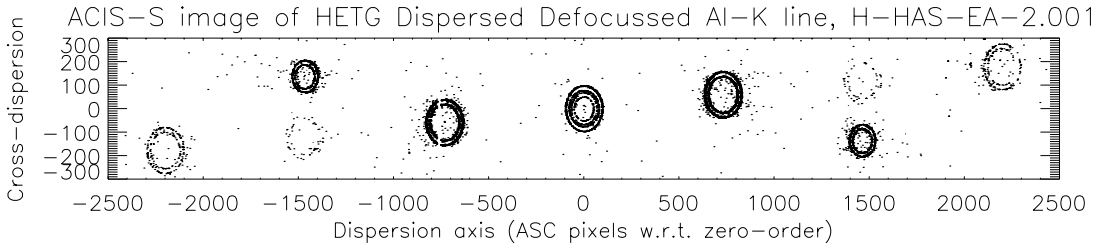

Figure 5.9: ACIS-S defocussed image of HETG dispersed Al-K line. The HEG and MEG diffracted orders are clearly identified by the corresponding HRMA shells in their images. For the MEG, orders $m = \pm 1, \pm 2, \pm 3$ are visible.

5.6 Status of the HETG XRCF Analysis

The table below summarizes the status of the HETG XRCF analysis efforts. Only a few of the measurement projects listed here have reached the level of "adequate" analysis. Analysts are generally from the HETG and ASC/MIT groups; brackets indicate contributors expected beyond this preliminary report.

Table 5.8: Analysis Status Code

Status code	Analysis status
-	not yet analyzed
X	very preliminary analysis
XX	adequate analysis
XXX	complete analysis

Table 5.9: Status of HETG XRCF analyses

Section	Analysis Effort	Prime Analyst	Status
	LRF:		
6.2	Periods and Angles	Dewey	XX
6.3	Core: Period and Roll Variations	Dewey	XX
6.4	MEG mis-aligned gratings	Dewey	XXx
6.5	Between Core and Scatter	Dewey	x
6.6	Scatter Tests	Marshall	XXX
3.3	Scatter Theory	J.Davis	XXx
6.7	Offaxis and Defocus Tests	-	-
6.8	ACIS-S Rowland Conformance	Stage	XXX
	Efficiency and Effective Area:		
7.2	Alignment Tests	Dewey	X
7.3	XRCF Source Characteristics	Dewey	XXX
7.4	Phase 1, EIPS Data	Dewey	XXx
7.5	Phase 1, Monochromator Data	-	-
7.6	Efficiency with ACIS-2C Data	-	-
7.7	Area with ACIS-S	Schulz	XXx
7.8	Molecular Contamination	Marshall	XXx
7.9	Area with HRC-I	Flanagan	XX
7.10	High-Order Efficiencies	Flanagan	XX

Section 6

XRCF LRF Measurements

6.1 Overview

Verification of the HETGS Line Response Function (LRF) at XRCF is performed in a variety of complimentary ways. First, the basic periods and diffraction angles are measured using the beam center technique in Phase 1. The width of the LRF core is measured primarily in Phase 1 using HSI images of Al-K and Mg-K lines and more accurately with slit scans of the Mg-K line. These measurements are used to set the values of the grating dp/p and alignment roll.

Specific data sets are analyzed in order to measure the MEG mis-aligned gratings and the HEG scatter.

Coarser slit scans as well as images of the narrow lines can be analyzed to search for grating-induced structure in the LRF region between the core and the wide-angle scatter.

Finally, quadrant shutter-focus tests in the HRMA-HETG-ACIS-S configuration verify at a coarse level the matching of the ACIS-S geometry to the desired Rowland curvature.

6.2 Periods and Angles

Objective: The Period and Angle analysis is used to determine the dispersion direction angles and a measure of the grating periods based on the dispersion distance of known narrow lines.

6.2.1 Analysis Method

At XRCF Encircled Energy measurements of the diffracted orders were performed with HXDS Beam Centering in order to precisely locate the diffracted images. The available EE data sets are listed in Table 6.1.

The beam centers obtained from these measurements are put into data files, `beam_cen_yymmdd.rdb`. The centers are reported in HXDS coordinates (`ypos, zpos` as in the .sum files) in microns, Figure 6.1. Each of these data files is analyzed with `xrcf_beam_cen_werr.pro` to get a best-fit period and angle (with errors) for each grating, Figure 6.2. The results are put, along with sub-assembly predicted values, into a results file, `beam_cen_results.rdb`, Figure 6.3.

For these analyses the following parameter values were assumed: Rowland distance = 8788.04 mm, hc = 12.3985, Al-K is at 1.4867 keV, and TOGA rowland distance = 5366.55 mm.

The Period and Angle contents of this results file are plotted using `beam_cen_plots.pro` and shown in Figures 6.4 and 6.5. The weighted-average period for each grating based *only* on the XRCF Al-K data sets is shown in the plot titles. The HETG opening angle and the HETG mean angle (MEG HEG bisector) are also calculated and plotted.

Phase	Date code	Line	Orders	TRW IDs (runids)
R	960827	Al-K	MEG -1,0,+1	102931, 102926, 102929
			HEG -1,0,+1	102938, 102933, 102935
1C	961223	Al-K	MEG 0,+1,-1	C-HXF-EE-3.003,4,10
			HEG 0,+1,-1,0	C-HXF-EE-3.005,6,13,5a
1D	970104	Al-K	MEG 0,+1,-1,-3,+3	D-HXF-EE-3.004,5,6,12,13
			HEG 0,+1,-1,-2,+2	D-HXF-EE-3.007,8,9,14,15
1D	970116	Mg-K	MEG 0,+1,-1	D-HXF-EE-3.021,22,23
			HEG 0,+1,-1	D-HXF-EE-3.024,25,26
1E	970208	Al-K	HEG 0,-2,+2	E-HXF-EE-3.007,14,15
			MEG -3,+3	E-HXF-EE-3.007,14,15

Table 6.1: Beam Center Measurements of Diffracted Order Locations

6.2.2 Results and Discussion

The opening angle between HEG and MEG is measured very close to the expected 10 degree design value. The absolute HETG dispersion angles, nominally at ±5 degrees, show a −0.225 degree offset from the mechanical axes. The origin of this difference was traced after-the-fact in the lab to low accuracy in the initial alignment of the optical and mechanical axes of the polarization alignment setup. This offset, however, is within the HETG design requirement of ± 0.5 degree.

Agreement between measured and expected periods of the gratings depends on the accuracy of these ingredients: i) the line wavelength, ii) the focal-plane detector spatial calibration, and iii) the Rowland spacing value. By taking a ratio of measurements some of these terms can be cancelled. For example, HEG and MEG measured periods here have the first three terms in common, thus the ratio of HEG to MEG period is insensitive to the accuracy of these ancillary values. Specifically, the XRCF measured MEG to HEG period ratio is very close to the lab-derived ratio based on the LR periods in Table 4.3. Specifically we have: $R^{\rm XRCF}_{\rm MEG/HEG}/R^{\rm lab}_{\rm MEG/HEG} = 0.999910 \pm 0.000100$.

The XRCF measured HETG/LETG period ratio differs significantly from the ratio expected from the lab measurements (where $p^{\rm lab}_{\rm LETG} = 9912.16$ Å) giving: $R^{\rm XRCF}_{\rm HETG/LETG}/R^{\rm lab}_{\rm HETG/LETG} = 1.00077 \pm 0.00015$. Because the line wavelength and detector are common, this difference either represents an inaccuracy of the absolute grating periods from their assumed lab-derived values or a difference in the assumed identical Rowland spacings at XRCF by of order 6 mm.

Assuming that the lab-derived grating periods are accurate, the HETG Rowland spacing at XRCF appears close (to 1 part in 10,000) to the value inferred from mechanical design plus known shim information, 8782.8 mm, while the LETG Roland spacing appears consistent with a spacing derived from laser-range finder measurements, 8788.8 mm. This difference in spacing is plausible at XRCF given the non-flight, independant insertion mechanisms in use and the various mechanical tolerances and shimming which took place to align the gratings to each other and the HRMA. Flight data should shed light on what the likely mechanism for the disagreement is; the working hypothesis is that there is an HETG-LETG spacing difference that is not yet uncovered.

To-do:

- Improve analysis of EE data
  - Add mst_date and run_id values to 961223 and 970104 data files.
  - Re-do full analysis: .pha files to .sum files
  - Plot .sum files, compare with expected 1D scans (simulations); defocus?
  - Better "center" location and errors using 1D simulated shapes
- (Explain the LETG / HETG difference in spacing)
- Is the TOGA MEG period difference due to old LR version used for TOGA?
- Why the HEG Al/Mg difference? (by 1 part in 4000)
- Use HSI observations for period determination too.
- Use HRC and ACIS-S data sets to determine period/angle as well, *e.g.*, H-HAS-PI-18.001 and H-LAS-PI-18.002.

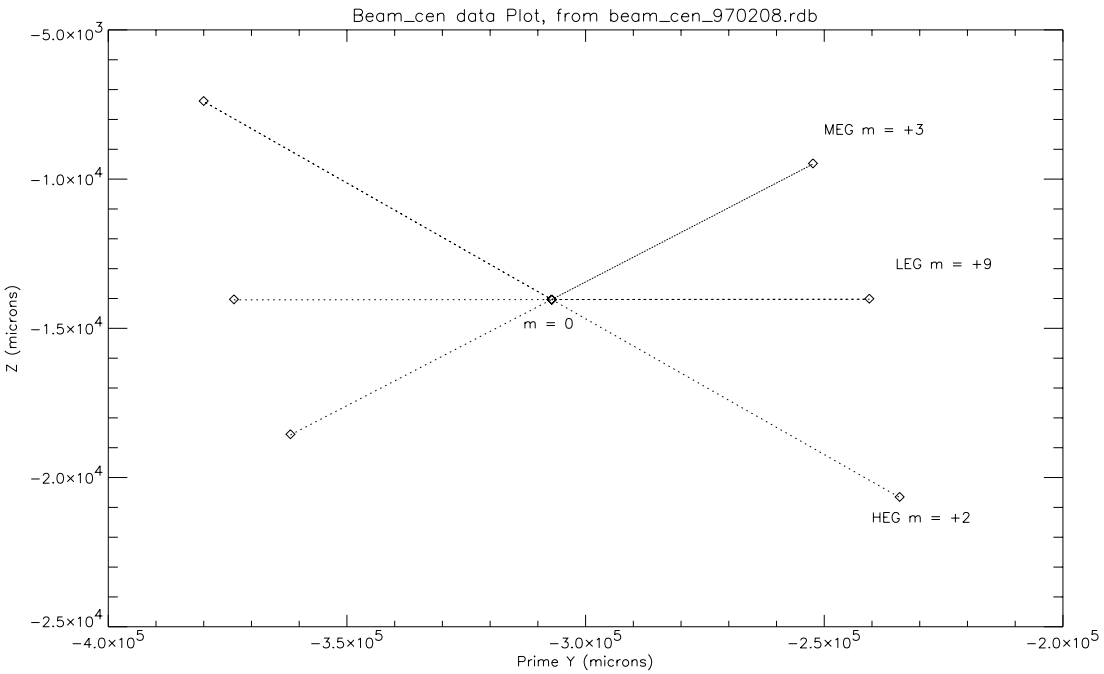

Figure 6.1: Beam center example plot

```
Output from xrcf_beam_cen_werr.pro , Fri Sep 12 13:08:01 1997
Input data file :  beam_cen_970208.rdb

Grating Order Prime Y Z Energy Y_err(um) Z_err(um)
HEG 0.00000 -307097.00 -14035.000 1.4867001 5.00000 5.00000
HEG -2.00000 -380012.00 -7383.0000 1.4867001 20.0000 20.0000
HEG 2.00000 -234206.00 -20650.000 1.4867001 20.0000 20.0000
MEG -3.00000 -361832.00 -18549.000 1.4867001 20.0000 20.0000
MEG 3.00000 -252366.00 -9473.0000 1.4867001 20.0000 20.0000
MEG 0.00000 -307097.00 -14035.000 1.4867001 7.00000 7.00000
MEG 0.00000 -307102.00 -14037.000 1.4867001 7.00000 7.00000
LEG -9.00000 -373666.00 -14028.000 1.4867001 20.0000 20.0000
LEG 9.00000 -240552.00 -14007.000 1.4867001 20.0000 20.0000
LEG 0.00000 -307102.00 -14037.000 1.4867001 5.00000 5.00000

Calculate Angles and Periods to best-fit the data:
(keeping the Rowland distance at 8788.04 )

LEG angle = 0.0090 +/- 0.0122 [ currently = 0.0059]
LEG period = 9910.03 +/- 2.11 [ currently = 9903.90]

Errors between measured and calculated Y,Z (microns):
Y: -373666.00 - -373663.67 = -2.3
Y: -240552.00 - -240549.66 = -2.3
Y: -307102.00 - -307106.67 = 4.7
Z: -14028.000 - -14034.498 = 6.5
Z: -14007.000 - -14013.502 = 6.5
Z: -14037.000 - -14024.000 = -13.0

MEG angle = 4.7396 +/- 0.0147 [ currently = 4.7412]
MEG period = 4003.27 +/- 1.03 [ currently = 4000.77]

Errors between measured and calculated Y,Z (microns):
Y: -361832.00 - -361832.25 = 0.3
Y: -252366.00 - -252366.25 = 0.2
Y: -307097.00 - -307099.25 = 2.2
Y: -307102.00 - -307099.25 = -2.8
Z: -18549.000 - -18561.501 = 12.5
Z: -9473.0000 - -9485.4993 = 12.5
Z: -14035.000 - -14023.500 = -11.5
Z: -14037.000 - -14023.500 = -13.5

HEG angle = -5.1991 +/- 0.0110 [ currently = -5.1908]
HEG period = 2002.25 +/- 0.39 [ currently = 2000.95]

Errors between measured and calculated Y,Z (microns):
Y: -307097.00 - -307105.00 = 8.0
Y: -380012.00 - -380008.00 = -4.0
Y: -234206.00 - -234202.00 = -4.0
Z: -14035.000 - -14022.667 = -12.3
Z: -7383.0000 - -7389.1638 = 6.2
Z: -20650.000 - -20656.170 = 6.2
```

Figure 6.2: Period and angle analysis output

```
#filename:  beam_cen_results.rdb
#
# Results of the XRCF HETG/LETG beam center analyses
# are compiled here along with sub-assembly values.
#
# These results are from running the idl procedure:
# IDL> xrcf_beam_cen_werr, 'beam_cen_YYMMDD.rdb'
# where YYMMDD is the dataset date code in the table below.
#
# The LETG period is taken from the MPE web page, the
# LETG period error is 1 part in 10000 (Predehl).
#
# 7/8/97 dd
# 7/9/97 dd Added TOGA (960827) values (both sub-assembly and XRCF)
# 7/10/97 dd Changed LEG sub-assembly period error.
# 7/18/97 dd Change MEG Flight and TOGA LR-NIST values based
# on NIST "M" sample period of 400.800 nm (instead
# of 400.770 nm).  Old lines:
# sub TOGA HeNe MEG 4000.68 2.0 5.0 0.5
# sub LR-NIST HeNe MEG 4001.13 2.0 5.0 0.5
# 8/20/97 dd New values from re-analysis using 8788.04 as spacing
#
phase dataset source grating p perr ang angerr
S S S S N N N N
sub TOGA HeCd LEG 9912.36 0.99 0.0 0.5
sub TOGA HeNe MEG 4000.96 0.10 5.0 0.5
sub TOGA HeCd HEG 2001.04 0.05 -5.0 0.5
Rehears TOGA Al-K LEG 9911.27 7.76 -0.9073 0.0449
Rehears TOGA Al-K MEG 4002.75 1.27 3.9489 0.0181
Rehears TOGA Al-K HEG 2001.33 0.64 -5.9974 0.0180
sub MP E HeCd LEG 9912.16 0.99 0.0 0.5
sub LR-NIST HeNe MEG 4001.41 0.10 5.0 0.5
sub LR-NIST HeCd HEG 2000.81 0.05 -5.0 0.5
XRCF 1C 961223 Al-K LEG 9910.48 1.92 -0.0435 0.0119
XRCF 1C 961223 Al-K MEG 4003.24 0.78 4.6935 0.0221
XRCF 1C 961223 Al-K HEG 2001.98 0.19 -5.2474 0.0110
XRCF 1D 970104 Al-K LEG 9910.05 1.92 0.0062 0.0111
XRCF 1D 970104 Al-K MEG 4003.81 0.62 4.7453 0.0088
XRCF 1D 970104 Al-K HEG 2002.06 0.17 -5.1879 0.0049
XRCF 1D 970116 Mg-K LEG 9911.57 5.33 0.0087 0.0308
XRCF 1D 970116 Mg-K MEG 4003.98 1.31 4.7313 0.0186
XRCF 1D 970116 Mg-K HEG 2002.52 0.33 -5.1917 0.0093
XRCF 1E 970208 Al-K LEG 9910.03 2.11 0.0090 0.0122
XRCF 1E 970208 Al-K MEG 4003.27 1.03 4.7396 0.0147
XRCF 1E 970208 Al-K HEG 2002.25 0.39 -5.1991 0.0110
```

Figure 6.3: Beam center results file

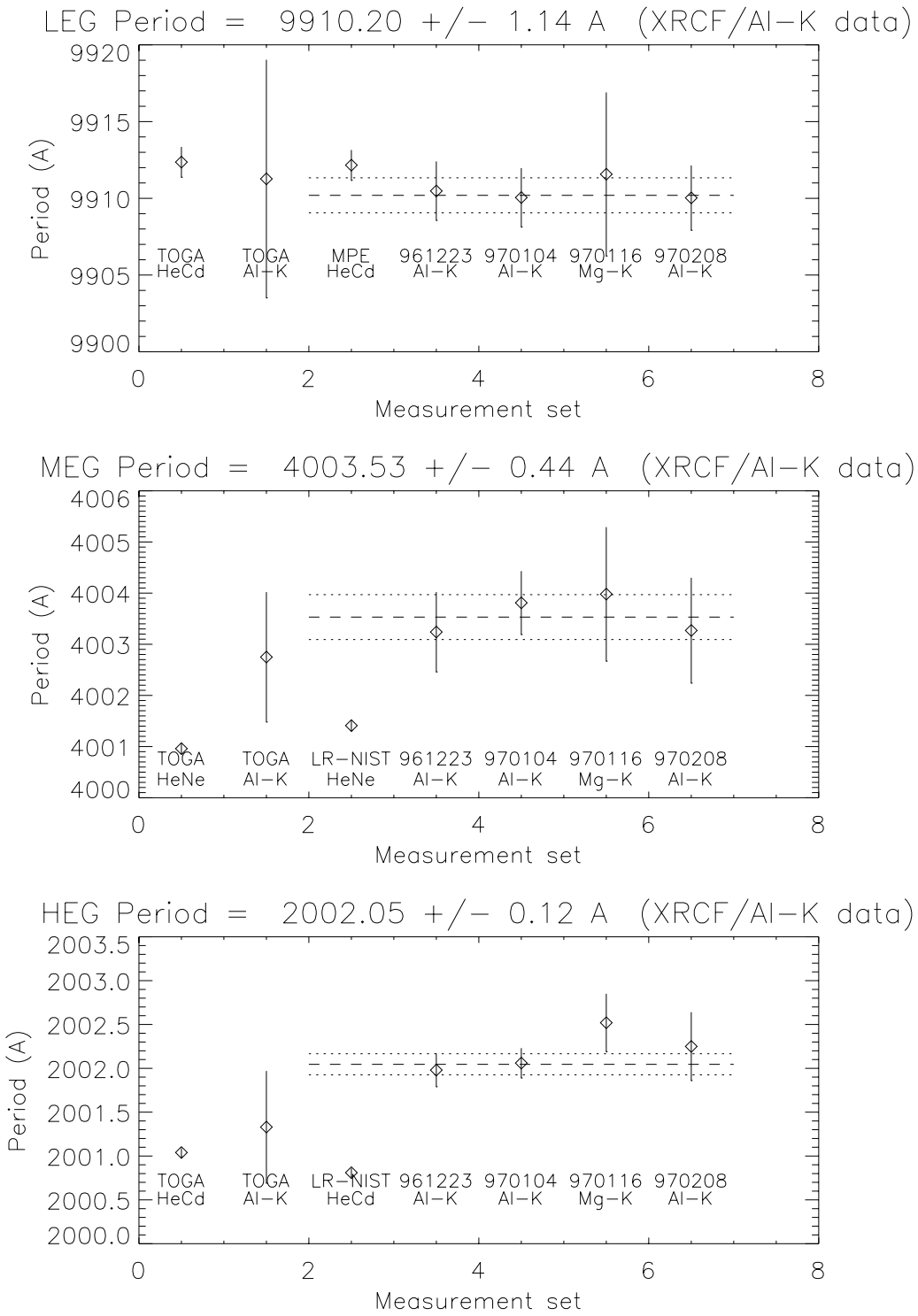

Figure 6.4: Measured Grating Periods. Parameter values assumed: $X_{\rm RS} = 8788.04$ mm, $hc = 12.3985$, Al-K is at 1.4867 keV, and for TOGA $X_{\rm RS} = 5366.55$ mm. Note that the XRCF derived periods for both MEG and HEG are larger by ≈500 ppm than the LR-NIST values, Section 4.1.2.

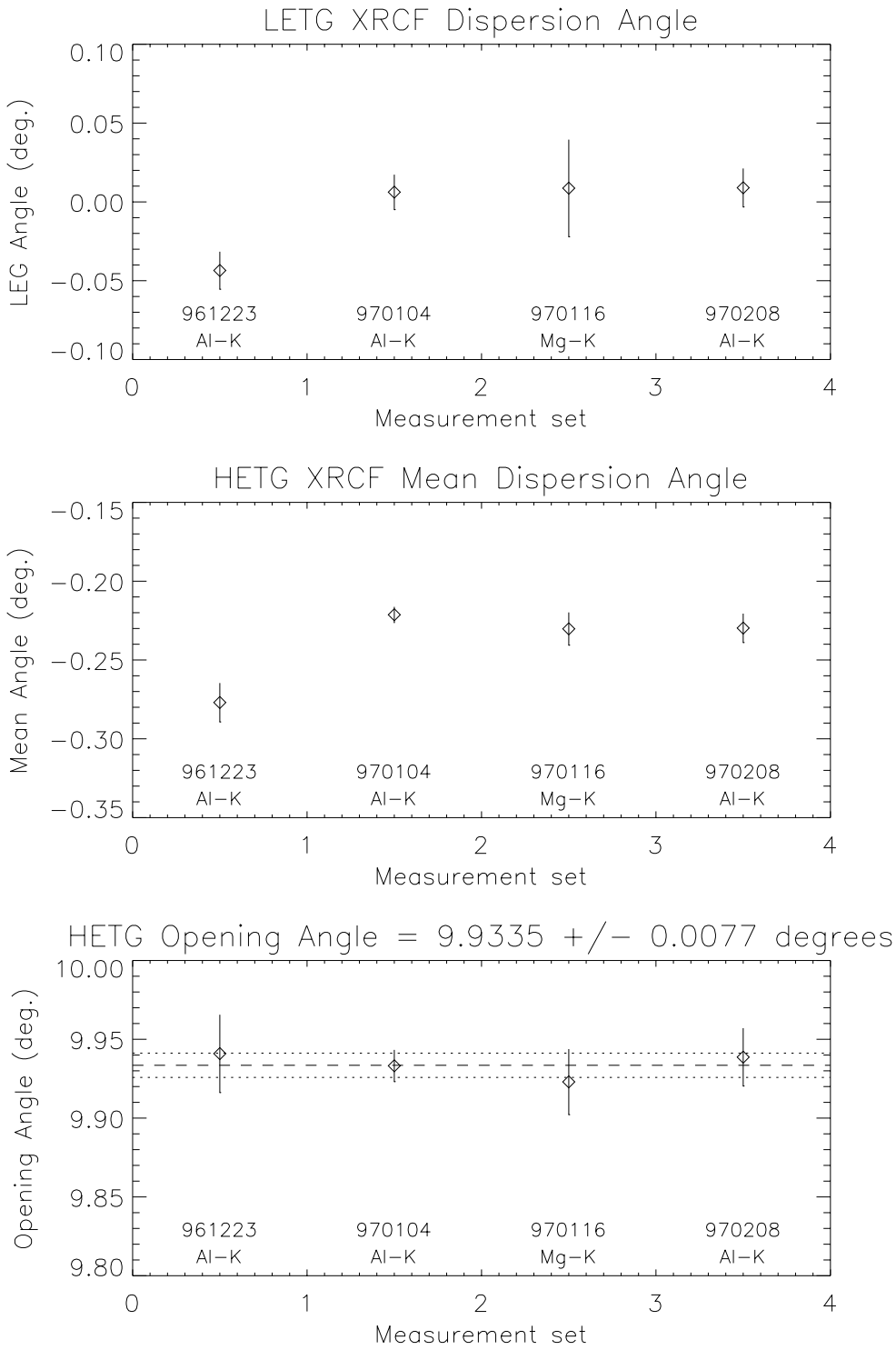

Figure 6.5: Measured Dispersion Angles. The LETG and HETG (mean) dispersion angles (w.r.t. HXDS axes) track very well through the XRCF Phase I subphases. The HETG opening angle is very stable as would be expected.

6.3 LRF Core: Period and Roll Variations

Objective: Imperfections in grating fabrication produce blur in the dispersion and cross-dispersion directions. These blurs are dominated, respectively, by the rms period variation and and the rms roll (alignment) variation. The core of the diffracted image is studied and compared with the core of the no-grating (or zero-order) image to measure the size of these variations.

6.3.1 Zero-order effects

HSI images of the MEG and HEG zero-order Al-K line are very similar to HRMA-only images as demonstrated by the 1-D projection comparisons of Figure 6.6. This result confirms the expectation that there are no HETG LRF effects in the zero-order. The data sets used in the comparison are listed in Table 6.2. Note that these data sets must be combined in order to compare them: HRMA shells 1 and 3 are combined and compared with the combination of the four MEG quadrant images – both if these then represent the image from the complete shells 1 and 3.

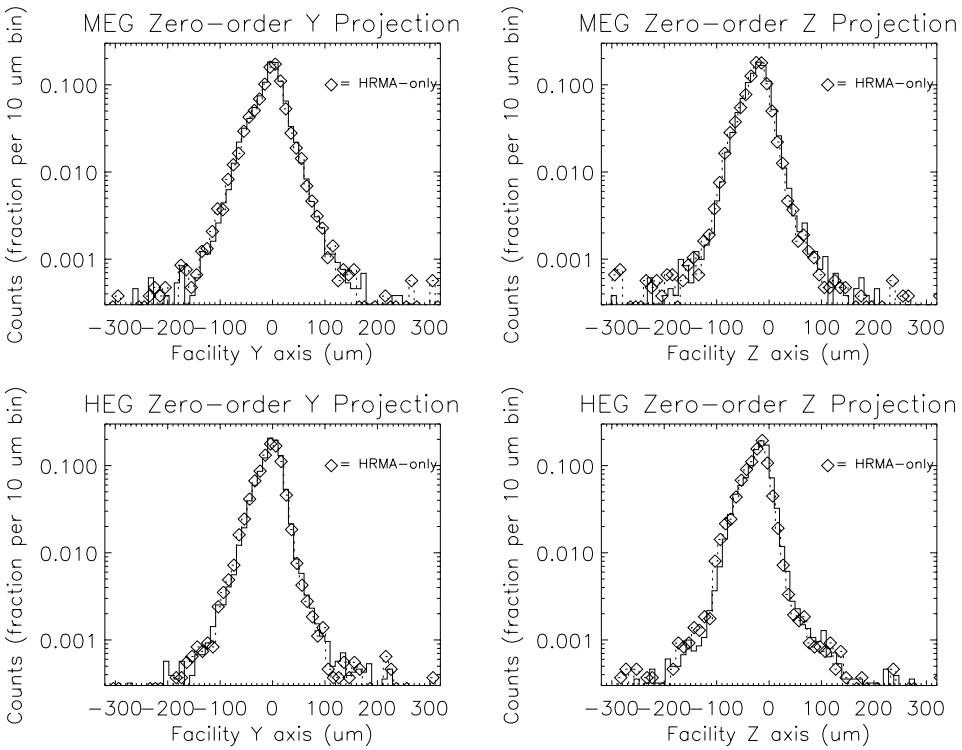

Figure 6.6: No MEG, HEG Zero-order effects. One-dimensional projections of the HSI images from the HRMA (diamonds) are compared with the coresponding zero-order grating-image projections (solid lines).

Table 6.2: HSI data sets for zero-order image comparisons.

Optic	TRW ID	Date	run id(s)
MEG	D-HXH-SF-1.002	970103	107301,2,3,4
HEG	D-HXH-SF-1.003	970103	107310,11,12,13
Shell 1	D-IXH-PI-3.004	970104	107546
Shell 3	D-IXH-PI-3.005	970104	107547
Shell 4	D-IXH-PI-3.006	970104	107548
Shell 6	D-IXH-PI-3.007	970104	107549

6.3.2 Focus tests

The focus tests (Focus Check FC and Shutter Focus SF) were performed by cycling through the quadrants of the mirror. When examining the 0th order, the inner shells were closed for images of the MEG 0th order and opened (while closing the outer shell pair) for the HEG 0th order measurement. The displacement of the image centroids gave an estimate of the detector defocus using a simple thin lens approximation and the knowledge that the detector was already placed within 0.5 mm of the desired focus position. The insertion of gratings was not expected to have an effect on detector focus location, and this was observed to the measurement accuracy of about 25 microns. Furthermore, once the fixed offset of about 180 microns was corrected, an additional defocus measurement gave an answer consistent with zero defocus error. All 0th order images were shaped as bowties or hourglasses, depending on the set of open shutters, as expected, due to mirror scattering, which redistributes photons preferentially perpendicular to the scattering surface.

Higher order images were examined in order to verify the placement of the gratings and detectors on the Rowland circle. The detector was offset by the amount appropriate to the Rowland circle and a shutter focus was performed. It was in such a test, D-HXH-FC-1.010, that the MEG mis-aligned gratings were discovered, Section 6.4.

Data from D-HXH-FC-1.010, Figure 1.8, were crudely analyzed to obtain $E/dE \approx 978$ for a Gaussian fit to the LRF core. In the cross-dispersion direction a value of $\gamma = 2$ arc minutes was determined (including astigmatism contributions.) Because of HSI angular QE variations and possible small scale position nonuniformity, the main PSF core data set is the 1D slit scans of the diffracted Mg-K line, below.

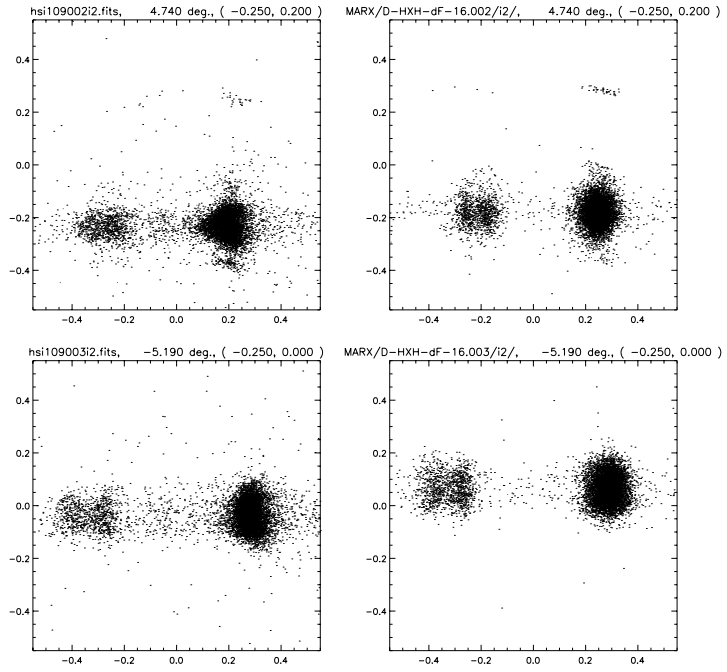

Figure 6.7: Mg-K HSI images: data and **MARX** . The left plots show the Mg-K line as observed with the HSI in MEG +3 and HEG +2 orders. The plots at right are **MARX** simulations as described in the text.

6.3.3 1D Scans of Mg-K LRF

The direct approach to resolution measurement would be to use an X-ray source with an intrinsically narrow line at low energy. The best candidate emission line for this function was the Mg-Kα line at 1.254 keV. Lower energy K lines have resolvable natural line widths (e.g. O-K or C-K) and the L lines (of Ti, Fe, and Ni, for example) were generally much weaker and substantially more complex. Because the grating-induced effects are more visible at low energies (high dispersion) we used the approach of observing the Mg-K line at high order. Using a set of slits, the HEG+1, HEG+2, MEG+1, and MEG+3 Mg-K images were scanned directly ("PSF/1D" measurement) to measure the LRF and the cross-dispersion profile. These set of measurements are summarized in Table 6.3. Figure 6.7 shows measured and simulated HSI images of the Mg-K

Table 6.3: Mg-K PSF/1D slit scan measurements summary. The TRW ID for these measurements is of the form: D-HXF-P1-19.0NN. Each run id tabulated consisted of many iterations as the slit was stepped across the image. Analysis of the raw pha data was carried out by Pete Ratzlaff and Jeremy Drake of the ASC using XSPEC fitting methods.

grating	aperture	m=0	m=+1	m=+2(+3)	Notes
HEG	10x200v+5	109056	109057	109058	Figures 6.8 and 6.11
"	80x500v	109064	109065	109066	
MEG	10x200v-5	109061	109062	109063	Figures 6.9 and 6.11
"	80x500v	109068	109069	109070	
HEG	10x200h	109078	109079	109080	Figure 6.10
MEG	10x200h	109072	109076	109075	Figure 6.10

line in high-order; it is these lines that are being scanned with the FPC. Figures 6.8 and 6.9 show examples of the dispersion-direction 10 μm slit data and simple fits to them for the HEG and MEG diffracted orders.

A variety of effects go into the diffracted image formation and so in order to evaluate any one effect it is best to include all of them. This is carried out by using a detailed **MARX** simulation and then comparing the simulated 1-D projections with the measured 1-D projections. This has been carried out with manual supervision and a fit criteria based on "by-eye" agreement of the measured and modeled LRFs. The resulting parameters produce simulations which do agree reasonably with the measurements, *e.g.*, Figure 6.7. In this simulation the simulated HSI does not include additional PSF blur nor the angular dependance of the QE, these are likely contributors to the differences seen.

More detailed comparisons of the simulated and measured PSF/1D slit scan data are shown in Figures 6.10 and 6.11. To emphasize the core behavior of the LRF these plots show the normalized cummulative fraction, that is the integral of the LRF. The **MARX** simulations were adapted for XRCF use as described in Section 2.3.1. The specific parameters which were then "tuned" to get model-data agreement are briefly discussed in the following paragraphs.

Cross-Dispersion Direction. The key parameter here is the grating rms roll value. In order to include explicitly the MEG mis-aligned gratings **MARX** uses "sector" files which allow the specification of grating alignment and period parameters for certain regions (sectors) of each of the four shells. The agreement seen in Figure 6.10 for the cross-dispersion scans is very good. For the MEG the mis-aligned gratings are explicitly included and the rest of the gratings roll rms is modeled as the sum of two gaussian distributions centered at +1 and -1 arc minute w.r.t. the nominal axis and each with an rms value of 1.5 arc minutes. For the HEG a more pronounced bi-gaussian distribution is observed and modeled: the gaussians are offset by -1.35 and +1.65 arc minutes, each with 1 arc minute rms, and in a relative ratio of 55:45. The IDL procedure `xrcf/make_facet_tables.pro` uses these values to create a appropriate sector file values.

Dispersion Direction. The dispersion direction LRF depends not only on the grating dp/p value but the characteristics of the X-ray line istelf. There is reasonable agreement seen in Figure 6.11 however this required some adjustments. The Project Science web page gives the Mg-K line a width of 1.1 eV, that is $E/dE = \approx 1100$. The simulations here used $E/dE = 1800$ in order to get the simulated HEG +3 line width narrow enough with an HEG dp/p value of 146 ppm. The MEG +2 simulated line was too narrow and so the MEG dp/p value has been increased to 235 ppm to get the agreement shown. Both of these results are sensitive to the precise focus conditions and so may be refined after a more systematic defocus study. Because the HEG and MEG dispersion direction scans are carried out with different slits there can also be a focus offset between the two data sets in addition to the know FOA translation offset.

In order to improve this analysis we could: (i) use SAOsac XRCF rays as the **MARX** input colored by a realistic spectrum, and (ii) systematically explore the effects of defocus noting differences in focus are possible for the HEG and MEG dispersion scan data sets due to the use of different slits.

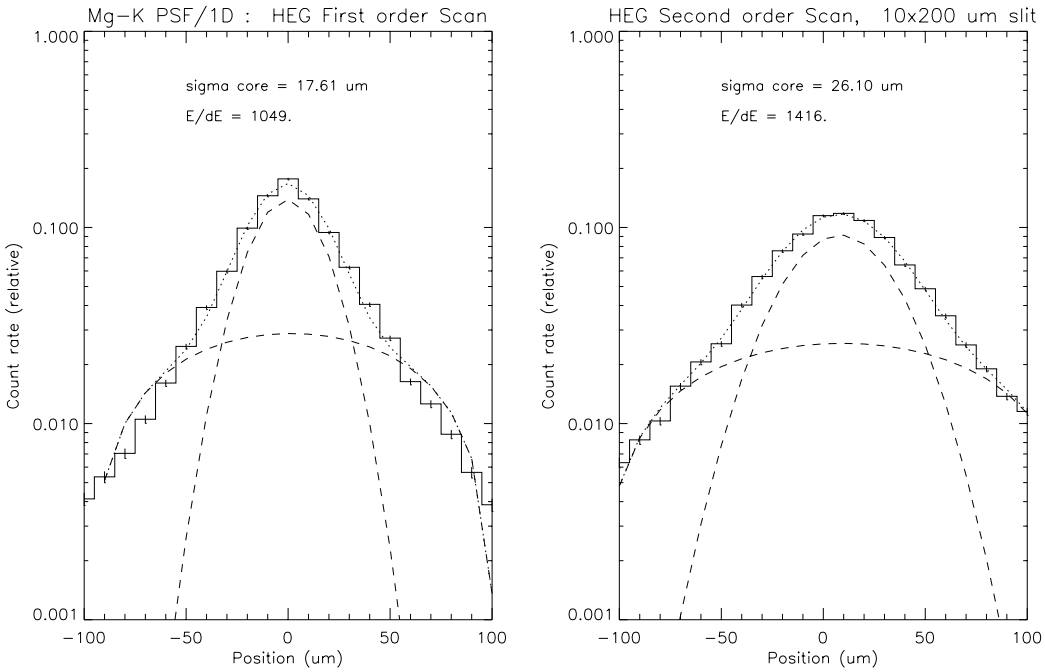

Figure 6.8: Slit scans with the FPC across Mg-K HEG 1st and 2nd orders. Gaussian approximations to the cores indicate high resolving powers are being achieved.

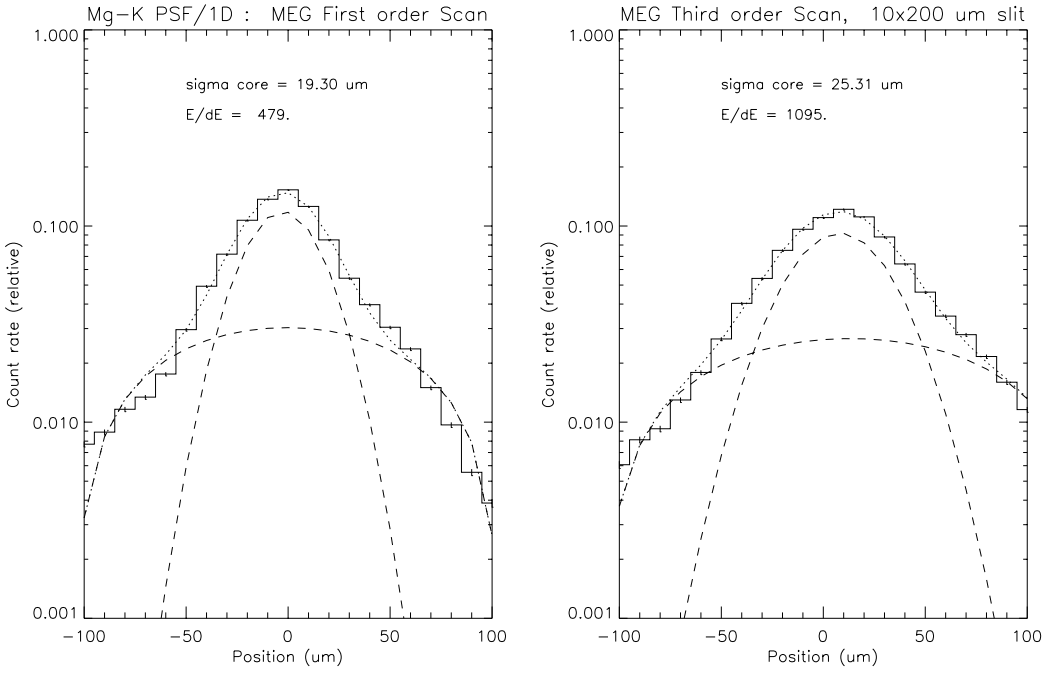

Figure 6.9: Slit scans with the FPC across Mg-K MEG 1st and 3rd orders. Gaussian approximations to the cores indicate high resolving powers are being achieved.

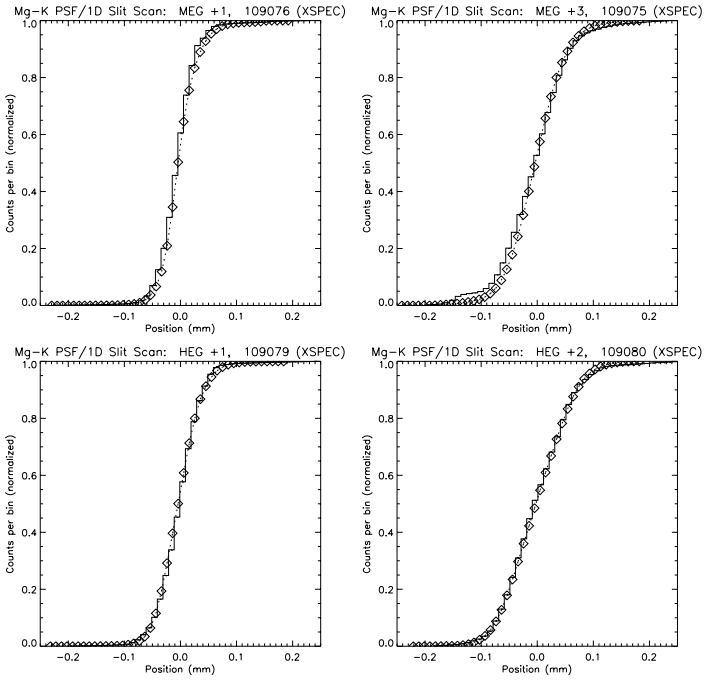

Figure 6.10: Mg-K cross-dispersion scans: data and **MARX** . Tuning of the **MARX** sector files provides good cross-dispersion agreement.

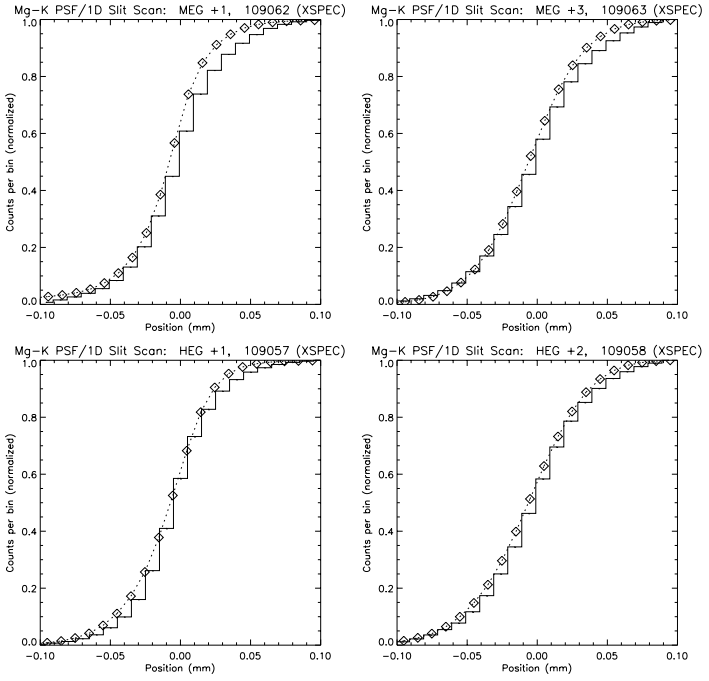

Figure 6.11: Mg-K dispersion scans: data and **MARX** . The Mg-K line is modeled as a gaussian with $E/dE = 1800$, the HEG dp/p is 149 ppm and the MEG dp/p is 235 ppm.

6.3.4 LRF Measurements with the Flight Detectors

As detailed in Tables 5.6, 5.7, and 7.5, there were only a few on-axis, in-focus data sets taken in the HRMA-HETG-Flight_detector configurations. These are explicitly listed in Table 6.4.

Table 6.4: LRF data sets with the flight detectors.

Detector	TRW ID	Source	Notes
ACIS-S	H-HAS-SF-1.001	Al-K	
ACIS-S	H-HAS-SF-1.003	”	
ACIS-S	H-HAS-SF-18.001	”	
HRC-I	G-HHI-FC-1.003	Mg-K	

6.3.5 Results

The E/dE measurements made so far are tabulated in Table 6.5 and plotted in Figure 6.12.

To-do:
Create XRCF E/dE predictions ($m = 1, 2, 3$) for comparison with results.
Analyze all data available
Remove HRMA effects to determine grating-only contribution

Data Set	Grating	Energy	Order	E/dE	dp/p rms limit
FC (Fig.1.8)	MEG	1.486	3	978.	$<$ 435. ppm
1D scan	HEG	1.254	1	1049.	$<$ 405. ppm
1D scan	HEG	1.254	2	1418.	$<$ 300. ppm
1D scan	MEG	1.254	1	479.	$<$ 888. ppm
1D scan	MEG	1.254	3	1095.	$<$ 389. ppm
MARX	MEG	-	-	-	235 ppm
MARX	HEG	-	-	-	146 ppm

Table 6.5: Results of some XRCF LRF core measurements. The as-operating E/dE values produce upper limits on grating dp/p values. The best-model **MARX** parameters from PSF/1D data are shown as well.

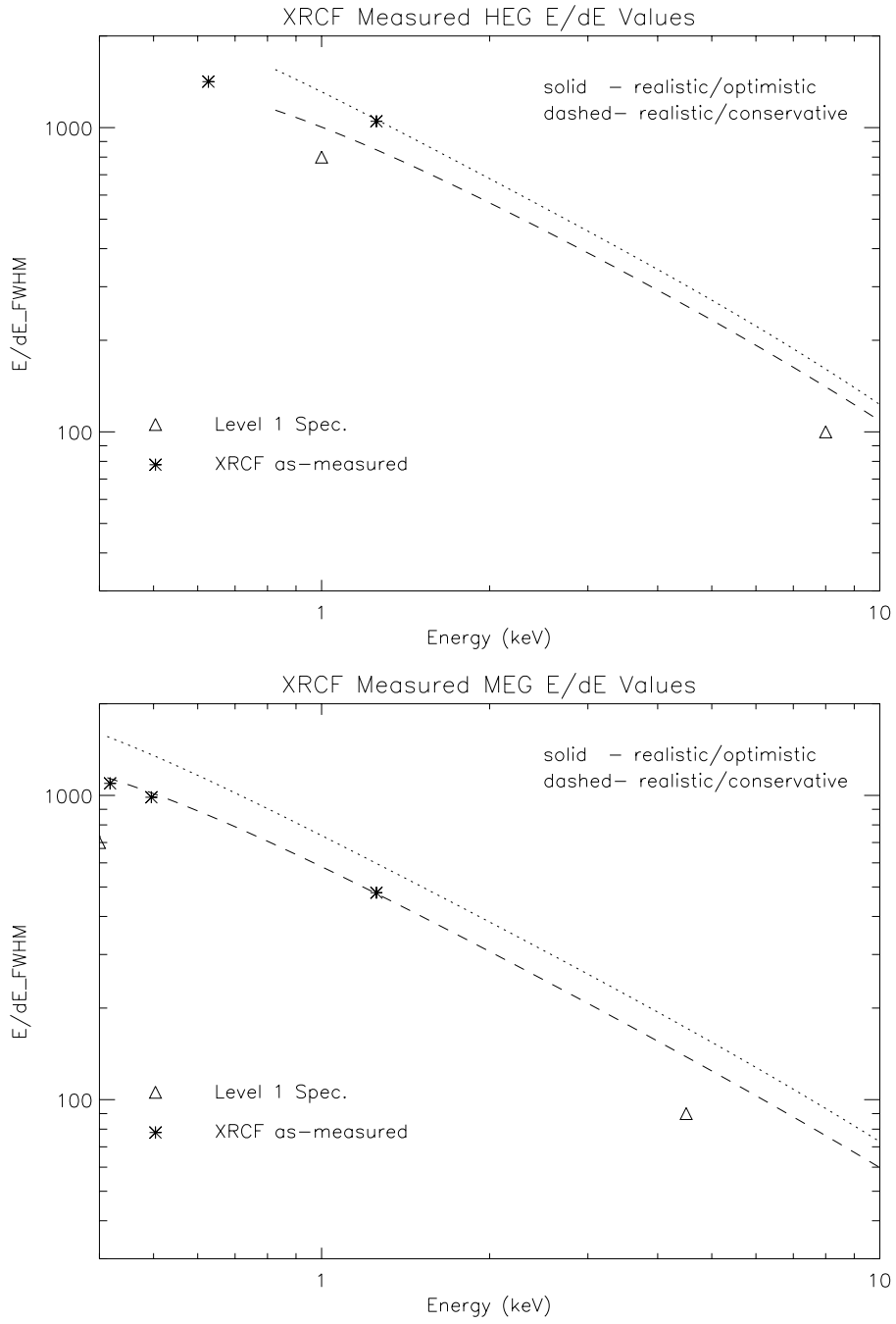

Figure 6.12: XRCF E/dE Measurements. Resolving Power for the HRMA-HEG and HRMA-MEG as measured at XRCF during Phase I. The E/dE values(*) are from Table 6.5 and the high-order points are plotted at an energy of E/m.
Various flight error budget curves are plotted for reference only (see Figure 2.3 for their details.)

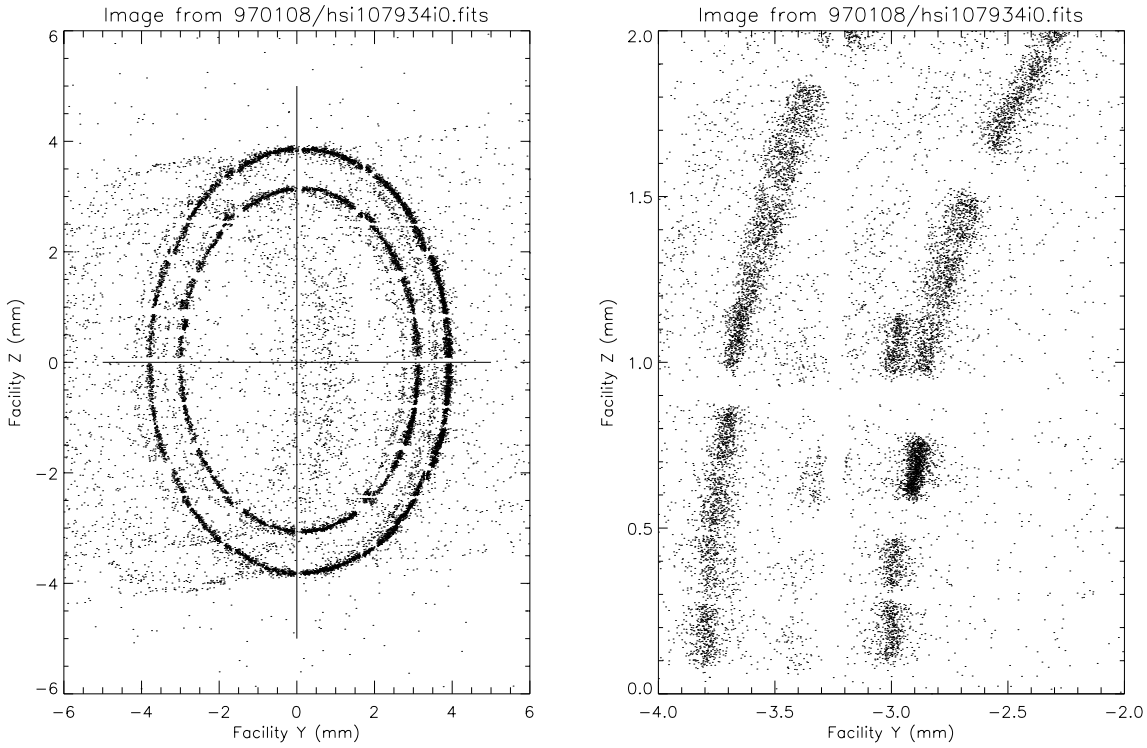

Figure 6.13: Defocussed HSI image of the MEG Al-K 3rd order, measurement D-HXH-AL-27.001. Individual grating facets are visible in this image of the two MEG rings of gratings. An Al-K satellite line, Al-Kβ, and O-K lines are visible as weaker features. At right a blowup shows mis-aligned facets by the doubling up of the facet images near the center. In these unprocessed HSI image the uncorrected HSI "gaps" are visible.

6.4 MEG Mis-Aligned Gratings

Objective: Identify the grating facets responsible for the cross-dispersion outlier images and measure their parameters for inclusion in the instrument model.

Surprisingly, the images of MEG Al-Kα in third order showed several additional images at the same dispersion distance as the Al-Kα line, these are the weak features at +400 and -100 in HSI Z seen in Figure 1.8. Using the images from single quadrants of focus check measurements, four such features were initially discovered. The features individually were 2-6% of the power in the quadrant image. Several of the images were displaced in the cross-dispersion direction by 120 microns and a fourth deviated by almost 400 microns, corresponding to rotations of the dispersion direction by 7 arc minutes and 24 arc minutes, respectively. Such large rotations were not expected, based on subassembly measurements (*e.g.*, Figure 4.16).

A variety of tests and analyses were carried out in order to confirm the mis-aligned gratings hypothesis, identify the specific mis-aligned gratings, and accurately measure the deviations in order to model the effect. A total of six "mis-aligned MEGs" are now explicitly included in **MARX** version 2.20 using the parameters derived below.

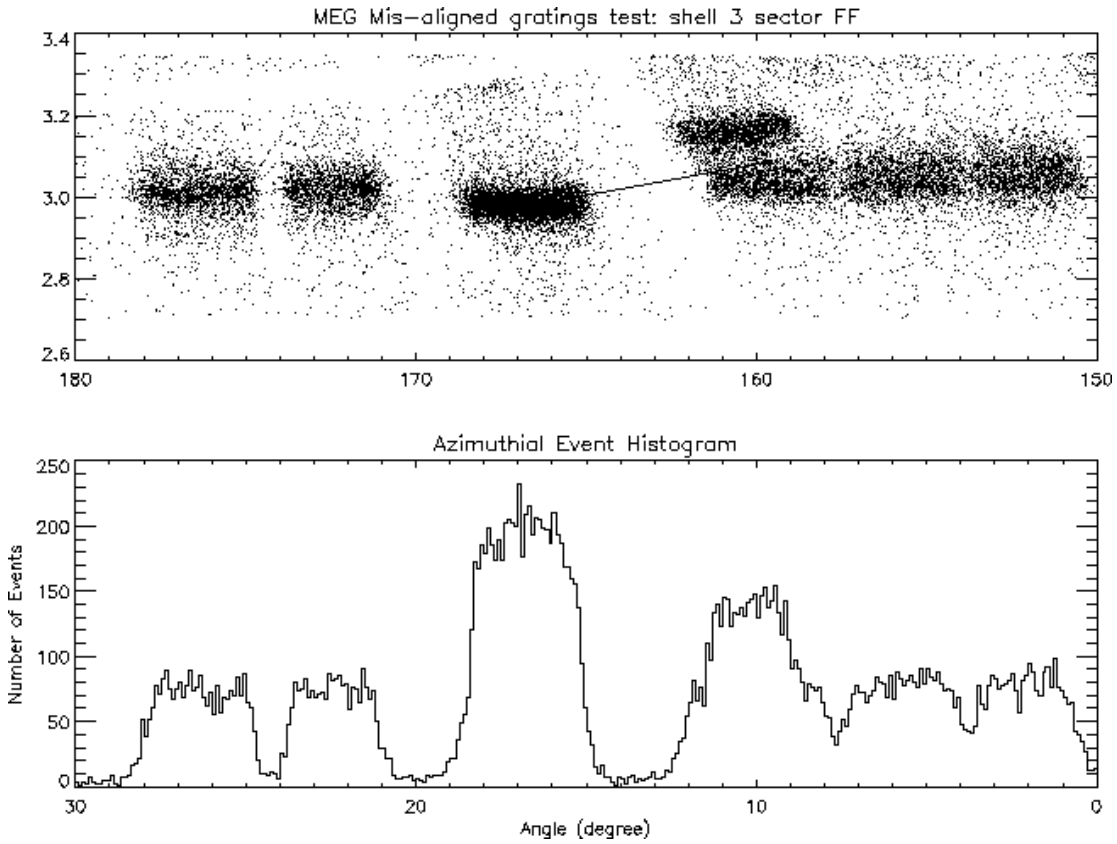

Figure 6.14: Shell 3 sector FF Events plotted in radial vs. azimuthal coordinates (top) and event histogram (bottom). The 7 gratings in shell 3 sector FF are numbered 1 through 7 from right to left. The grating in location 3FF4, bright in 3rd order, is rotated such that its image has moved left. The grating in location 3FF5 has rotated in the other direction by 23 arc minutes to almost the location of 3FF3.
In memory of Tom, grating 3FF1, its diffracted events visible on the right, is inscribed with "Thomas H. Markert" instead of a grating ID.

6.4.1 Mis-aligned grating identification

A defocussed image of the MEG +3 order Al-K line (Alignement test) reveals the individual facets, Figure 6.13. This is measurement D-HXH-AL-27.001, run id 107934, taken on 1/7/97 (logged as 1/8/97) with a defocus of 65.54 mm. A grating mis-aligned in roll will show up here by having its image shifted along the z' axis – this can be seen for the "400 μm offender" at around coordinates Y = -3 mm, Z = +1 mm where the regular set of grating images has a gap and a doubled facet. The 3rd order MEG Al-K is diffracted $\approx$ 55 mm in the dispersion direction, so a 30 arc minute grating roll results in a 0.48 mm z' shift.

The events in each sector (A through FF) of each shell (1 and 3) have been converted from facility Y, Z values into R, theta about the ring center, Figure 6.14. The events for each shell-sector can be viewed by plotting the appropriate angular range (0 degrees is along the +Y axis, south; positive angles are right-hand rule about X, e.g., towards +Z) and radial (shell) range. The gaps between facets are generally visible. In this theta-R space the cross-dispersion direction is indicated with an arrow of length 30 arc minutes of grating roll and pointing in the direction

Shell	Quadrant	$I_{\rm grat}/I_{\rm Ave.\ others}$ ($m=+3$)	roll (arc min.) (± 0.6)	HESS ID
1	Bottom, not visible	.	$\approx +3$	1E4
1	South	1.5 $\pm$0.2	-5.8	1F4
3	Top	0.6 $\pm$0.05	7.6	3EE2
3	North	3.1 $\pm$0.2	-8.7	3FF4
3	"	1.0 $\pm$0.05	+24.8	3FF5
3	Bottom	1.9 $\pm$0.2	+7.0	3E1

HESS ID	Grating	Lab ID	Fab ID	Al-K 3rd order	Al-K 1st order
1E4	ME1402	187	F07M010	1.5-1.8 %	15-18 %
1F4	MF1502	192	F07M017	1.4-1.6 %	18 %
Shell 1	All			1.59 %	16.3 %
3EE2	ME1411	189	F07M012	1.8-2.0 %	17-19%
3FF4	MD1312	201	F07M027	2.3-4.9 %	6.9-7.8 %
3FF5	MD1307	195	F07M020	1.3-1.6 %	15-17 %
3E1	ME1405	185	F07M008	1.5-1.7 %	18 %
Shell 3	All			1.54 %	15.9 %

Table 6.6: Mis-aligned MEGs. *Upper table*: Information on the identified misaligned gratings and their location on the HESS. These six gratings were detected by analysis of the defocussed image, as in Figure 6.14. Five of the six gratings can be seen in the MEG +3 Focus Check images taken by shell and quadrant; these images were analyzed to obtain the roll angles and intensity ratios shown. The grating at location 1E4 has too small a roll to be measured in the focussed images.
Lower table: Information on the specific grating facets mounted at these HESS locations. In particular the X-GEF predicted efficiency at Al-K in first and third orders is given. The shell averaged Al-K 1$^{\rm st}$ and 3$^{\rm rd}$ order efficiencies for the these shells are also given for reference.

of "unscrewing" (+ righthand about +X). A histogram of counts vs theta helps identify the gratings, gaps, etc. The orientation of these plots is as if standing in the center of the HESS HRMA-side looking radially out towards the sector: grating 1 of the sector is to the right and grating 7 (or 9) is to the left (larger angles.)

By analyzing each shell and sector in this complete image 6 MEG gratings were found to be mis-aligned by 3 to 24 arc minutes, Table 6.6. Note that all of these gratings are from fabrication Lot F07M. In fact these are 6 of the (only) 11 lot F07M gratings that are on the flight unit. The other five are installed in HESS locations 3EE3, 1FF5, 1F1, 3F5, 3F2 and do not appear to be measureably mis-aligned. Further lab tests have confirmed that fabrication irregularities produced excess stress gradients in the grating polyimide support structure leading to inaccurate polarization alignment measurement values.

6.4.2 Mis-aligned grating angles

Both the initial discovery and subsequent quantification of the mis-aligned MEGs were done using high-order (MEG=+3, HEG=+2) Focus Check measurements at XRCF. These measurements are listed in Table 6.7. An important aspect of these measurements is the ability of the shutters at XRCF to isolate a single shell-quadrant of the optical system. In this way the mis-aligned gratings can be localized on the HETG as well as intensity-enhanced relative to the other gratings in the image.

Grating-Order	Shutters	TRW ID	Date code	run id(s)	Notes
MEG +3	MEG,SCAN	D-HXH-FC-1.010	970104	107463-6	Figure 1.8
HEG +2	HEG,SCAN	D-HXH-FC-1.011	970104	107467-70	
MEG +3	1,SCAN	D-HXH-FC-28.001	970109	108026-29	Figure 6.15
MEG +3	3,SCAN	D-HXH-FC-28.002	970109	108030-33	Figure 6.16
MEG +3	ALL,ALL	D-HXH-FC-28.003	970109	108034	
MEG -3	ALL,ALL	D-HXH-FC-28.004	970109	108035	
MEG +3	1,SCAN	E-HXH-FC-28.001	970205	111316-9	
MEG +3	3,SCAN	E-HXH-FC-28.002	970208	111488-91	
HEG +2	4,SCAN	E-HXH-FC-28.005	970208	111492,4,5,6	
HEG +2	6,SCAN	E-HXH-FC-28.006	970208	111497-500	

Table 6.7: MEG and HEG High-order Focus Checks w/HSI.

Figures 6.15 and 6.16 show the MEG +3 order quadrant images for shell 1 and 3 from XRCF tests D-HXH-FC-28.001 and 'FC-28.002. In the spot diagrams the dispersion axis has been aligned with the plot X-axis with higher dispersion to the right, *i.e.*, higher energies to the left where the satellite line is visible. The image shape varies from quadrant to quadrant due to the scattering properties of the HRMA as modified by the angular dependance of the HSI QE. The mis-aligned gratings create distinct images that are slightly elongated due to HRMA scattering in the local plane of reflection.

Histograms of the z' value of the detected events are also formed and shown in the figures. These histograms are fit with one to three gaussians in order to measure the locations of the mis-aligned images with respect to the main quadrant image. These offsets were converted to an angular roll offset and are presented in Table 6.6.

The ratio of the mis-aligned image intensity to that of the main image would be 1:26 and 1:20 for quadrants in shells 1 and 3 if all gratings had the same $3^{\rm rd}$ order diffraction efficiency; in fact they do not as indicated by the $I_{\rm grat}/I_{\rm Ave.\ others}$ ratio in Table 6.6. For example, the grating in location 3FF4 show 3.1 times this expected intensity – most likely due to the gratings higher $3^{\rm rd}$ order efficiency.

Note that these data sets are taken with the HSI which displays a marked QE angular dependence. Likewise the exact defocus condition of the images is in some question. With these caveats the results presented here are probably reasonably accurate. Further refinement can be carried out by (i) including the HSI QE variations in a **MARX** simulation, (ii) using SAOsac XRCF rays as the **MARX** input colored by a realistic spectrum, and (iii) varying the defocus to get the best simulation-data agreement. Finally the mis-aligned grating angles can then be adjusted for best fit.

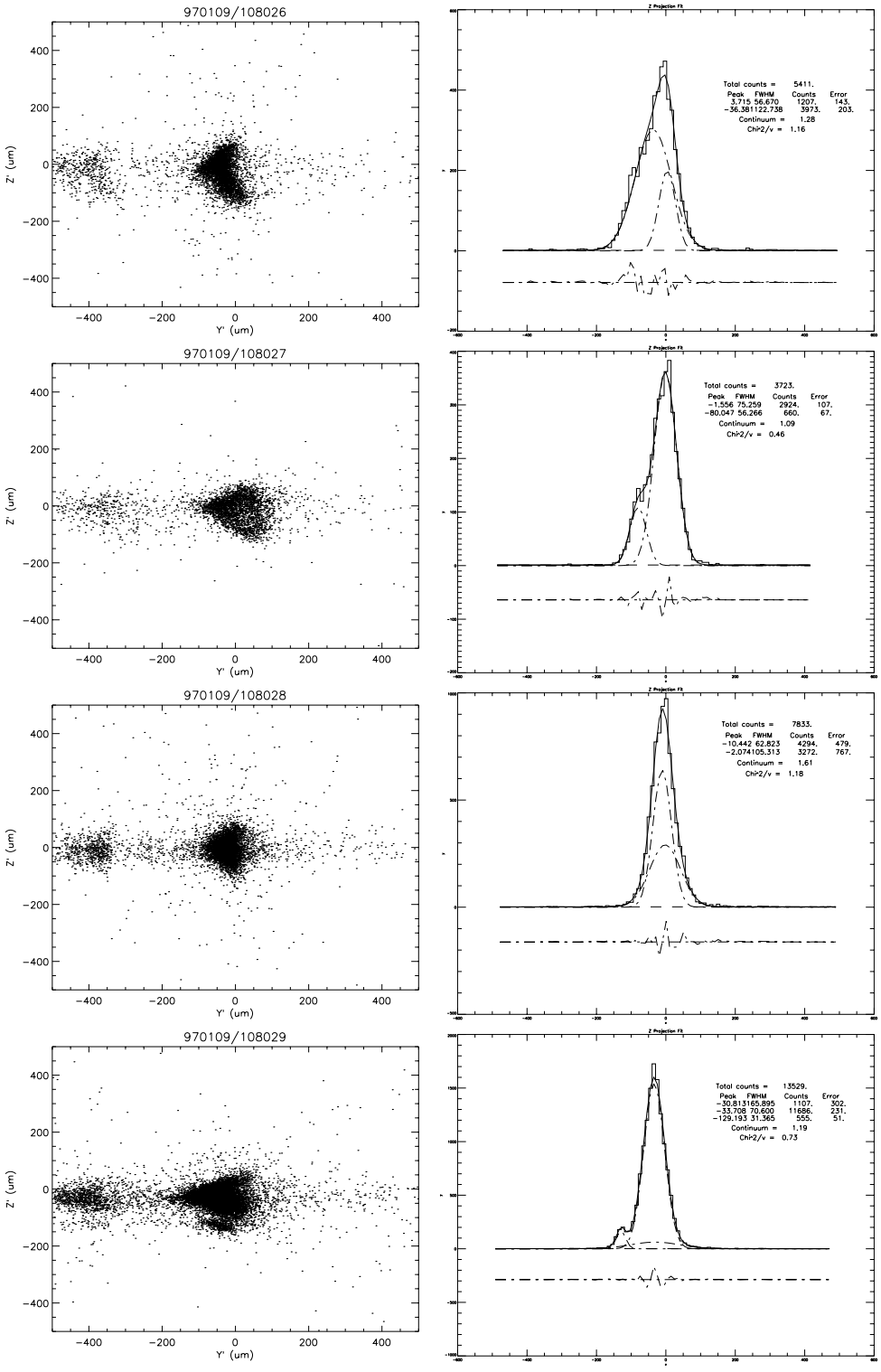

Figure 6.15: D-HXH-FC-28.001: Shell 1 MEG +3 order quadrant images; the quadrants are Top, North, Bottom, South from top to bottom. Only one mis-aligned grating appears on shell 1: at HESS location 1F4 in the South quadrant. See the text for further explanation.

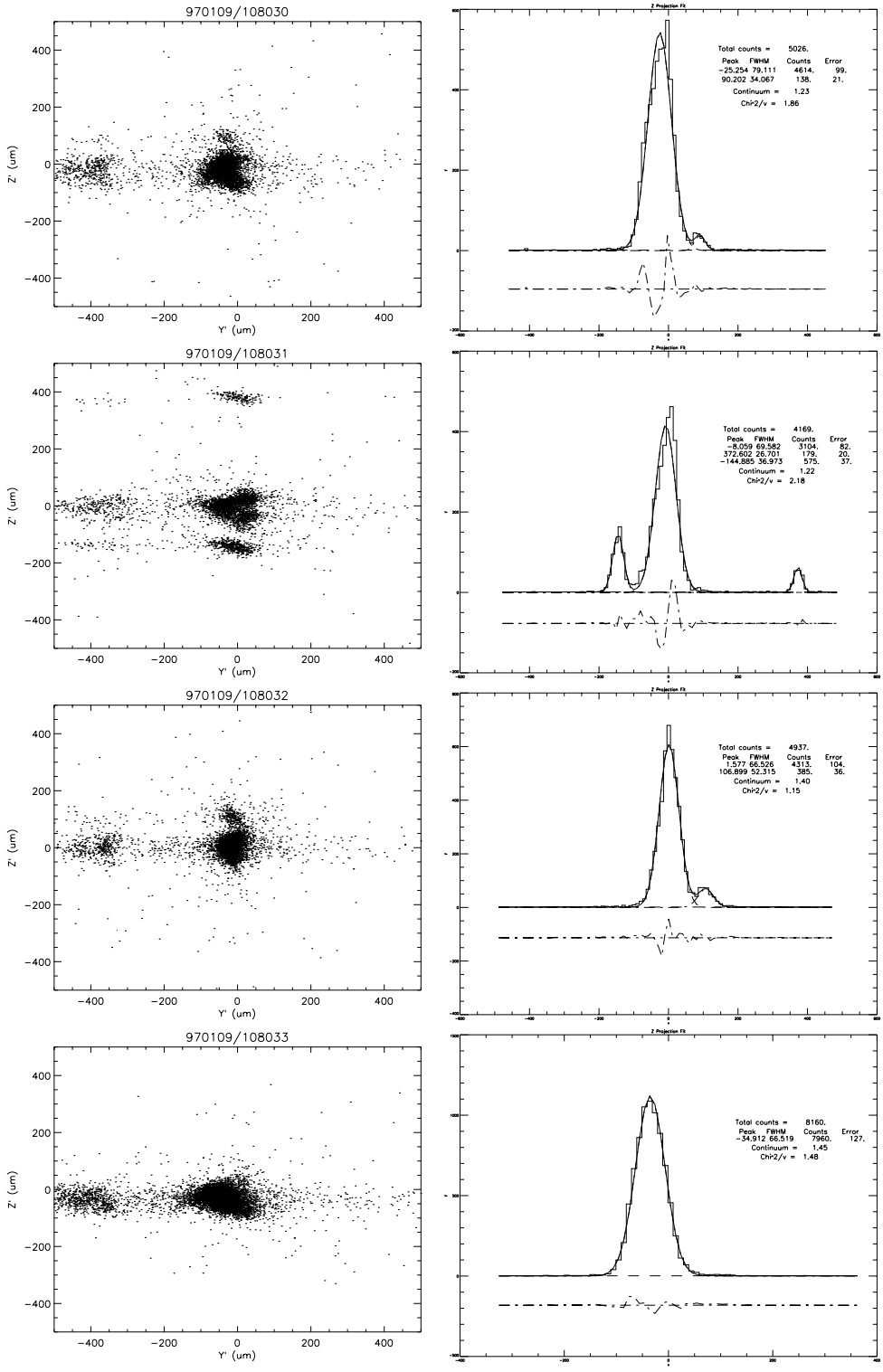

Figure 6.16: D-HXH-FC-28.002: Shell 3 MEG +3 order quadrant images; the quadrants are Top, North, Bottom, South from top to bottom. Four mis-aligned gratings appear on shell 3: one in the Top quadrant (3EE2), two in the North quadrant (3FF4, 3FF5), and one in the Bottom quadrant(3E1). See the text for further explanation.

6.5 "Wings": Between Core and Scatter

Objective: Determine the detailed structure of the grating effects on the PSF in the region between the LRF core and the scatter region. If necessary modify the LRF model to include this line structure.

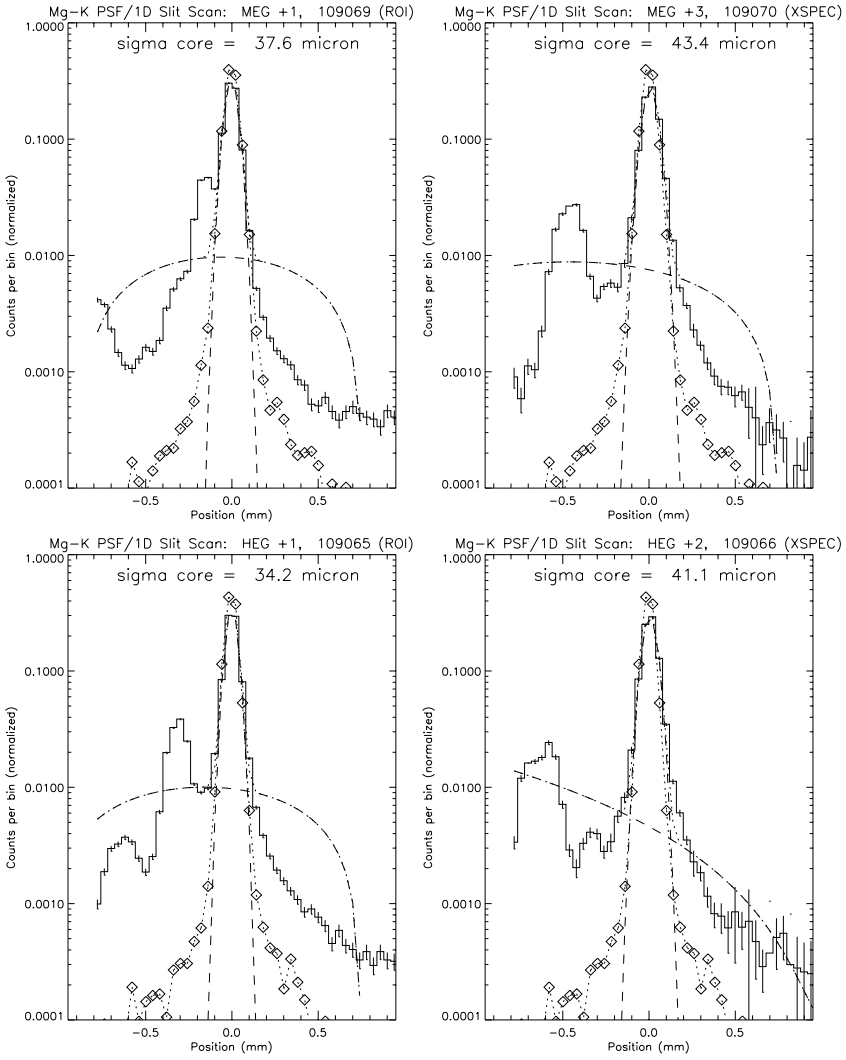

Figure 6.17: MEG and HEG Mg-K PSF/1D wing scans. The FPC with an 80 micron wide slit was scanned across the MEG and HEG diffracted orders of the Mg-K line the "80x500v" entries in Table 6.3. The resulting data are shown by the solid histograms with one sigma errors. The zero-order was likewise scanned and is shown for comparison by the diamond symbols and dotted line. The Mg-K satellite line is seen at the high energy (left) side of the line and excess (above zero-order) counts are seen in the LRF to the low energy (right) side of the main line. More research is needed to determine if these events represent the actual source spectrum or if they are an LRF effect of the gratings themselves.

An upper limit to the HETG-added LRF wings comes from XRCF wide-slit scans of the Mg-K line, where an 80 μm by 500 μm slit was scanned across the zeroth, first, and a higher order image for both the HEG and MEG grating sets.

It is useful to define a quantitative measure for the amplitude of the wing relative to the core which can be applied to both zeroth-order and dispersed data. The LRF is specified by a function $L(\lambda)$ which gives the "spectral density" in, say, "counts/Å" at each wavelength, λ. The core of this LRF is often reasonably fit by a Gaussian, let A_G be the area of that core-fitting Gaussian, and λ_0 its centroid.

In a region several FWHM from the core the LRF *in this region* may often be reasonably fit by a Lorentzian. If A_L and W_L are the area and width of such a Lorentzian then in the wing region we have approximately:

$$L_w(\lambda) \approx \frac{A_L\ W_L}{2\pi\ \Delta\lambda^2} \tag{6.1}$$

where $\Delta\lambda = \lambda - \lambda_0$.

Note that only the product of the Lorentzian width and area appears in the above expression - the Lorentzian wing fit has essentially a single degree of freedom (if λ_0 is fixed from the Gaussian fit.) The relative level of the wings compared to the core can then be quantified by the parameter:

$$V_w = \frac{A_L\ W_L}{A_G\ 2\pi} \tag{6.2}$$

which is seen to have units of wavelength but is more illuminatingly described as "fraction per Å times Å^2" as suggested by its use in the equation: $L_w(\lambda) = A_G\ V_w\ \Delta\lambda^{-2}$. The value of V_w is used in the following to quantify the size of the LRF wing in a region relative to the core area for a variety of data sets; because these values are generally small the values below are given in units of %/Å $\times$ Å^2.

Corollary 1: The wing value defined above behaves in a simple way with diffraction order for the case where the contribution to the LRF is the same for all orders when expressed in "spatial coordinates", *e.g.*, the wings due to a mirror blur. Because the effective dispersion constant, *e.g.*, in mm/Å, is different for the different orders, the wing level value in higher-order, when measured in wavelength space, is reduced to $1/m$ of the first-order equivalent value. Of course, if the source itself has a wing in its spectrum, in "spectral coordinates", then the measured wing level in wavelength space will be the same in all diffracted orders.

Corollary 2: If a Lorentzian line shape, with parameters A_L and W_L, is convolved with a unit-area Gaussian, then the value of A_G measured for the resulting line shape will be very close to the Lorentzian area A_L. However in the wing region, several Gaussian FWHM's from the core, the convolution will have little effect on the shape. Then the wing level measured will be given simply by $V_w = W_L/2\pi$ and hence the Lorentzian linewidth, W_L can be determined from the measured wing value.

At XRCF the Mg-K 1.254 keV (9.887 Å) PSF was scanned in 40 μm steps by an 80 μm x 500 μm (CD width) slit for mirror shell sets $1 + 3$ and $4 + 6$ separately. These scan data were broken into two 80 μm spaced data sets, offset by 40 μm from each other, and simultaneously fit in ISIS for a Gaussian in the core and Lorentzian in the wings, Figure 6.18; the wing level parameter V_w is then calculated as described above.

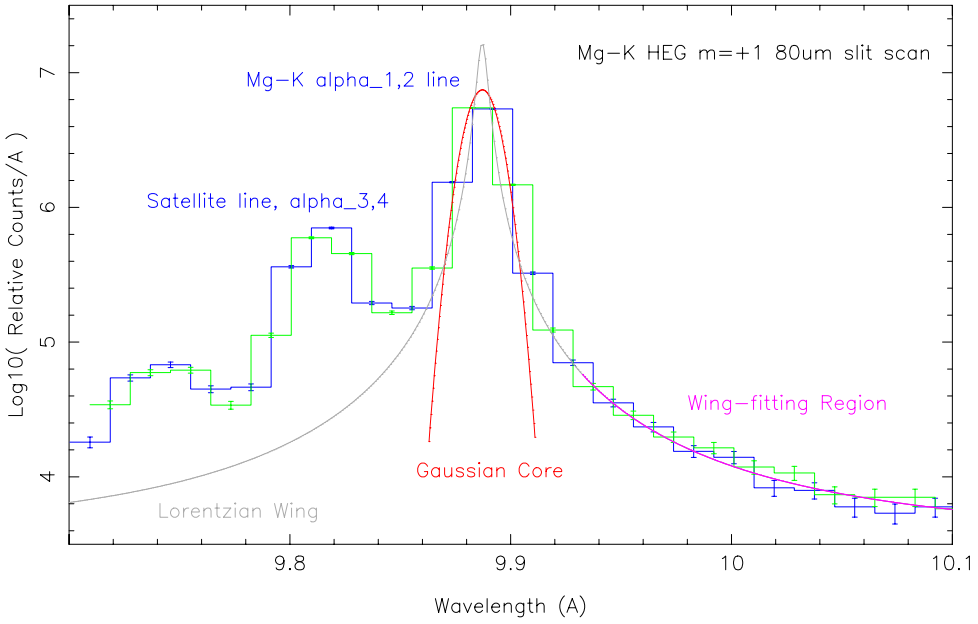

Figure 6.18: Line response function (LRF) wing measurement. At XRCF a focal-plane proportional counter with an 80 μm by 500 μm aperture was scanned across the dispersed Mg-K line image; two scans offset by 40 μm of the HEG $m = +1$ order are shown here. To measure the wing level, the core of the LRF is fit with a Gaussian and a region in the wings is fit with a Lorentian; a ratio of the fit parameters quantifies the wing level, please see the text for details. These wing measurements are then used to set limits on any HETG contribution to the LRF wings; for example, most of the wing seen here is due to the natural Lorentzian line shape of the Mg-K line and not the HETGS instrument.

The zeroth-order measured wing levels were translated to equivalent first order wavelength scales and give 0.020 and 0.045 %/Å $\times$ Å^2 for the HEG and MEG shell sets respectively in the 500 μm cross-dispersion width measured. Note that the HEG $m = 1$ scale is equivalent to the MEG scale with $m = 2$ and so by Corollary 1 the HEG value would be one half of the MEG value if the HEG mirror shells $(4 + 6)$ had the same level of scattering as the MEG shells $(1 + 3)$.

The Mg-K dispersed images were also scanned, *e.g.*, Figure 6.18, and the resulting wing level values are reasonably fit by a model which assumes contributions from a source-intrinsic wing level V_s and an instrumental wing contribution. The measured value of V_s is of order 0.06 %/Å $\times$ Å^2.

The Mg-K natural line shape is expected to be Lorentzian [2]. Using Corollary 2 the measured wing value of the Mg-K line, ≈ 0.06 used to estimate the natural Lorentzian linewidth of the Mg-K line: $W_L = 2\pi \times 0.06 \times 10^{-2}$ Å $= 0.0038$ Å. The E/dE corresponding to this 0.0038 Å width for the 9.887 Å line is thus $E/dE = 2600$ which is consistent the lower limit previously estimated from the HEG LRF core scans of 1800. Hence, the measured source wings are mostly due to the natural line width and line shape of the Mg-K line.

At most the HETG is adding additional wing components to the LRF at a level of ≈ 0.020 %/Å $\times$ Å^2 at 1.254 keV.

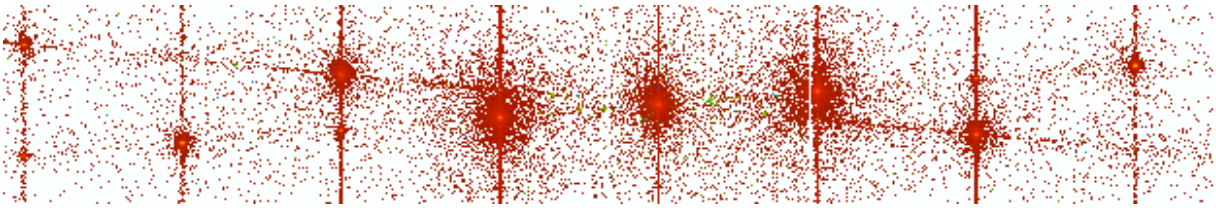

Figure 6.19: ACIS-S image from test H-HAS-SC-7.002. HEG scattered events are seen in this monochromatic exposure at XRCF. The XRCF Double Crystal Monochromator was tuned to the Tungsten 1.3835 keV line. HEG scattered events are clearly visible concentrated along the HEG dispersion direction on either side of the HEG first-order and near the one-half-order region. In contrast, the MEG shows no such events.

6.6 Scatter Tests

Objective: Measure or set upper limits on the wide-angle contribution of the grating to the LRF, *i.e.*, the "scatter". Investigate the energy dependance of the scatter and the ability to fit it with a model.

Publication(s): Davis *et al.* [21]

6.6.1 Scattering Data and Results Overview

This section describes the phenomenon, gives examples of and summarizes the data sets and presents the analysis results.

Several calibration tests were designed to probe the pattern of the scattering and its dependence on energy. The tests were performed at the AXAF X-ray Calibration Facility (XRCF)[98]. The double crystal monochromator (DCM) source was used to reduce spectral contributions far away from the central energy. For the first four tests, the DCM was tuned to an W-M emission line from the source. For the remaining tests, the DCM was scanned from 5 keV to 9 keV in 1 keV steps for 5 different data sets. The list of tests is shown in Table 6.8.

Figure 6.20 shows the scattering features observed at 1.775 keV as determined by the extensive Phase G tests. The fractional scattered light integrated over each of several half-order regions at different energies is shown graphically in Figure 6.22. More words about the behavior with energy, reference the scattering theory, and comment on how (if at all) it will be included in MARX/models.

To-do:
How and do we need to include scatter in our instrument model?

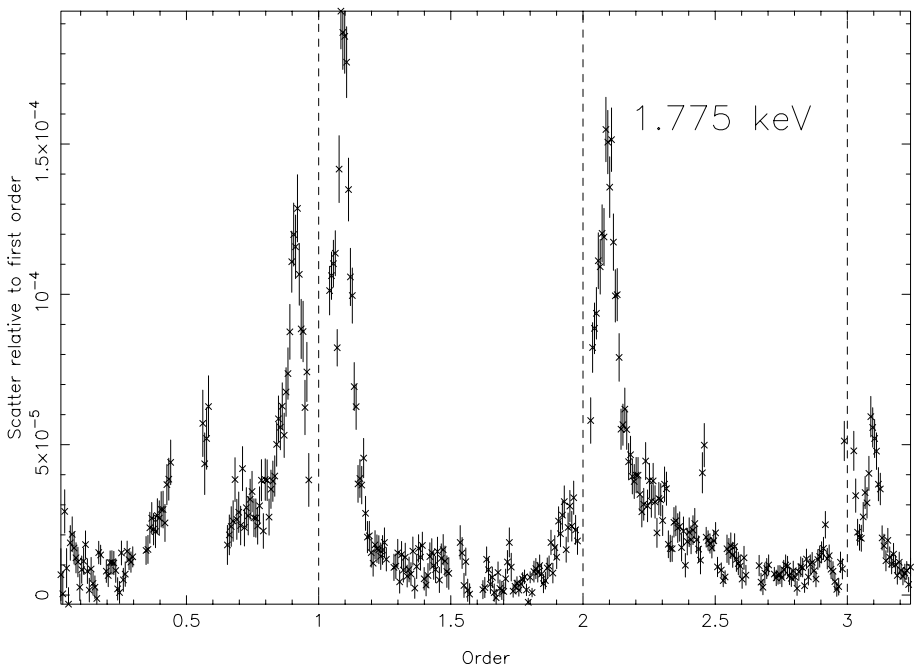

Figure 6.20: Measured HEG scatter at 1.775 keV. The HEG scattering-per-bin normalized to the counts expected in the first order is plotted as a function of diffraction location expressed as a non-integral diffraction order; the bin size here is 0.00716 orders. Note the strong scattering peaks immediately to the left and right of first order and near second and third orders. "Half-order" scattering also appears around $m = 0.5$.

TRW ID	Detector (Grating)	Energy(ies) (keV)
D-HXH-PO-13.002,4,6,8 (970121/hsi109761,3,5,6.fits) D-HXH-PO-13.001,3,5,7 (970121/hsi109754,5,7,8.fits)	HSI (HEG) HSI (MEG)	1.7754 1.7754
G-H2C-SC-88.00{1-5}	ACIS-2C0	1.7754
H-HAS-SC-7.001	ACIS-S	1.3835
H-HAS-SC-7.002	ACIS-S	1.3835
H-HAS-SC-7.003	ACIS-S	2.035
H-HAS-SC-7.004	ACIS-S	2.035
H-HAS-SC-7.005	ACIS-S	5.00, 6.00, 7.00, 8.00, 9.00
H-HAS-SC-17.006	ACIS-S	5.00, 6.00, 7.00, 8.00, 9.00

Table 6.8: Scattering tests used for data analysis. For an overview of AXAF calibration, see Weisskopf *et al.*[98].

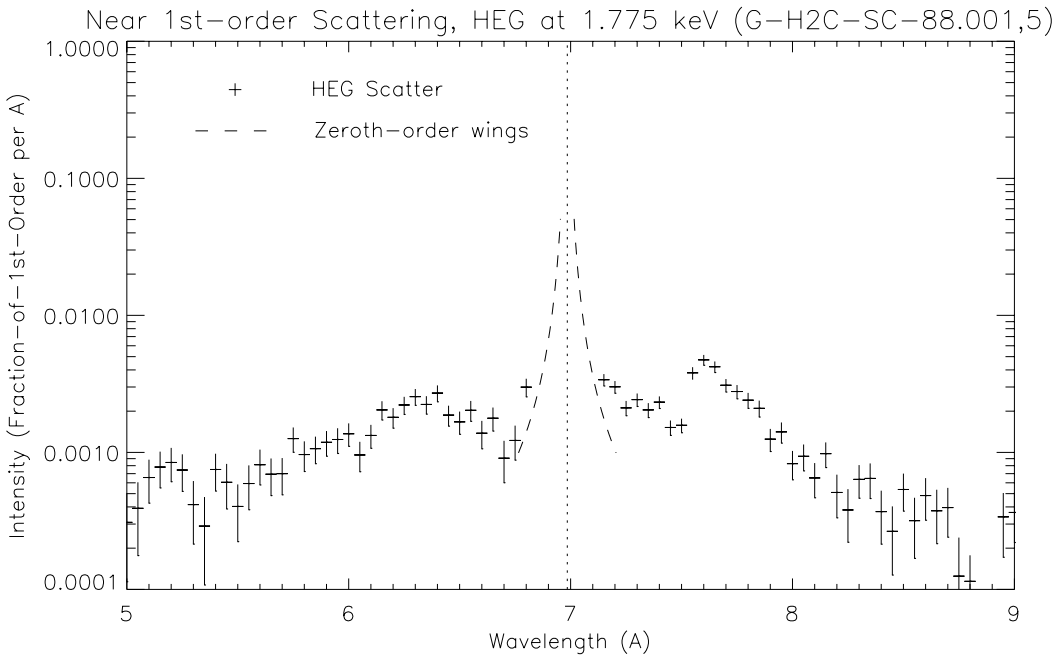

Figure 6.21: HEG Scatter and Wings. The low-level scatter in the HEG spectrum is shown here in the wavelength region within 30 % of the first order peak. Plotted on the same scale is the expected LRF wing level due to the mirror zeroth-order scatter in the 5 pixel wide cross-dispersion direction. Note that the measured scatter is above the LRF wings but is still small compared to the main LRF peak: generally contributing less than 0.01 % of the main response into a three FWHM wide region (0.036 Å). This near-to-first-order scatter is most relevant in practice as it will not be excluded by ACIS order selection.

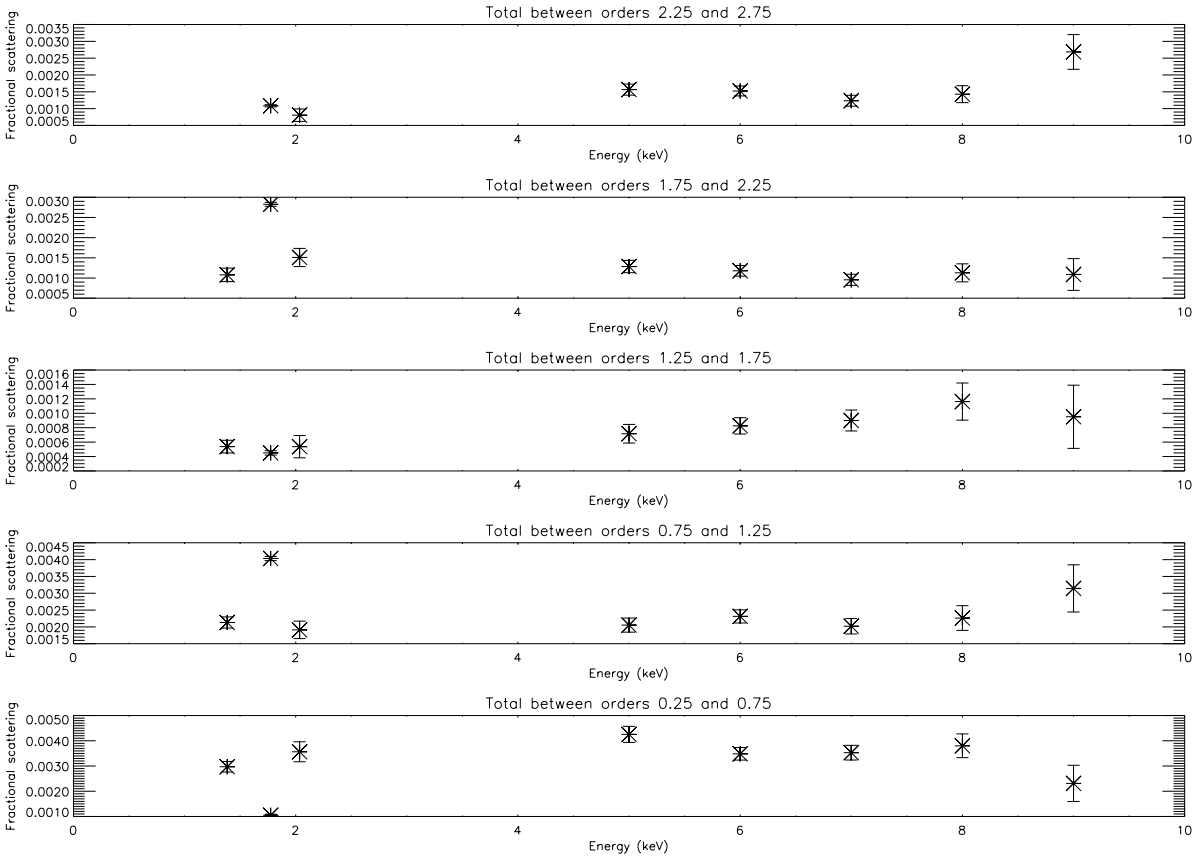

Figure 6.22: A summary of the results of the 1.775 keV scattering data analysis. The values are normalized to the total of the +1 and -1 order count rates. Due to the systematic errors in background subtraction, bad columns, etc., the fractional scattering at 0.5 order at 1.775 keV has been systematically underestimated – by as much as a factor of 2 or 3. Error estimates are due to statistical uncertainties only. Note that most scattering fractions are relatively independent of energy above 2.0 keV.

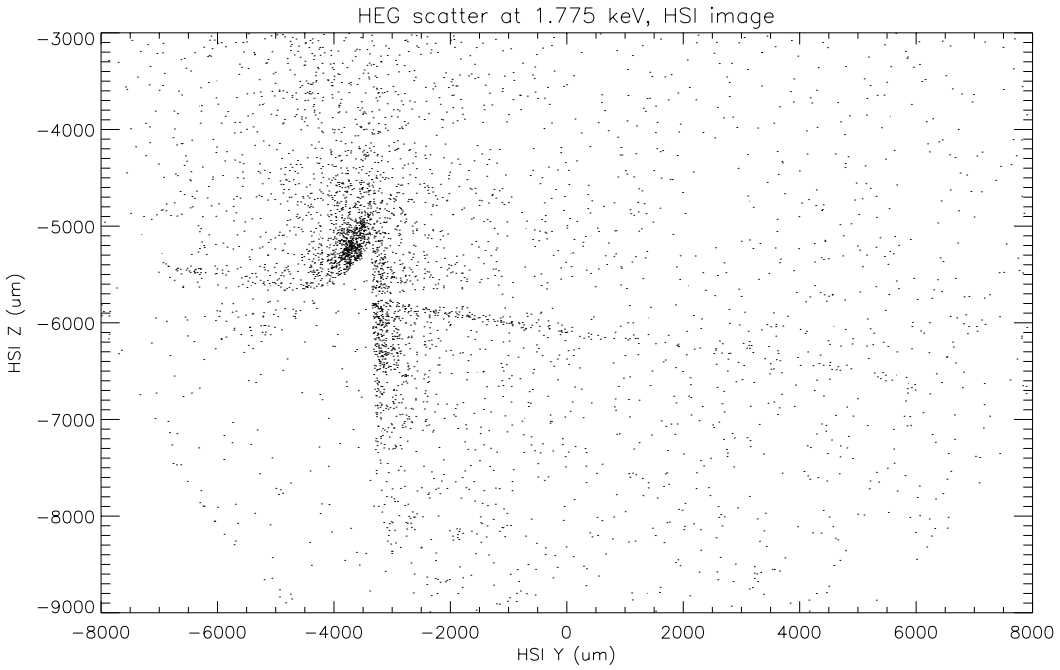

Figure 6.23: Phase I HEG scatter test. The core of the HSI image of the DCM monochromatic 1.775 keV line in HEG first order is blocked by the HSI cusp (triangular low-count region.) Extending from the cusp along the HEG dispersion axis are scattered 1.775 keV photons. Of order 0.4% of the line flux is scattered.

6.6.2 Phase I HSI Scattering Tests

A test series was developed to search for near line scattering wings (PSF/Outer, Scattering) that would be a concern when measuring absorption features near bright lines. The Double Crystal Monochromator (DCM) was tuned to the bright line W-Mα at 1.775 keV in the anode spectrum. The current was turned to the lowest possible value to get a count rate for the total line and then the current was turned to the highest possible value for the scattering test. The image was placed on a detector mask "cusp" in order to block the core of the image but allow photons beyond $E/100$ of the target line. Mirror scattering was expected but would be azimuthally symmetric, while grating line scatter was expected preferentially along the direction of dispersion, so would be distinguishable from mirror scattering. After a long integration at high current, a total of 100,000 counts would be obtained from the core of the line (without the blocking cusp), so the test could detect scattered power levels below 0.1% of peak.

The result, Figure 6.23, was somewhat surprising at the time: although there was no obvious evidence for power along the dispersion direction near the line, there were clearly significant events dispersed 1-10 mm from the line. In order to verify that the DCM had no significant spectral leakage that could cause the observed effect, we tuned the DCM off of the bright line by only 15 eV. The DCM resolution at 1.775 keV is about 5 eV, so very little power was expected and the current was turned up to its maximum setting. There were no events at the expected dispersion location of 1.775 keV, indicating that it had been suppressed at a level better than one part in 10^5. We concluded, therefore, that the gratings were incoherently diffracting a modest fraction of the line emission to large dispersion distances. This fraction was estimated at 0.4% over a 10 mm span.

Subsequent modelling and further tests indicated that minor bar location variations could cause an incoherent redistribution of monochromatic light. The grating-bar variations needed can be quite small, of order a few percent of the the distance between bars, Section 3.3.

To-do:
Create normalized scattering plot from HSI data and compare with '2C data (Figure 6.20) for normalization check.

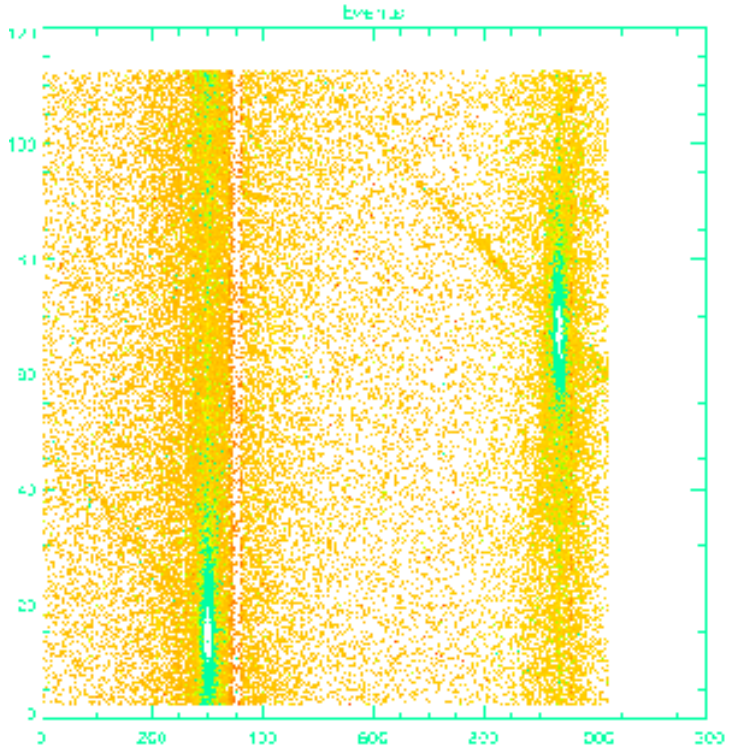

Figure 6.24: ACIS-2C event plot showing HEG scatter at 1.775 keV. The range shown is 114 rows tall by 1024 columns wide. Zero-order is off the chip to the left, MEG first order is on chip at left and HEG first order is on chip at right. The scattered light from the HEG is visible as the upper-left-to-lower-right diagonal streak through the HEG first order; this is the HEG dispersion direction. Due to the wrapping of the ACIS-2C readout mode used, this scattered light appears to go through the MEG first order. Note that the MEG produces no scattered light as there is no 'lower-left-to-upper-right' streak along the MEG dispersion direction.

6.6.3 ACIS-2C Scattering Tests: G-H2C-SC-88.00{1-5}

The W-Mα line at 1.7754 keV was the brightest line to which the DCM could be tuned. The shape of the scattering was investigated at this energy using a long integration and the highest DCM current. The test was performed using the backside illuminated CCD in the ACIS-2C[1] (chip 0), which is a non-flight AXAF detector developed specifically for ground testing and calibration. Five separate exposures of about 900 s each were obtained, shifting by 22 mm between exposures to span a dispersion distance similar to that of the flight detector. The CCD is about 24 mm across, so there was a 2 mm overlap between adjacent exposures. The pixel spacing of the detector was 0.024 mm, which was precisely measured during fabrication (M. Bautz, private communication). The CCD was operated in a "fast" mode where 114 rows of data were obtained every 0.66 s, in order to reduce pile-up near the dispersed orders. The frames are shifted downward by 114 rows after each exposure, so the dispersion lines are "wrapped". Event recognition was disabled for the final two rows (wrapped rows were not considered), so there are no events in these two rows (producing a gap that occasionally crosses the dispersion line).

[1] See `http://space.mit.edu/HETG/acis2c.html` for more details of the ACIS-2C detector

For this test, the HETG was used in combination with the DCM set to the bright W Mα line at 1.775 keV, and the HRMA with all shells open. The detector is the backside illuminated chip (ID 0, detname was "w148c4") in the ACIS-2C detector. The detector was run in 114 row mode, so the integration times were about 0.66 s. In this mode, the MEG and HEG spectra criss-cross through the detector window, Figure 6.24. In order to map the so-called "scattered" light out to +3 order, the '2C0 was positioned by the FAM to 5 locations 22 mm apart along the +Y axis. Since the actual level in the lines was not of primary concern, the cores of the dispersed orders were allowed to pile up.

The reduction and analysis were done in IDL. The data came in FITS format as the result of second floor processing at the XRCF and was read into IDL using the **mrdfits** routine. Besides the event data, various test- and ACIS-specific FITS keywords were read. The keyword values were used to set system parameters and calibration values such as the detector gain, the grating period, mirror focal length and Rowland distance. The event finding algorithm used in quicklook processing does not process the last two rows of data, even though the charge in these rows is collected. This feature is evident as a 2 pixel wide gap. PH data for each event consisted of 25 values in a 1-D array.

The procedure for reducing these observations started with event lists which included the event location in the 114x1024 window, the event time, and pulse heights for the 5x5 event island.

1. Various FITS keywords were read: ONTIME to get the exposure time, OBS_ID to get the TRW ID, WINSIZE to get the ACIS-2C window size (in pixels), CCD_ID to get the character setting which chip in the 2C was being used (so the detector name is assigned to ACIS-2C0 to indicate the BI chip in the 2C), DETNAM to get the chip serial number, and TLMAX4 to determine the number of columns allowed. The TRW ID is parsed into components to give the XRCF phase, grating, and detector assembly.

2. The chip serial number is used to set the chip gain parameters. For the chip used in these tests, w148c4, no "official" values were available, so the gain was set to 0.322 DN per eV, estimated from the PH distribution so that the highest peak would centered at the DCM energy, 1.775 keV.

3. The 25 PH values were reordered from the subassembly order, which places the center event first, to the flight order, where the center event is 5th in the array. The event PH amplitude is formed as the sum of all 25 PHs. The "ASCA" grading criterion is applied to the 3x3 PH data but is not used in processing. The event amplitudes are converted to energy using the chip gain and offset parameters.

   See figure 6.25 for the pulse height distribution for the entire 5 image data set. The input is monochromatic at 1.775 keV and background is negligible. Thus, the pileup peaks are apparent and there is a tail of incomplete charge collection events below 1 keV. The ACIS-2C0 gain parameters vary significantly over the entire array, so peaks are broad.

4. Randomized event chip coordinates by $\pm$ 0.5 pixel.

The event positions were randomized within a pixel in order to prevent digitization effects in subsequent analysis, which involved fractional pixel shifts and rotations. The locations were shifted to place the zero point at the 0th order location in facility coordinates and rotated so that the MEG or HEG dispersion direction would be horizontal. Events for each exposure were processed separately due to detector rotations and shifts.

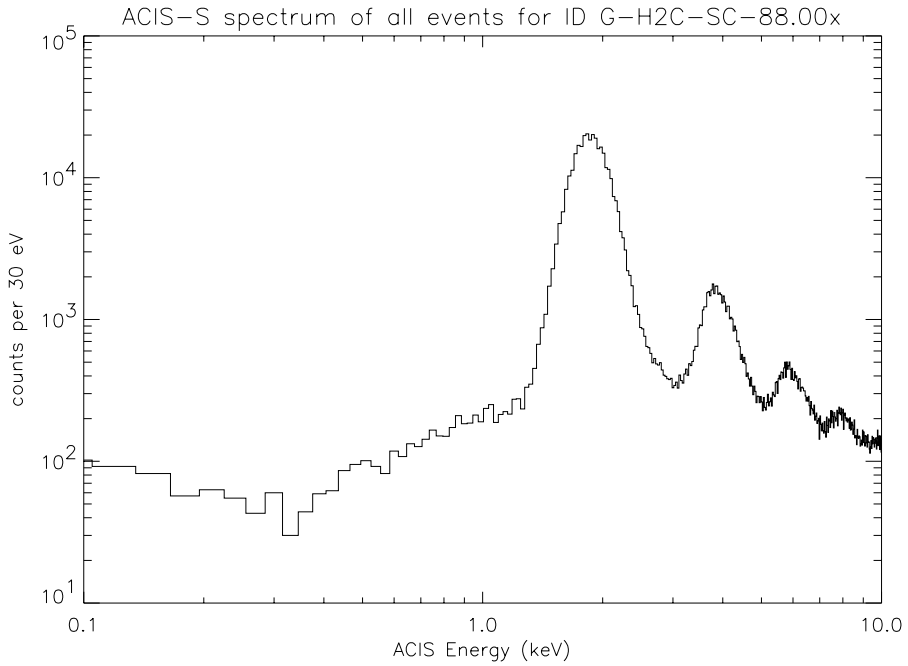

Figure 6.25: Pulse height distribution for the entire five image data set, converted to energy in keV. The input is monochromatic at 1.775 keV, so all features are related to pileup or incomplete charge collection

1. Offset by FOA loc (584, 72.8), then rotated -0.58 degrees to convert from chip (real) XY to XRCF YZ. The rotation angle and offset were estimated from the first image where the FAM position was set to (0,0) so that the 0th order image would be centered and the HEG scattering would be horizontal after HEG rotation below.

2. Offset by FAM Y and Z shifts. Coordinates are now in pixels from 0th order. Subsequent analysis showed that the commanded and reported values, both specifying no motion in Z and 22 mm motions in y only, gave incorrect results.

3. Rotated XRCF YZ coordinates by the grating dispersion angles (HEG: -5.2 degrees, MEG: 4.7 degrees), determined from the value of the angle of the MEG-HEG bisector, -0.225 degrees and the MEG-HEG opening angle, 9.934 degrees, taken from analysis of Phase I EE data (see Section 6.2). New coordinates are dispersion y' and cross-dispersion distances z' in pixels. NOTE: The rotation is about the (virtual) 0th order location, not chip FOA, so the rotations are distinguishable (as with HSI).

4. Coordinates are scaled to physical units (mm) using 24 microns per ACIS pixel.

A detector-based energy was computed using the 25 pulse heights and the detector gain, 0.322 eV per DN. In order to reduce background, data were screened to include only events with inferred energies in the 1.3 to 4.4 keV range, which gave events with one or two photons each.

The wavelengths for each event, assuming it was dispersed into first order, were computed using the grating equation $\lambda = |p \sin\beta|$, where p is the grating period (either 4001.13 Å for the MEG or 2000.81 Å for the HEG), $\tan\beta = y'/X_{\rm RS}$, y' is the dispersion distance, and $X_{\rm RS}$ is the Rowland spacing, taken to be 8782.8 mm. See Section 11.3.2 for a discussion of these values.

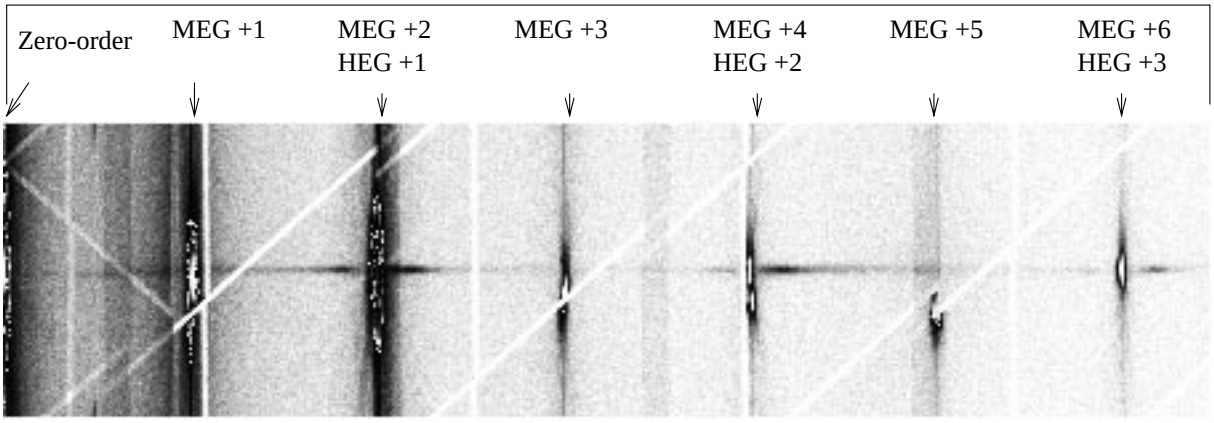

Figure 6.26: This image is the result of binning data from HETGS scattering tests G-H2C-SC-88.00{1-5} along the HEG dispersion direction. The anomalous scattering is apparent as the broad, dark horizontal streaks in the image. Wavelength increases to the right from the zeroth order at far left. Three HEG orders are observed as well as MEG orders in between. Note the near coincidence of MEG 4th order and HEG 2nd order about 2/3 of the way from the left end. The diagonal features are due to 2 pixel gaps in the event finding algorithm while vertical features are due to bad pixels masked out or to changes in exposure due to regions of overlap between shifted exposures. Scattering is brightest near the HEG +1 and HEG +2 orders.

The events were "unwrapped" modulo the 114 row period in order to center the dispersion axis. The unwrapping depends only on the cross-dispersion distance, z': the event z' values are offset by plus or minus W to put them in the range $-W/2$ <z'< $W/2$, where W = 114 × 0.024 mm.

The events were then combined and binned in 0.05 Å (HEG) or 0.1 Å intervals (MEG).

The images are shown in figures 6.26 and 6.27. Background was estimated using a 30 pixel region well away from the dispersed light. The dominant source of background was due to mirror scattering, which is azimuthally symmetric about the 0th order image and all dispersed orders. Many artifacts of the detector are visible but the anomalous scattering is obvious along the HEG direction and is absent along the MEG direction.

Some of the conclusions that can be drawn from the binned images follow.

1. The MEG shows no detectable scattering. This is evident on many images but no quantitative limits have been measured yet.

2. The cross-dispersion profiles were fitted with Gaussians of variable location, width, background, and normalization at each wavelength bin for HEG scattered light only in order to diagnose effects of the data reduction procedures. An aperture subtraction technique could not be applied immediately because it was apparent that the initial assumptions about the FAM motion were incorrect. Figure 6.28 shows results from one reduction run. Fits have been eliminated where unreasonable centroids, widths, or intensities were obtained, causing gaps in the plots. Some bad data points remain, however, and have to be reviewed individually.

3. A pattern of rotated spectra in each measurement was corrected by applying a rotation in the ACIS-2C0 frame about the FOA. A "global" drift remained; centroid values in figure 6.28 drift downward by about 1.0 arcsec as the wavelength increases from 5 Å to 21

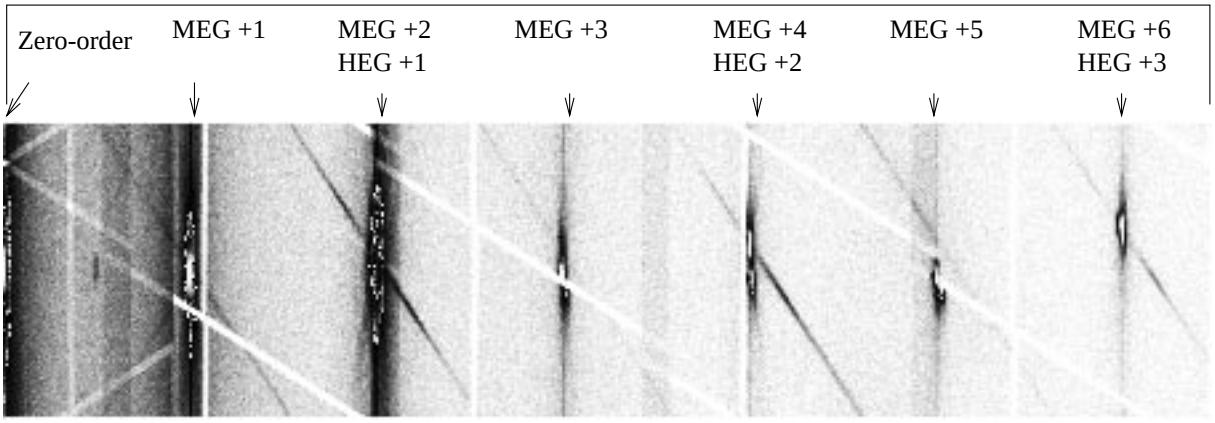

Figure 6.27: An image derived from tests G-H2C-SC-88.00{1-5} as in Fig. 6.26 but binned along the MEG dispersion direction and binned at 0.1 Å bins (so the image size is about the same as the HEG image). The same detector features are apparent, such as stripes where there are no events. The HEG scattering shows up as steep, wrapped, dark, diagonal lines. No MEG scattering is observed, so stringent upper limits can be set. The faint elliptical image between zeroth and first order is the first order dispersed image of the DCM output at twice the tuned energy.

Å. This drift is corrected with a 0.016 mm Z shift for each 22 mm FAM motion. This drift could be caused by a difference between the FAM and XRCF Y axes (defined in phase C) of 0.04 degrees.

4. The total counts in the cross dispersion profiles are given by the integral over the Gaussian, which is proportional to the fitted normalization and the fitted σ. These data, also shown in figure 6.28, show the dispersion peaks expected at multiples of 7.0Å and at the wavelengths halfway between due to the MEG. Bad fits often occur at these locations because the profiles are not Gaussian when the line cores are so dominated by event pileup. The wavelengths are measurably different from the expected values, reaching a maximum deviation of 0.5 Å at the HEG +3 location, expected to be observed at 21.0 Å. The wavelength errors are eliminated by assuming that the FAM moved 22.25 mm on each step, 1.1% too far. The FAM was commanded to move 22.000 mm and FAM log data agree, so the source of the discrepancy is not known at this time.

5. For the remaining analysis, a simple aperture extraction method was sufficient because the spectrum was level and smooth. The source aperture was defined to be 2.5 arcsec (5 pix) wide and background was estimated from a region 11-26 arcsec above the source. Figure 6.29 shows the count spectra derived in these two regions.

6. Subtracted background and normalized to expected rate in first order of 1700 cps. Figure 6.20 shows the net scattered light after dividing by the estimated exposure time. There are still background subtraction errors near the MEG and HEG orders but the overall subtraction is good off the lines so that the scattered light is apparent.

7. Added points at +1, +2, +3 orders affected by pileup in order to make a figure that combines the dominant grating orders from HEG "coherent" diffraction with the HEG incoherently diffracted or scattered light. The total scattered light gives 17 count/s and is normalized to the count rate expected from the W-M line in +1 order, which is estimated to be about 1700 count/s. Thus, the total of the incoherently scattered light is estimated to be about 1% of the power in first order. The scattered light is occasionally detected at

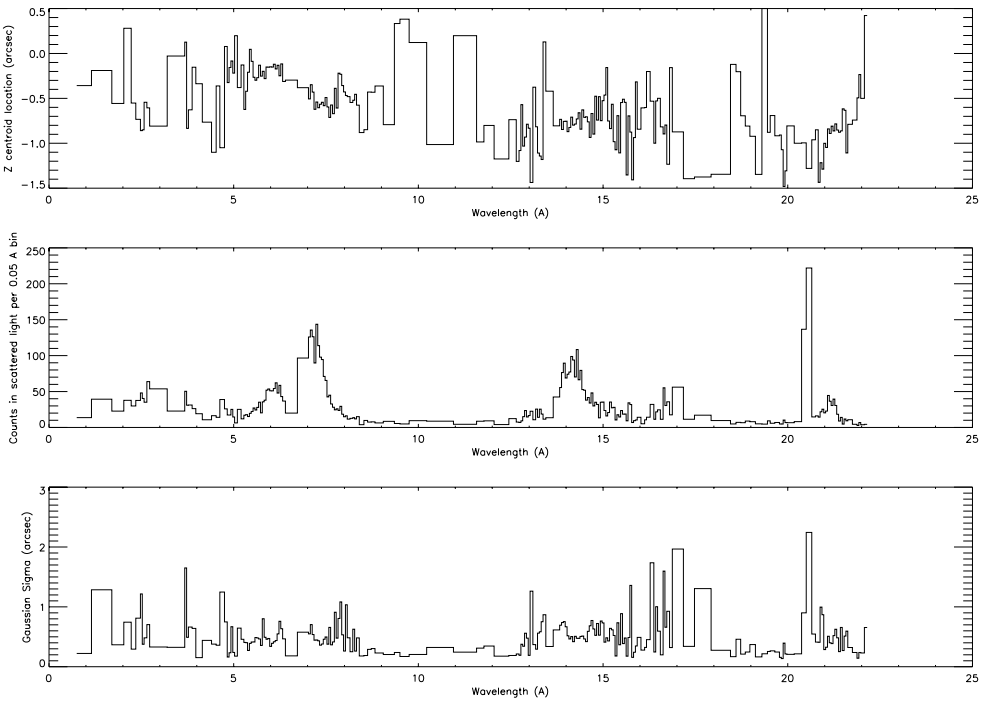

Figure 6.28: Fitting Gaussian functions to the HEG scattered light cross-dispersion profiles. *Top curve* The centroid location in arc seconds from a fiducial horizontal reference. Note that the centroid drifts downward by about 1.0 arcsec as the wavelength increases from 5 Åto 21 Å. *Middle curve* The inferred total counts in the Gaussian fits. Scattering peaks appear near 7 Å, 14 Å, and 21.2 Å. Bad fits occurred at the HEG and MEG orders. These should have been at 3.5 Å (or 7.0 Å for the MEG +1), 7.0 Å (HEG +1), 10.5 Å (MEG +3), 14.0 Å (HEG +2, MEG +4), etc. At HEG +3, the line is observed at 20.5 Å, compared to the expected value of 21.0 Å, thus wavelengths of orders showed systematic error. The wavelength errors are eliminated by assuming that the FAM moved 22.25 mm on each step, 1.1% further than the commanded motion. *Bottom curve* The fitted Gaussian sigma parameter; good fits give values near 0.5 arc sec (about 2 ACIS pixels, as expected).

values approaching 2×10^{-4} of the flux in order +1. The detection limit is about a factor of 20 below this value.

The exposure time (see Figure 6.30) was computed for each wavelength based on the wavelengths of the detector edges for each exposure, and was used to compute count rates as a function of wavelength. The exposure for each wavelength bin was estimated by setting up dummy "events" at the chip corners. These events were sent through the same transformations as the photon events. The chip exposure time was added to array elements corresponding to all allowed wavelength bins. Energies were computed from the dummy-event wavelengths. Accumulated exposures for each (overlapping) ACIS-2C0 position. The events were concatenated. Figure 6.30 gives the resultant exposure time as a function of wavelength, adding all 5 chips.

The result was normalized to the estimated count rate of the first dispersed order, which was not directly observed due to significant event pile-up. The zeroth order count rate was estimated by modeling the profile of the trail of the zeroth order image that occurs when the CCD is parallel shifted. The trail receives an exposure of 40 μ sec per row for each CCD frame and for each window per frame. There were 9 windows (at 114 rows per 1024 row frame) per frame, 100 frames of data (only the first portion was examined) and 25 rows of the 114 row window were combined, giving a total exposure in the trail of 0.9 sec. The one-dimensional profile of the trail region is shown in Figure 6.31. Fitting two Gaussians to the trail gave about 1200 $\pm$ 100 counts in each component while a detailed model based on the beam normalization detector (BND) data only predicted 1170 in the broad, flat component and 1280 in the Gaussian component. The broad component was modeled as an intensity gradient that varied by a factor of two (as given by the BNDs) across the HRMA aperture and then adjusting the defocus and centroid until a good match was obtained to the observed profile. The normalization was not adjusted but was fixed by the north and south BND count rates.[2] Fitting a Gaussian after subtracting the model of the flat component gave 1180 $\pm$ 80 count, so the model agrees well with the data. The first order count rate, $R_{1,HEG}$, was then estimated as $R_{0,HETGS}A_{1,HEG}/(A_{0,HEG}+A_{0,MEG})$, where A_m is the predicted effective area at 1.7754 keV for order m and the grating subset (either HEG or MEG). The model predicts a count rate for HEG 1st order (both sides) of 2980 count/s and 5420 count/s in the MEG 1st order.

Detector and grating order artifacts were eliminated after close examination of the raw data. MEG orders 1, 3, and 5 caused systematic errors at 3.5, 10.5, and 17.5 Å while HEG orders 1, 2, and 3 required excising data at 7, 14, and 21 Å. The excised regions were generally 0.3 Å wide and no scattering due to the grating was apparent in these regions. Bad exposure corrections due to the 2 row gap were eliminated near 4.3, 11.2, 2.2, and 18.4 Å while bad columns in the detector required eliminating data near 18.95, 1.30, and 8.85 Å. The result is shown in Figure 6.20. The total scattered light from 0th order through 3rd order is 1.00$\pm$0.01 % of HEG first orders based on this data set.

A similar analysis of the MEG data shows no significant detections of scattered light. There are systematic background subtraction errors as the HEG scattered light contributed to the background. Nevertheless, the MEG scattered light density never appears to exceed a value of 5×10^{-6} per 0.014 order. The total scattering is difficult to estimate given the systematic errors but appears to be less than 5×10^{-5} between orders 1 and 3 while the comparable HEG scattering is 6×10^{-3}.

[2]See the AXAF Project Science web page `http://wwwastro.msfc.nasa.gov/xray/xraycal/bu/bucat.html` and the figure linked from "TAP2", tap2.eps. RunID 112250 shows a good example of the profile of the DCM beam when tuned to a bright line. Additional data taken during the XRCF rehearsal phase with a BND centered in the XRCF vacuum pipe were used to chart the 1.775 keV line and the nearby continuum. Note that the north and south BNDs are placed about 70 cm to either side of the HRMA aperture center while the top and bottom BNDs are centered in XRCF Y coordinates.

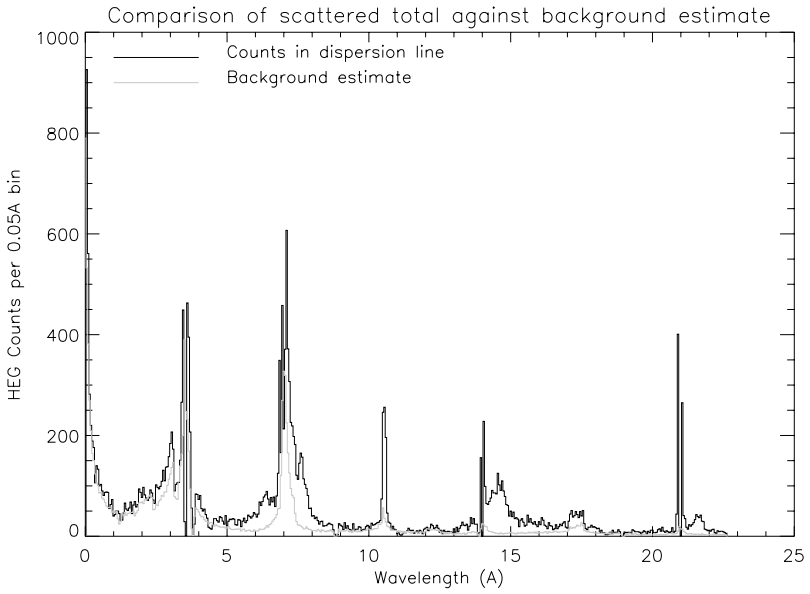

Figure 6.29: Estimated "background" and the count spectra in the source region. Note that the background increases towards 0Å due to mirror scattering from 0th order. The orders show up in background due to mirror scattering and when the MEG image does not land on top of the HEG image; e.g., at 10.5 and 17.5 . (Note wavelengths have been corrected for the FAM motion error mentioned in figure 6.28.)

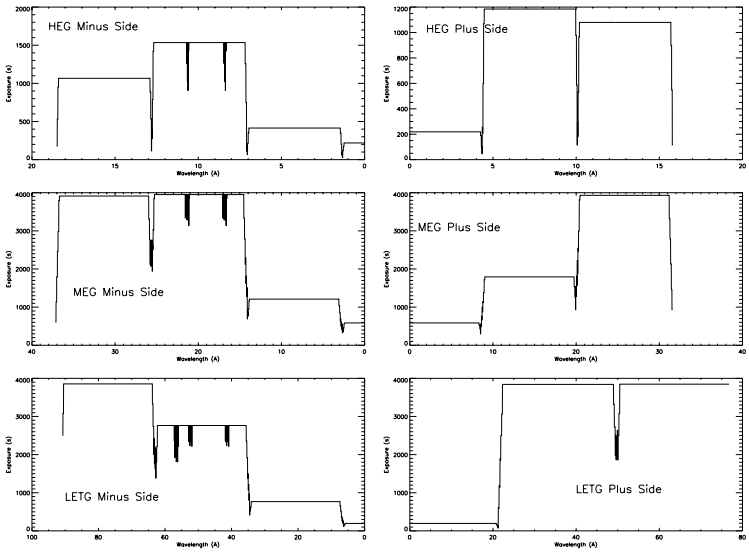

Figure 6.30: This figure shows the exposure function derived for tests G-H2C-SC-88.00{1-5}. Regions where two adjacent observations overlapped show twice the average exposure and there is double exposure near zeroth order as data from the negative dispersion direction is included.

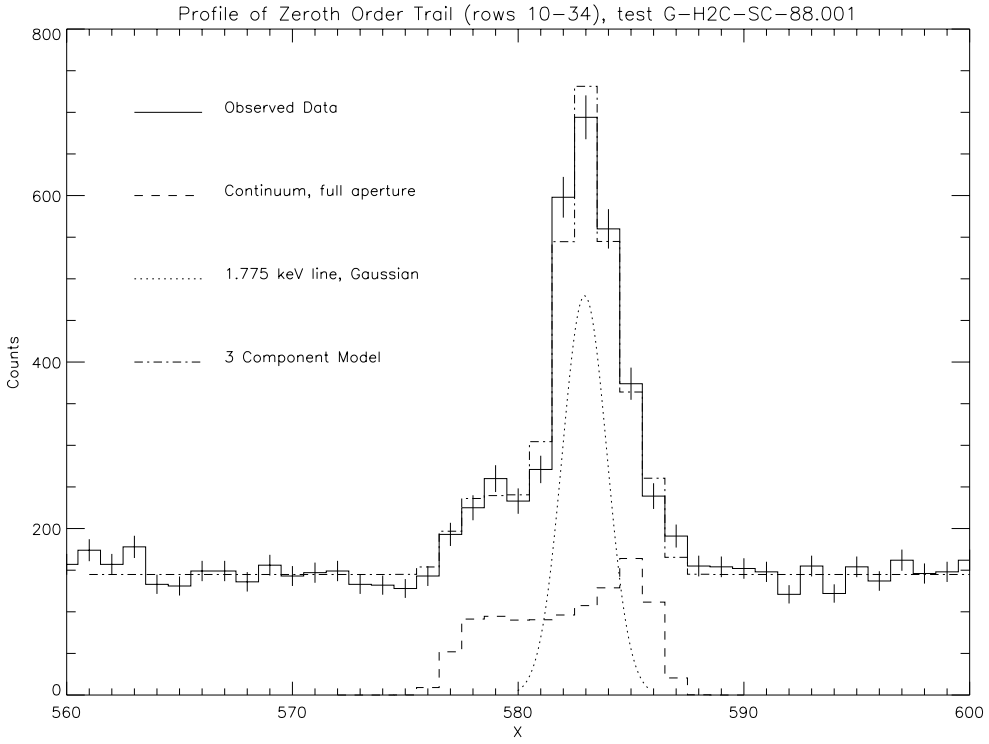

Figure 6.31: Profile of the zeroth order image in test G-H2C-SC-88.001. The profile was obtained by summing 25 rows far from the image centroid so that pile-up would not be a concern. The profile was fitted with three components: 1) *dashed line* the pedestal of the profile is dominated by off-line continuum as the beam pattern does not fill the mirror aperture and the detector was (unintentionally) placed slightly out of focus; 2) *dotted line* a Gaussian which approximates the pattern produced by the DCM when tuned to a source emission line; and 3) the uniform background is primarily due to mirror scattering.

6.6.4 ACIS-S Scattering Tests: H-HAS-SC-7.002, 7.004, and 17.006

The ACIS-S was used in phase H for these scattering tests, so there were no problems associated with windows or shifting of the detector. In the first test, the DCM was tuned to the W M_ζ 1.384 keV line. In the second test, the DCM was tuned to the W M_γ 2.035 keV line. For the third test, the DCM was scanned from 5.00 keV to 9.00 keV in 1.00 keV steps. The HETGS dispersion relation constants derived from phase C data were verified to a part in 2400 using the first data set. The data reduction steps were essentially identical for these tests except that for H-HAS-SC-17.006 time selections were needed to separate the periods when the DCM energy was constant. In addition, for the last test only, the five axis mounts (FAM) that moves the ACIS-S relative to the HRMA was positioned at Y=0.25 mm in XRCF coordinates.

The ACIS-S was run in the timed event mode so there was no ambiguity between MEG and HEG. The DCM current was set at the highest possible value, which caused significant pile-up in the dispersed orders and made zeroth order readout trail bright enough to measure in order to estimate the beam flux. The trail was somewhat fainter than in the tests taken at 1.775 keV, so total counts in a 3 column region starting 200 rows on either side of the zeroth order image were compared to a similar region rotated 15° from the vertical. The exposure time in the zeroth order trail was 40μs/row/frame $\times(1024 - 2 \cdot 200)$ rows, or 25ms per frame. Events were selected so that the energy derived from the ACIS pulse height was within 100 eV of the expected value. The event positions were transformed using the grating constants into wavelengths and a simple extraction was performed using a window 0.2 mm wide around the dispersed events while background was measured in a region 0.2 to 0.8 mm from the dispersion line. An additional rotation of -0.13° was required to make more horizontal dispersion lines; this rotation could be either in the ACIS to XRCF coordinate frame or could be a residual error in measuring the HETG to XRCF coordinate frame. Data near 0th order were eliminated from the final results as background measurements failed to account for the azimuthal symmetry of the 0th order (mirror) scattered light. Data near orders were also eliminated in general. The results are shown in figures 3.30 and 3.31.

6.7 Offaxis and Defocus Tests

Objective: Compare the XRCF grating data taken under offaxis and defocus conditions to predicted images from **MARX** in order to validate the model in these conditions.

6.8 ACIS-S Rowland Conformance

Objective: Use the ACIS-S quadrant shutter focus measurements to measure the conformance of the ACIS-S to the designed Rowland curvature. *Publication(s):* Stage *et al.* [91]

This section analyzes XRCF tests designed to verify the Rowland geometry design of the HETGS. In particular, we test for the expected focal properties described in Section 2.1. Using a line source and configurations of shutters which sequentially illuminates the four quadrants of the HETG/HRMA entrance aperture at a time, we determine the offset of the ACIS-S detector surface from best focus position at the location of each imaged order. The ACIS-S detector is tiled to approximate the Rowland circle. Looking at the projection of events in the dispersion direction, the best focus lies along this Rowland circle and little defocus is expected. For cross-dispersion direction profiles, the best focus lies in the focal plane, tangent to the Rowland circle at the zeroth order image location, and so a defocus is expected.

Because of extensive subassembly testing, we can restrict this analysis to ACIS placement (focus, tilt) issues. Subassembly results we will make particular use of are that the ACIS-S is properly curved and the HRMA mirror shells each have slightly different focal lengths. The data from these tests are adequate to demonstrate that the ACIS-S at XRCF has been positioned very close to best focus, and with a marginally statistically significant small rotation about the z-axis.

6.8.1 Shutter Determination of Image Defocus

At XRCF, a shutter system was installed between the HETG and ACIS-S. Four shutters per HRMA/HETG shell divide the HETG into quadrants: Top (T) centered on the ACIS $-Z$ direction, North (N) centered on the ACIS $+Y$ direction, Bottom (B) centered on the ACIS $+Z$ direction, and South (S) centered on the ACIS $-Y$ direction. This gives a total of sixteen programmable shutters, used here four at time. The detector offset from best focus at a given imaged order can be determined by comparing the position of the light from each quadrant.

To understand how the focus calculation works, we consider first a simplified HETG/ACIS-S arrangement, shown in Figure 6.32. In a Rowland transmission grating, facets are located on the Rowland circle or Rowland torus (created by rotating the Rowland circle about the ACIS y-axis), as explained in Section 2.1, see also Figure 2.1. The offset from best focus is found with similar triangles. We trace the rays from facets on opposite sides of the Rowland circle: if the detector is placed on the Rowland circle, the rays from each side coincide and focus. If the detector is placed in front of or behind the Rowland circle, the rays from the different sides of the ring do not image at quite the same location on the detector. The ratio of this image separation to the defocus of the detector from the Rowland circle, should be the same (by similar triangles) as the ratio of the diameter of the grating ring (2 times the "Effective Radius" shown) to the Rowland diameter at XRCF. The effective radii of the four grating shells are given in Section 11.3.1.

Figure 6.33 shows the rays from such an "effective" ring when the N and S quadrants are illuminated. We use Cartesian coordinates centered at the zeroth order. The image produced by an illuminated quadrant can be measured by the y and z coordinates of its centroid, *e.g.*, the N quadrant image is measured at (N_y, N_z). As we trace the rays from the the HETG to the focus at zeroth order, the light from the N quadrant remains at a more positive value of y

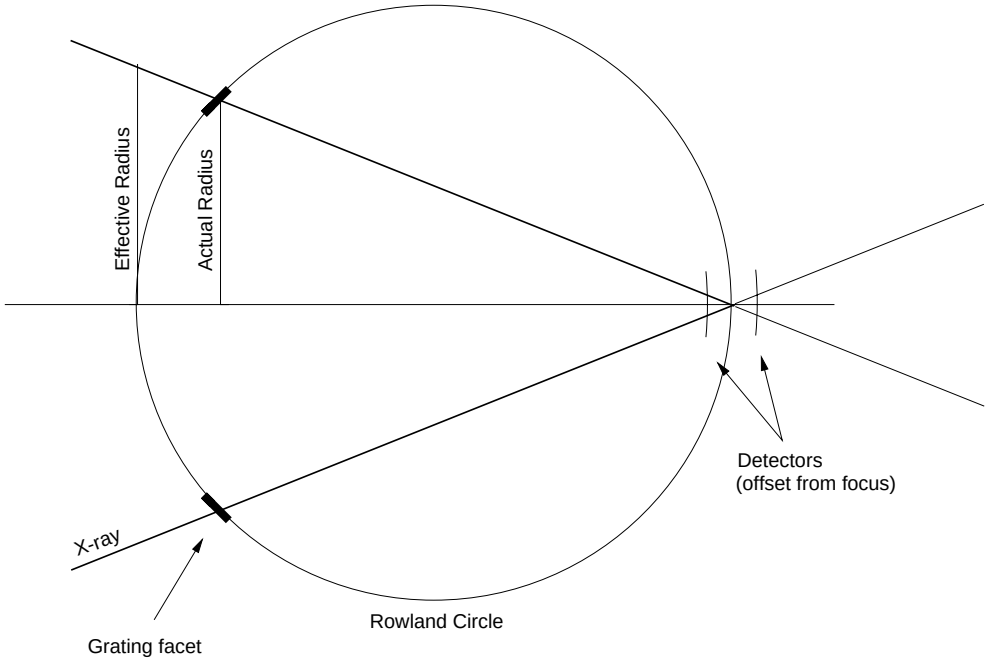

Figure 6.32: Schematic of the Rowland circle grating arrangement. The slope of the incident X-rays shown is given by the "Effective Radius" divided by the Rowland cirlce diameter, $X_{\rm RS}$. As the detector is offset from its in-focus position, images from opposite sides separate; this separation combined with the slope allows the amound of defocus to be measured.

than the light from the S quadrant. At the Rowland circle, the images converge at best focus, and beyond this point the rays cross and the S quadrant light is at a more positive value of y. To determine the offset of the detector if we measure the separation of these two images in y somewhere before or after the Rowland circle, we use Equation 6.3:

$$\frac{X_{\rm offset}}{N_y - S_y} = \frac{X_{\rm RS}}{2R_{\rm HETG}} \tag{6.3}$$

where $X_{\rm RS}$ is the Rowland spacing (diameter). Here the sign of the offset indicates if we are displaced towards the mirrors ($N_y - S_y > 0$), or away from them ($N_y - S_y < 0$).

Images from the Top and Bottom quadrants are used to check cross dispersion focus. The cross-dispersion best-focus is located at the tangent plane perpendicular to zeroth order. So, we expect the detector to always be offset towards the HETG when we use equation 6.3 with $B_z - T_z$ replacing $N_y - S_y$. Otherwise, the situation is the same: the top and bottom rays do not cross until focus at the tangent plane, and prior to crossing the Bottom ray maintains a more positive value of z. We expect the measured cross-dispersion focus offset to agree with the formula given in equation 2.2, that is, the offset is the distance from the Rowland circle to the tangent plane, $\Delta X_{\rm Rowland}$.

From symmetry, we expect that the other two separations, $B_y - T_y$ and $N_z - S_z$, should both be zero. Any deviations from zero indicate asymmetries in the gratings or mirrors.

The actual HETG consists of HEG and MEG grating sets. The ACIS-S y-axis runs in between

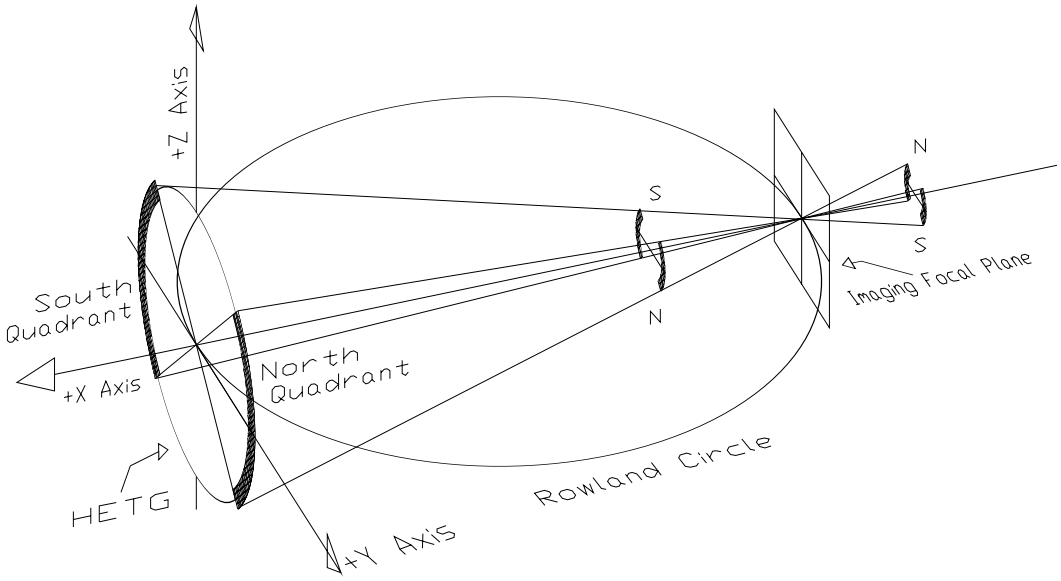

Figure 6.33: Quadrant shutter test schematic. X-rays focussed by the HRMA enter from the left, where they are intercepted by the HETG. The shutters for the North and South quadrants are open. We trace the light for zeroth order to focus on the Rowland circle. For the zero order, the dispersion direction focus (on the Rowland circle) and cross-dispersion direction focus (in the imaging plane) coincide. Before the focus, the center of the N quadrant photons is located at a more positive value of y than the S quadrant. At dispersion focus on the Rowland circle, the orders overlap at the same value. Past focus, this order is reversed.

Table 6.9: Properties of HETG and HRMA shells. Radii are from Table 11.1, effective areas are from `'/hrma/cip/hrmaD1996-11-01XeffareaN0004.rdb`, and the focus estimates are from HRMA XCRF Phase 1 Test Analysis Results, Chapter 26.

Shell	HETG Radius $R_{\#}$ (mm)	Shell Effective Area $M_{\#}$ (cm^2)	Relative Focus Estimate (mm)
1	521.66 ± 0.1	316.309 ± 14.450	-302
3	419.90 ± 0.1	207.793 ± 5.342	0
4	370.66 ± 0.1	165.578 ± 5.496	+277
6	275.44 ± 0.1	94.759 ± 2.993	-152

the HEG and MEG dispersion axes, and is slightly curved with respect to the x-axis to follow the Rowland circle. Since the ACIS-S only follows a small fraction of the Rowland circle, the ACIS-S coordinates (measured on the chips) are approximately the same as Cartesian coordinates centered at zero order. However, some care must be taken in understanding when the differences are important and what geometrical approximations are being made.

Although the HEG and MEG dispersion direction axes are rotated ± 5 degrees from the ACIS y-axis, we have chosen to measure the separations between imaged orders from a pair of quadrants along the ACIS y and z axes. For an angle of 4.5 degrees, the $N_y - S_y$ could have a fractional error of as much as $1 - \frac{1}{\cos 4.5} = 0.003$, or 0.3%. The corresponding erroneous $N_z - S_z$ separation for a detector offset of 70 microns would be 0.39 microns (instead of zero). These kinds of errors are extremely small compared to the uncertainties in the positions of the imaged orders, and we may ignore these effects.

Another complication results from the fact that all four shells in a quadrant are illuminated at once. Consequently, each quadrant image contains photons from not one but two mirror/HETG shells. With the detector far from focus, it is possible to resolve the images of the two shells, *e.g.*, in Figure 5.8. For the data taken here, however, the ACIS-S is close to in-focus and mirror blur dominates the image; the shells are not resolved in the resulting "spot." To model the offset of the "spot" in this case, then, we have to consider the shell-weighted geometric centroid of the illuminated quadrants to get the "effective radius" in the simple similar triangles calculation.

The calculation is quite simple. First we determine the geometric centroid of a quarter-arc:

$$\frac{C_{\rm QA}}{r} = (\frac{5\sqrt{2}}{3 + \frac{3\pi}{2}}) = 0.916845 \tag{6.4}$$

This gives a single location on the axis of interest (for Top or Bottom, z, for North or South, ACIS y) we expect the photons from the ring to be clustered at. Then, for the HEG gratings, we weight these two positions by the two HEG effective radii with the effective area of the mirror shells,

$$R_{\rm Eff,HEG} = \frac{(R_4 M_4 + R_6 M_6) C_{\rm QA}}{M_4 + M_6} \tag{6.5}$$

Likewise for the MEG,

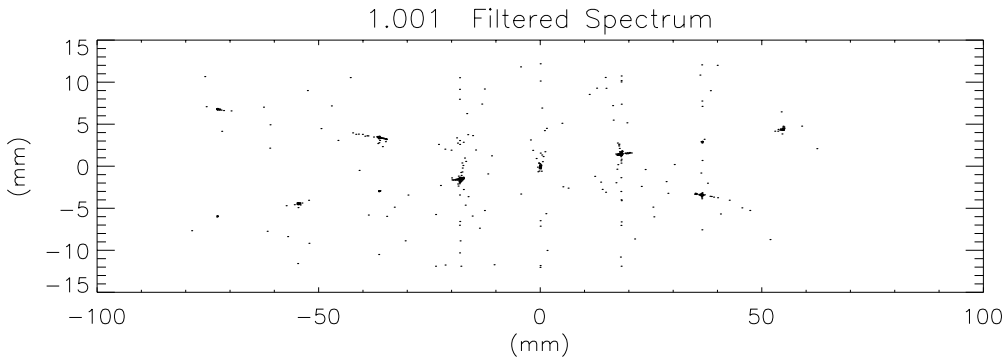

Figure 6.34: H-HAS-PI-1.001 Filtered Spectral image. Displayed are the events in the '1.001 data set after energy (1.2 to 1.8 keV) and grade selection (0,2,3,4,6).

$$R_{\mathrm{Eff,MEG}} = \frac{(R_1 M_1 + R_3 M_3) C_{\mathrm{QA}}}{M_1 + M_3}$$

Finally, using the data in Table 6.9, we calculate the following ratios to use in Eqn.(6.3):

$$\frac{X_{\mathrm{RS}}}{2R_{\mathrm{eff,HEG}}} = 14.25 \tag{6.6}$$

$$\frac{X_{\mathrm{RS}}}{2R_{\mathrm{eff,MEG}}} = 9.95$$

6.8.2 Data Analysis

The shutter focus (SF) tests H-HAS-PI-1.001 and H-HAS-PI-1.003 which we analyze here used the XRCF Al source, imaging the Al-K line and continuum complex at 1.486 keV. The nearly monochromatic line was imaged usefully in orders -2, -1, 0, and +1 with the HEG and -3, -1, 0, +1, and +3 with the MEG (even orders had very small numbers of counts). The ACIS telemetry was processed by the PSU ACIS team, and we start with their event files for our analysis. In order to facilitate rebinning the data to different bin sizes, the detector integer pixel coordinates are uniformly blurred by ±0.5 pixels and converted to real-valued distances in millimeters. We further applied PHA selection to energy conversions and grading. For the analysis here we selected events with ASCA grades 0,2,3,4,6, and PHA energies in the range of 1.2 to 1.8 keV. The entire H-HAS-PI-1.001 data set, after grade selection, is shown in Figure 6.34. The durations of the tests were approximately 13 ksec and 4 ksec, and in the second test the source intensity was significantly increased. The source intensity of the second run was sufficient to generate pile-up in the lower orders, most noticeably in MEG ±1.

The order of quadrant cycling was derived from XRCF log files and determined to be Top, North, Bottom, South. The data are continuous, but the divisions between quadrants were easily determined from examination of the zeroth order position data against time. The rms displacement of photons from zero, a result of scattering perpendicular to the mirror surface, is much greater in the z direction for the Top and Bottom quadrants than North and South,

Table 6.10: Number of Events per Order/Quadrant. Maxima are typically MEG ±1 and 0. Minima are generally HEG -2.

Grating	Order	Top	North	Bottom	South
1.001					
HEG	-2	44	29	20	32
HEG	-1	261	204	178	200
HEG	1	242	223	174	214
HEG/MEG	0	441	305	245	318
MEG	-3	54	54	64	63
MEG	-1	617	508	455	570
MEG	1	608	523	414	529
MEG	3	76	72	55	50
1.003					
HEG	-2	37	47	34	71
HEG	-1	240	264	224	272
HEG	1	260	318	223	259
HEG/MEG	0	192	231	139	234
MEG	-3	81	86	84	110
MEG	-1	414	473	372	527
MEG	1	376	417	336	418
MEG	3	99	107	99	95

which scatter primarily in the y direction. Blocks of time were selected to maximize the events counted for each quadrant. Table 6.8.2 lists the number of events in each imaged order for each quadrant.

Centroid Determination

To find the y and z centroids of each image "spot" for each order and quadrant, an IDL program extracted the events in the vicinity of each order in the appropriate time interval. These events were then used to make y and z projection histograms. The bin widths used to create the histograms were 0.0157 mm and 0.0164 mm for the '1.001 and '1.003 data sets, respectively. They were chosen from a range of widths from sizes less than a quarter pixel to larger than a pixel as the widths which produced the most typical values of reduced χ^2 for the ACIS-S placement fits discussed later in this section. Generally, the one sigma error on a calculated parameter was larger than the spread in values from using different binsizes in the histogramming. The resultant histograms of the imaged "spot"s were fit with one dimensional Gaussian curves. The parameters of the fit were amplitude, mean (centroid), standard deviation, and a constant background.

Determining Detector Defocus and Tilt

With confidence established in the centroids and error bars calculated for the real XRCF test data, the separations of centroids of the quadrant pairs were then used in Equation 6.3 to find a set local offsets of the detector from focus. The focus offsets determined from the data are plotted in the panels of Figure 6.35. The "Primary Offset" panels show the dispersion direction values. With the dispersion-direction focus, a linear relation between the defocus and distance of the order from zeroth order indicates the correct Rowland curvature. The constant in the fit indicates the translation of the entire detector along the optical axis. A statistically significant slope indicates that the detector surface has a rotation about the z axis from nominal.

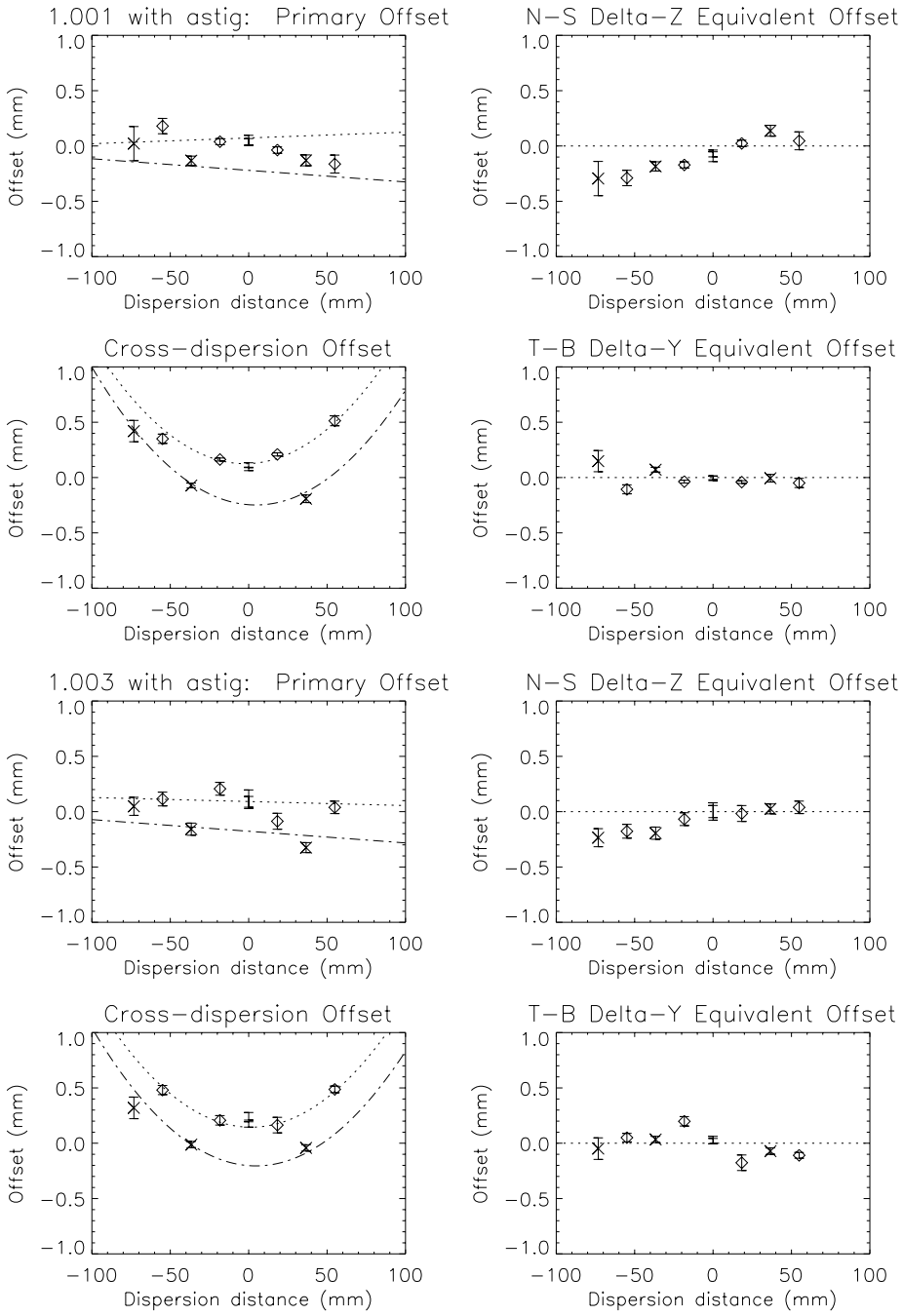

Figure 6.35: Quadrant shutter test results. The results from the '1.001 and '1.003 tests; '1.001 is in the upper four plots. The plots show the focus offsets at each order: HEG results are plotted as squares and dash-dot lines. MEG results are plotted as triangles and dotted lines. The zeroth orders are not plotted as they are not used in fits; however, the zeroth order error bars have been plotted for comparison. Upper left: Linear fit to dispersion direction offsets. Lower left: Quadratic fit to cross-dispersion direction offsets. Upper and lower right: Equivalent offsets for the $N_z - S_z$ and $B_y - T_y$ separations. These points are expected to agree with zero.

Table 6.11: Focus Estimates of HRMA Shells...

	Focus Offset from Shell 3		
Shell	Avg. (μm $\pm$ 1 μm)	Y	Z
1	-302	-188	-415
3	0	0	0
4	+277	320	235
6	-152	-146	-158

For the cross-dispersion measurements, the "Cross-dispersion Offset" panels, a quadratic variation in focus is seen and expected based on the value of the Rowland curvature. This defocus will be superimposed on top of the same linear tilt and offset terms as in the dispersion direction case.

We solve for the overall detector defocus and tilt parameters by simultaneously fitting the dispersion and cross-dispersion direction defocus values.

HRMA Focus and Astigmatism

A significant and relevant result of independent HRMA testing is that the individual mirror shells have different focal lengths, values for which have been taken from the HRMA XRCF Phase 1 Testing Analysis Results, Chapter 26. The values given in Table 6.9 were calculated from the E-67 test data given in the HRMA report, using the equation,

$$\text{Offset} = \text{PrimeX} - (\delta N) \tag{6.7}$$

where δN is the offset from the PrimeX location to the best focus in Y, Z, or the average of the two. The results have been adjusted to set Shell 3 at zero offset. The HRMA document gives the averages values in its Table 4; however, since we separately determine the Y and Z focuses through the dispersion direction and cross-dispersion direction data, it is more useful for us to consider those values directly. The HRMA scanning tests and analysis were similar to those presented here. The major difference is that the scanning was done shell by shell in addition to quadrant by quadrant, allowing determination of the focus to each shell. For our purposes, we will need to combine (weighting by effective area) the focii offsets for each pair of shells used in the MEG or HEG.

We see immediately that individual mirror shells suffer astigmatism– the Y and Z direction photons focus at slightly different positions. These astimatism can be easily calculated (taking care to shift the Z focus offsets so they measure offsets relative to the Y Shell 3 focus), and combined for shell pairs (again weighting by effective area) to produce the expected HEG and MEG astigmatism. These values are included in the fitting routines as a constant added to the constant translation term in the quadratic fit, and are approximately +53 μm for the MEG and -25μm for the HEG. Including the astigmatism terms improves the fits, as is shown in Table 6.12 below, where we show fit parameters after fitting with and without the astigmatism. Graphs of the astigmatic fits are given in Figure 6.35.

The HETG provides only a minor aberration to the HRMA focussed rays, so the separation in the MEG/HEG focus distances, and the primary/cross dispersion astigmatism should be dominated by the HRMA focal properties.

Table 6.12: Linear Fit Results for '1.001 and '1.003 Data Sets.

Grating	Data	Translation (Y) (mm)	Translation (Z) (mm)	Tilt (arcmin)	reduced χ^2
No Astigmatism in Model					
MEG	1.001	0.115 ± 0.008	same as Y	1.9 ± 1.2	11.8
"	1.003	0.129 ± 0.017	same as Y	-1.1 ± 1.3	2.3
HEG	1.001	-0.238 ± 0.017	same as Y	-3.5 ± 1.5	4.5
"	1.003	-0.195 ± 0.017	same as Y	-3.6 ± 1.4	3.3
With Astigmatism in Model					
MEG	1.001	0.072 ± 0.008	0.126 ± 0.008	1.8 ± 1.2	7.3
"	1.003	0.092 ± 0.017	0.145 ± 0.017	-1.3 ± 1.3	1.8
HEG	1.001	-0.220 ± 0.017	-0.245 ± 0.017	-3.6 ± 1.5	3.3
"	1.003	-0.177 ± 0.017	-0.202 ± 0.017	-3.6 ± 1.4	3.7

Lookin at the graphs, is immediately apparent that the fits are dominated by the cross-dispersion direction data. Considering the 1.001 data set, we see good agreement of the fits with the MEG and HEG cross-dispersion direction data, and the HEG data in the dispersion direction. The MEG dispersion direction fit appears poor, primarily as a result of the poor match to the MEG+3 image. Comparing the results to the '1.003 data set, we again see reasonably good agreement in the cross-dispersion fits and the HEG dispersion direction fit. The MEG ± 1 points deviate from the dispersion direction line in a way consistent with pile-up effects explained below. Notice that the MEG ±3 data points agree well with the dispersion direction fit.

In both the '1.001 and '1.003 tests, the T-B Delta-Y results agree well with zero, as we expect. Notice that the MEG ± 1 order images in the '1.003 test deviate, again likely as a result of pile-up. The N-S Delta-Z shows some deviations in the minus orders, but they do not appear to be very significant at the two-sigma level.

Pileup in MEG First Orders

The MEG ±1 extracted regions from the '1.003 and '1.001 are reproduced in Figure 6.36 below. In the '1.001 data and more clearly in the simulations, the line and a small, nearby satellite line are both clearly visible in the dispersion direction (y) graphs. We see the Gaussian fit keys to the main line with no difficulty. However, comparing to the '1.003 test, we find it more difficult to identify the nearby satellite. This is because pile-up in the peak of the line has reduced the peak event rate, hence it is reduced relative to the satellite and surrounding continuum, which are relatively unaffected. The Gaussian fit is no longer as effective at finding the main line. Consequently, the centroid is shifted towards the zeroth order. The effect on the focus depends on the relative shift between the two quadrants being compared. Clearly, MEG -1 Top is less shifted towards the zeroth order than MEG -1 Bottom; the resulting difference in centroid position is larger than it should be. Consequently, we obsevere an exaggerated offset from zero, as seen in the $B_y - T_y$ graph in Figure 6.35. It is harder to tell what we expect from the North and South quadrant fits, but clearly the characteristic zigzag shape of the MEG data in the dispersion direction and T-B Delta Y graphs for '1.003 is a result of pile-up-induced fit errors.

Discussion

Despite the apparent poor fit of the MEG data to the dispersion direction, overall the results for the position of the ACIS-S detector are reasonably good. The translation constants in Table 6.12 indicate that the detector was placed between the MEG and HEG best focii, and the values

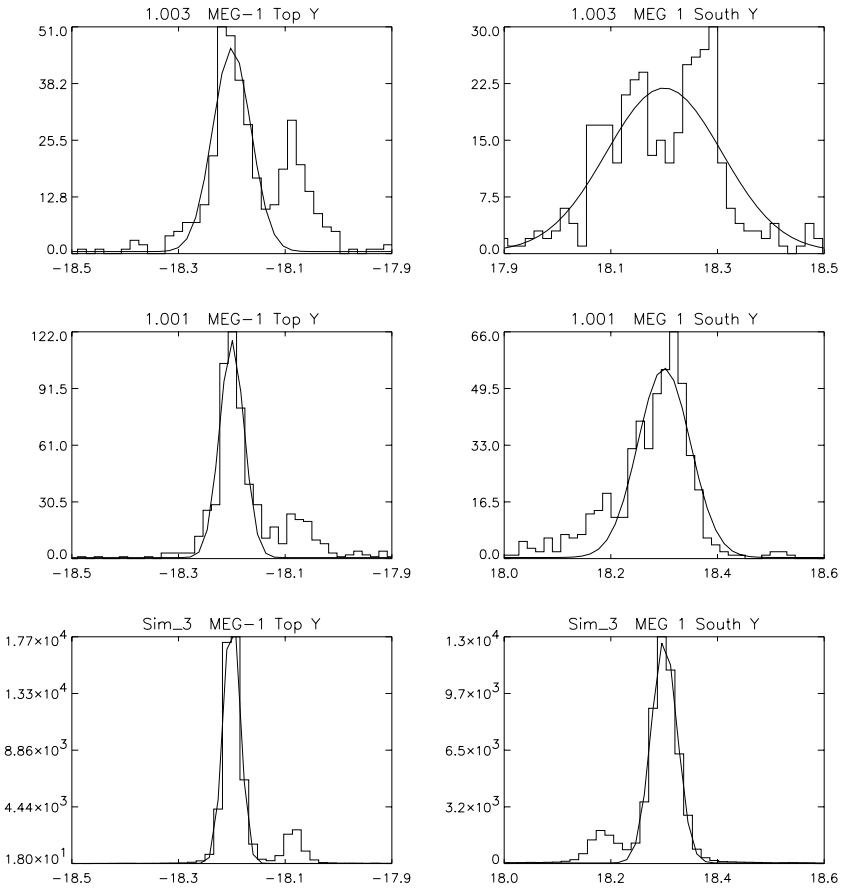

Figure 6.36: MEG Pile-up effects in Al-K line. Pictured at the top are two dispersion direction histograms from the '1.003 data set in which pile-up has degraded the main line peak compared to the smaller satellite. Below them are two examples of the same imaged orders from the lower intensity '1.001 data; we can see the fitting routine largely ignores the satellite line which is has far fewer counts than the main line. At the bottom are the same two orders as fit in the high event count **MARX** simulation; since the simulation is unpiled we see the main line dominates the fits.

Table 6.13: Comparison of MEG and HEG separations

Test	MEG pos (mm) Y	HEG pos (mm) Y	MEG-HEG (mm) Y
1.001	0.072 ± 0.008	-0.220 ± 0.017	0.292 ± 0.018
1.003	0.092 ± 0.017	-0.177 ± 0.017	0.259 ± 0.024
HRMA	0.114 ± 0.001	-0.150 ± 0.001	0.264 ± 0.001
Test	MEG pos (mm) Z	HEG pos (mm) Z	MEG-HEG (mm) Z
1.001	0.126 ± 0.008	-0.245 ± 0.017	0.371 ± 0.018
1.003	0.145 ± 0.017	-0.202 ± 0.017	0.347 ± 0.024
HRMA	0.250 ± 0.001	-0.092 ± 0.001	0.342 ± 0.001

Table 6.14: Two Sigma Tilt Limits

Data	Tilt (arcmin)	Max (arcmin)	Min (arcmin)
1.001	-1.0	3.0	-4.9
1.003	-2.5	1.7	-6.7

from the '1.001 and '1.003 tests agree within two sigma:

$$\text{MEG}: \quad 0.072 \pm 0.008 \text{ mm} - 0.092 \pm 0.017 \text{ mm} = 0.020 \pm 0.018 \text{ mm}$$

$$\text{HEG}: \quad 0.220 \pm 0.017 \text{ mm} - 0.177 \pm 0.017 \text{ mm} = 0.043 \pm 0.024 \text{ mm}$$

In addition, we can compare the separations of the MEG and HEG for the two tests. These values compare well with values derived from the HRMA shell focus offsets for the expected focus of the MEG and HEG (correcting signs to match orientations). These values are given in Table 6.13

We see excellent agreement, between the tests, of the separation expected between the photons arriving from the high and medium energy mirror shells/gratings.

The detector offset results indicate that the detector appears to have been placed between the best focus of the HEG and MEG, which is undoubtedly the best place for it to sit.

The tilt results, by contrast, have large uncertainties. They tell us that, to the accuracy achievable with the limited number of data points, the detector has been placed with a non-statistically significant rotation of about 1 arcminutes about the ACIS-z axis. Freezing the other parameters of the analysis, we examine the χ^2 for the fits for a range of tilt values to determine the two sigma error bar for the tilt measurement. These results combine the MEG and HEG data, and find the best overall tilt on the basis of combined χ^2 for the complete data set. The two sigma error limits are given in Table 6.14.

The overall tilt results, as we might have expected from the separate HEG, MEG results, agree with zero tilt, and slightly favor a rotation of about -1.5 arcminute (closer to the HRMA on the plus order side).

Table 6.15: Chip gap differences

Chip Gap	Inferred Error (mm)	Direction
S0 to S1	0.00087	too small
S1 to S2	0.015	too small
S2 to S3	0.082	too large
S3 to S4	0.013	too large
S4 to S5	0.0048	too small

6.8.3 Analysis By-products

Two useful checks can be extracted from the data analyzed here. One is simply a check on the HEG–MEG opening angle. The centroids can be used to directly determine the angle between the MEG and HEG spectra. The expected opening angle is 9.934 ± 0.008 degrees, Section 11.3.2. The observed spread from fitting the HEG or MEG order centroids is 9.933 ± 0.002 degrees, which certainly agrees nicely.

The second is to check the average locations of the imaged orders against the expected distance along the dispersion axis obtained from the grating formula. Deviations here indicate possible errors in the chip gaps used to do the level 1 processing of this data. The results of these comparisons showed small sized errors in the overall position of imaged orders. The inferred chip-to-chip errors are listed in the table below. Data from the MEG +1 was neglected because it falls so close to the S3/S4 chip gap. It is believed these effects are more likely the result of processing effects (integer pixel chip gaps) than Rowland effects, so to prevent any such calibration errors from affecting the fits here, the theoretical positions were used for fitting the detector location.

6.8.4 MARX Simulations

The **MARX** simulator provides the ability to simulate XRCF shutters, so simulation of these XRCF tests is possible. A custom SAOSAC ray-trace was used as the input for our simulations. **MARX** simulations were used to verify the analysis technique, and also revealed that the **MARX** shutter codes are "Bottom-North-Top-South." Using a **MARX** development version (2.17), a high event count simulation of the XRCF SF tests was run to create an event pool for Monte Carlo simulations discussed below. Pile-up effects were not simulated. To recreate XRCF conditions, the following changes were made to the **MARX** parameter file to account for the finite source distance and other variations from flight configuration:

- SourceDistance,r,a,537.583,,,"Enter Source distance (meters) (0 if infinite)"
- DetOffsetX,r,a,-194.832,,,"Enter Detector X offset from nominal (mm)"
- SpectrumType,s,a,"FILE","FLAT—FILE",,"Select spectrum type"
- SpectrumFile,f,a,"H-HAS-PI-1.001.spec",,,"Enter input spectrum filename"
- SAOSACFile,s,a,"H-HAS-PI-1.001-s.fits",,,"Enter marx input source/output ray filename"
- SAOSAC_Color_Rays,b,a,yes,,,"Color SAOSAC rays?"
- HRMABlur,r,h,0.300100,0.0,,"Enter HRMA Blur angle (arc seconds)"

- HETG Sector1 File,f,h,"/nfs/spectra/d8/MARX/HETG-1-facet.tbl",...1-6

- RowlandDiameter,r,h,8587.97,1000,,"Enter Rowland Torus Diameter (mm)"

Most changes adjust for the finite source distance and characteristics of the XRCF source. Note the detector offset and the adjusted Rowland torus preserve the total Rowland spacing, 8588.0mm - (-194.8mm) = 8782.8mm. In addition, the parameter files have to be altered to set the shutters. Separate **MARX** output was created for each quadrant, and the results subsequently concatenated and analyzed with the same software as used on the XRCF data.

The complete, high event **MARX** run has 1,360,839 detected events. When processed, it yields the results in Table 6.16, and plotted in Fig. 6.8.4. We see a separation of the HEG and MEG focal planes of $\delta_{\rm MARX} = 276 \pm 3\mu$m (non-astigmatism data). Not surprisingly, the **MARX** $N_z - S_z$ and $T_y - B_y$ plots show almost exact agreement with zero (the **MARX** HRMA and HETG are highly azimuthially symmetric). There is no significant tilt of the detector.

The **MARX** simulations were also useful for verifying the technique used to analyze the data and assign error bars to the centroid location values. The high event **MARX** run provided a pool of events from which to extract Monte Carlo subsets to test the accuracy of the centroiding fits.

Careful attention was paid to the accuracy of using a Gaussian fit to find the centroid of the imaged "spot"s. Given that most orders contained only a few hundred counts, was it possible that these events were highly or disproportionately scattered events? Was the width of the Gaussian smaller than the possible offset that a small number of scattered events could produce, particular in the highest orders, such as the HEG -2 image? To answer these questions, an extensive Monte Carlo test was designed using a very high count **MARX** simulation.

For the Monte Carlo test, a very high event count simulation of the SF tests was used as an event pool from which hundreds of data subsets were selected. The subsets contained exactly the same numbers of counts in each imaged order as the real data sets, and histograms were created and centroided using the same programs. The **MARX** simulation used a special set of SAOSAC rays representing the XRCF source as an input.

After determining the centroids for the data subsets, for each imaged order and each quadrant, we calculated the standard deviation of the centroid positions using the positions from all of the Monte Carlo subsets (ignoring any individual gaussian fit sigmas, using only the gaussian means as the centroid position). These standard deviations of centroid position were compared to fit (Gaussian) sigma values from the real data set. The Monte Carlo results showed that the standard deviations of the centroid values were always less than the Gaussian sigmas. The Gaussian fit's statistical error was larger than any random shifts of the mean caused by the low numbers of events.

While our XRCF data fits are better using the astigmatism calculation, the **MARX** simulation results show less consistent improvement. Analysis in which the astigmatism was allowed to vary while holding the other parameters constant showed that the **MARX** simulations favored almost non-existent astigmatism, suggesting that the astigmatism found in the XRCF tests was not included in the SAO raytrace input used in these **MARX** simulations. However, since the astigmatism is a real effect in the mirrors, and our results improve when it is considered, the final values for the XRCF data fits are calculated with the astimatism.

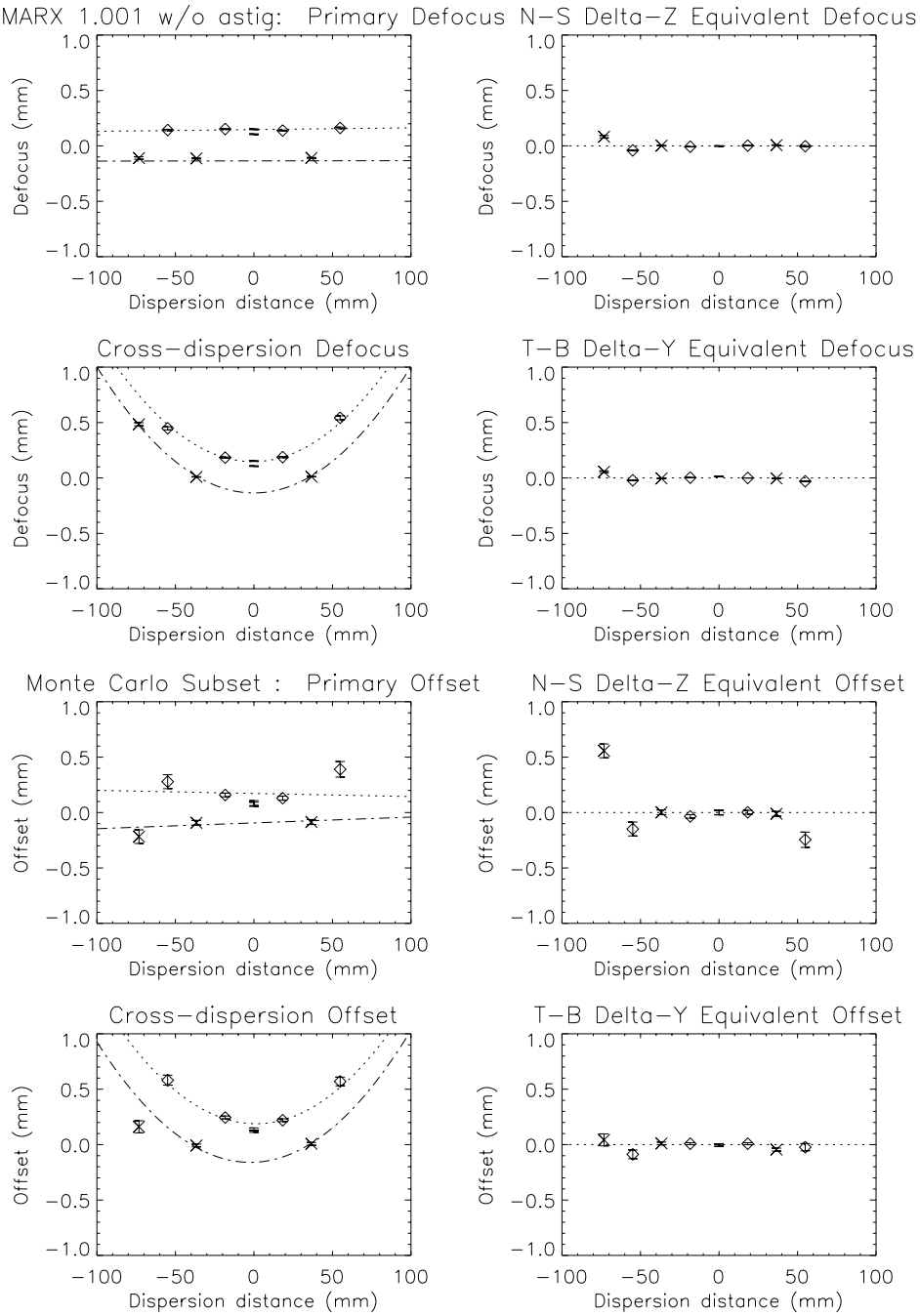

Figure 6.37: **MARX** quadrant shutter test simlulation results for high event and subset data. The upper graphs show the results of the high event count simulation of '1.001. The lower graphs show a subset matched to the number of '1.001 counts in each order, fit with the same programs. The shifts in focus offset of the imaged orders between the two simulations shows the effect that low event rates can have on centroid position. The plots show the focus offsets at each order: HEG results are plotted as squares and dash-dot lines. MEG results are plotted as triangles and dotted lines. The zeroth orders are not plotted as they are not used in fits; however, the zeroth order error bars have been plotted for comparison. Upper left: Linear fit to dispersion direction offsets. Lower left: Quadratic fit to cross-dispersion direction offsets. Upper and lower right: Equivalent offsets for the $N_z - S_z$ and $B_y - T_y$ separations. These points are expected to agree with zero.

Table 6.16: Linear Fit Results for **MARX** Simulations

Grating	Data	Translation (Y) (mm)	Translation (Z) (mm)	Tilt (arcmin)	reduced χ^2
MARX No Astigmatism in Model					
MEG	1.001	0.147 ± 0.002	same as Y	0.54 ± 0.24	3.8
”	1.003	0.144 ± 0.002	same as Y	0.17 ± 0.24	3.8
HEG	1.001	-0.135 ± 0.001	same as Y	0.06 ± 0.11	23.5
”	1.003	-0.138 ± 0.001	same as Y	-0.15 ± 0.12	14.9
MARX With Astigmatism in Model					
MEG	1.001	0.129 ± 0.002	0.183 ± 0.002	0.59 ± 0.24	24.4
”	1.003	0.126 ± 0.002	0.180 ± 0.002	0.27 ± 0.24	25.2
HEG	1.001	-0.115 ± 0.001	-0.140 ± 0.001	0.10 ± 0.12	1.3
”	1.003	-0.118 ± 0.001	-0.143 ± 0.001	-0.11± 0.12	3.5

6.8.5 Conclusions

While the XRCF test data suffers from both low counts in the high orders, and pile-up effects in the lower orders, as well as containing only a relatively small number of imaged orders, it is sufficient to verify that the Rowland geometry is correct. The ACIS-S detector is placed between the MEG and HEG best foci, and there is no statistically significant tilt (rotation) of the detector determinable with this data. The quadrant pairs which test asymmetry show some deviations from zero, but do not appear to be highly significant. The separation of the HEG and MEG foci is recoverable from the data and agrees well with both similar HRMA XRCF tests and **MARX** simulations. The astigmatism in the mirror shells is also recoverable and agrees well with that inferred from the HRMA tests. There are no indications of serious deviations from the Rowland geometry.

6.9 LRF Synthesis

Objective: Provide a synthesis of the LRF measurement and conclusions regarding the accuracy of the **MARX** modeling of the HETGS LRF.

Section 7

XRCF Efficiency and Effective Area Measurements

7.1 Overview

7.1.1 Diffracted Order Sign Convention

Note: By convention the sign of a diffracted order is given by the corresponding sign of the image location reported by the detection system:

Phase 1, HXDS – the $m = +1$ order is in the $+Y_{\rm xrcf}$ direction

ACIS-2C – the $m = +1$ order is in the $+Y_{\rm xrcf}$ direction

ACIS, HRC – the $m = +1$ order is in the $+Y_{\rm Det}$ direction, that is in the $-Y_{\rm xrcf}$ direction

7.1.2 Effective Area

One of the key calibration activites to be carried out at the XRCF is the measurement of the effective area of the AXAF. For the HETGS this effective area depends on the performance of the HRMA, HETG, and ACIS-S, that is:

$$A_{hetgs}(E, m, \text{mode}) = \sum_{s=1,3,4,6} A_s(E)\ G_s(E, m)\ QE_{acis}(E, \vec{X}, \text{mode}). \tag{7.1}$$

where the three contributing elements are the HRMA single shell effective areas (A_s), the effective HETG grating efficiencies (G_s) for the mirror shells, and the ACIS-S photon detection efficiencies (QE_{acis}). Here E denotes the dependence on energy, m the diffraction order, *mode* the event identification in the CCD (here, for example, we will consistently use the sum of

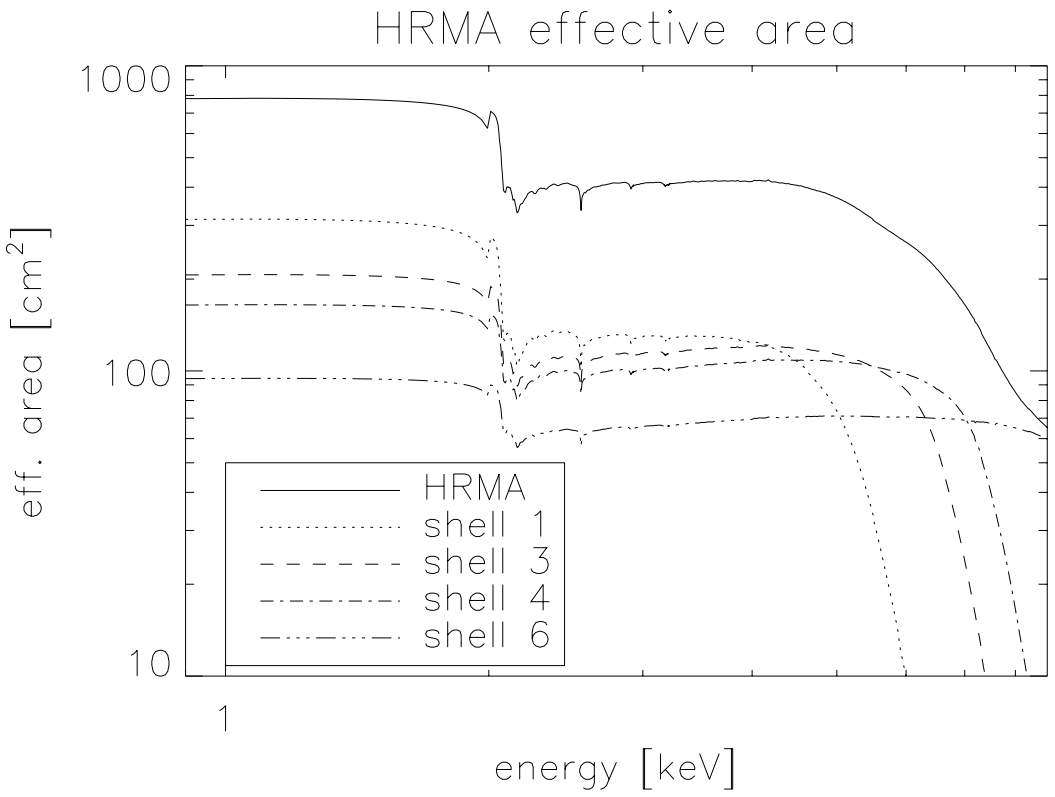

Figure 7.1: HRMA effective areas. The straight line shows the total area, followed by the ones for each shell (courtesy of the AXAF MST).

ASCA grades 0,2,3,4,6 and TE-mode), and the $\vec{X}$ dependences from spatial dependencies in the detector array, i.e FI/BI efficiencies and gap locations between the devices.

Figure 7.1 shows the total AXAF HRMA on-axis effective area at XRCF and its contributing single shell areas. Mirror shells 1 and 3 cut off at energies around 5 and 6.5 keV, while shells 4 and 6 extend up to 7 and 9 keV. The decrease near 2 keV is due to the iridium M-edge in the reflective mirror coating. The effective area sum, equation 1 above, then adds s = 1 and 3 for the MEG area and 4 and 6 for the HEG area.

The grating efficiencies have been determined from laboratory measurements, Section 4.2, where the diffraction efficiency of each flight grating was measured at several energies and orders and positions within each facet. Figure 7.2 show the predicted efficiencies for MEG and HEG. Displayed are the zeroth order (solid line) and the 1st and 3rd positive order in MEG, and the 1st and 2nd order in HEG, which are the dominant orders for each grating.

In general each CCD device has its own characteristics. However, since not all quantum efficiency functions are yet avalable, we have to use templates for each CCD type. Figure 7.3 shows the quantum efficiencies for the FI device in I3 of the imaging array versus the BI device in S3 of the spectroscopy array. The functions already include the transmission characteristics of the flight filters. The use of these templates is reasonable since FI devices are quite similar and we only expect systematic deviations of the order of 5%. The difference between the two BI devices (S1, S3) should not be significantly larger. However, as we will show during the analysis, the

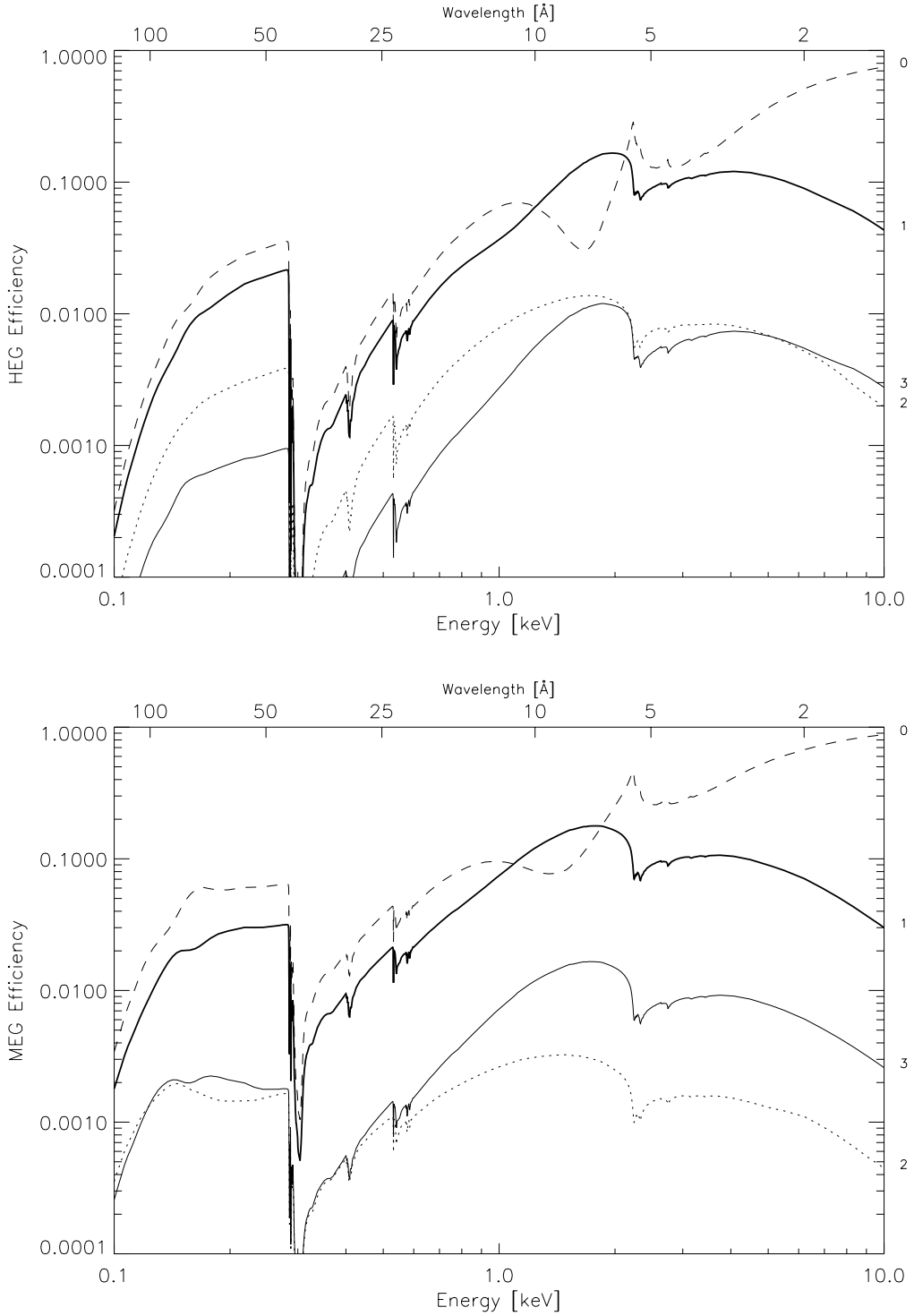

Figure 7.2: HEG and MEG diffraction efficiencies based on ground data. These single-sided efficiencies are the HEG and MEG efficiencies averaged over the sets of facets and weighted by the mirror shell areas. The diffraction order is labeled by the integers to the right of the plots. These are version N0004 efficiencies.

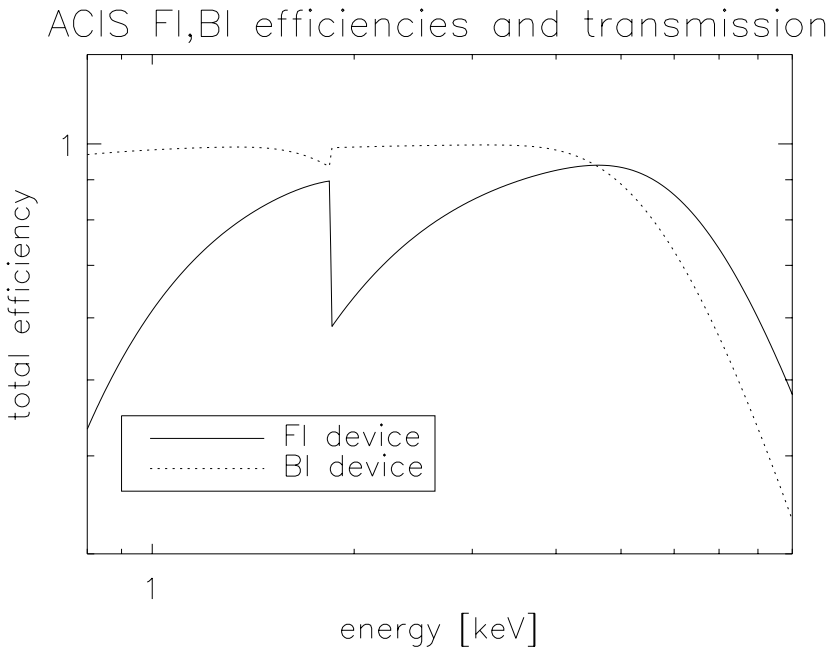

Figure 7.3: ACIS-S efficiencies. The product chip quantum efficiency times optical blocking filter filter transmission is plotted as a function of energy for the FI device I3 in ACIS-I and for the BI device S3 in ACIS-S (courtesy of the MIT ACIS team).

differences are visible in the data.

7.1.3 Divide and Conquer

An important step in the effective area calibration process is the division of XRCF testing into Phase 1 and Phase 2. In Phase 1 more traditional X-ray detectors are used to test the HRMA and HETG; this removes the flight detector complexities, uncertainties, and limitations. In this phase it is useful to consider the *optic effective area (OEA)* which represents the ability of the optics to collect photons at energy $E_{\rm line}$ into order m. This quantity does not include the detector quantum efficiency and so is a property of the optics only:

$$OEA_{2\pi}(E_{\rm line}, m) = \frac{\text{focal plane photons/s in line}-\text{order}}{\text{source flux in line}} \quad [\frac{\text{photons/s}}{\text{photons/cm}^2\text{s}} = \text{cm}^2] \qquad (7.2)$$

Note that we get the usual cm^2 units, as for example in the HRMA-only effective area analysis[51]. The subscript "2π" (steradians) is used to indicate that this is the effective area over the full focal plane (half sphere) behind the HRMA and includes all structure in the diffracted order, *e.g.*, LEG support structure pattern. Low-level scattering by the HEG, Sections 3.3 and 6.6, is not considered a contribution to these integer diffraction orders, however. From a prediction or modeling point of view, the optic effective area for the mirror-grating combination is calculated from the following terms:

$$OEA_{2\pi}(E_{\rm line}, m) = \sum_{s=1,3,4,6} A_s(E_{\rm line})\ G_s(E_{\rm line}, m) \tag{7.3}$$

where the terms have been defined in Section 1.4.1. Going a step further, the ratio of optic effective areas can be used to measure the grating diffraction efficiency $G_s(E_{\rm line}, m)$ itself.

7.1.4 Order Ratios

A further simplification in the experiment can be made by measuring the grating efficiency as a ratio of grating-in to grating-out effective areas. This technique reduces the dependencies on the properties of the mirrors, detectors, or X-ray source.

Finally, for higher orders, the ratio of the higher order to the first order can be determined. These results can be compared with subassembly predictions. This approach has several advantages. It is not necessary to know the incident beam flux, mirror response, or absolute detector efficiency. The beam need not be spectrally pure, since only dispersed orders are used in this analysis. However, variations in detector uniformity must be considered, as they can affect the result, that is:

$$\frac{R_{\rm m^{th}}}{R_{\rm 1^{st}}}(E) = \frac{QE_{\rm Det}(E, \vec{X_m}) \sum_{s=\rm config} A_s(E) G_s(E, m)}{QE_{\rm Det}(E, \vec{X_1}) \sum_{s=\rm config} A_s(E) G_s(E, 1)} \tag{7.4}$$

where $QE_{\rm Det}(E, \vec{X_*})$ is the quantum efficiency of the detector at the different detected spatial regions ($m^{\rm th}$ and 1st orders) and the other terms have been previously defined. Note that the case where $m = -1$ is useful for uncovering detector uniformity effects and is applied to the flight detectors in Sections 7.7 and 7.9.

7.1.5 Test Strategy and Overview

The 1st-order HRMA-HETG effective area curves can be divided (somewhat arbitrarily) into 5 regions where different physical mechanisms govern the effective area of the optical (mirror-grating) system:

below 1 keV – The polyimide membrane of the gratings is dominating the area changes, with edges due to C, N, and O.

1-2 keV – The phase effects of the grating cause an increasing enhancement of the diffraction efficiency.

2-2.5 keV – Edge structure from the mirror (Ir) and grating (Au) dominates, sharply reducing effective area.

2.5-5.5 keV – Effective area is slowly varying, with some low-amplitude Ir and Au edge structure.

5.5-10 keV – The mirror reflectivity and grating efficiency are decreasing rapidly with energy.

Most of the effective area tests carried out at XRCF, Tables 5.4 and 5.5, were designed to illuminate the HRMA with a near monochromatic beam in order to sample one energy at a time. For example the Phase 1 tests with the EIPS using non-flight detectors, Section 7.4, tests using the ACIS-S and HRC-I as a detectors in order to test the predictions of high order efficiencies, Section 7.10, and tests using the Double Crystal Monochromator in order to examine the HETGS effective area at a wide range of discrete energies, Section 7.7.

In contrast, a set of tests employed the Electron Impact Point Source (EIPS) at high voltage and current in order to obtain a bright continuum, Section 7.8. These data can then be used to probe for unexpected spectral features or deviations near the sharp M edges due to the iridium on the HRMA and gold in the gratings. An original purpose of the tests was to test for molecular contamination on the mirrors by examining the mirror Ir M edge decrement, so the tests were given the designation "MC".

The result of combining these types of effective area tests is confidence in the instrument model in terms of both absolute effective area and detailed variation with energy.

7.2 Alignment Tests

Objective: Compare the defocussed ("ring focus") images with and without the HETG inserted to look for any gross vignetting that would indicate a decentering of the HETG with respect to the HRMA rays.

Using data from the no-grating ring-focus image C-IXH-RF-1.005 (961223/106856) and the grating-in "alignment" image C-HXH-AL-4.002 (961223/106860), the sector-by-sector grating-in/grating-out ratio is measured. The measured ratios are shown in Figure 7.4 for shells 1 and 6 (wide histograms.) Also plotted is a simple estimate of each grating's zero-order diffraction efficiency (from the X-GEF facet measurements) as it varies around the shell. The measured ratios have been adjusted by an overall normalization. This very preliminary analysis shows rough agreement between the measured and predicted efficiency variations; a more detailed analysis should allow vignetting and decenter limits to be placed on the as-installed HETG at XRCF.

To-do:
Re-analyze the images on a finer scale
Use the detailed X-GEF model parameters to create zero-order efficiency values.
Analyze the reference BND data to set absolute scale for normalization.

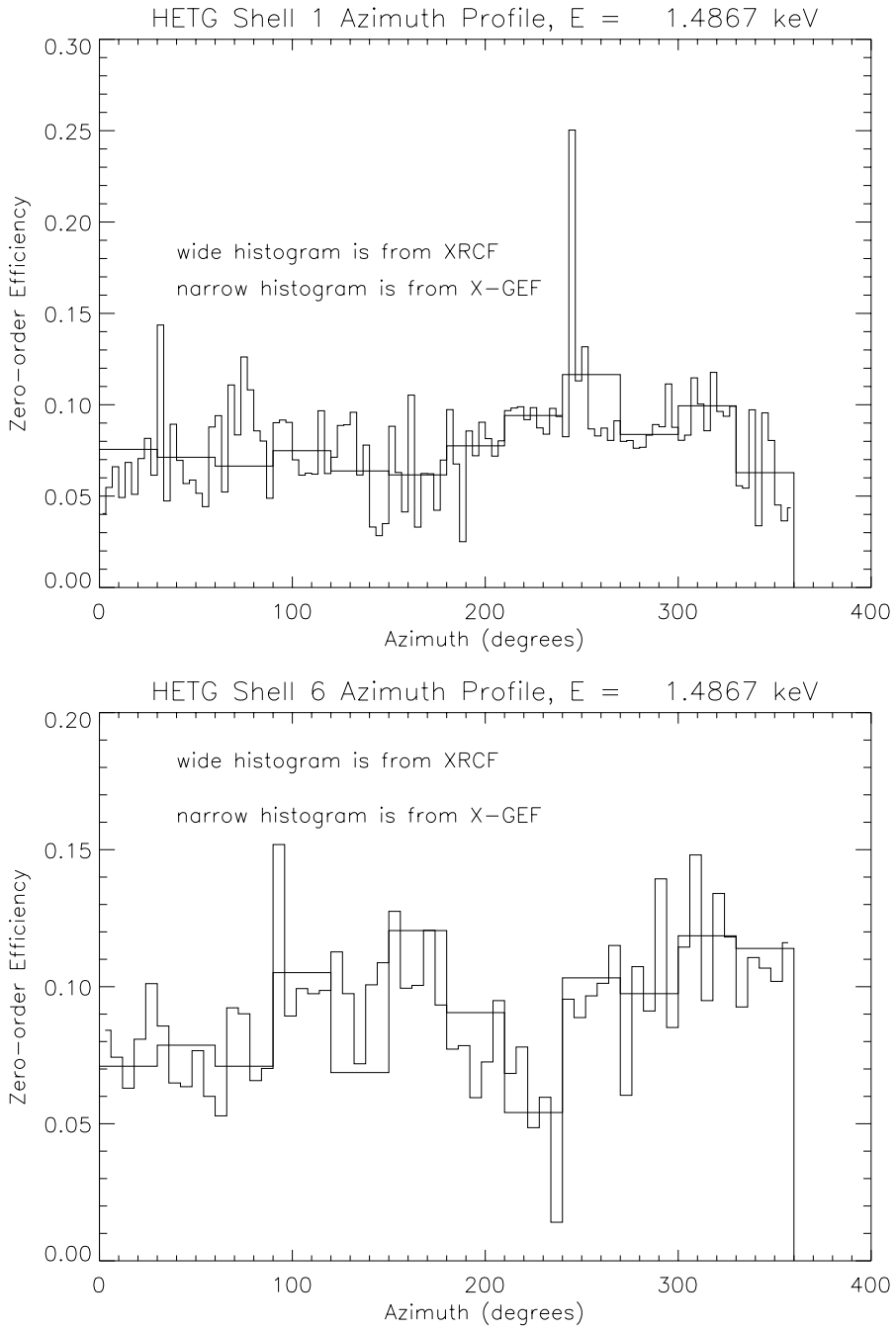

Figure 7.4: "Alignment" Test Results, Shells 1 and 6.

7.3 XRCF Source Characteristics

7.3.1 Source Spectra and Efficiency Measurements

Objective: Use the HSI images of the various source lines to create a grating-derived high resolution spectrum of the source.

During Phase I calibration the HSI detector[26] provided imaging capability at high event rates. Companion HSI exposures were taken for most of the FPC/SSD effective area tests expressly for the purpose of being able to see the dispersed images that the focal plane aperture was sampling. Through application of the grating equation these images also yield high-resolution spectra of the sources; Fe-L and Ti-K HRMA-grating-HSI spectra are shown in Figures 7.6 and 7.5.

The model spectra plotted in these figures consist of a Kramer continuum[22] plus a number of Gaussian lines with widths and intensities set to approximate the HSI-measured spectra. The line energies are fixed at tabulated values for identified lines. Comparison of the measured and modeled spectra has been done by eye, facilitated by the use of normalized cummulative plots, examples of which are shown at the bottom of Figures 7.6 and 7.5. Generally we have spectra of these lines with all three AXAF gratings. Because of the high spectral resolution of the HRMA-grating systems, the actual line widths and shapes can be resolved for many lines especially with the MEG and HEG gratings, *e.g*, the Fe-L and O-K lines here. Other lines, like the Ti-K lines shown in Figure 7.5, are narrower than the instrument resolution and are modeled as delta functions.

Source spectra from grating-HSI observations are available at:
`http://space.mit.edu/HETG/xrcf_sources/sources.html`

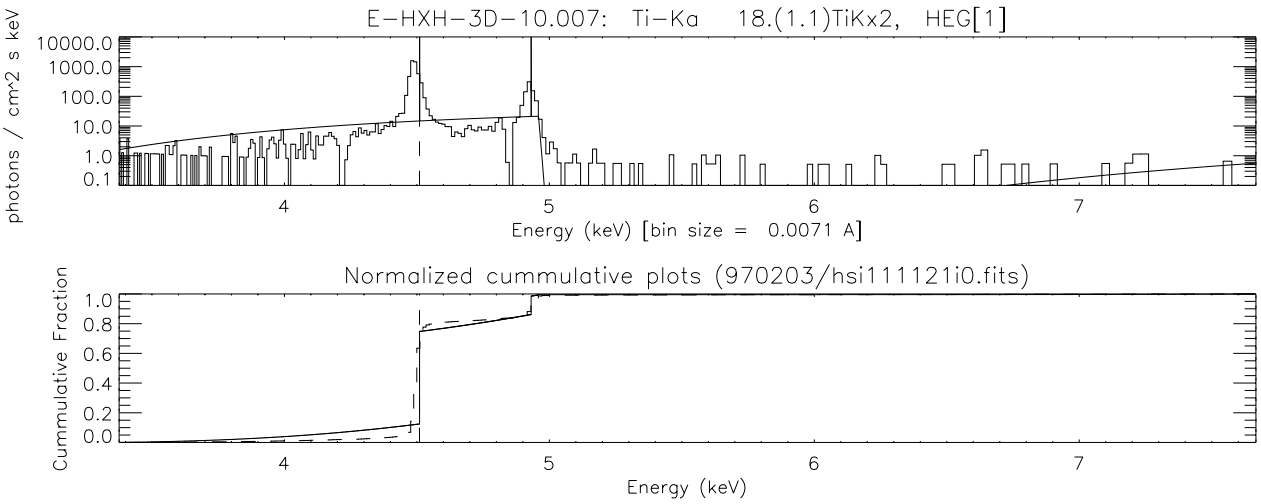

Figure 7.5: Ti-K line: HEG-HSI Spectrum and Model. *Top*: Measured Ti-K flux spectrum, calibrated by nominal parameters for the HRMA, HEG, and HSI; the Ti-Kα and Ti-Kβ lines are well resolved by the HEG dispersion. A model spectrum (solid) is plotted with the HEG-HSI-derived spectrum. *Bottom*: The data (dashed) and model (solid) spectra are compared by plotting the cummulative (integrated) normalized flux within the observed energy range. This plot provides a measured *vs.* modeled comparison of the relative line and continuum fluxes in spite of spectra differences, *e.g.*, here the measured and modeled line widths differ.

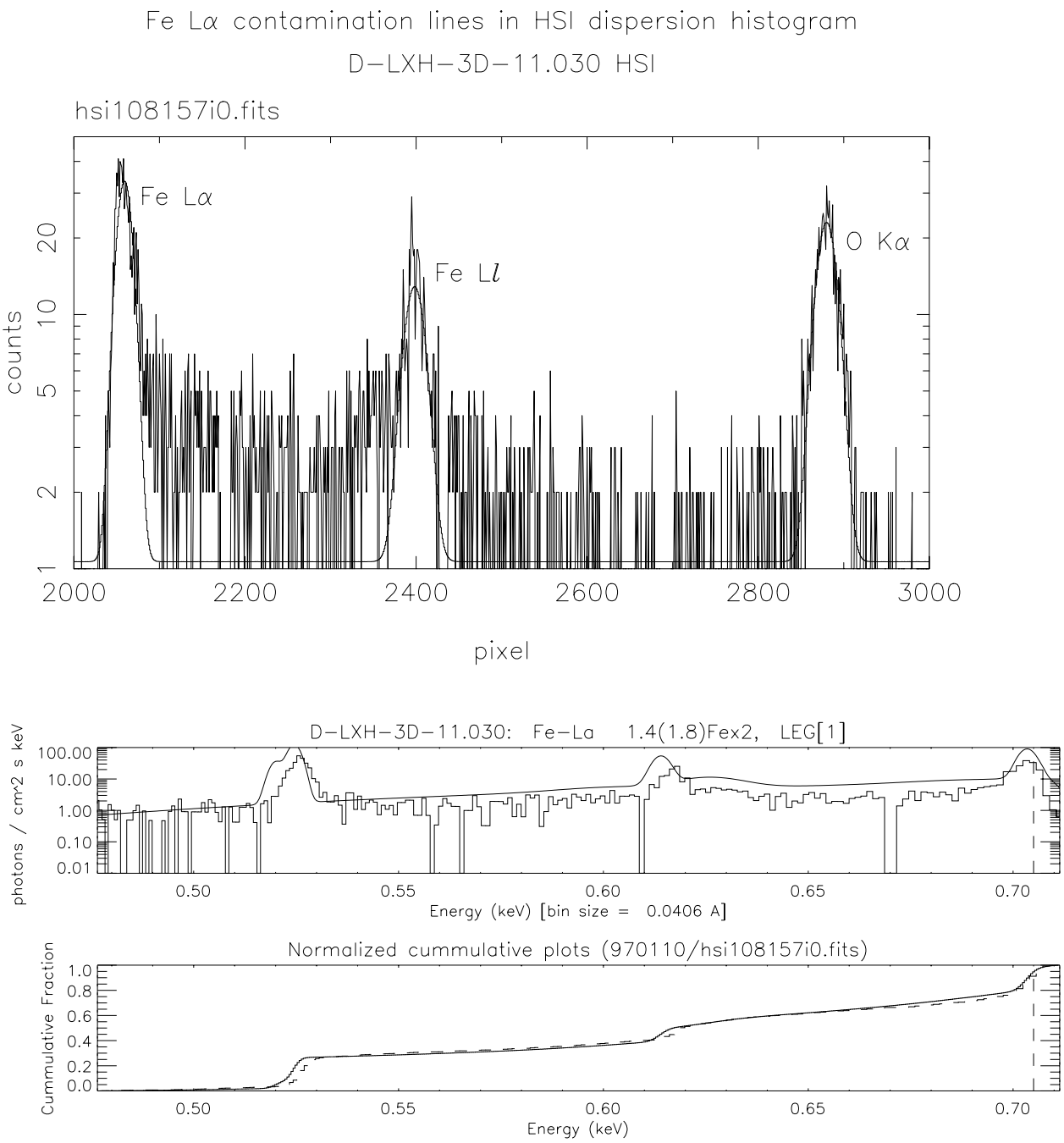

Figure 7.6: Fe-L line: LEG-HSI Spectrum and Model. *Top:* The High Speed Imager (HSI) positioned at the location of the LEG first-order for the Fe-Lα line; the detected events are binned by their location along the dispersion axis ($Y_{\rm xrcf}$). *Middle*: The counts spectrum is converted to a flux *vs.* energy spectrum using nominal calibration parameters for the HRMA, LEG, and HSI. A smooth model spectrum (see text) is plotted with the LEG-HSI spectrum. *Bottom*: The data (dashed) and model spectra (solid) are compared by plotting the cummulative (integrated) normalized flux within the observed energy range. This plot provides a comparison of the relative line (abrupt jumps) and continuum (sloping regions) fluxes in spite of data-model variations in line location, width, and overall normalization, *e.g.*, the small difference in measured *vs.* modeled energies due to inaccurate HSI position analysis.

7.3.2 Beam Uniformity Effects on Efficiency Measurements

Objective: Evaluate the effect of non-uniform illumination on "grating-in grating-out" efficiency measurements in Phase I and on relative efficiency measurements in Phase II.

7.4 Efficiency: Phase 1, EIPS Data

Objective: Derive the diffraction efficiency of the HEG and MEG using Phase I "grating-in grating-out" measurements made at fixed (non-scanned, non-continuum) energies.

Publication(s): Dewey *et al.* [23, 24]

7.4.1 Introduction and Overview

In Phase 1 of AXAF testing at the X-Ray Calibration Facility (XRCF), calibrated flow proportional counters (FPCs) and solid-state detectors (SSDs) were used both in the focal plane and as beam-normalization detectors. This use of similar detectors in the beam and focal plane combined with detailed fitting of their pulse-height spectra allowed accurate measurements of the HRMA absolute effective area with minimum influence of source and detector effects.

This paper describes the application of these detectors and fitting techniques to the analysis of effective area and efficiency measurements of the AXAF transmission gratings, the High Energy Transmission Grating (HETG) and the Low Energy Transmission Grating (LETG). Because of the high dispersion of these gratings the analysis must be refined. Key additional ingredients are the inclusion of detailed X-ray source models of the K and L lines based on companion High-Speed Imager (HSI) microchannel-plate data and corrections to the data based on high-fidelity ray-trace simulations.

The XRCF-measured efficiency values that result from these analyses have systematic errors estimated in the 10–20 % range. Within these errors the measurements agree with the pre-XRCF laboratory-based efficiency models of the AXAF grating diffraction efficiencies.

In this paper we report on progress towards the detailed analysis of the Phase 1 measurements which were designed to measure the grating effective area and efficiency using the FPC and SSD in the focal plane. First the general concepts of effective area and efficiency are reviewed; next the general XRCF Phase 1 measurement configuration is described including summary properties of the gratings and examples of the acquired data and their simplistic analysis. As will be demonstrated, analysis improvements require detailed knowledge of the source spectral composition which we derive from contemporary Phase 1 HRMA-grating-HSI observations of the source. Using the resulting spectra, accurate ray-traces of the system allow us to better understand the FPC/SSD data. Finally, analysis making use of the detailed source spectra and simulations is being carried out to derive accurate grating efficiency values and assess measurement errors.

7.4.2 Measurements and Example Data

In this paper we focus on the Phase 1 measurements that used the conventional electron impact X-ray source (EIPS) and that had either the FPC or SSD as the focal plane detector. There are of order 160 grating measurements of this kind and over 50 no-grating measurements of direct relevance.

The measurement process involved positioning the detector aperture D at one or more locations in the focal plane and acquiring simultaneous pulse-height spectra from the focal plane detector

and the BNDs. We illustrate our analysis methods with example data sets taken with the Fe-L and Ti-K source lines, Table 7.1. Note that non-grating measurements were made as well (Grating = NONE) to allow a direct measurement of efficiency by dividing the grating-in by the grating-out effective areas.

Examples of the pulse-height spectra obtained for some of these Ti-K and Fe-L measurements are presented and described in Figures 7.7 and 7.8.

Table 7.1: XRCF Phase 1 Grating Effective Area Measurements at Ti-K and Fe-L. These measurements are used to illustrate the analysis. A two-mean-free-path source filter was used with these measurements to reduce above-line continuum. For the Ti-K measurements a $D = 2.0$ mm aperture was used; for the Fe-L measurements $D = 1.0$ mm. The BND detector FPC_HN was fully open for all measurements here except for '9.004 where it was closed to a nominal 36 mm diameter.

TRW-ID	Source	Shells	Grating	Orders	date/runid/iteration
E-IXF-3D-9.001	Ti-K,TiKx2	1,3,4,6	NONE	–	970203/111140i0
E-HXF-3D-10.001	”	4,6	HEG	1,2,3,0,-1,-2,-3	970203/111126i0–’i6
E-HXF-3D-10.002	”	1,3	MEG	1,2,3,0,-1,-2,-3	970203/111123i0–’i6
E-LXF-3D-9.004	”	1,3,4,6	LEG	1,-1	970203/111144i0,’i1
D-IXF-3D-11.003	Fe-L,Fex2	1,3	NONE	–	970110/108163i0
D-IXF-3D-11.004	”	4,6	NONE	–	970110/108164i0
D-HXF-3D-11.020	”	4,6	HEG	1,0,-1	970110/108161i0–’i2
D-HXF-3D-11.019	”	1,3	MEG	1,0,-1	970110/108162i0–’i2
D-LXF-3D-11.018	”	1,3,4,6	LEG	1,0,-1	970110/108165i0–’i2

7.4.3 Problems with Effective Area Analysis

A simple calculation of the measured optic effective area, Equation (7.2), from the pulse-height spectra would be:

$$OEA_D(E_{\rm line}, m) \;=\; \frac{R_{\rm fp}}{QE_{\rm fp}(E_{\rm line})} \Big/ \frac{R_{\rm BND}}{A_{\rm BND@HRMA} \;\times\; QE_{\rm BND}(E_{\rm line})} \qquad (7.5)$$

The subscript D indicates the measured optic effective area is into a finite focal plane aperture. The detector rates R are the counts per second in the pulse height “bumps” and the BND effective area $A_{\rm BND@HRMA}$ is the equivalent geometric area of the BND detector at the HRMA aperture and, together with the quantum efficiencies QE, provides the absolute calibration.

There is poor agreement between this simple analysis and our expectations especially for the dispersed $|m| = 1$ effective areas which are shown in Figure 7.9 and often appear lower than predicted. As the next sections will show, the source spectra often consist of multiple lines which are not resolved by the FPC detectors but are spatially separated in the focal plane by the grating diffraction. Thus, the BND is measuring several lines while the focal plane detector because of its finite aperture may be seeing only one or a fraction of the source lines. By measuring the source spectra and simulating the measurements we can implement improved analysis techniques.

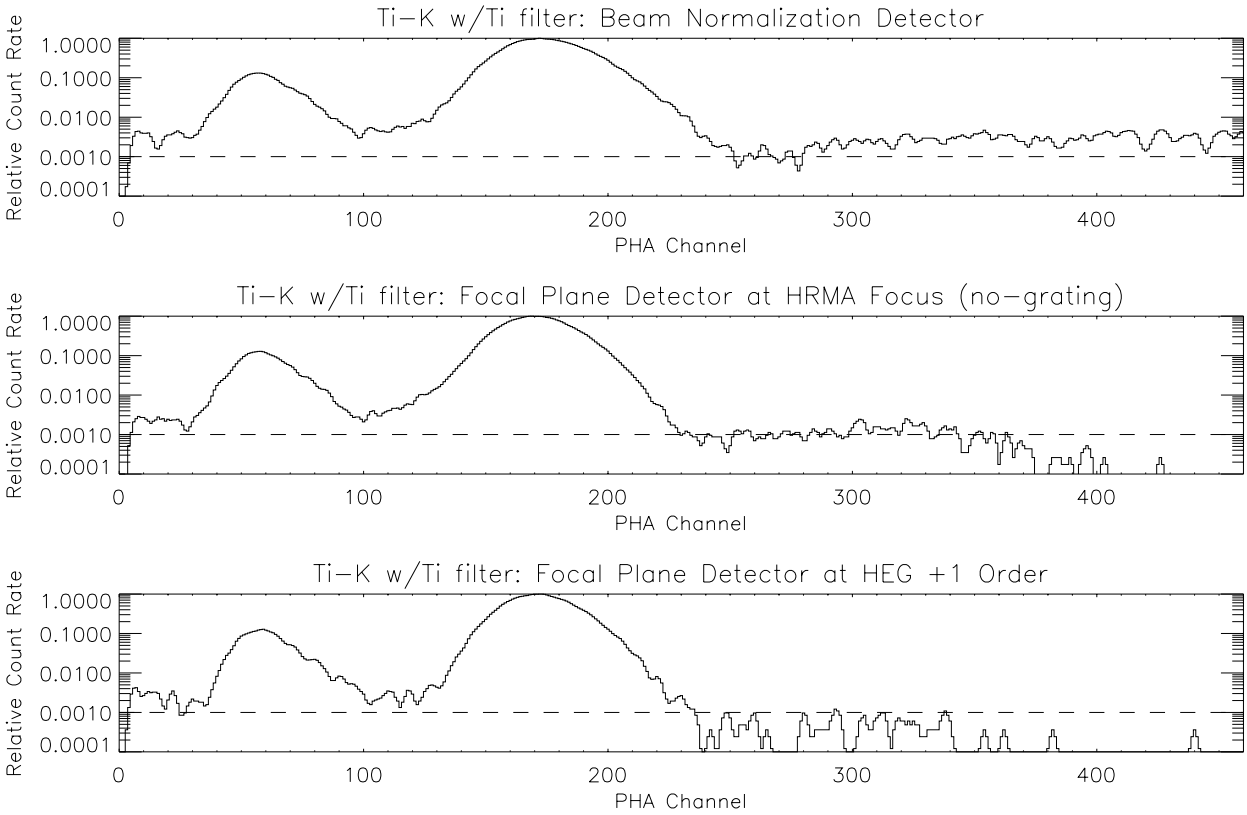

Figure 7.7: Examples of FPC Spectra for Ti-K Tests. The main features at this high energy, 4.51 keV, are the main photo-peak around channel 170 and the Ar escape peak around channel 60. *Top*: the spectrum seen by the BND FPC_HN directly viewing the source, continuum well-above the line energy is visible (channels 280 and up). *Middle*: the spectrum from FPC_X2 in the focal plane after the HRMA (no grating): the high-energy cutoff of the HRMA is visible in the continuum above channel 370. *Bottom*: the spectrum at the HEG $m = +1$ diffraction order – the detector here is seeing an essentially monochromatic input of the Ti-Kα line. To better show the differences in continuum, the histograms here have been smoothed and a dashed reference line at a relative rate of 10^{-3} has been included.

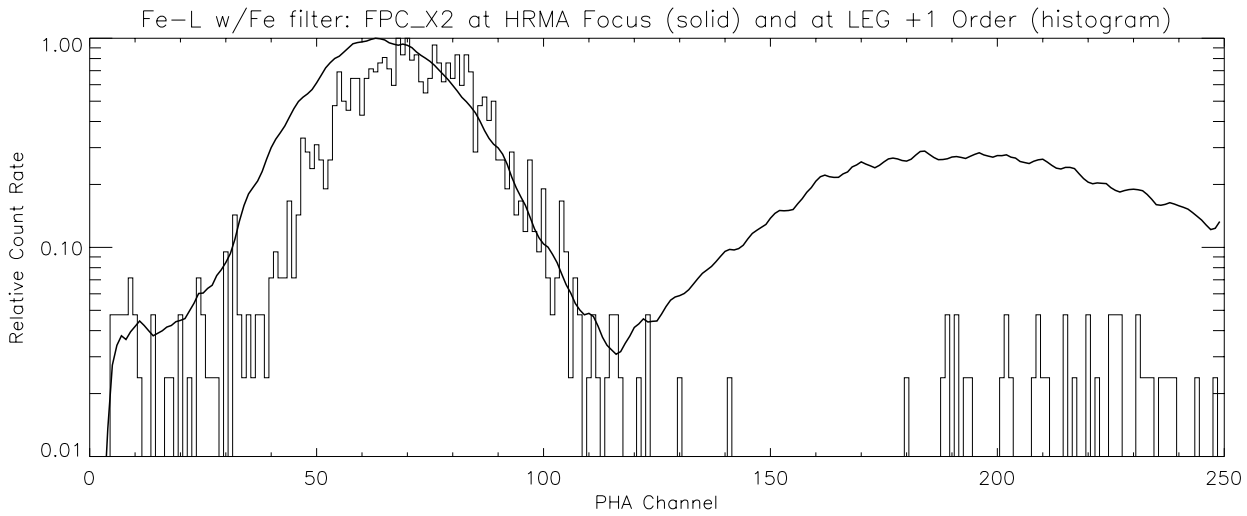

Figure 7.8: Examples of FPC Spectra for Fe-L Tests. The histogram-style curve shows the spectrum seen at the LEG $m = +1$ order: this is the monochromatic response to the 0.705 keV Fe-Lα line with some 2.1 keV $m = 3$ continuum counts around channel 220. The smoothed solid line shows the FPC_X2 spectrum at the HRMA focus without a grating (BND spectra are comparable): the "Fe-L bump" is visible peaking at channel 65 and continuum above the filter edge appears above channel 120. The extension of the bump to lower energies is due to the presence of unresolved lines, see Figure 7.6.

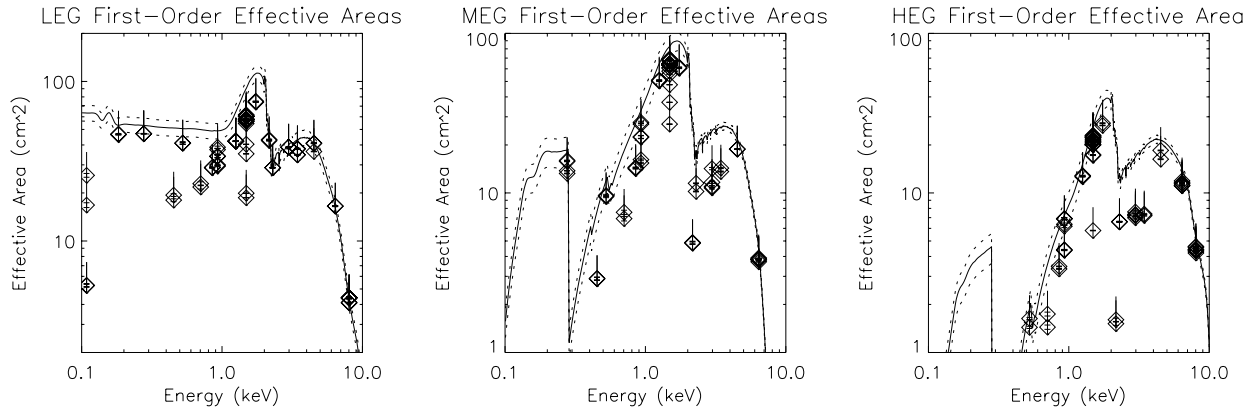

Figure 7.9: The problem with the standard effective area analysis: these plots show the grating first-order effective areas, calculated from simply extracted, uncorrected count rates, compared with model predictions[90]; these first-order effective areas are often measured low due to the presence of multiple and contaminating lines in the source spectrum.

7.4.4 Ray-trace Simulation of Phase 1 Measurements

It would be straight forward to use the grating equation and parameters of the measurement to decide which region of the detailed source spectrum will fall in the detector aperture D. While this approach works, it has difficulty including a variety of effects such as: broad lines that may overfill the aperture D, HRMA and grating PSF effects which blur the events, higher grating diffraction orders of higher-energy source photons, and the LETG support structure diffraction pattern. In the end it is best to accurately model the complete source-HRMA-grating-detector system to completely understand what the detector sees.

The "Model of AXAF Response to X-rays" simulation package[62] (MARX, 2.04) has been used as the engine to produce these simulations. Custom IDL code was produced to create modified MARX parameters for a given XRCF measurement, see Section refsec:marx.

Simulated focal plane images for the the diffracted Ti-K and Fe-L lines are shown in Figure 7.10. These simulations can be used to calculate several quantities relevant to the efficiency measurements being analyzed here:

- The encircled energy correction value $EE_{\rm corr}$ is the ratio of the number of all line events to the number of line events that fall in the aperture.
- The pulse-height distribution of events that are within the detector aperture can be formed and used to estimate what fraction of the measured count rate is due to a given line or feature in the sectrum.
- The simulations can also be used to assess the sensitivity of either of the above values to variations in the aperture placement in the focal plane.

The use of these simulation-derived values is described in the context of our efficiency analysis in the next section.

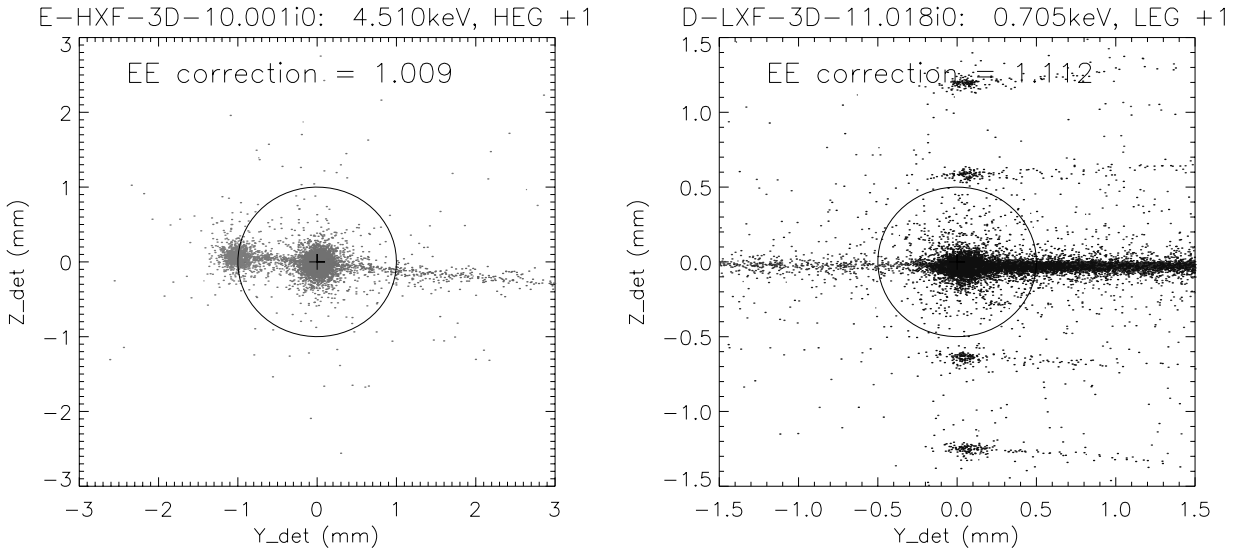

Figure 7.10: Ti-K and Fe-L simulated first-order images. In order to better undestand the FPC/SSD aperture measurements, the AXAF ray-trace package MARX was adapted to simulate XRCF measurements. These figures show the spatial distribution of events relative to the detector aperture used in the measurement. *Left*: The FPC aperture, 2 mm diameter circle, is centered on the Ti-Kα line; the Ti-Kβ line, at aperture edge, is partially included in the aperture and hence in the resulting pulse-height spectrum. The EE correction value of 1.009 indicates that very little of the Ti-Kα line flux is outside of the aperture. *Right*: Simulation of this Fe-Lα measurement clearly shows the LETG coarse-support diffraction pattern extending in the cross-dispersion direction, $Z_{\rm det}$. The bright continuum on the low-energy (right) side of the line is cut off by the Fe-L filter just above the line. The continuum streak to the high-energy side (left) of the Fe-Lα peak is actually 2.1 keV continuum that has been diffracted into the LEG +3 order.

7.4.5 Analysis Formalism

Now that we've seen the source and aperture effects, it is clear that the "failure" of the analysis specified by Equation (7.5) is due primarilly to inaccurate or contaminated values for the measured rates and the effects of the aperture. In addition, the best estimate of the effective flux at the HRMA entrance requires a detailed beam uniformity analysis and consideration of data from all of the BND detectors. These effects are included in the revised equations:

$$OEA_{2\pi}(E_{\rm line}, m) = EE_{\rm corr} \times OEA_D(E_{\rm line}, m) = EE_{\rm corr} \times \frac{\mathcal{R}_{\rm fp}}{QE_{\rm fp}(E_{\rm line})} \Big/ F_{\rm effective}(E_{\rm line}) \tag{7.6}$$

$$F_{\rm effective}(E_{\rm line}) = \left\langle \frac{BU_{\rm corr}\ \mathcal{R}_{\rm BND}}{A_{\rm BND@HRMA} \times QE_{\rm BND}(E_{\rm line})} \right\rangle_{\rm BNDs} \tag{7.7}$$

where the $\mathcal{R}$'s are the rate in a specific line or narrow energy region, an explicit encircled energy correction factor, $EE_{\rm corr}$, converts from the count rate measured in an aperture to the total focal plane rate, and the incident flux is now an average over the properly weighted ($BU_{\rm corr}$) BND measurements taking into account beam uniformity variations[78, 93].

The grating effective diffraction efficiency, Equation (1.5), is measured as the ratio of the optic effective area with the grating in place to the optic effective area without the grating (HRMA-only):

$$G^{\rm meas}_{\rm config}(E_{\rm line}, m) = \frac{OEA^{\rm g}_{2\pi}(E_{\rm line}, m)}{OEA^{\rm H}_{2\pi}(E_{\rm line})} \tag{7.8}$$

where the g superscript refers to grating-in measurement and the H superscript is a HRMA-only measurement.

7.4.6 Count Rate Corrections

In general pulse-height analysis is performed to provide measured focal plane and BND rates, R, in some, possibly broad, energy range. A "line-fraction-correction" L, can be defined for each pulse-height spectrum to convert this measured rate to an estimate of the rate in a line or narrow energy region: $\mathcal{R} = L \times R$. The value of L can be numerically determined from the simulation of a measurement as the ratio $\mathcal{R}_{\rm sim}/R_{\rm sim}$; this requires precise definitions of $R_{\rm sim}$ and $\mathcal{R}_{\rm sim}$, however.

To determine $R_{\rm sim}$ from a simulation, the analysis method itself must be faithfully modeled. In order to determine $\mathcal{R}_{\rm sim}$, that is the count rate in the line, the "line" must be defined. Because some lines are in fact naturally broad and continuum is present in the modelled spectra, it is convenient instead to talk of a spectral "feature"; here a useful and reasonable definition of the feature is "all photons in the range $E_{\rm line} \pm E_{\rm line}/100$" – thus continuum under the line is part of the feature as well.

Substituting $\mathcal{R} = L \times R$ into Equation (7.8), many of the terms will (exactly or very nearly) cancel leaving:

$$G_{\rm config}(E_{\rm line}, m) = \frac{EE^{g}_{\rm corr}\ L^{g}_{\rm fp}}{EE^{H}_{\rm corr}\ L^{H}_{\rm fp}} \quad \times \quad \frac{R^{g}_{\rm fp}/(R^{g}_{\rm BND}/A^{g}_{\rm BND@HRMA})}{R^{H}_{\rm fp}/(R^{H}_{\rm BND}/A^{H}_{\rm BND@HRMA})} \tag{7.9}$$

Thus, the simple count-rate based efficiency, the ratio on the right, is corrected for after-the-fact by simulation-derived parameters. This "feature-fraction" correction (the product $EE_{\rm corr}\ L_{\rm fp}$) can be calculated and applied to different pulse-height analysis methods.

The next sections describe our specific analysis efforts that implement this approach to more accurately calculate the measured grating efficiency. In all cases the $EE_{\rm corr}$ factor is derived from the ray-traces and post-applied. Two of the analysis methods (ROI and "counts-in-bump") have non-trivial L values, the third method ("counts-in-line") includes the source spectral information "upstream" of the pulse-height analysis and so has $L = 1$.

7.4.7 Region-of-interest (ROI) Analysis

The most simple pulse-height analysis method determines a count rate based on the total number of counts in a region of interest, for example the counts in channels 20 through 120 in the Fe-L spectra of Figure 7.8 may be summed. This has the advantage of simplicity and computational speed and robustness. Likewise the quantity $R_{\rm sim}$ can be generated with high accuracy for a coarse region of interest by counting all events in an energy range.

The very robustness of the ROI analysis points to its main defect: because the data are not evaluated with respect to any model there is no check that the assumed model is realistic (except perhaps when the ROI limits are viewed on the pulse-height histogram), errors in lines present, detector operation, continuum levels, etc. can all cause erroneous results without an indication of a "failure" of the assumptions.

For our purposes the ROI analysis with the corrections applied serves as an initial robust result and a sanity check and guide to the more complex and detailed fitting analyses, below. The results of the corrected ROI analysis are shown by the "x"s in Figures 7.13 and 7.14.

7.4.8 JMKMOD "counts-in-bump" Analysis

An improvement on the simple ROI analysis is the detailed pulse-height spectral fitting provided by the JMKMOD software[25, 94]. This software is an add-on package to the XSPEC[102] x-ray spectral fitting package and was created to model the XRCF FPC and SSD detectors. Figure 7.11 shows the application of the JMKMOD model to a Ti-K BND spectrum. Because these detectors cannot resolve the Kα and Kβ peaks, the fitting process is not able to reliably determine accurate count rates for the separate lines – rather the combined count rate in the Kα plus Kβ "bump" is determined.

Two main advantages of this fitting technique over a simple ROI analysis are: i) the measured data are fit by a model and therefore data quality and measurement assumptions are tested

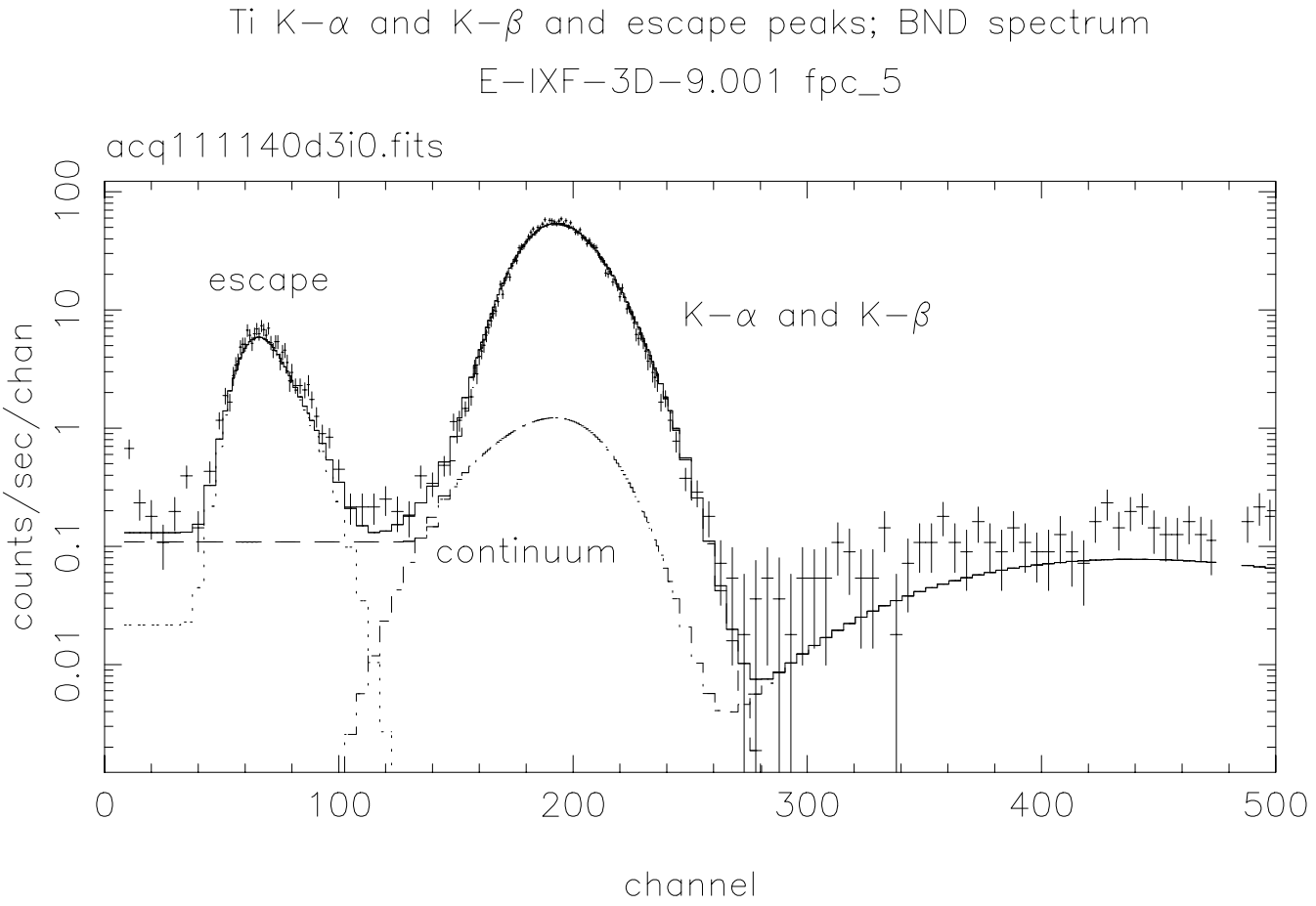

Figure 7.11: JMKMOD fit to Ti-K BND. Three of the components of the JMKMOD spectral model are highlighted here: the main Kα plus Kβ photo-peak, the Ar escape peak, and the broadband continuum generated by the source and given structure by the Ti source filter.

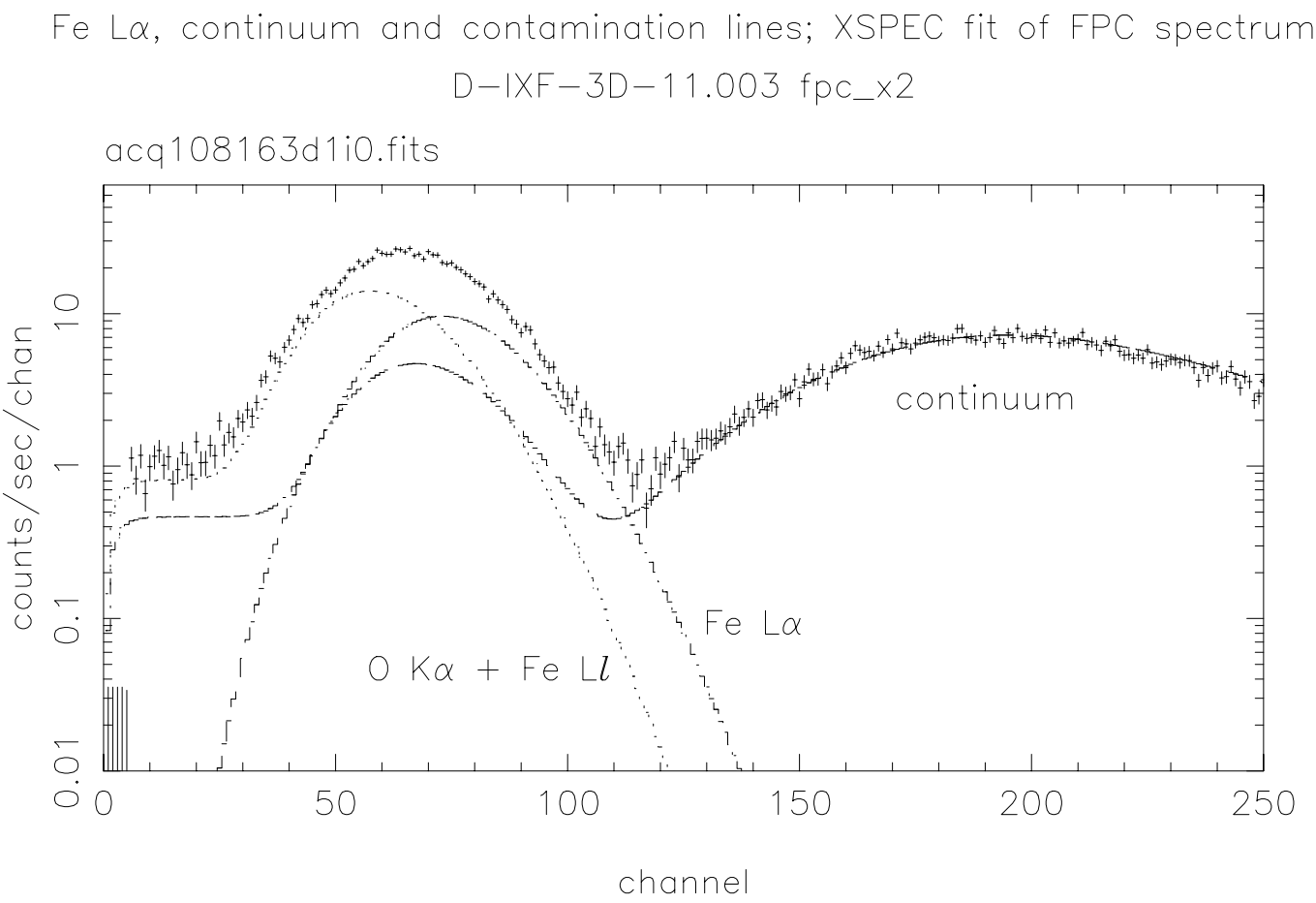

Figure 7.12: JMKMOD fit to Fe-L FPC_X2. In this "counts-in-line" analysis the three known source lines have had their relative intensities fixed based on the HSI-derived relative fluxes; the continuum component is allowed an independent normalization in the fit. The fit intensity of the Fe-Lα line is the rate in the line, that is $L = 1$ and $\mathcal{R} = R$. A good fit to the data indicates an agreement of the source model with the data to an accuracy allowed by the detector resolution and count statistics.

and ii) the continuum level in the spectrum is measured rather than depending on a modeled continuum.

The measured rate R is similar to the ROI rate but does not include a continuum contribution; this requires that slightly different values for the line fraction corrections L be applied in Equation (7.9). As a starting point, however, the efficiency results from this "counts-in-bump" analysis were corrected with the same correction as the ROI results and are shown in Figures 7.13 and 7.14 by the triangular symbols. As in the ROI case, the correction has the greatest effect on the efficiency of the L-lines of Mo, Ag, and Sn; its effect on the Ti-K HEG first-order efficiency is an increase of 9.3 %.

7.4.9 JMKMOD "counts-in-line" Analysis

Rather than applying the L line-fraction corrections to the rates in a region or bump, it is possible to fit the pulse-height spectra using as input a modeled source spectrum. Lines and

features which are resolved in the spectrum can be fit with independent intensities; those that are poorly resolved must have their relative intensities fixed. This technique has the potential advantage over the "counts-in-bump" analysis in that the assumed model is directly tested against each pulse-height data set.

An example of a JMKMOD "counts-in-line" fit to a non-grating focal plane spectrum is shown in Figure 7.12. All three lines in the Fe-L spectrum, have had their relative intensities fixed based on the HSI counts spectrum, Figure 7.6, and modeled HSI, grating, HRMA, and FPC properties. The fit intensity of the Fe-Lα line is then directly the line rate, $\mathcal{R}$, *i.e.*, $L = 1.$.

The only correction required to this analysis is the ratio $EE^g_{\rm corr}/EE^H_{\rm corr}$ which corrects for finite aperture effects; for LEG measurements this correction can be as much as a ≈ 10 % increase. For the dispersed orders of the broad low-energy lines (Be-K and B-K) this ratio must be calculated using an accurate source spectral line shape and source filter transmission curve.

The efficiency results of this "counts-in-line" analysis are shown by the square sysmbols in Figures 7.13 and 7.14.

7.4.10 Discussion

The agreement of the XRCF-measured efficiencies with the laboratory-measurement-based efficiency predictions shown in Figures 7.13 and reffig:megheg0 is a wonderful confirmation of the grating diffraction models and facet-by-facet laboratory measurements: taken on their own, these XRCF Phase 1 EIPS measurements do in general verify the laboratory-based efficiency models at the 10–20 % level in most energy regions.

These analyses are nearly complete, what remains is to study and assign systematic errors to these measurements, *e.g.*, by obtaining error estimates for the HSI-derived source spectra and folding them through the analysis methods. Other potentially large systematic errors yet to be accounted for in the analyses are thought to originate in the FPC detectors in ways that are difficult to account for in the detector models. Apparently subtle effects, such as a bowing outward of the FPC windows due to internal gas pressure and obscuration and reflection of focussed focal plane light by the supporting wire mesh, are calculated to affect HRMA measurements at levels below a percent[51]. However, the former of these effects can be more important at the lowest energies where the detectors and windows are more optically thick: the window bowing alters the effective thickness and location of the window seen by incoming photons, and low energy photons penetrate to smaller depths in the detector. One of the next major challenges is to understand these detector effects and to account for them in the refined spectral modelling process (§6) in order to determine more accurate fluxes at the telescope aperture and focal plane.

In the case of the LETG, which is designed to operate at wavelengths as long as 170 Å (0.07 keV), the lowest energies available for efficiency and effective area measurements—provided by the B (183 eV) and Be (108 eV) EIPS—pose special difficulties because of the very low QE of the XRCF detectors in this regime. Here, detector background and counting statistics can be significant sources of error; during the Be tests for example, the HRMA BND count rates were generally too low to be of any quantitative use for beam monitoring and normalization, and the "Building 500" FPC detector provides the only means of determining the beam flux.

In the near future, these analysis techniques will be applied to the Phase 1 measurements made with a monochromator as the source in place of the EIPS source. The spectral analysis may in general be cleaner (no closely spaced L-lines for example), however the monochromators do

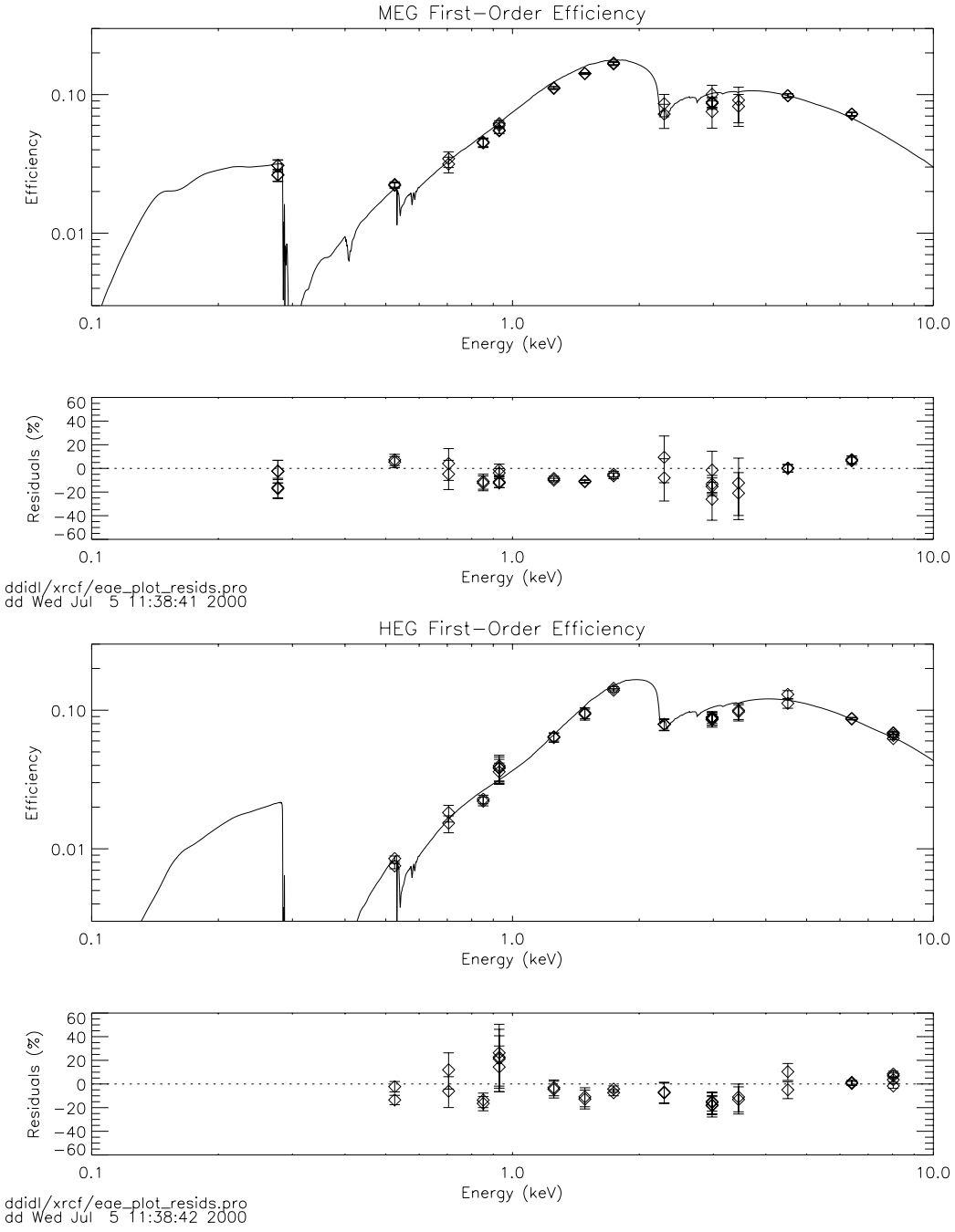

Figure 7.13: Phase 1 XRCF MEG and HEG Efficiencies: 1st order. The measured first-order efficiencies are compared with the pre-XRCF model predictions, based on facet-by-facet laboratory measurements. The plotting symbols indicate the pulse-height analysis methods: "x"s are from region of interest rates (Section 7.4.7), triangles are from "counts-in-bump" rates (Section 7.4.8), and the squares are based on "counts-in-line" rates (Section 7.4.9). Statistical errors are generally less than 3 %; understanding and reducing the systematic errors, estimated to be of order 10–20 %, is an ongoing effort.

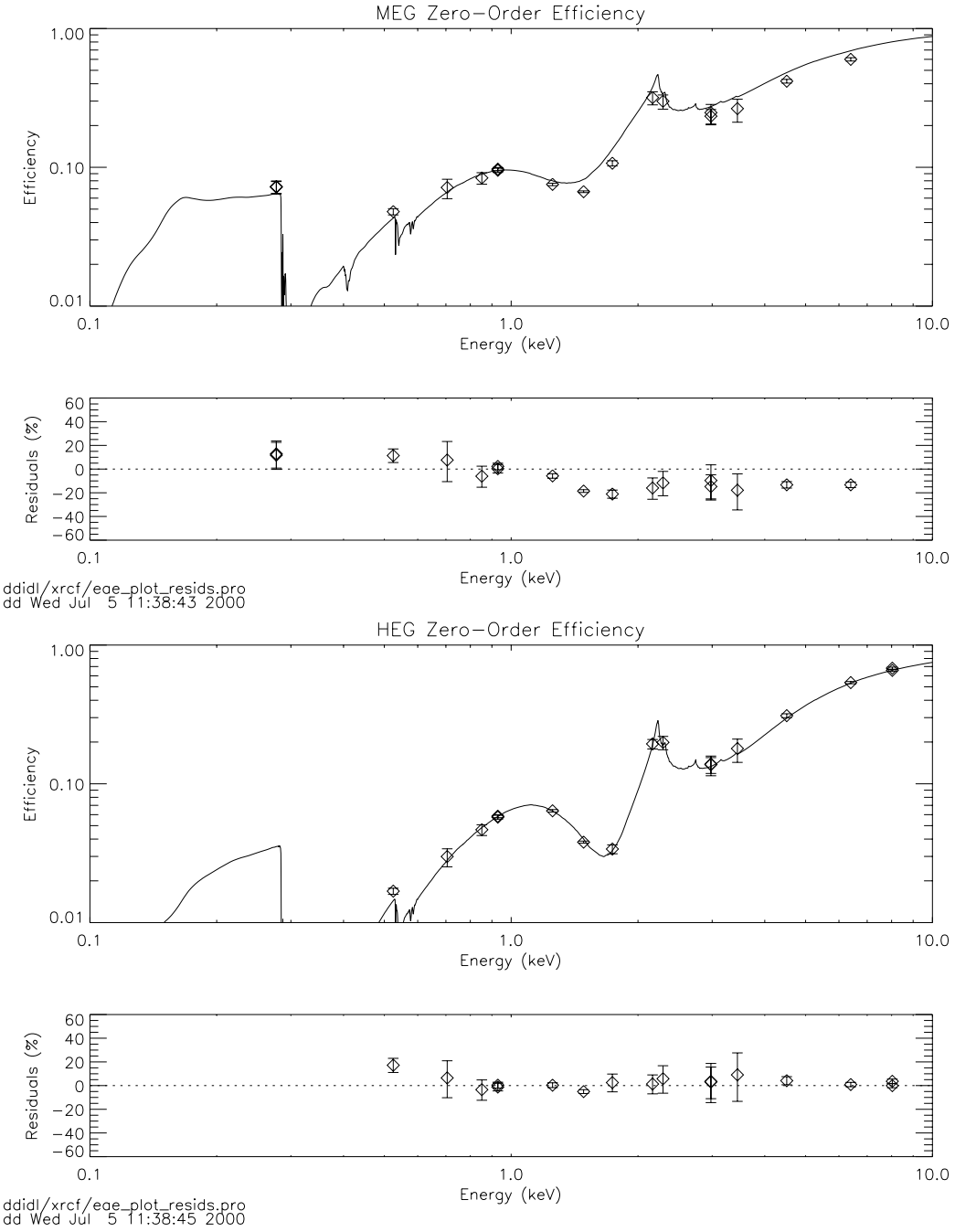

Figure 7.14: Phase 1 XRCF MEG and HEG Efficiencies: 0 order. The measured zero-order efficiencies are compared with the pre-XRCF model predictions, based on facet-by-facet laboratory measurements. The plotting symbols indicate the pulse-height analysis methods: "x"s are from region of interest rates (Section 7.4.7), triangles are from "counts-in-bump" rates (Section 7.4.8), and the squares are based on "counts-in-line" rates (Section 7.4.9). Statistical errors are generally less than 3 %; understanding and reducing the systematic errors, estimated to be of order 10–20 %, is an ongoing effort.

have substantial beam uniformity variations[93] that must be dealt with.

The ultimate target of all our analyses is to produce grating efficiency models that are of sufficient accuracy that they are not a dominant source of uncertainty in the flight HRMA+grating+detector optical system. When all known sources of systematic error have been included in the modelling processes and flux determinations, it is hoped that the final uncertainties in the individual grating efficiency measurements will be as low as 2-3 %. At this level, the XRCF measurements will be capable of providing quite stringent tests of the grating efficiency models.

To-do:

- create ffs_dkr.rdb to have accurate corrections for dk's ratio values.
- Pete to analyze D-LXF-3D-12.003a (in place of '12.003)
- Pete: "too much continuum in XSPEC fits to Fe-L,O-K, Si-K, Ti-L contnorm in 109286, 109287?
- CMDB mods for Be-K D-LXF-3D-12.003a : w/filter and 10 mm aperture and B-K 22.043 (10 mm aperture), re-MARX simulate, new ff corrections
- Improve Si-K line source model, what is 2.03 keV line in Si-K spectra? I think the Zr filter lets this line appear in FPC measurements...: Brad suggests it is W line!
- dd modify his Fe-K Mn filter to include the little lead in it...(is this the one?
- re-do HSI spectral analysis using new HRMA EA curves: check Mo line for any HRMA-induced "lines"?
- Two-step source line intensity process: use HSI spectra to decide what lines are present and then use SSD spectra to set relative normalizations where possible, e.g., Ti-K Ka and Kb.
- include support grid effect in MARX simulations
- resimulate (eae_sim) with new released MARX version
- include DeltaZ aperture errors in feature_fraction error estimate
- Make page or two of HSI source spectra plots...
- Make a no-grating BND simulation too...
- Double check the HRMA 1,3 - 4,6 area fractions used to convert shell measurements to other shell combinations
- Pete's Be and B analysis: broad line over fills aperture.
- Make sure released rdb files have N and S 's in column def.s
- Create simulated .pha files from MARX to check analysis techniques.
- Analyze the Phase 1 monochromator data - easier and harder!

7.5 Efficiency: Phase 1, Monochromator Data

Objective: Derive efficiencies of the HEG and MEG using the monochromator scan data.

7.6 Efficiency: ACIS-2C Data

Objective: Derive the diffraction efficiency of the HEG or MEG using ACIS-2C "grating-in grating-out" measurements made at fixed (non-scanned, non-continuum) energies.

To-do:
Create automated analysis s/w similar to the Phase I Fixed energy analysis.
Generalize the rdb results table (eae_weffics.rdb) to include these '2C results, etc.

7.7 Absolute Effective Area with ACIS-S

Objective: Derive the HETGS(ACIS-S) effective area and compare it to HRMA, HETG, and ACIS-S measurements and predictions. ACIS effects that must be understood include: pileup, grade effects, exposure times.

Publication(s): Schulz *et al.* [90]

XRCF measurements of the flight AXAF High Energy Transmission Grating Spectrometer throughput were used to determine absolute effective areas. The results are compared with component models of the HRMA, HETG, and the ACIS-S. The comparison provides an independent view on HETG efficiencies as well as the detector efficiencies along the dispersion direction. As detailed in Table 5.7, three source configurations were used to measure the absolute HETGS effective area: EIPS, DCM, HIREFS. Of these the most extensive data set is from the DCM and its analysis and results are described.

Using the XRCF double crystal monochromator measurements in the range from 0.9 to 8.7 keV, the effective areas in the 1st order MEG were determined with an accuracy of better than 10%, in the 1st order HEG better than 15% throughout most of the energy range. This is within the goal set for the XRCF measurements to refine state of the art composite component model predictions, which in future will allow us to draw conclusions on the in-flight HETGS absolute effective area.

For a detailed description of ACIS we refer to the ACIS Team Calibration Report[5] and publications [6]. Briefly, the CCD array, illustrated in Figure 1.2, consists of two different types of CCDs: four front illuminated devices (FI) and two back illuminated devices (BI). These are arranged in a linear array and designated S0 to S5 from left to right in the Figure, from -Y to +Y in AXAF coordinates. S1 and S3 are the two BI devices. The position of the 0th order image, is marked in the Figure by the small black box, is on the back-illuminated device S3. This will also be the a launch-locked focal position for AXAF.

In this article we focus on measurements performed with the Double Crystal Monochromator (DCM), in which an energy range of 0.9 to 8.7 keV was covered. During this phase "H" of XRCF testing the ACIS-S array was the only flight detector in the focal plane for these set of measurements. The setup also included several Beam Normalization Detectors (BNDs), here we make use of the four BNDs positioned at the HRMA entrance plane.

7.7.1 Approach and Data Sets

7.7.1.1 Effective Area Measurement Approach

The measured effective area of an HETG order is the ratio of the count rate of that particular order received by the CCD array to the incident source flux at the HRMA entrance plane:

$$A_{meas}(E_{DCM}, m, \text{mode}) = \frac{\text{focal plane counts/s in order}}{\text{source flux atHRMA}} \quad [\frac{\text{counts/s}}{\text{photons/cm}^2\text{s}} = \text{cm}^2 \frac{\text{counts}}{\text{photon}}] \tag{7.10}$$

TRW-ID H-HAS-EA-	DCM crystal	Energy eV	Increment eV	steps	∼cts/step
8.001	TAP	950	50	5	41000
8.002		1200	50	5	45000
8.003		1400	30	11	28000
8.004		1860	20	8	35000
8.005		2050	30	11	12000
8.006	Ge1	2500	150	11	18000
8.007		4000	200	6	18000
8.008		5000	250	9	28000
8.009		7200	500	4	23000

Table 7.2: List of HETGS effective area measurements with the DCM at XRCF. The energies listed are the start energies of each set. Exposure times varied between ∼1000 and 2000 s for each energy.

This measured quantity thus depends on the specific analysis methods, such as event identification in the detector array as well as the flux determination method in the BNDs. The uncertainty of the result involves the statistical error of the determined count rates and any statistical and systematic errors from each of the four the BND fits. Another systematic uncertainty is present in the determination of the subassembly grating efficiency measurements shown in figure **??**. Those are not included in the uncertainty of the XRCF data. In the higher orders the uncertainty in the measured effective area is dominated by counting statistics.

7.7.1.2 DCM Measurement Set

The energy scans taken with the DCM include a total of 70 steps; Table 7.2 summarizes these measurements. The measurements were divided into 9 blocks with different increments. The first 2 blocks consisted of 8 steps of 50 eV starting from 950 eV, the next 3 blocks covered an energy range between 1.4 and and 2.4 keV in 30 eV steps, followed by 150 eV steps until 4 keV. The increments were then increased up to 500 eV until 8.7 keV.

In order to get sufficient photon counting statistics in the diffracted orders, the high voltage of the tungsten source was steadily increased above 2.5 keV. The total number of counts for each energy step then varied between 1.1×10^4 to 4.5×10^4 counts. Figure 7.15 shows a typical measurement, which included 11 steps between 2.5 and 4.0 keV. The detector was moved 40 mm out of focus along the optical axis towards the HRMA in order to spread the focal image over as many detector pixels as possible. The dispersed images appear as rings reflecting the two outer mirror shells in the MEG, the two inner shells (and therefore smaller rings) for the HEG. Each order appears as a sequence of rings separated by the dispersed increment of 150 eV.

The analysis uses DCM measurements only, that is energies above 950 eV. This has one particular shortcoming for the calibration of the HETGS, which is that except for some data from the S0 device in the HEG +1st order, the two outer CCDs S0 and S5 are not in the dispersion range of the bright 1st orders.

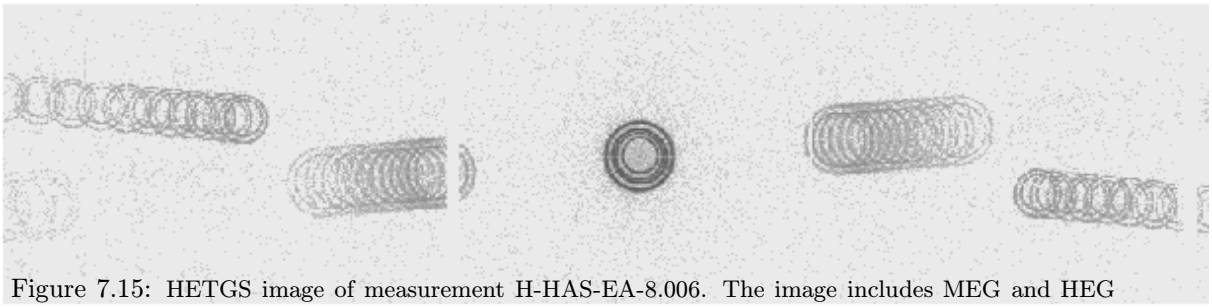

Figure 7.15: HETGS image of measurement H-HAS-EA-8.006. The image includes MEG and HEG 1st order. Each order consists of 11 steps 150 eV apart. In this closeup view the chip gap between S2 and S3 is seen to the left of zero order cutting through the MEG diffracted rings; the S3-S4 gap is seen at far right cutting through the HEG rings.

7.7.1.3 Beam Normalization Data

In order to monitor the source flux illuminating the telescope a system of beam nomalization detectors were positioned in the facility[98]. One set was positioned close to the X-ray source, and one set at the entrance plane of the HRMA. For our analysis we are primarily interested n the flux at the HRMA entrance plane; the beam is quite large at that stage, therefore we need to determine the source flux at various position within the beam in order to compensate for non-uniformities in the beam. Four gas flow proportional counters (FPCs) were placed at +Z (FPC-T, top), -Z (FPC-B, bottom), -Y (FPC-N, north), and at +Y (FPC-S, south) od the HRMA aperture at a radial distance of slightly larger than the outer shell radius. The denominations 'top', 'bottom', 'north', and 'south' reflect the actual orientation within the test chamber at XRCF. The analysis of the FPC data for the DCM scans has been performed by the AXAF project scientist team at MSFC. For details of this analysis we refer to the AXAF Project Science Calibration Report and references therein ([99, 93]).

Figure 7.16 shows the flux at the four BNDs during each of the 70 energy steps of the DCM separated into a diagram for lower and for higher energies. The behaviour of the beam flux in the two energy domains is quite different. The reason for this lies in the DCM and its X-ray source. As described above, between 1.3-2.0 keV three prominent lines appear in the spectrum. The intrinsic optical properties of the DCM crucially imprint onto the uniformity of the beam: the lines will appear at only certain angles, which translate to different locations at the HRMA entrance plane. Hence the lines result in strong non-uniformities. The DCM then was tuned in a way that the major gradient in line flux appeared between FPC-S and FPC-N, while the other two remained in reasonable aggreement, i.e only one gradient appeared across the beam. At higher energies the four monitors are well in aggreement, major discontinuities in the flux versus energy flunction appeared only when the crystal type in the DCM was changed.

7.7.2 ACIS-S/HETG Data Reduction

The event lists used for this analysis were provided by the ACIS team at Penn State University, who separated the telemetry data stream into the proper test segments and performed the basic processing of CCD data in terms of bias subtraction and ACIS flight event grading. Starting from the resulting event lists, the further reduction of the data involves several more steps. First of all, the test segments (first column in table 7.2) still contain a number of energies depending on the the number of DCM steps performed. The single energy events were extracted and written into separate energy lists with a well defined exposure time. Since in this analysis we restrict the event selection to one single grade set, we have to re-grade the data into the sum

of ASCA grades 0,2,3,4,6, which are basically a subset of the 255 ACIS flight grades. One then spatially extracts each order by using the grating dispersion relation

$$sin(\theta) = \frac{m\lambda}{p} \tag{7.11}$$

where m is the order of diffraction (an integer 0, $\pm 1, \pm 2$, ...), p is the grating period and θ is the dispersion angle. Knowledge of the dispersion axis and the grating-to-detector distance, the Rowland distance, allows a conversion of the angle θ to a physical location on the detector.

Each extracted order has a pulse height spectrum from its location on a particlar CCD. After applying the specific gain correction for each device, ideally we then should see one single peak with a FWHM of the spectral resolution of the device at that particular energy. In reality this is not the case for many reasons and it is crucial to select a proper PHA region-of-interest in order to select all the counts that are from the line source only. These considerations are detailed in the pileup section below.

A further correction comes to the data from flux losses when a single order's image intersects a gap between CCD devices; an example of this is seen in Figure 7.15. The effect is quite prominent when it occurs and the probability that it effects an order near gaps is high since the diameter of an order image is more then 5 mm in the MEG and about half that size in the HEG at 40 mm intrafocal position. Flux losses sometimes amounted up to 45% in the case of the HEG. Therefore every time an image partially hit a gap (the gap is about 0.43 mm wide) we calculated the portion of the rings (note that at lower energies the image always had 2 rings from 2 contributing shells) and applied this portion as a correction factor to the flux. The method, however, has its flaws, *e.g.* when the gap was between a FI and BI device, which in the low and in the high energy domain have significantly different quantum efficiencies. However, the systematic errors introduced in these domains were less than 1% and thus disregarded.

7.7.3 Pileup in the Data Sets

7.7.3.1 Pileup Basics

All the effective area measurements performed at XRCF were primarily optimized for flux in the higher order in order to get sufficient statistics. Naturally this will cause pileup in the CCD detector array at least in zero as well as in some of the lower orders.

A recent analysis by the ASC ACIS team, Allen *et al.* 1998[3], showed that pileup affects the data in different ways and also shows differently in front- and back-illuminated CCDs. Pileup basically occurs when two or more photons incidently hit the same 3x3 detection cell. Two photons of the same energy would be detected as one event at twice the pulse height of a single photon, three photon at three times the pulse height and so on. Naturally this process has to be flux dependent. At very high fluxes will also allow two or more photons only partially contained within the 3x3 detection cell, which will then cause an enhanced background in between the main and pileup peaks.

In this respect it is more appropriate to think in terms of "fluences" rather than fluxes. Fluence descibes the incident photon density, i.e how many photons strike the CCD within one frametime per unit area, i.e. "ph/s/cm^2" or "ph/s/pix^2".

Higher fluences cause events to overlap more often, which then causes the detection algorithm to issign a higher number grade. This effect is called grade migration and causes a systematic depletion of standard grades, here the ASCA grade set 0,2,3,4,and 6. This migration is likely to be only effective at energies above $\sim$ 3 or 4 keV, when the sizes of charge clouds increase significanty.

Grade migration may not be the only effect of overlapping charge clouds. In the case when a very large charge cloud created by a high energy photon overlaps with a "normal" single or double pixel event, the 3x3 detection cell algorthm may not be able to detect any event anymore. In this case the charge would is lost.

7.7.3.2 Demonstration: the Zero-order Data

Zero-order data sets were not designed for effective area analysis because in order to get sufficient statistics in the higher orders, the source flux had to be high, especially at high energies. Therefore the zero order data will be entirely dominated by pileup effects in the CCD. They thus serve as useful pileup example.

The simplest way to identify pileup is to determine higher order pileup peaks in the pulse height spectrum. For energies below 3 keV it is possible to detect higher order pulse heights corresponding to up to 4 photons hitting the same event detection cell. The corresponding number of counts is then summed up and added back to the single photon count rate. The left diagram of figure 7.17 already includes that summation. Clearly above about 3 keV this procedure starts to fail because higher order pulse heights fall beyond the maximum pulse height channels. Therefore we observe a large drop in the measured effective area. In a first attempt to estimate the amount of piled-up photons we fit the ratio of the non-piled-up fraction to the measured piled-up fraction in the range 0.9 to 2.5 keV. In this range we were able to recover piled-up photons for up to 4 photons hitting an single detection cell. This could be done by a power law of index 0.27. We extrapolated this function into the high energy range and added that flux to the count rate above 2.5 keV. We also had to take in account that the source flux above 2.5 keV increased by a factor of 8 and scaled that function simply by that increase. Since pile-up is actually a stochastic process we could have also estimated the missing higher order counts out of a poisson distribution. In any case the resulting area was still short of the expectation by up to 45%.

Following the method to correct for grade migration as descibed by Allen *et al.* 1998 the grade distributions of all measurements above 3 keV were compared to the ones obserbed during subassembly analysis, i.e. data that were evidently free of migration effects. This results in another energy dependent correction factor. We thus calculated the grade migration correction factor for our data sets applied it to the data. Again the result above 6 keV was still short by about 20%. Allen *et al.* 1998 also apply a correction for lost charge and indetected events. Above 6 keV simply applied those correction factors from table 1 in [3] for the case of S3. The result can be seen in the right handed diagram of figure 7.17. The area now seem to fit the expectation, although a clear overcorrection is visible. However, we have to emphasize, since we did not in particular detemine the lost charge correction for our own data sets, the result is merely an estimation. It however demonstrates that those corrections applied by [3] are indeed necessary and in a reasonable order of magnitude. The applied corrections induce additional systematic errors to the data, which are *not* reflected in the error bars in the right handed diagram of figure 7.17.

7.7.3.3 Pileup in diffracted orders

The quantitative evaluation of pileup levels in the diffracted orders is still under investigation. The expected pileup level is low in all orders, however there are severall aspects to consider. For example, one major obstacle is, that at energies below 2 keV the first orders in HEG and MEG spatially mix with higher orders of the W lines generated by the DCM. For energies around 1 keV this emission interferes with the first pileup peak in the pulse height spectra.

Another problem is introduced by the design of the measurements at higher energies. In order to avoid overlaps of MEH and HEG images, the out-of-focus distance of originally 40 mm was gradually reduced with increasing incident photon energy. This hasd the effect that although flux stays constant, the fluence, i.e flux per unit area, increases. Therefore grade migration and charge loss effects will appear in the first order images. In addition that eefect is more likely to affect HEG orders, simply because of the smaller image size.

7.7.4 Effective Area Results

7.7.4.1 Zero-order Effective Area

The treatment of the effective area measurements for the zero order is in different from the ones for 1st and higher orders. In addition to the high pileup discussed above, we are not able to separate the MEG and HEG incident flux throughout the entire energy band. This is because in order to avoid any confusion of the higher order image rings with each other, the detector array was gradually moved back into the focal plane above 2.5 keV. Figure 7.15 shows the zero order image as it appeared beween 2.5 and 4.0 keV. The detector here was already moved back from 40 mm out of focus to 20 mm. It is clear that a separation of the inner two rings from the outer ones, in perticluar separating the images of mirror shells 3 and 4, would already introduce a significant systematic uncertainty. Above 4.0 keV, where the out-of-focus position was 10 mm and less, the separation of the inner rings would have become impossible.

We can use the zero order data in the low energy domain in order to fine tune the beam normalization in the range between 1.3 and 2.5 keV.

The top diagram in figure 7.16 shows quite a strong gradient between FPC-S and FPC-N flux, indicating strong beam non-uniformities. In the range 2.0 - 2.5 keV the FPC-N, however, shows an unsually large drop in flux. In order to minimize these effect on the analysis of the higher orders, we attached constant weights to each of the normalization fluxes in the range between 1.3 and 2.5 keV. Then we simply tuned those weights for each detector until the data in this range matched the values just below 1.3 and just above 2.5 keV. The result is shown in the left diagram of fig 7.17. For the other portions of the energy band, the normalization flux was simply the average over all four BNDs. Below 1.3 keV we observed an agreement with the expectation of better than 5%, between 1.3 and 2.0 keV the uncertainty is determined by the scatter induced by the BND uncertainties and thus can reach 30%; between 2.0 and 3.0 keV it is again near 5%.

7.7.4.2 Plus-Minus Order Asymetry

Figure 7.18 shows the +1 to -1 order ratio for HEG as detected by ACIS-S. The plot shows significant (up to 35%) departures from unity. Based on other measurements, grating asymmetry

is not expected to account for the structure seen in here. Thus, these arise from variations within the detector. The jumps seen at 1.7 keV and 2.9 keV coincide with points at which one of the orders traverses a boundary between a frontside-illuminated (FI) and a backside-illuminated (BI) device. Between these energies, the +1 and -1 orders are both captured on FI chips, but outside that range one order falls on a BI chip, the other falls on a FI chip. It is clear that this strong residual structure, due to the detector, will complicate interpretation of the higher order ratios in Section 7.10. It is worth remembering that in the present analysis the quantum efficiency functions were not yet avaliable for each device rather templates were used for each CCD type. Thus, these kinds of chip-to-chip discontinuities are to be expected.

7.7.4.3 1st and 3rd order effective areas for the MEG

The MEG is optimized to supress efficiency in even orders. In the following we do not present results for any even MEG order. The top diagram of figure **??** shows the the subassembly expectation for the sum of the positive and negative 1st and 3rd MEG orders, i.e. in order to apply to single orders one has do divide these values in half. Considering the fact that efficiencies for single 3rd orders are a factor 10 to 20 lower than 0 order efficiencies we should not expect a significant contribution from pile up effects. In the 1st order single side efficiencies, however, we do have to expect a similar amount of piled-up photons at energies below 2.2 keV as we observed in 0th order, since the efficiencies are of comparable magnitude. At higher energies the efficiencies are between a factor 5 and 15 lower, which reduces the probability of pile-up accordingly. In the following we therefore will not apply any other correction than to add all the counts found in detected higher pile up orders in the pulse height spectra.

Figure 7.19 shows the effective areas determined for the -1st (top, m1) and +1st (bottom, p1) order of the MEG. All data points are confined within 3 CCDs, S2-4. The -1st order covers S2 for all energies below 4.2 keV, and S3 for all higher energies, the 1st order covers S4 for energies below 1.5 keV, and again S3 for all the higher energies. In both orders it is clear that measurements around the tungsten Mα line at 1.75 keV (width $\sim$ 150 eV) have to be disregarded; although we are able to clean the focal plane data from that emission, we cannot entirely do so in the BNDs. Around 1.3 keV we see some scatter in the data, which is also induced by the uncertainty of the BNDs of the order of 10 to 20%. At all other energies, with a few exceptions, we measured the effective area to an accuracy of 5 to 10%. At high energies above 6 keV counting statistics do not allow a determination better than 10%.

We compare these measured effective areas to the expected area distribution from equation 1. To first order we find a remarkable match of the data to the expected distribution. However, there are notable deviations, which are at the limit or exceed the 5% uncertainties of the data points. At +1st order, the very low energy data points stay below the expectation by an amount of somewhat less than 5%. There may be a similar trend in the -1st order, however here without significance. Also in the -1st order above approximately 2.5 keV and below 4.2 keV, the measured areas stay consistently above the calculated function, again by only a small amount. All of these effects happen on CCDs, where we have used a template QE from a different device. The amount of these effect also matches the expected variation between the QEs for different devices. A strong argument against these effects being intrinsic to the grating itself is the fact that in +1st order the area between 2.5 keV and 4.2 keV matches precisely the expectation: this portion covers device S3, which is the template BI device.

Figure 7.20 shows the areas determined for the MEG 3rd orders. Again, except for a couple of data points, the general trend shows that the measured values match nicely the expectation. However, the statistics already limit the significance to less than 20%. Therefore we will not

present higher order data in this context. Those results will be presented in terms of efficiency ratios for combined order by [31] in this volume.

7.7.4.4 1st and 2nd order effective areas for the HEG

The bottom diagram of figure **??** shows the the subassembly expectation for the sum of the positive and negative 1st and 2nd HEG orders. The 2nd order efficiency, comparable to the 3rd order efficiency in the MEG, is low enough to ensure that results will be not be affected by pile up. For the first order, we face a similar situation to the MEG first order, i.e. pile up is sufficiently corrected for by adding the 2-photon peak in the pulse heights back to the measured count rate. This peak is detectable thoughout the whole band pass.

Figure 7.21 shows the effective areas determined for the -1st (top, m1) and +1st (bottom, p1) order of the HEG. Note, that the HEG has considerably less efficiency below 2.5 keV than the MEG. Therefore counting statistics are worse than in the MEG. Below 1.5 keV we cannot determine the effective area better than 20%, above 1.5 keV and below 5 keV the uncertainties are of the order of 10-15%. Again the range around 1.75±0.15 keV is not reliable and should be disregarded.

Within the given uncertainties, the measured values again fit quite well with the expected function. At -1st order, like observed in the MEG the area between approximately 2.5 and 4.2 keV stay consistently above the expectation, which again points towards a slightly higher CCD efficiency at high energies in S2. A major effect is observed above 5 keV in both orders. Here we already observe signs of pileup through grade migration. Above 7 keV the effect that charge is completely lost is also clearly visible in the data. The MEG -1st order does show a similar trend around 5 keV at a much lower scale, because of the lower incident fluence in the larger MEG image size.

Figure 7.20 shows the areas determined for the HEG 2nd orders. The measured values match the expectation. But like observed in the MEG 3rd orders, statistical uncertainties the significance to less than 20%. For higher order results we refer to Section 7.10.

7.7.5 Conclusions

We analysed effective area measurements performed at XRCF with the HETGS, by using the DCM energy scans in the energy range from 950 eV to 8700 eV. The measurements were designed to produce sufficient flux in the 1st and higher orders, therefore the 0th order measurements were dominated by pile-up effects. Table 7.3 summarizes the measured effective areas for a selected set of energies. The analysis resulted in the following:

• The absolute effective area of the combined 0th order in MEG and HEG was measured to an accuracy better than 5% in the range 0.9 and 3.0 keV. The larger uncertainties were introduced by systematic errors from the DCM. At energies above 3 keV the measurements were entirely dominated by pile-up effects and the effective area in this range could only be verfied with an uncertainty above 20%

• The absolute effective areas of the 1st orders were determined with an accuracy between 5 and 10% for the MEG and between 10 and 15% for the HEG over most of the energy range. Above ∼5 keV counting statistics degrades significantly.

E	0th	MEG 1	MEG -1	MEG 3	MEG -3	HEG 1	HEG -1	HEG 2	HEG -2
eV	cm^2	cm^2	cm^2	cm^2	cm^2	cm^2	cm^2	cm^2	cm^2
1000	58.9±2.5	18.3±1.1	19.4±1.4	0.0±0.0	0.9±0.3	4.9±0.7	6.5±0.8	–	–
	56.8	21.0	21.0	1.6	2.0	4.6	7.3	1.0	1.0
1200	53.6±3.3	38.8±2.7	41.5±2.8	2.9±0.7	3.9±0.8	11.9±1.5	12.6±1.5	–	–
	56.5	40.4	40.4	4.0	4.0	9.1	12.2	1.9	1.9
1400	56.7±4.6	65.0±4.6	61.1±4.4	6.3±1.4	5.7±1.4	21.3±2.6	21.4±2.6	–	3.3±1.0
	50.1	60.1	60.1	5.9	5.9	16.8	20.4	2.5	2.5
1610	48.4±3.1	75.0±3.8	60.3±3.4	6.2±1.0	6.4±1.1	24.2±2.2	21.9±2.1	3.0±0.8	3.3±0.8
	51.0	75.0	66.5	6.4	7.2	24.1	27.2	2.7	2.7
2140	95.0±3.8	29.6±2.0	21.8±1.7	1.8±0.5	2.0±0.5	16.7±1.5	17.4±1.5	1.1±0.4	1.6±0.5
	94.3	27.5	18.9	1.7	2.5	14.5	14.5	1.0	1.5
2500	74.0±3.0	20.8±1.6	18.8±1.5	1.7±0.4	1.6±0.4	12.2±1.2	12.6±1.2	0.6±0.3	1.0±0.3
	80.0	20.8	16.1	1.4	1.8	10.5	10.5	0.8	1.2
3100	94.9±4.1	25.4±2.2	23.1±2.1	2.4±0.7	2.2±0.6	17.8±1.8	17.9±1.8	1.3±0.5	1.3±0.5
	93.2	24.6	21.2	1.8	1.8	17.3	14.9	1.2	1.4
4000	129.6±4.2	26.2±1.9	27.4±2.0	2.2±0.6	2.3±0.6	19.7±1.7	21.5±1.7	1.5±0.5	1.7±0.5
	134.9	24.5	23.1	2.0	2.0	20.7	19.5	1.4	1.4
5000	131.5±6.11	14.6±2.1	11.4±1.8	1.4±0.6	1.5±0.7	14.7±2.1	16.9±2.2	1.0±0.5	1.1±0.6
	149.5	14.6	14.5	1.3	1.3	17.8	18.7	1.2	1.2
6000	122.7±7.6	4.7±1.5	4.7 ±1.5	0.5±0.5	0.6±0.5	7.7±1.9	9.6±2.2	0.6±0.5	0.8±0.6
	105.7	5.0	5.0	0.4	0.5	11.7	13.8	0.7	0.8
7000	53.7±5.3	0.8±0.7	0.9 ±0.7	0.1±0.2	0.1±0.2	4.8±1.6	5.6±1.7	0.3±0.4	0.5±0.5
	56.7	0.8	0.8	0.1	0.1	6.2	8.0	0.4	0.5
8200	16.0 ±3.8	0.1±0.3	0.0 ±0.2	0.0±0.1	0.0±0.1	1.5±1.2	1.5±1.2	0.1±0.3	0.2±0.4
	21.2	0.0	0.0	0.0	0.0	1.9	2.7	0.1	0.1

Table 7.3: Table of results of measured versus predicted effective areas if the HETGS for selected energies. The stated uncertainties include only counting statistics and BND uncertainties. The second row for each energy lists the expected effective area from the HRMA XRCF model and the ACIS and HETG subassembly predictions. Note, that because the predictions are derived from subassembly data, they itself have an uncertainty of up to 5%.

• The measured areas in the 1st orders for the MEG and HEG match the expectation from the XRCF HRMA measurements combined with the subassembly results for the ACIS-S and the HETG to quite a high degree. In detail: the MEG -1st order data from device S2 revealed significant variations that could be traced to variations in quantum efficency of device S2 in ACIS-S with respect to the applied QE template; the HEG measurements above 5 keV seem to be affected by local beam non-uniformities. A careful evaluation is still in progress.

• Although dominated by large statistical uncertainties the measured effective areas for the MEG 3rd and the HEG 2nd orders are very well in agreement with the expectation.

For the future this analysis has to be complemented by XRCF measurements using the EIPS single line sources, which allow us to study the energy range below 0.9 keV as well as the 0th order at high energies under less piled-up conditions. The DCM results for the HEG 1st order have to be fine tuned at high energies by including the measured beam unifomity maps. The 1st order results for both grating types should be refined by applying the actual QE functions for each CCD in the detector array as soon as they become available. Finally the grating results should be cross-calibrated with ACIS stand-alone measurements performed at XRCF. From the results of this analysis and once the outstanding issues are resolved, we will be able to refine our grating models in order to accurately predict the in-flight HETGS absolute effective area.

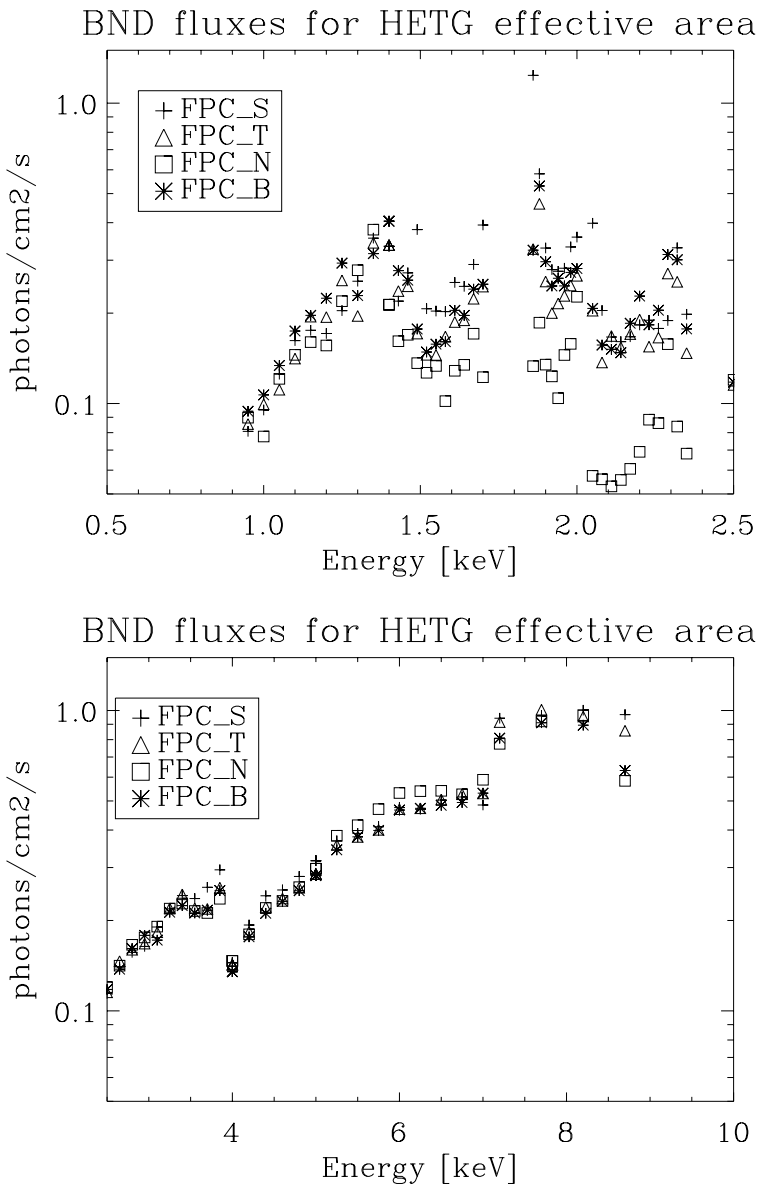

Figure 7.16: BND flux around the HRMA aperture as a function of energy, below and above 2.5 keV .

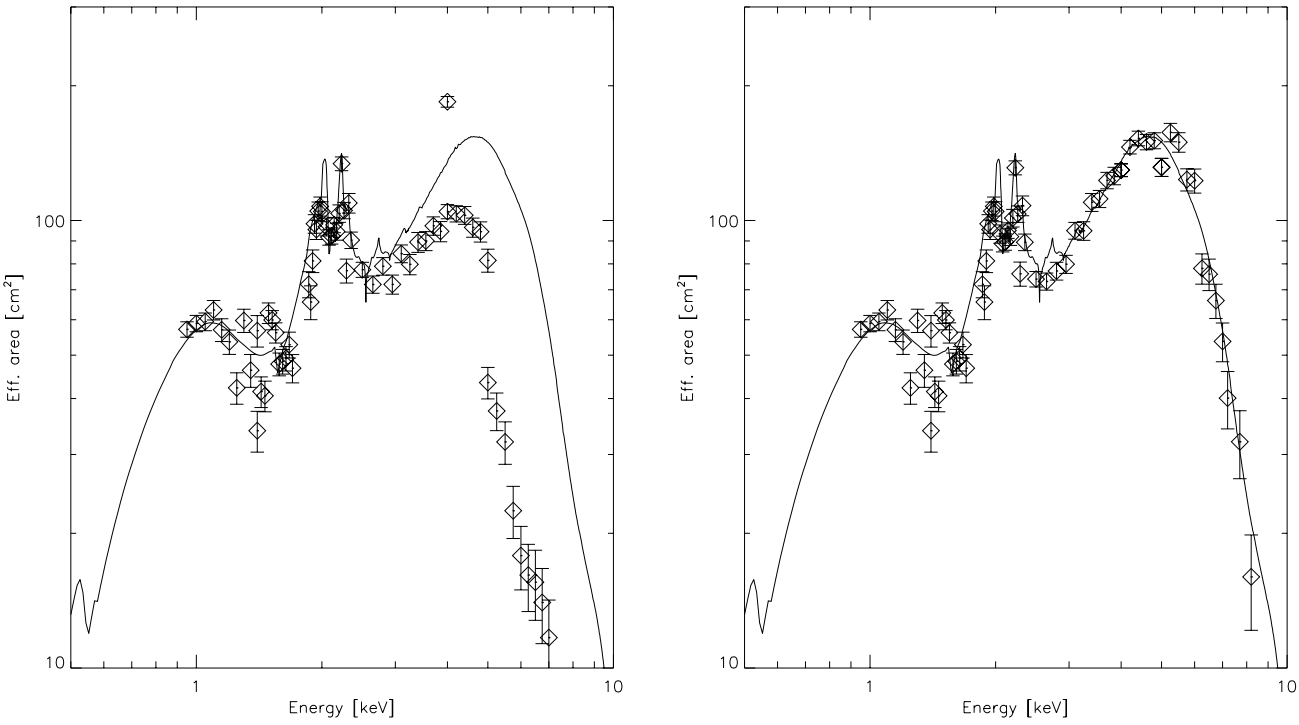

Figure 7.17: Comparison of the measured and expected effective area for the combined 0th order of MEG and HEG as a function of energy. The left hand diagram shows the result without, the right hand diagram with pile up correction as described in the text.

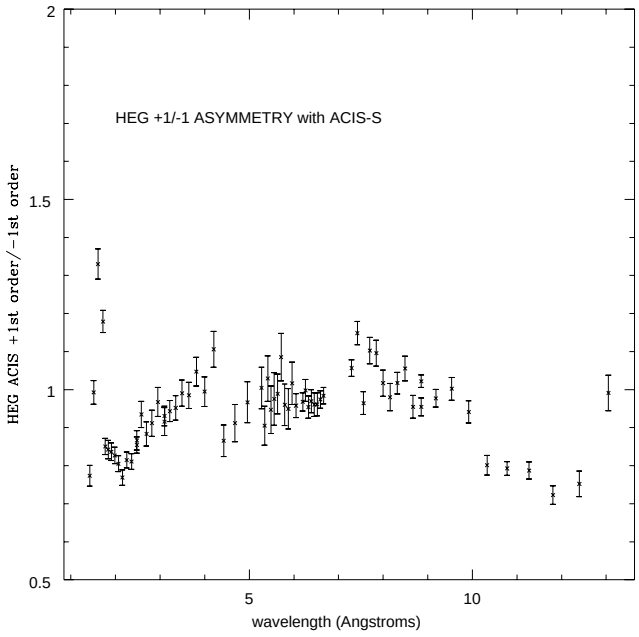

Figure 7.18: Ratio of +1 to -1 for HEG grating on ACIS-S. Structure is due to detector effects.

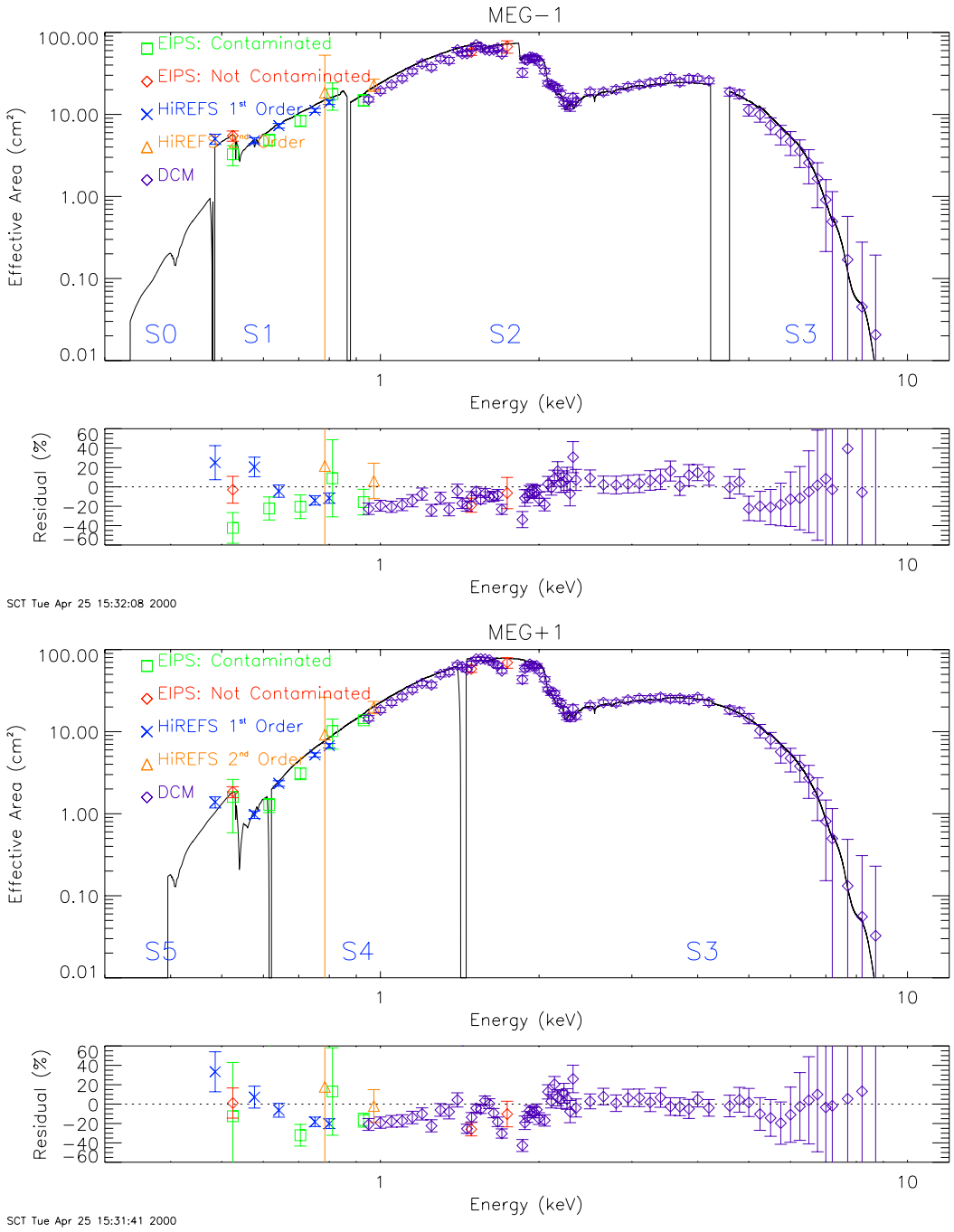

Figure 7.19: Comparison of measured absolute effective areas at XRCF of the MEG 1st order to the expected effective area. Negative orders cover S2 and S3 (from low to high energies), the gap appears just above 4 keV. Positive orders cover S4 and S3 with the gap at 1.5 keV.

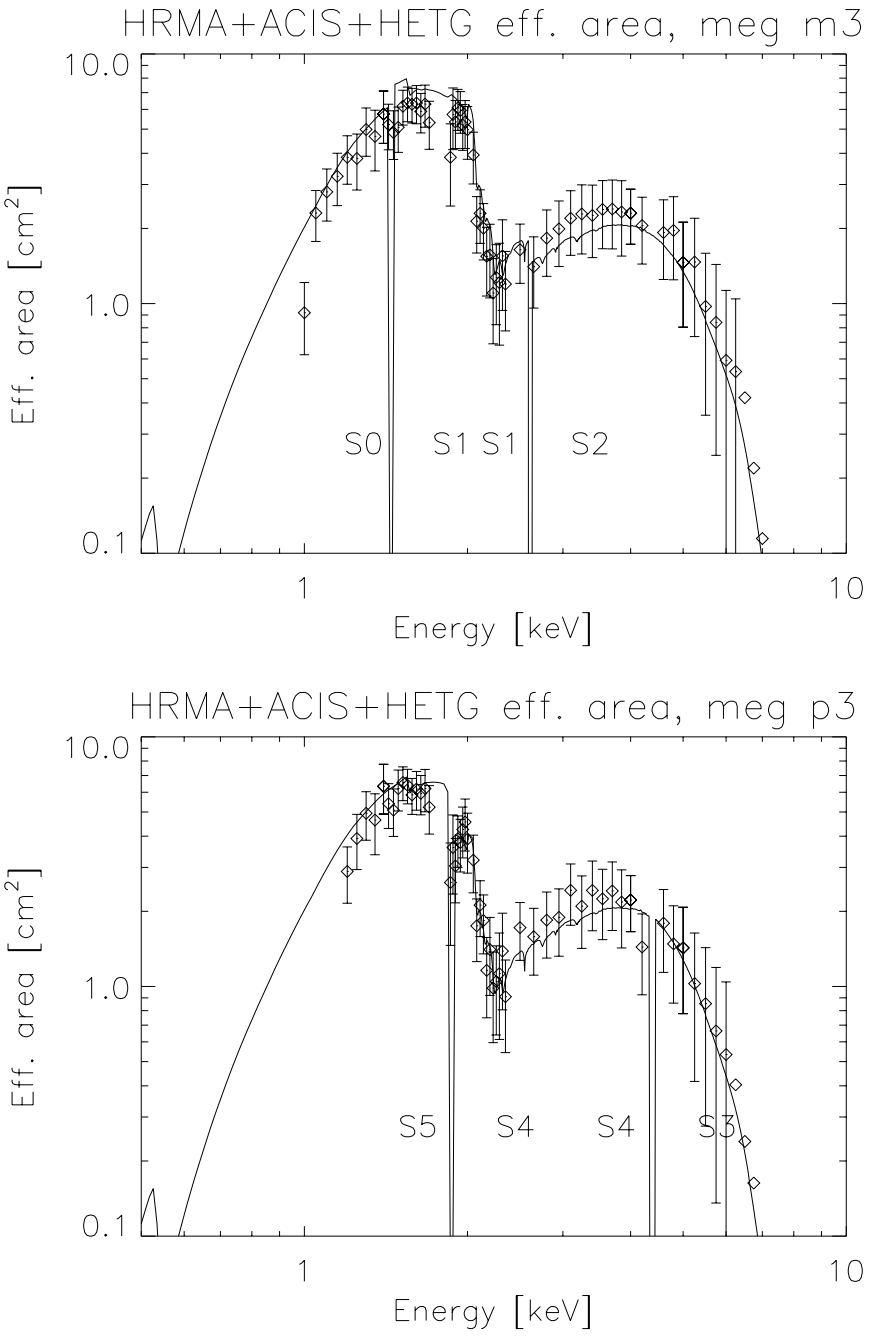

Figure 7.20: Measured absolute effective areas at XRCF of the MEG 3rd order.

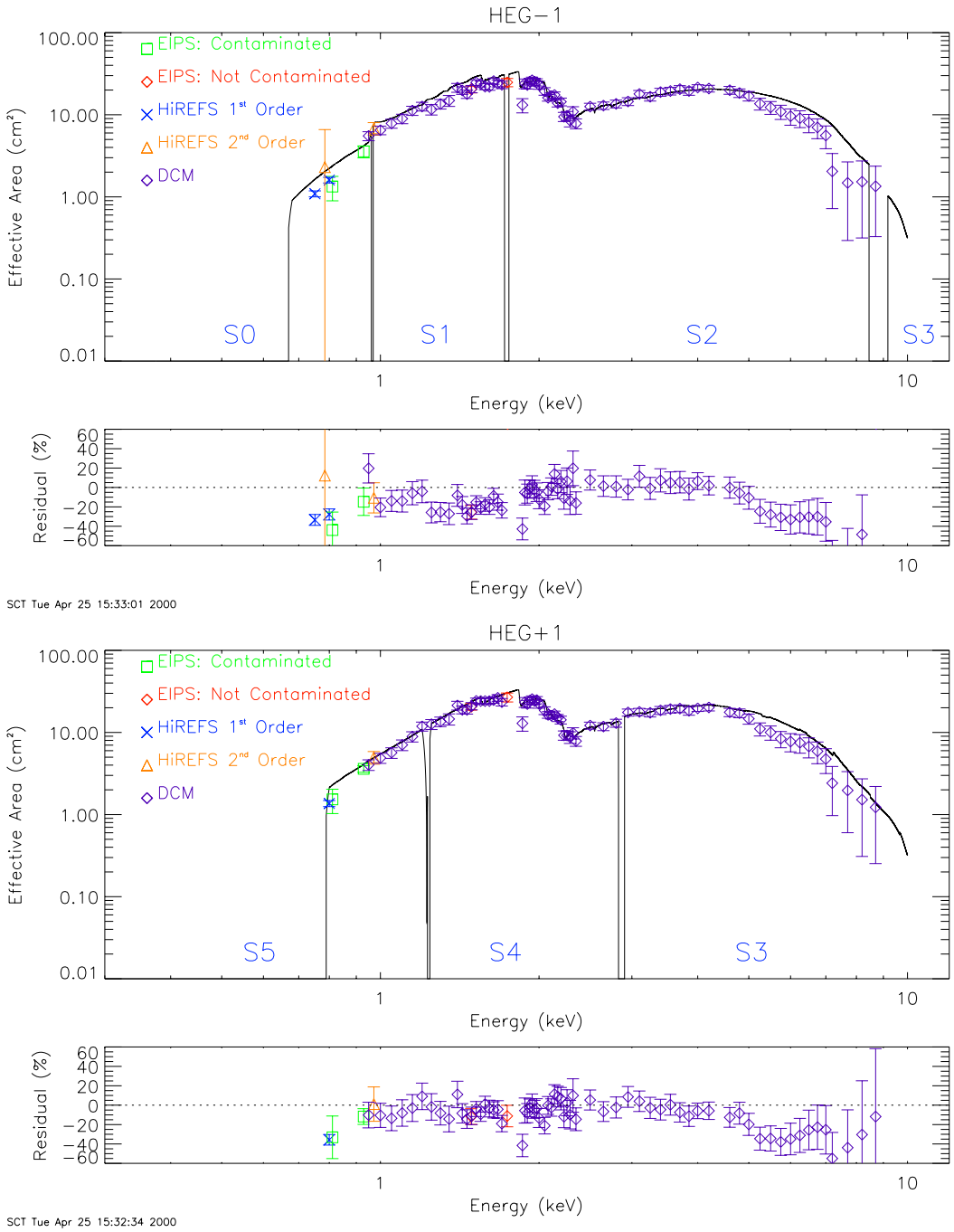

Figure 7.21: Comparison of measured absolute effective areas at XRCF of the HEG 1st order to the expected area distribution. Negative orders cover S1 and S2 (from low to high energies), the gap between the two appears 1.7 keV. Positive orders cover S5, S4, and S3 with the gaps at 1.3 and 2.9 keV respectively.

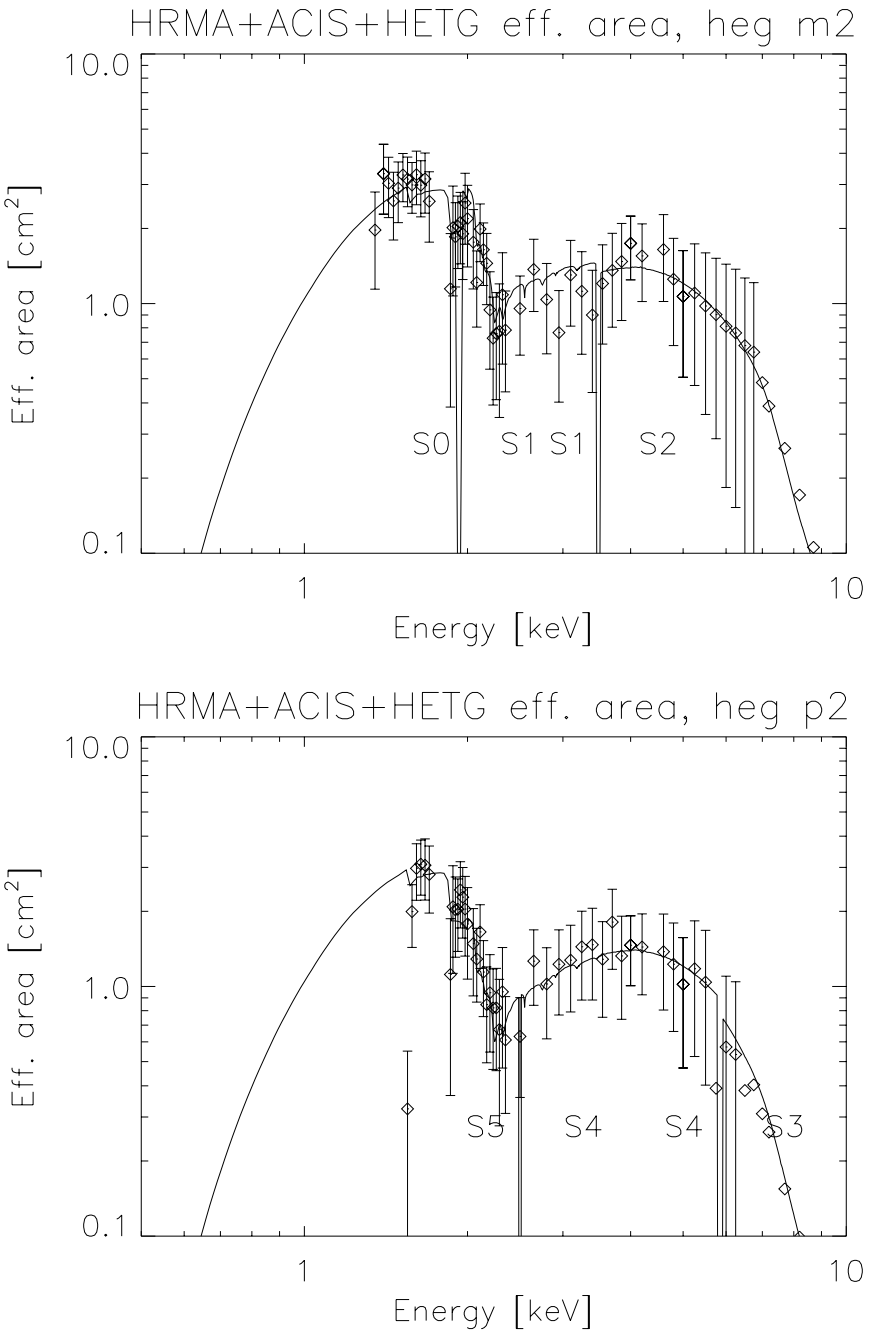

Figure 7.22: Measured absolute effective areas at XRCF of the HEG 2nd order.

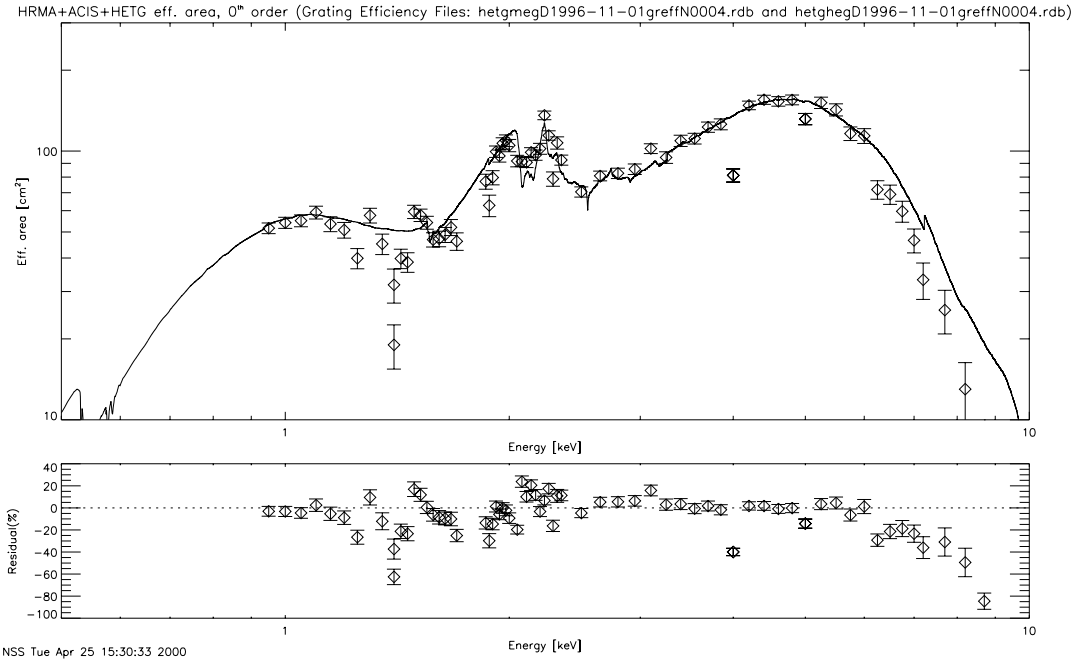

Figure 7.23: Plot of measured and modeled absolute effective areas for the HETGS HEG and MEG combined *zeroth* order with residuals.

7.8 Relative Effective Area: Molecular Contamination

Objective: Verify our detailed grating and detector spectral models and search for unexpected spectral features by observing a continuum source with the HETGS.
Publication(s): Marshall *et al.* [61]

In order to probe for small scale spectral features of the HETGS effective area, we performed tests at XRCF using the Electron Impact Point Source (EIPS) with the Cu and C anodes and operated at high voltage and low current in order to provide a bright continuum at high energies. In fact the continuum was bright enough to obtain 100-1000 counts *per spectrometer resolution element* over most of the useful energy range of the HETGS. The ACIS-S was used to discriminate orders and to provide high throughput with negligable pileup it was operated in continuous clocking (CC) mode.

Many spectral features are observed but most of them are emission lines attributable to the source spectrum. We find that the current models for the HETG efficiency and HRMA effective area predict very well the observed fine structure near the Au and Ir M edges where the models are most complex. Edges in the detector filter and quantum efficiency (QE) curves are somewhat more sharply defined in the data than in the current models.

By comparing the positive and negative dispersion regions, we find no significant efficiency asymmetry attributable to the gratings and we can further infer that the QEs of the ACIS-S frontside illuminated (FI) chips are consistent to $\pm 10\%$. On the other hand, we derive the ratio of the QE for the backside illuminated (BI) chips relative to that of the FI chips and show that it deviates from the expected ratio. This deviation may result from grade differences due to operation in CC mode while most calibration data are obtained in timed event mode.

To do: include Carbon results, can mc test confirm chip gap values?

7.8.1 Observations and Data Reduction

7.8.1.1 General

The tests that were reduced are given in table 7.4, taken at the XRCF on 1997 April 25 between 0341 and 0806 UT. For each of these tests, the EIPS was fitted with the Cu anode set to maximum voltage, 20 kV, and minimum current, 0.1 mA, in order to achieve the highest continuum but

Test ID	Grating	HRMA Shells open	Open Quadrant pattern
H-HAS-MC-3.001	HETG	1,3 (HEG subset)	NS, TB
H-HAS-MC-3.005	HETG	4,6 (MEG subset)	T, N, B, S
H-LAS-MC-3.009	LETG	all	T, N, B, S

Table 7.4: This table shows the set of tests used in the data analysis. For an overview of AXAF calibration, see Weisskopf *et al.*[98]. The HETG high energy gratings (HEGs) have periods near 2000 Å and are arrayed to receive light from the inner pair of HRMA mirrors while the HETG medium energy gratings (MEGs) have periods near 4000 Å and correspond to the outer mirror pair. The quadrant pattern represents the order in which the north (N), south (S), top (T) and bottom (B) quadrants were opened in order to reduce the telemetry saturation.

keep the total count rate down without using filters. In order to prevent possible radiation induced damage due to the bright zeroth order image, the detector assembly was "dithered" using the five axis manipulator (FAM). A serpentine pattern was used. Long motions in the cross dispersion direction allowed us to reduce the data in large sections at fixed offset along the dispersion direction. Dithering had the advantage of smoothing over detector gaps and any other features.

The ACIS-S was run in the continuous clocking mode and "faint" mode so that three pulse height values were obtained for each event. The detector telemetry limit in this mode is about 393 events/s (see the AXAF Proposer's Guide[75]). As it was, the source was so bright that the ACIS-S telemetry limit was reached easily. Shell quadrants were closed to reduce the count rate to a manageable level during the tests and approximately equal exposure was obtained for all shells.

As described in the AXAF Proposer's Guide[75], when the telemetry limit is reached, CCD buffers fill and data may be lost. To allow the buffers to empty in each shell quadrant configuration, the mirrors were exposed for 15 min and then closed for 5 min. Exposure is then determined by counting frames, since frames are never only partially lost. The good frames are determined by examining the average counts per frame within the time intervals during which the shutters were open. These time intervals were then examined manually to ensure that closed shutter periods were excluded in the results and to make sure that all good frames were included. The exposure per frame is given by the time to read out 512 rows at 10 μs per column per row and 285 rows per column, giving 1.459 s. The exposure was determined for each CCD separately because the buffers are independent. The pixel boundaries of each chip were transformed into wavelengths by the same method used for the events (see section 7.8.1.2) and then both sides were added to obtain the exposure functions shown in figure 7.24.

All events from columns containing hot pixels were eliminated from the data and from the exposure function. The hot pixels were most apparent in detector coordinates because the detector was dithered during the observations. Known hot pixels[75] were apparent in the first two observations (3.001 and 3.005) but two new ones showed up in the LETGS observation (3.009) in columns 225 and 232 of the S3 ACIS-S CCD. Another, much milder hot pixel showed up at column 670. The previous hot pixels (columns 383 and 792) were not observed. The new hot columns (or pixels) are somewhat surprising because the test 3.009 immediately followed test 3.005 and the ACIS electonics were not changed.

7.8.1.2 Event Processing

The overall event processing approach was the same for each test. First, the details of the dithering were measured and events were shifted to compensate. Both the actual FAM shift in XRCF Y coordinates and the times of the shifts were measured from the centroids of bright emission lines in detector coordinates. The Cu-Kα_1 (8.02783 keV) at $m = +1$ was used for test 3.001, while the $m = +2$ line was used for test 3.005 and the $m = +3$ line of cu-Lα (at 0.9297 keV, or 13.336 Å) was used for test 3.009. These data, shown in figure 7.25, indicated that the actual FAM Y shifts for all three tests were 0.18 mm, compared to the commanded values of 0.20 mm.[1] The actual time between Y shifts was observed to be about 561.5 frames, or 819.2 s, which is consistent with the expected value of 820 s.

[1]Irregularities in the FAM positioning were found in analysis of the HETGS scattering test[60, 21]. The sense of the deviation from the commanded motion was 10× smaller and had the opposite sign to the deviation determined here, however.

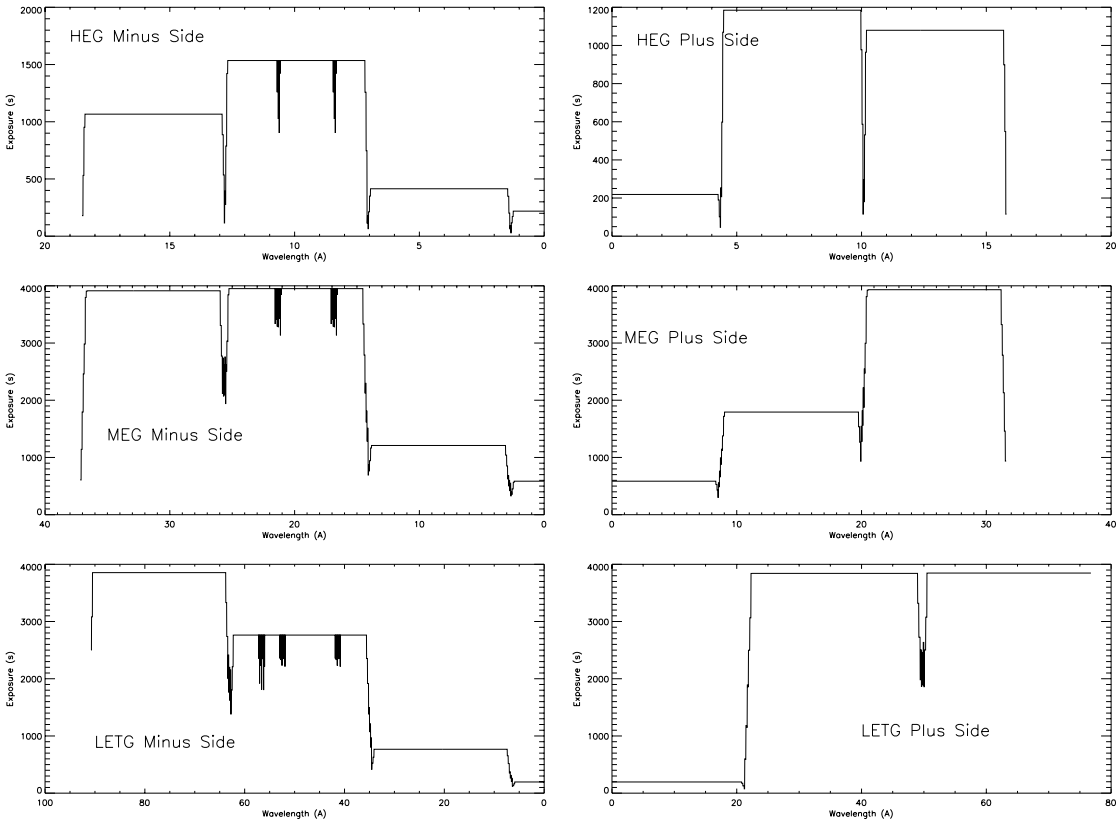

Figure 7.24: Exposure as a function of wavelength for each test and for the positive and negative orders separated. The details of the tests are given in table 7.4. Wavelengths are determined from the dispersion relation for an assumed first order spectrum. The ACIS-S CCDs start with S0 on the left and end with S5 on the right. CCD gaps are apparent; the exposure doesn't go to zero due to shifting of the detector assembly along the dispersion direction during the tests. The zeroth order (and origin) was always on the S3 CCD, a backside illuminated (BI) CCD. Several series of shallow dips result from the elimination of columns on the S1 (BI) CCD containing hot pixels and again were shifted to different locations in wavelength space as the detector was moved.

Second, event dispersion distances from zeroth order were computed based on a trial position for the zeroth order (normally determined by the absolute positioning of the FAM). By comparing the positions of lines in the positive and negative sides, the zeroth order position was measured to within a detector pixel (24 μ).

Third, a wavelength, λ_1, for each event was computing under the assumption of first order using the observed dispersion distance for that event and the grating periods, angles and Rowland distances derived from previous XRCF measurements[24]. For the HETGS, the dispersion distances are not directly observed, only the projection along the XRCF Y axis so the projected distance was corrected by $\cos\alpha$, where α is the angle from the dispersion direction to the XRCF Y axis.

Fourth, events are selected by order using the energy, E, computed from the event pulse height. Events were assigned to order m if $|E - hc/(m\lambda_1)| < \delta E$, where h and c are the Planck constant and the speed of light, respectively, and δE is 250 eV (or 150 eV in the case of the LETG observation), larger than the detector energy resolution.

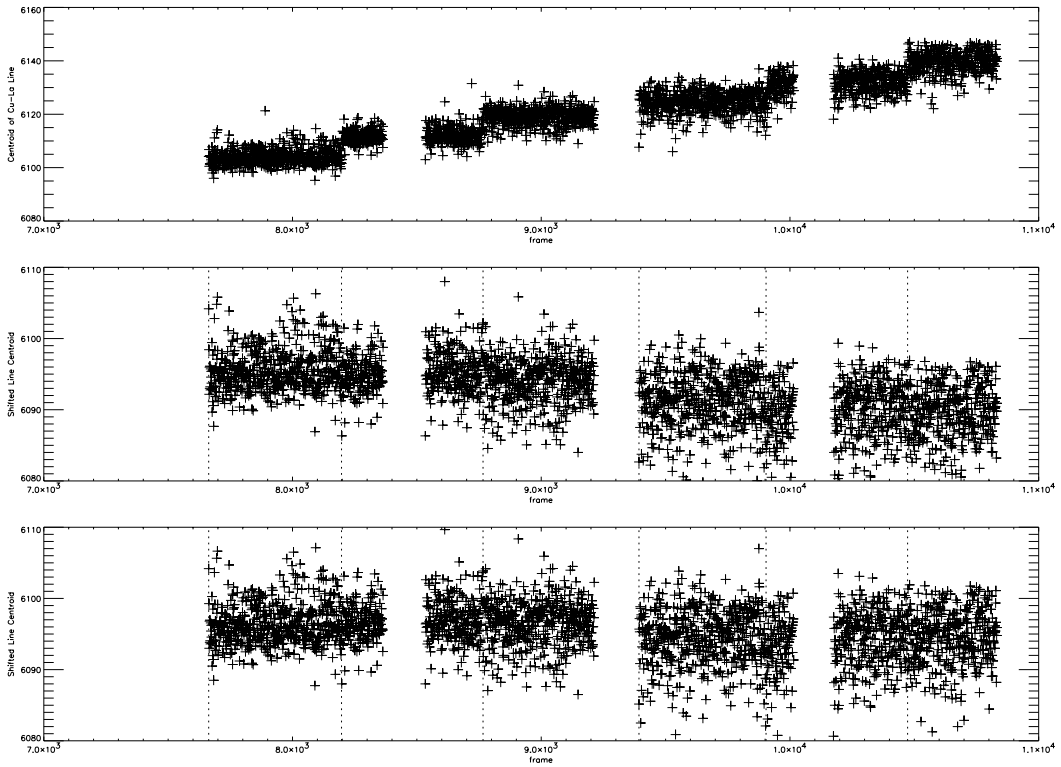

Figure 7.25: Centroid of the Cu-Lα line (at 13.336 Å) in detector coordinates as a function of ACIS frame (in continuous clocking mode) for test H-HAS-MC-3.005. *Top:* Raw centroids showing the systematic shifts due to dither, where the detector is moved in the $+Y$ direction every 820 s, or 562 frames. *Middle:* Centroids are corrected for shifts of 0.20 mm, which was the commanded value. Dashed lines indicate times when the shifts took place. A residual trend remains, indicating an error in the dither magnitude. *Bottom:* Centroids are shifted by 0.18 mm at each shift time to eliminate the secular drift.

Finally, events were selected according to CCD grade. The CCD grades were determined from the event pulse heights as in timed exposure mode except that only the 3 pulse heights from the event row were available instead of a 3×3 event "island". Thus, certain ACIS grades were not observed, such as those like ASCA grade 2 and 6, which are normally included in the event selection. Similarly, although grades 1 and 5 are normally eliminated in processing, since these grades require detecting corners of the event islands, there were no such grades available. Thus grading had little effect on the event selection.

7.8.2 Formation and Interpretation of the Continuum Spectra

A model of the effective area was generated from a HRMA effective area model recent HETG and LETG efficiency functions, the ACIS-S flight filter model and the ACIS-S FI QE model. All data files used here are available from the AXAF Science Center (ASC) calibration group web page (`http://asc.harvard.edu/cal/cal.html`) and were derived from instrument and telescope team characterizations of the AXAF components.

Because of the high spectral resolution of the grating spectrometers, it is important to use finely gridded models, especially near the spectral features such as the Au M and Ir M edges. The

HRMA effective area (EA) was generated by the AXAF telescope science team and is posted to their web site (`http://hea-www.harvard.edu/MST/mirror/ www/xrcf/hrma_ea.html`). They adjusted the model of the EA so that the prediction would conform to various XRCF measurements such the SSD continuum data[55] and they incorporated details of Ir reflectivity based on updated optical constants[40, 41]. For our purposes, the gradual variation of EA with aperture size will not have a significant effect because we are searching for spectrally small effects, so we used the EA integrated over 2π. The HETGS efficiencies incorporate details of the Au edges as described in Section 3. The ACIS flight filter transmission model was fitted to synchrotron data[5] and should include fine structure around the Al and O edges. The ACIS-S CCD QEs are taken from detailed QE curves for two "template" CCDs: one FI chip in the ACIS-I array and one BI chip (S3) in the ACIS-S array[5]; the data from the ASC web page were supplemented with QE values in the 0.05-0.20 keV range with data from a fit to BI QEs by the ACIS/MIT team (see the `QDP` plot of the w134c4r QE on `http://acis.mit.edu`).

Events were binned into histograms before forming a spectrum. The source flux, $f(E)$ (in photon cm^{-2} s^{-1} keV^{-1}), is estimated by combining the data from the positive and negative orders. Denoting the positive side with + and the negative side with −, the expected number of counts in a pixel at energy E is given by

$$\begin{aligned} C_+ &= fA\epsilon_+ TQ_+ t_+ dE \\ C_- &= fA\epsilon_- TQ_- t_- dE \end{aligned} \tag{7.12}$$

where C_- and C_+ are the counts in a pixel at energy E, Q_+ and Q_- are the QEs of the ACIS-S detectors, ϵ_+ and ϵ_- are the efficiencies of the grating into positive and negative orders and are assumed to be equal to ϵ, A is the effective area of the HRMA, T is the transmission of the ACIS-S optical blocking filter, and t_+ and t_- are the exposure times. The quantity dE is the energy width of the pixel based on the derivative of grating dispersion relation (for orders $|m|$ = 1) which is very nearly linear:

$$dE = hcE^{-2}P\frac{\delta x}{D}cos(\alpha) \tag{7.13}$$

where P is the grating period, D is the Rowland distance, and δx is the physical size of an ACIS-S pixel, 0.024 mm. The count spectra for the two sides were combined using an estimator that is not sensitive to situations where the counts on one side were small or zero (due to gaps between CCDs):

$$\hat{f} = \frac{C_+ + C_-}{A\epsilon T dE(Q_+ t_+ + Q_- t_-)} \tag{7.14}$$

The spectra derived from each test are shown in figures 7.26, 7.27, and 7.28. The Cu-L line series (consisting of α, β, η, ζ, and $\beta_{1,2}$) is quite prominant in all spectra and makes it difficult to search for weak features in the 0.8-1.05 keV region. The Cu-Kα and Kβ lines are apparent at the high energy end so the nearly featureless continuum from 1.05 keV to 7.9 keV could be used for the purposes of this project. The O-Kα and C-Kα lines are also apparent in the MEG and LETG tests and are somewhat broad.

There are features that can be attributed to high orders from the strongest lines, in spite of the pulse height selection. It appears that these high orders can be detected because of a low pulse height tail that extends from the energy of the line down to the background level. These high order lines are especially noticeable in the LETGS spectrum (see figure 7.28). For example, the Cu-Lα line has an energy of 0.9297 keV but there are a significant number of events with ACIS pulse height energies in the .15 to .45 keV range. When the emission line is dispersed to

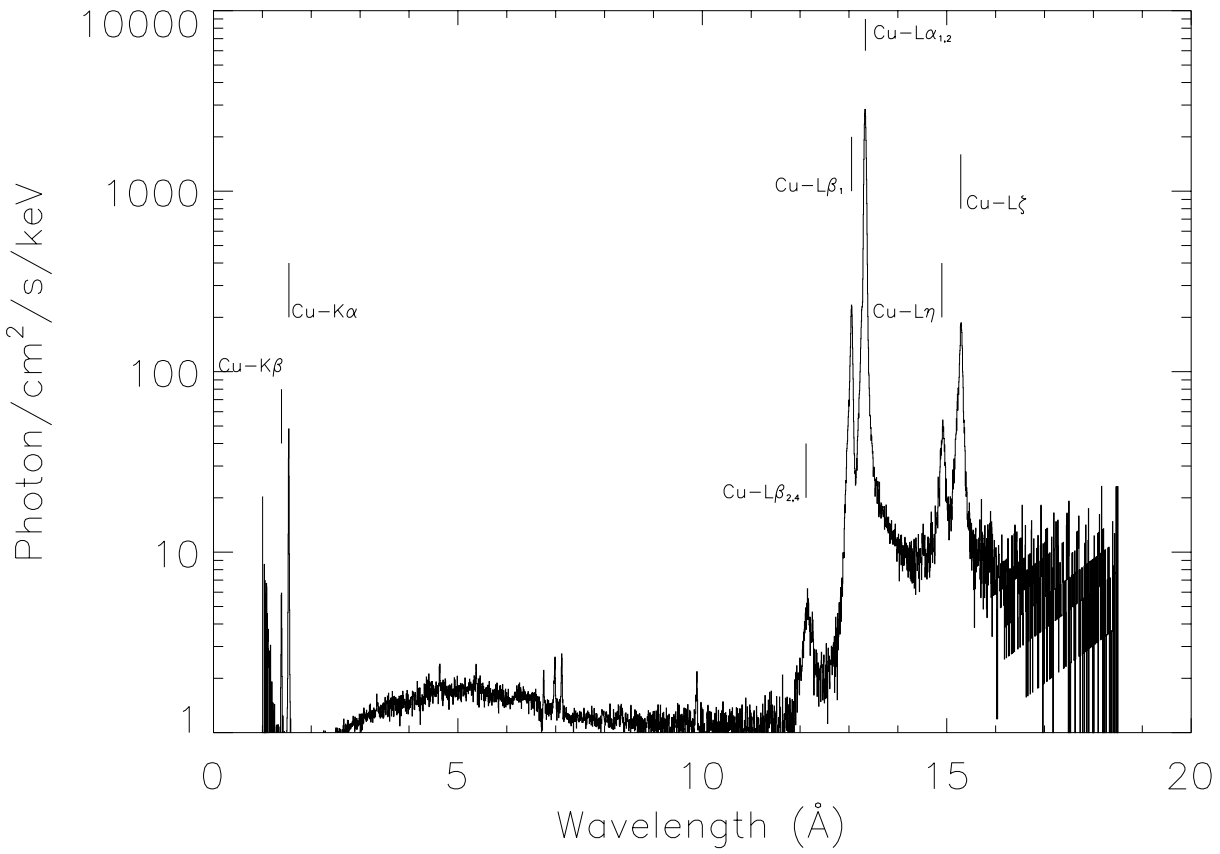

Figure 7.26: Spectrum of the source measured by the HEG portion of the HETGS (test H-HAS-MC-3.001). The strong emission lines were easily identified and are marked. The Cu-L lines are broad and have wings that make modelling difficult near them. Weak features are identified in figure 7.29. The continuum in the range between the Cu-K and Cu-L lines is well fitted with a 10th order polynomial with a few emission lines.

$m = 4$, the events are dispersed to a distance corresponding to 0.31 keV, where the pulse height selection accepts events in the 0.15-0.45 keV range. The pulse height distribution is discussed again in section 7.8.3.

Comparing the spectra obtained from each grating, we see that the continuum and line strengths are very similar but there are systematic deviations. These differences are not the subject of this analysis but may be ascribed to differences between CCD QEs, because each grating places a specific energy onto a different combination of ACIS-S CCDs. In section 7.8.3, we show that there are systematic deviations from the expected QE curves using data from within a single grating observation. This issue requires further investigation.

It is clear from the spectra that pileup is not a significant concern when analyzing these data. The peak count rates in the Cu-Lα and Cu-Kα lines gave count rates of order 10 count/s in the HEG observation. For an effective frame time of 0.00285 s in continuous clocking mode, we obtain only 0.03 count/frame, for less than 3% pileup. For the continuum regions, pileup is a

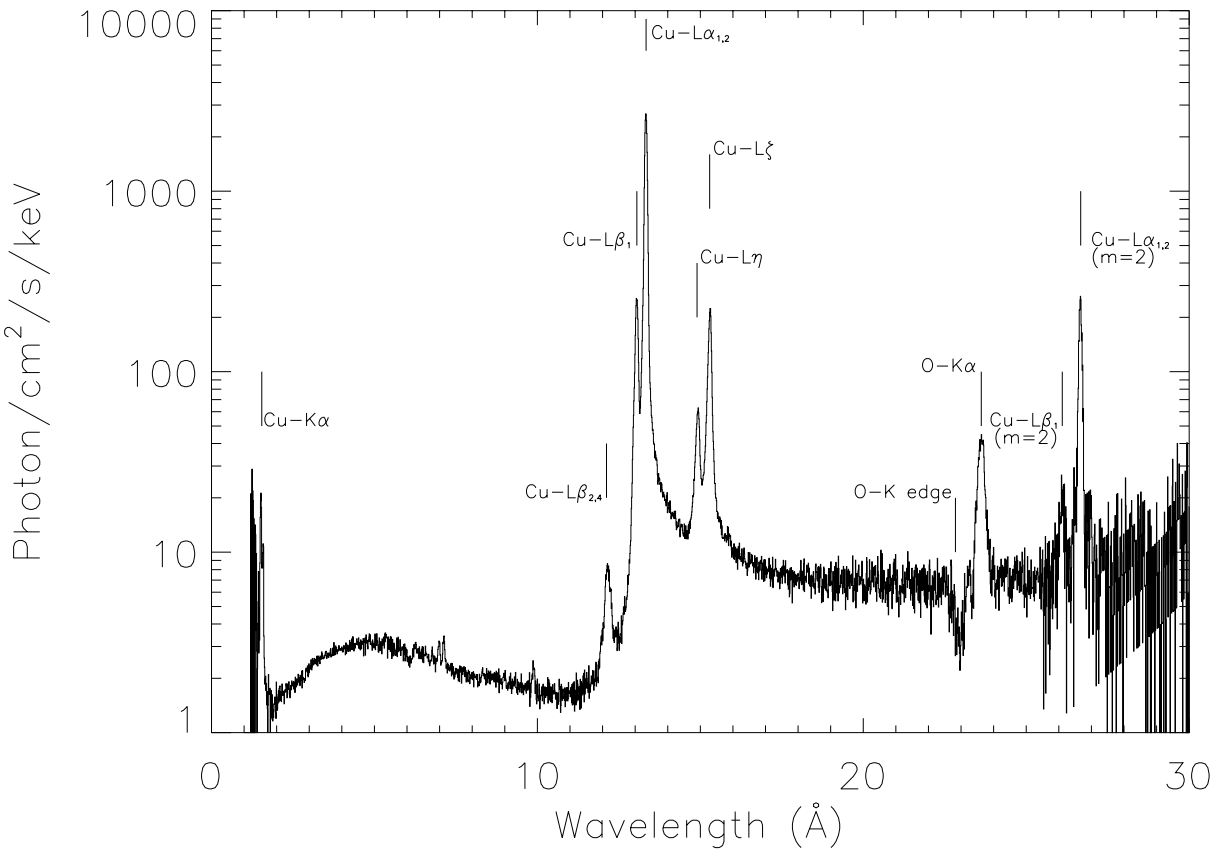

Figure 7.27: Spectrum of the source measured by the MEG portion of the HETGS (test H-HAS-MC-3.005). The Cu-L α (0.9297 keV), β_1 (0.9498 keV), η (0.832 keV), and ζ (0.8111 keV) are the strongest lines and O-Kα (0.5249 keV) is also easily detected. The line observed at 0.465 keV is actually Cu-Lα observed in second order that is picked up in this first order spectrum due to low pulse height events in the ACIS pulse height distribution. An O-K edge feature is apparent in the 0.53-0.55 keV range.

factor of >10 less. In the LETGS observation, the Cu-Lα line gives somewhat more counts per frame due to the lower resolution; there is as much as 30 count/s, for at most 10% pileup in this line. Again, the pileup fraction would be less than 1% for most spectral ranges of interest.

We have not yet computed a complete model for the source because the goal of the test was to use the continuum to search for edges and absorption lines which are not part of the source. The continuum shape is not well known *a priori* but is not required for our immediate purpose. The spectrum was estimated empirically from the HEG observations shown in figure 7.26 by fitting a 10th order polynomial so that we could examine the details of the edge and emission structure in more detail. The data are compared to the model in figure 7.29. Several emission lines due to contaminants in the source are apparent as deviations from the model. Other deviations are observed at the Al-K and Si-K absorption edges which are in the ACIS-S filter transmission model and the ACIS-S QE model, respectively. The data indicate that the edges are somewhat sharper than predicted. These deviations are caused merely by interpolating the coarsely gridded model files. When more finely computed models are made available, these edges

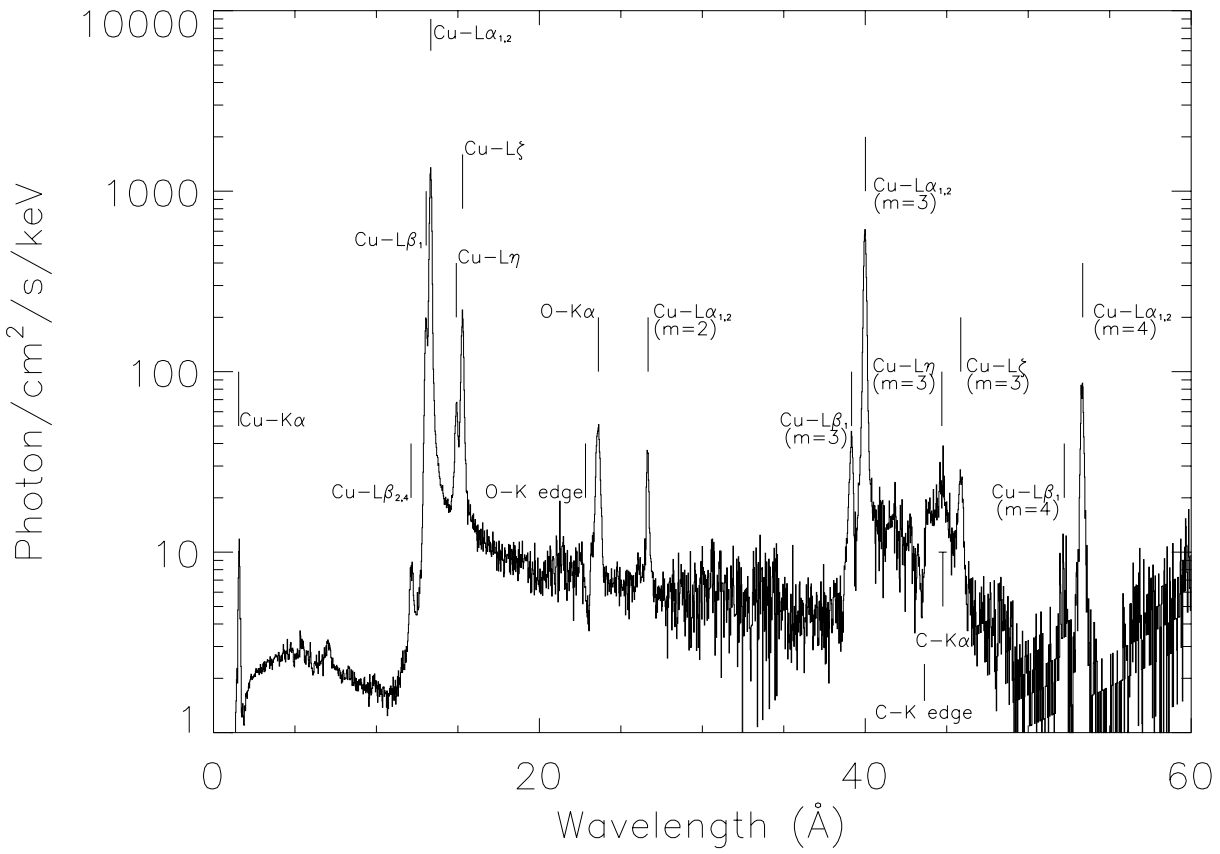

Figure 7.28: Spectrum of the source measured by the LETGS (test H-LAS-MC-3.009). The Cu-L series is observed in many orders due to the tail of the ACIS pulse height distribution. Note that the $m = 2$ lines are considerably weaker than the $m = 3$ high order lines, as expected for the LETGS. The O-K line is apparent, as in the MEG spectrum, and C-Kα is detected as a broad line component under the $m = 3$ version of Cu-Lη. Note the residual Cu-K edge at 0.28 keV.

should be more sharply defined and will be better modeled.

Another feature that is apparent in figure 7.29 is a deviation at 2 keV. This feature is in the model but not in the data and is caused by a sharp "edge" in the HRMA effective area model. This edge is not physical and was the result of patching newly determined optical constants to older Henke values at this point (R. Edgar, private communication). The feature should be eliminated in the next update to the HRMA effective area.

7.8.3 Comparison of Positive and Negative Sides

The ratios of the counts, $R = C_+/C_-$, in the two sides is dependent only on the QEs and the exposure times as long as the grating efficiency is the same for positive and negative orders. All subassembly and XRCF data to date have shown no differences between positive and negative

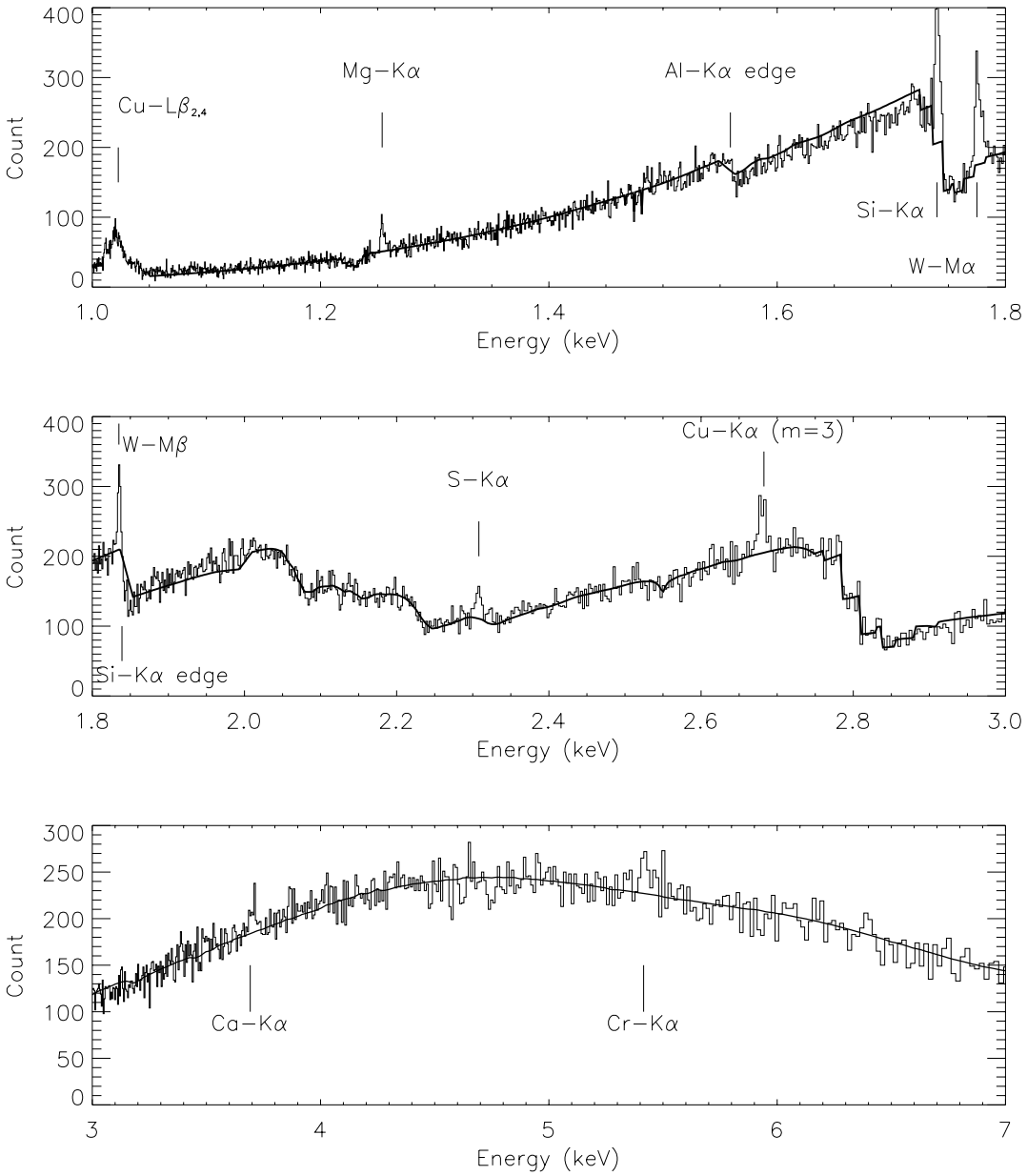

Figure 7.29: Detailed view of HEG-Cu spectrum and model features. The measured count spectrum for three separate energy ranges of the test with the HEG portion of the HETGS (test H-HAS-MC-3.001) are shown here. Emission line features that are intrinsic to the source are marked (e.g. Mg-Kα at 1.254 keV). Two absorption edges are marked (Al-K at 1.559 keV and Si-K at 1.839 keV) where the model of the ACIS-S filter (Al-K) and the detector (Si-K) are so coarsely gridded that the edge does not appear as sharply defined as the data indicate. The bumps and dips from 2.05 through 2.2 keV are the result of Ir M edges in the HRMA effective area and those in the 2.2 to 2.6 keV range arise primarily in the Au M edges of the HEG efficiency curve. Other sharp features are due to exposure variations. A significant deviation from the model occurs at 2.0 keV where the HRMA effective area has a feature that is not tracked by the data.

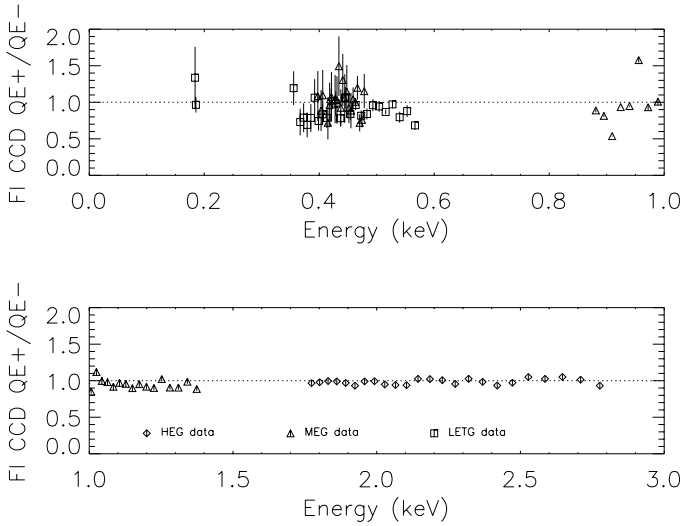

Figure 7.30: FI-to-FI count rate comparison. Ratio of the count rates from 30 pixel regions at the same dispersion distance from zeroth order but on two different frontside illuminated (FI) CCDs in the ACIS-S array. The different symbols indicated which grating data set was used to obtain the ratio. The ratios are comfortably close to unity for most of the energy range so that any deviations can be ascribed to variations of QE between FI CCDs. Data from regions near the Cu-L lines should be discounted because the analysis is very sensitive to the exact placement of the integration window around the emission lines. The analysis was designed primarily for regions where the spectrum varies slowly.

efficiencies, so we may examine the ratios of CCD QEs with these data. We kept track of which CCDs contributed to the ratios so that we could construct $R(E)$. When both orders were on FI CCDs, then all model curves cancel, so that we may test for differences in QEs between FI CCDs or check for grating positive-negative efficiency differences. Figure 7.30 shows the result. We see that there is remarkable consistency between FI CCDs, especially in the 1.8-2.8 keV region, once we discount the apparent discrepancies due to Cu-L lines. The analysis was designed for regions where the continuum was varying slowly, so it is not too surprizing that the L lines show deviations. These regions should be reduced separately and the effects of pileup should be taken into account.

The ratio of the fluxes determined for the BI CCDs could also be compared to those determined in the FI CCDs. The estimated fluxes already include the ratio of the BI to FI QEs. Figure 7.31 shows this ratio computed for each grating set. There are very significant, systematic deviations: 15-20% in the 2-4 keV band, 10-40% in the .5-.8 keV band, and differences greater than a factor of 2 below 0.35 keV. The FI QE in the latter region is extremely small and falling rapidly, so it is perhaps not too surprizing that there may be errors there. The fact that the QE ratio may be measured there may be more surprizing.

The deviations elsewhere, and especially in the 2-4 keV range, are more disturbing. Although investigations are in progress, we have identified an effect that may have bearing on this problem. In figure 7.32, we show the pulse height distribution for events detected by the S3 (BI) CCD and dispersed to a location consistent with energies in the range of 3.0 to 4.0 keV. The figure shows that there is a tail to the pulse height distribution (PHD) that contains a significant number of events and which deviates dramatically from the expected PHD measured from timed exposure mode data. This difference could arise from the inherent limitation of the on-board processing

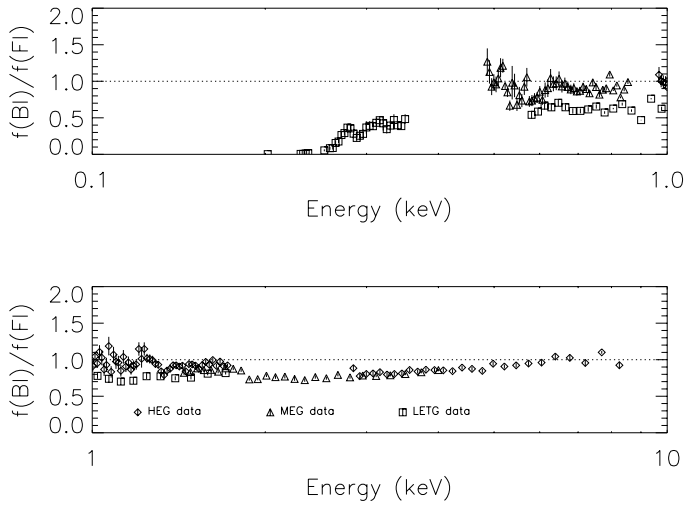

Figure 7.31: BI-to-FI count rate comparison. Ratio of the exposure and QE corrected fluxes from 30 pixel regions where the count rate from one side with a BI CCD is compared to that of a FI CCD on the opposite side at the same dispersion distance from zeroth order. The different symbols indicated which grating data set was used to obtain the ratio. This ratio indicates difficiencies in the ratios of the QE models for BI and FI chips. Investigations to explain the observed differences are currently focussed on the differences in event grade assignation between continuous clocking mode and the timed exposure mode normally used in calibration. As in figure 7.30, data points which are near or include the Cu-L lines should be discounted. Similarly, there is a point at Cu-Kα that is likely to be badly computed.

of continuous clocking mode event data. If an event is split such that a significant fraction of the charge appears in an adjacent row, then the event can be detected as two different events when operating in the continuous clocking mode.

7.8.4 Conclusion and Further Investigations

The tests proved extremely successful: we found no unusual features in effective area of the HETGS and LETGS to a level of about 5% and found that the models of the Ir and Au M edges agreed to within statistics in all cases. The detailed Ir M edge structure given most recent HRMA effective area curve match the data very well but there is a discontinuity at 2 keV which is not observed. The data were also used to show that the positive and negative orders of the gratings have consistent efficiencies and that the QEs of the frontside illuminated (FI) CCDs in the ACIS-S are all consistent. Finally, using the consistency of the positive and negative orders, we derive the ratio of the QEs of the backside illuminated (BI) CCDs relative to the FI CCDs and show that this ratio does not match the expected ratio of QEs. The reason for this discrepancy may be related to a change of event grades because ACIS was read out in the continuous clocking mode rather than in the timed exposure mode for which most calibration data exist. Finally, a pair of new hot columns (or pixels) was discovered that had not appeared in the preceeding tests.

These tests provided data that nicely validated the effective area model fine structure near known edges, so that we may be confident that spectral features in the spectrometer can be modelled adequately for observations after AXAF is launched. Concerns arise regarding the

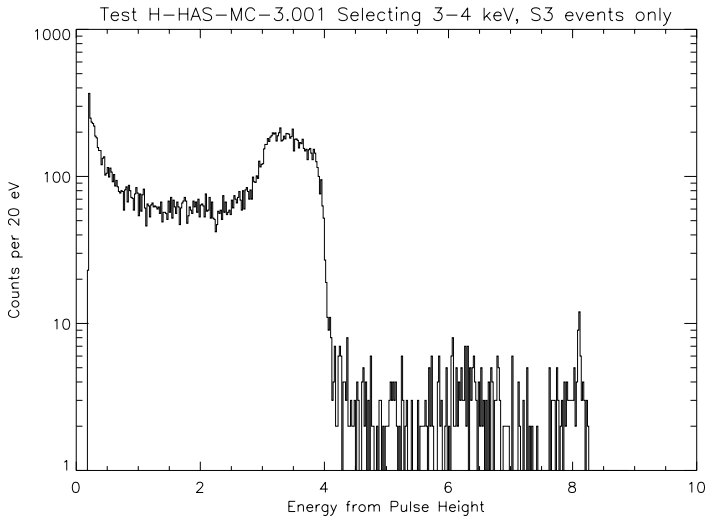

Figure 7.32: Pulse height distribution for CC data. The pulse height distribution (PHD) for a region of the S3 (BI) CCD selected from events whose dispersion corresponds to the 3-4 keV range, assuming $m = 1$ (taken from test H-HAS-MC-3.001). The peak in the 3-4 keV band is expected but the tail that extends to extremely low pulse heights contains much more power than expected. Normally, in timed exposure mode, of order 1% of events would appear in a small peak at 1.74 keV, which is the Si-K escape peak. The escape peak is not visible in this plot because it appears to have been swamped by events with partial charge collection.

HRMA effective area model near 2 keV that will be addressed by the telescope science team. In addition, we noted problems that may result from event loss.

One prospective reanalysis of the data would be to attempt to identify events that are actually associated with split events which were not recognized by the ACIS on-board processor. These events could be combined to improve the pulse height distribution so that the QEs of the BI and FI chips might be more closely comparable to that of timed exposure mode. Very little calibration data were taken in the continuous clocking mode but these data must be examined and modeled to see if the apparent QE differences we find can be explained.

There are grating observations of continuum sources that have yet to be reduced and analyzed. In one test, ACIS was read out in timed exposure mode, so we may be able to compare with the results from these observations. Pileup is expected to be more prevalent, however. Another series of tests involving continuous clocking mode employed the carbon EIPS anode, so data will be available for searching for features in the 0.8-1.1 keV region. A preliminary examination of the data[23] showed slightly different contaminants than observed in these copper anode tests.

These data can still be examined in a bit more detail for possible features in the O-K to Cu-Lζ energy range, spanning from about 0.5 keV to 0.8 keV. The details of the O-K edge structure have been measured at a synchrotron using polyimide filters similar to those used in the MEG, so these details should be incorporated into the HETGS grating efficiency curves.

7.9 Effective Area with HRC-I

Objective: Derive the HETGS(HRC-I) effective area and compare it to HRMA, HETG, and HRC-I measurements and predictions. HRC-I effects that must be understood include: quantum efficiency, quantum efficiency, and quantum efficiency.

Publication(s): Flanagan *et al.*[31]

7.9.1 HETG/HRC-I Tests at XRCF

The tests and data presented here are similar to the ACIS-S tests described in Section 7.7. The analysis here for the HETG-HRC-I does not currently include the BND data and hence only relative effective areas are described. In particular, the HRC-I detector uniformity and HETG grating symmetry can be assessed using the plus/minus first order ratio.

HETG was tested in combination with the HRC-I in Phase 2 at XRCF. The complete series consisted of one focus check at 1.254 keV, 33 effective area tests in a defocussed configuration, and one monochromator scan with 4 energies centered on 1.54 keV. These are listed in Table 7.5, along with the energy and range of dispersed orders on the detector.

Figure 7.33 shows the HRC-I with the HEG and MEG grating dispersion pattern at 7 keV. The HRC-I detector is square and the image of Figure 1 is presented in detector coordinates. The dispersion direction for the gratings is aligned approximately parallel to a diagonal of the detector, so that the number of orders detected is limited by the detector size and the intensity of the high orders. In general, the zero order position was displaced from the nominal imaging aim point in order to minimize accumulated dose in that region. Note that the direction of the bias angle of the microchannel plate is toward the top in the figure, and is not symmetric with respect to the dispersion direction. Details of the HRC-I and its calibration have been published by the HRC team[52, 53, 68].

7.9.2 Processing the HRC-I Data

The HRC data were processed in several steps. The raw data files were screened for lost major frames, converted from telemetry format and degapped. Starting with a compressed raw data file, file.rd.gz, the following steps are taken as summarized in the unix command line:

```
gunzip -c file.rd.gz | tm2ftm | nftm2prd -S/dev/null | nprd2epr -u1.0517 -v1.
0363 | nepr_sel -a4090 -P254 > file.nepr
```

The raw data file is uncompressed with `gunzip` then `tm2ftm` screens out lost major frames. Decomutation is preformed by `nftm2prd` with the option not to look at the rate data (`-S/dev/null`). Then `nprd2epr` degaps the data and makes an event list (where 1.0517 and 1.0363 are the u,v degap parameters). Finally, `nepr_sel` sets the amplifier saturation value to 4090 and the upper PHA value to 255. The file `file.nepr` is the desired event list file.

Run ID	TRW ID	Energy keV	HEG Orders	MEG Orders	Comments
i0810621	G-HHI-EA-7.048	7.0	+6 to-6	+3 to -5	
i0811327	G-HHI-EA-99.059	7.0	+4 to -4	+3 to -5	
i0810657	G-HHI-EA-7.047	6.3	+6 to -5	+8 to -5	
i0811342	G-HHI-EA-99.060	6.3	+4 to -4	+8 to -3	
i0810725	G-HHI-EA-7.046	5.76	+5 to -5	+8 to -5	
i0811356	G-HHI-EA-99.061	5.76	+4 to -4	+5 to -5	
i0810804	G-HHI-EA-7.045-1	5.66	+5 to -5	+8 to -9	
i0810756	G-HHI-EA-7.045	5.66	+5 to -5	+5 to -7	
i0810831	G-HHI-EA-7.044	5.48	+5 to -4	+7 to -5	
i0810855	G-HHI-EA-7.043	5.32	+5 to -4	+7 to -8	
i0810916	G-HHI-EA-7.042	5.25	+5 to -4	+8 to -7	
i0810936	G-HHI-EA-7.041	5.13	+4 to -4	+5 to -5	
i0810950	G-HHI-EA-7.040	5.05999	+4 to -4	+6 to -5	
i0811005	G-HHI-EA-7.039	4.96	+4 to -4	+5 to -7	
i0811019	G-HHI-EA-7.038	4.9	+4 to -4	+7 to -8	
i0811037	G-HHI-EA-7.037	4.8	+4 to -4	+7 to -5	
i0811054	G-HHI-EA-7.036	4.59999	+4 to -4	+7 to -5	
i0811114	G-HHI-EA-7.035	4.51	+4 to -4	+7 to -5	
i0811132	G-HHI-EA-7.034	4.0	+4 to -4	+7 to -7	
i0811155	G-HHI-EA-7.033	3.5	+3 to -3	+7 to -6	MEG 2 overlaps HEG 1, Not corrected.
i0811238	G-HHI-EA-7.032	2.29	+2 to -2	+4 to -4	
i0811414	G-HHI-EA-7.031	1.95	+2 to -1	+4 to -4	
i0811434	G-HHI-EA-7.030	1.7	+2 to -1	+3 to -3	
i0940311	G-HHI-EA-9.018	1.48693		+3 to -3	MEG only. Has contaminant line.
i0911019	G-HHI-EA-6.002	1.254		+2 to -2	MEG only. EIPS - broad line.
i0911034	G-HHI-EA-6.003	1.254	+1 to -1		HEG only. EIPS - broad line.
i0910739	G-HHI-FC-1.003-Q1	1.254	+1 to -1	+2 to -2	
i0910817	G-HHI-FC-1.003-Q2	1.254	+1 to -1	+2 to -2	
i0910854	G-HHI-FC-1.003-Q3	1.254	+1 to -1	+2 to -2	
i0910931	G-HHI-FC-1.003-Q4	1.254	+1 to -1	+2 to -2	
i0940337	G-HHI-9.019	1.17595		+1 to -1	MEG only. W contaminant line.
i0811452	G-HHI-10.003	1.54	+1 to -1	+3 to -2	Energy scan; analysis complete.
i0940357	G-HHI-9.020	0.95996			Not analyzed
i0902304	G-HHI-6.004	0.9297			Not analyzed. MEG only.
i0902318	G-HHI-6.006	0.9297			Not analyzed. HEG only.
i0940427	G-HHI-9.021	0.75996			Not analyzed
i0901229	G-HHI-6.005	0.705			Not analyzed
i0940505	G-HHI-9.022	0.70499			Not analyzed
i0900251	G-HHI-6.001	0.5249			Not analyzed. MEG only.
i0900336	G-HHI-6.001-b	0.5249			Not analyzed, MEG only, Contains O.

Table 7.5: Summary of all HETG-HRC-I data sets taken at XRCF.

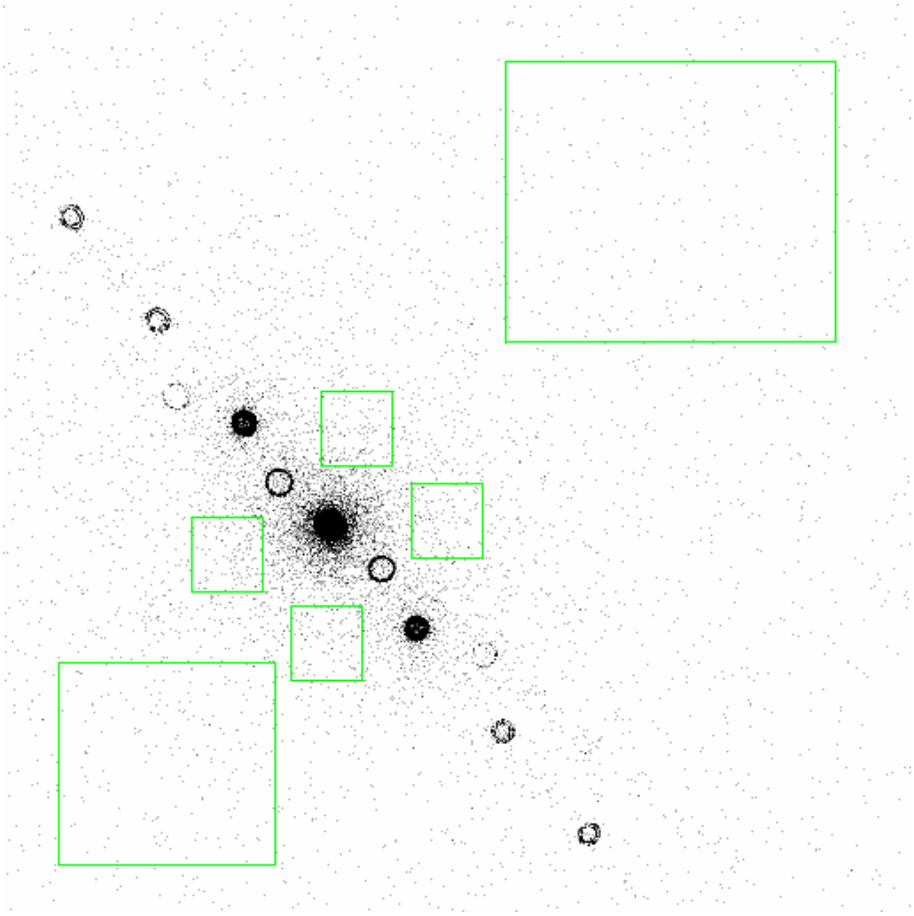

Figure 7.33: HETG-HRC-I image from test at 7 keV. Positive orders are dispersed toward the upper left in the figure. The large box, top right, is used to estimate detector background. The small boxes around zero order sample mirror-scattered events. The data have been "cleaned" to remove saturated events.

7.9.2.1 Event selection criteria

Two sets of event lists were then created, with different rejection criteria based on the saturation levels of the electronics (4096 for the amplifiers and 255 for the pulse height). This approach was prompted by considering the testing conditions early in Phase 2. In the first day of the HETG-HRC-I tests, the detector high voltage was set at a relatively high level and there was a considerably higher fraction of saturated events. This unusual saturation level[68] was decreased on subsequent days (the high voltage was lowered) and has been eliminated in the flight instrument.

Since readout saturation can also result in incorrect position assignment of the events (of order 1/2 mm or less), two separate analyses were performed on the data. In the case of "cleaned" data, all events with pulse height above 254 or with amplifier value above 4090 were rejected. In the second case, saturated events were included in the analysis (for which the data were termed "uncleaned"). There is evidence to suggest a higher proportion of saturated events in bright orders relative to faint orders. (This is currently under study.)

7.9.2.2 Background Subtraction

The technique employed for selecting regions of the grating readout was to display each dataset with SAOtng[80]. Each order of interest was captured in a simple rectangular box region, and the number of events within each box was determined. In order to estimate the effects of background and mirror scattering, several "background" regions were selected, as illustrated in Figure 7.33. The largest box, distant from the zero order, is assumed to reflect approximately detector backgound. The next largest box, while distant from the zero order, nevertheless was found to have a higher ($\sim$ 2 times) background rate and is assumed to contain mirror-scattered photons. The selection of small boxes centered among zero and 1st order had a much higher ($\sim$ 8 times) background rate, which is presumed due to mirror scattering around the zero order. (The c program which counts the events within the box region is /nfs/wiwaxia/h2/kaf/hrc/src/ssm/fits/nepr_sel_kaf.c.)

In the analysis, the simple detector background was used for background subtraction for all orders. This is appropriate for the distant high orders, but there may be mirror-scattered photons captured within the first order regions. Mirror scattering is on the 1% level or less, and by using the measured "scattered rate", we found that corrections to the ratios systematically increase it by 0.5% to a few percent, a negligible effect given the counting statistics and other errors. We have neglected this correction.

7.9.2.3 Detector Uniformity

Flat field tests to measure detector spatial uniformity were not performed with the settings used on the day on which most of the HETG-HRC data were taken. However, the HRC-I was known to be *more* uniform than on subsequent days, for which uniformity data are available[68] at 4.5 keV and 1.49 keV. At 4.5 keV, the HRC-I was found to be uniform to better than 5% over the central region. At 1.49 keV, the detector QE was not as uniform as at the higher energy, but was flat at the 10% level over the central region[68] out to a radius of 30 to 35 mm. Beyond this radius the QE dropped by $\sim$ 20%. No detector uniformity corrections have been applied to the measured ratios.

Error	magnitude	Comments
Counting Statistics	10% to 30%	accounted for in analysis
Background subtraction	up to 3%, systematic	only detector background used
bias angle	few percent	neglected
detector QE nonuniformity	5 to 10% within 35 mm radius; edges drop by 20%	neglected
Event saturation	10 % to 40% systematic	accounted for: all events included

Table 7.6: Corrections, systematic sffects and srrors in HETG-HRC-I analysis

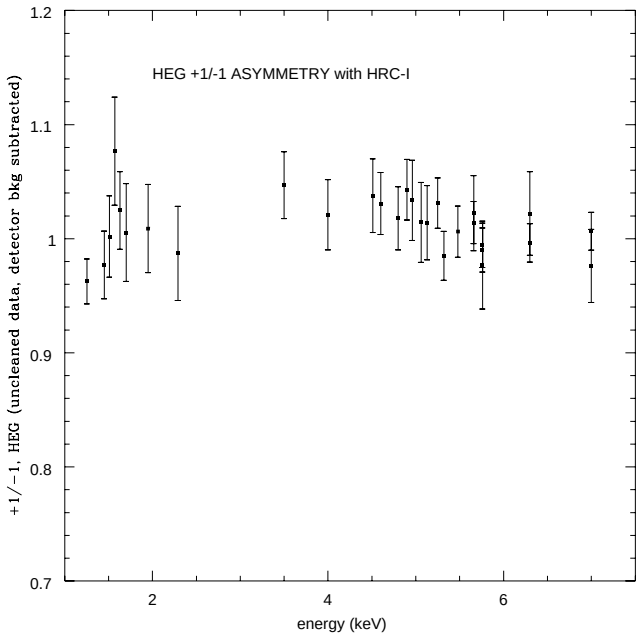

Figure 7.34: Ratio of +1 to -1 for HEG grating on HRC-I. In general, departures from unity are expected to be caused by intrinsic grating asymmetry, detector nonuniformity, or bias angle effects.

7.9.3 Plus/minus First Order Asymetry

It has been noted that the bias angle is not symmetric with respect to the dispersion direction. This can result in an asymmetric detection efficiency of a positive order with respect to its negative counterpart. The angle dependence of the QE is estimated to result in a difference[42] of at most a few percent, and correcting for bias angle has been neglected. In order to examine the potential effects of bias angle on the result, the ratio of the +1 order to the -1 order was taken. Any systematic asymmetry would most likely be ascribed to grating asymmetry in these orders, detector asymmetry due to bias angle, or to nonuniform QE effects across the detector (known to be small). The result is given in Figure 7.34 for the HEG grating, which is more likely than the MEG to show intrinsic asymmetry and which disperses across more of the HRC-I surface. The plot reflects asymmetry due to all effects: the asymmetry is obviously very small in comparison with other errors. Thus, neglect of bias angle and detector uniformity corrections is acceptable. Table 7.6 gives a summary of the various effects that have been discussed and their impact on the results.

7.10 Efficiency and Effective Area Synthesis

Objective: Collect, compare, and come to conclusions regarding all of the efficiency and effective area measurements, focussing on first orders. Also, calculate the relative efficiencies of the diffracted orders seen in the Phase 2 flight detector data in order to calibrate the HETG high-order efficiencies. The use of the two detector's data sets allows likely detector effects to be separated from HETG effects.

Publication(s): Flanagan *et al.*[31], Schulz *et al.*[90]

7.10.1 Overview

During Phase 2 XRCF testing some 54 HRC-I and ACIS-S EA measurements were made with the HETG inserted in the beam. Descriptions and analyses of these data sets are presented in Sections 7.7 and 7.9. The data from these tests can be used to test the predicted high-order efficiencies, expressed as a ratio of high-order to first-order efficiency; these predicted ratios are shown in Figure 7.35. Given that the intensity of higher orders is a strong function of grating bar shape[59], the extension of the subassembly model to very high orders is tenuous, underlining the need for direct measurement at XRCF. Thus, the measurements reported here provide a necessary complement to the limited set of laboratory high-order efficiency measurements that was made on each of the flight gratings. In addition, analysis of the data has yielded insight into both the HRC-I and ACIS-S instruments in aspects that were not fully examined at subassembly level.

7.10.2 HRC-I Data Sets

The HRC-I data sets and aspects of their analysis are described in Section 7.9. From Table 7.5 it is evident that HEG 2nd order is only available on the detector for energies of 1.7 keV and above. For the MEG gratings, 2nd order was suppressed and measurable at only a few energies, but third order was detectable at 1.49 keV and above. Energies below 1.254 keV were not analyzed for either grating since there were no higher orders falling on the detector. The breakdown of order by energy is given in Table 7.7.

Order	HEG Energy range	MEG Energy range	Comments
2	1.7 to 7.0	1.254, 1.7, 1.95, 2.29	not sufficiently detectable at other energies
3	3.5 to 7.0	1.48693 to 7.0	
4	4.0 to 7.0	1.95 to 6.3	not sufficiently detectable at 7.0
5	5.25 to 7.0	3.5 to 7.0	
6	6.3 and 7.0 only	3.5 to 6.3 except 5.13	
7		3.5 to 5.76 except 5.05999, 5.13	
8		4.9, 5.25, 5.32, 5.66, 5.76, 6.3	
9		5.66 only	

Table 7.7: Energy ranges of the measured HETG-HRC-I higher orders.

A detailed investigation showed that smearing of the image due to electronic saturation did *not* systematically affect the result: ratios remained unchanged to within $\sim 3\%$ regardless of whether

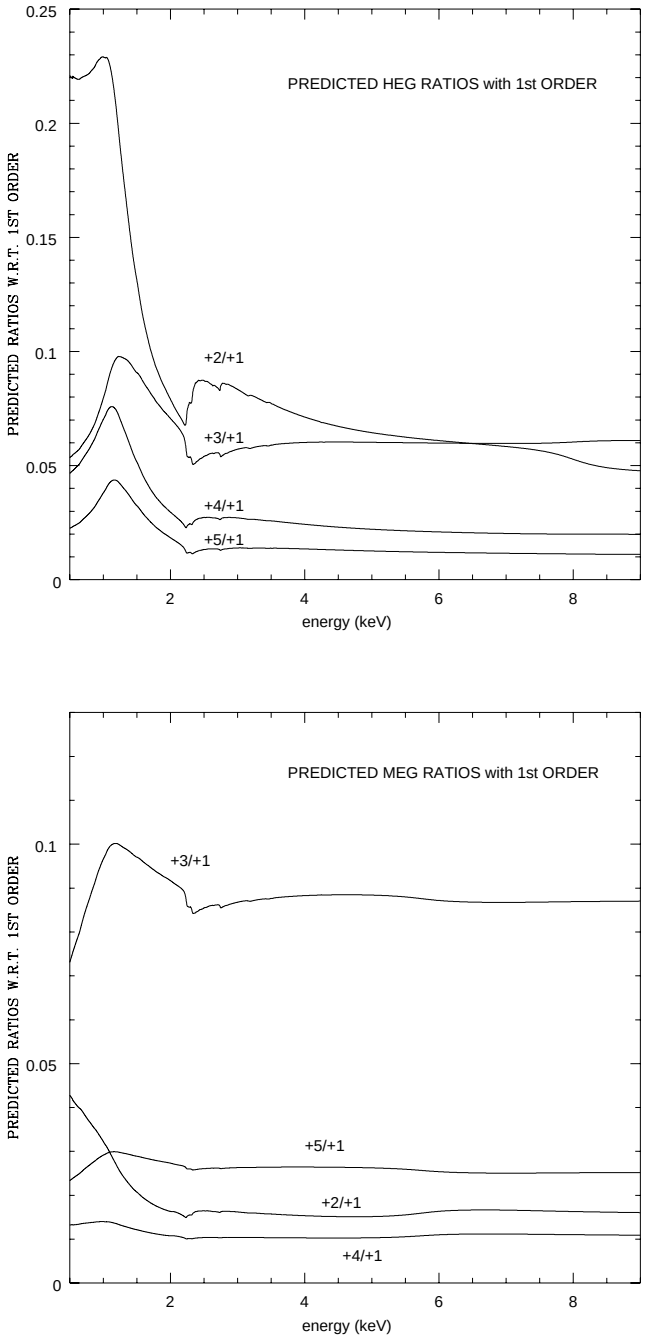

Figure 7.35: Predicted ratios of orders 2 through 5 with respect to 1st order for HEG (top) and MEG (bottom). These are based on subassembly calibrations.

or not the smeared events were captured within the counting region. This is understandable since the regions of interest used were large compared to the position errors due to saturation.

However, as mentioned in Section 7.9, there is evidence to suggest a higher proportion of saturated events in bright orders relative to faint orders. If so, then when "cleaned" data are used, ratios formed with a bright first order are systematically enhanced (by 10% to 40%). Therefore, since saturated events represent true X-ray events and their positioning errors do not compromise the analysis, we have chosen to use the "uncleaned" data set throughout this order-ratio analysis.

Grating	Order Ratio	Typical Counting Statistics	Assigned Subassy Error	Deviation from Predicted
HEG	2/1	10%	20 to 25%	-10 to -15%
	3/1	10%	50%	-35%
	4/1	15%	90%	-35%
	5/1	20%	90%	-60%
	6/1	20%	90%	-60%
MEG	2/1	15%	20 to 25%	$\approx$ correct
	3/1	10%	50%	-5%
	4/1	20%	90%	+25%
	5/1	20%	90%	-25%
	6/1	20%	90%	$\approx$ correct
	7/1	20%	90%	-25%
	8/1	30%	90%	$\approx$ correct
	9/1	30%	90%	-45%

Table 7.8: Comparison of Predictions with Measured ratios for HETG + HRC-I higher orders.

7.10.3 Discussion of HRC Order Ratios

Figure 7.36 shows the measured HEG ratios for 2nd, 3rd and 4th orders overlaid with the predictions of Figure 7.35. (Solid points are the ratios of positive orders, hollow points refer to negative orders. The error bars reflect only counting statistics.) The 5th and 6th order ratios are similar and are not shown. The measurements appear to be systematically suppressed relative to the predictions. The approximate magnitudes of these deviations are given in Table7.8 along with the typical errors due to counting statistics. Although the departures are within the errors assigned to the predictions, they exceed the counting statistics and other uncompensated correction effects, and are taken to be significant.

Figure 7.37 shows the shows the measured MEG ratios for 2nd, 3rd, 4th and 5th orders. In general, there is fairly good agreement with the predictions. Moreover, the higher ratios (orders 6 through 9) are similar, agreeing reasonably well with the subassembly predictions. These results are summarized in Table 7.8.

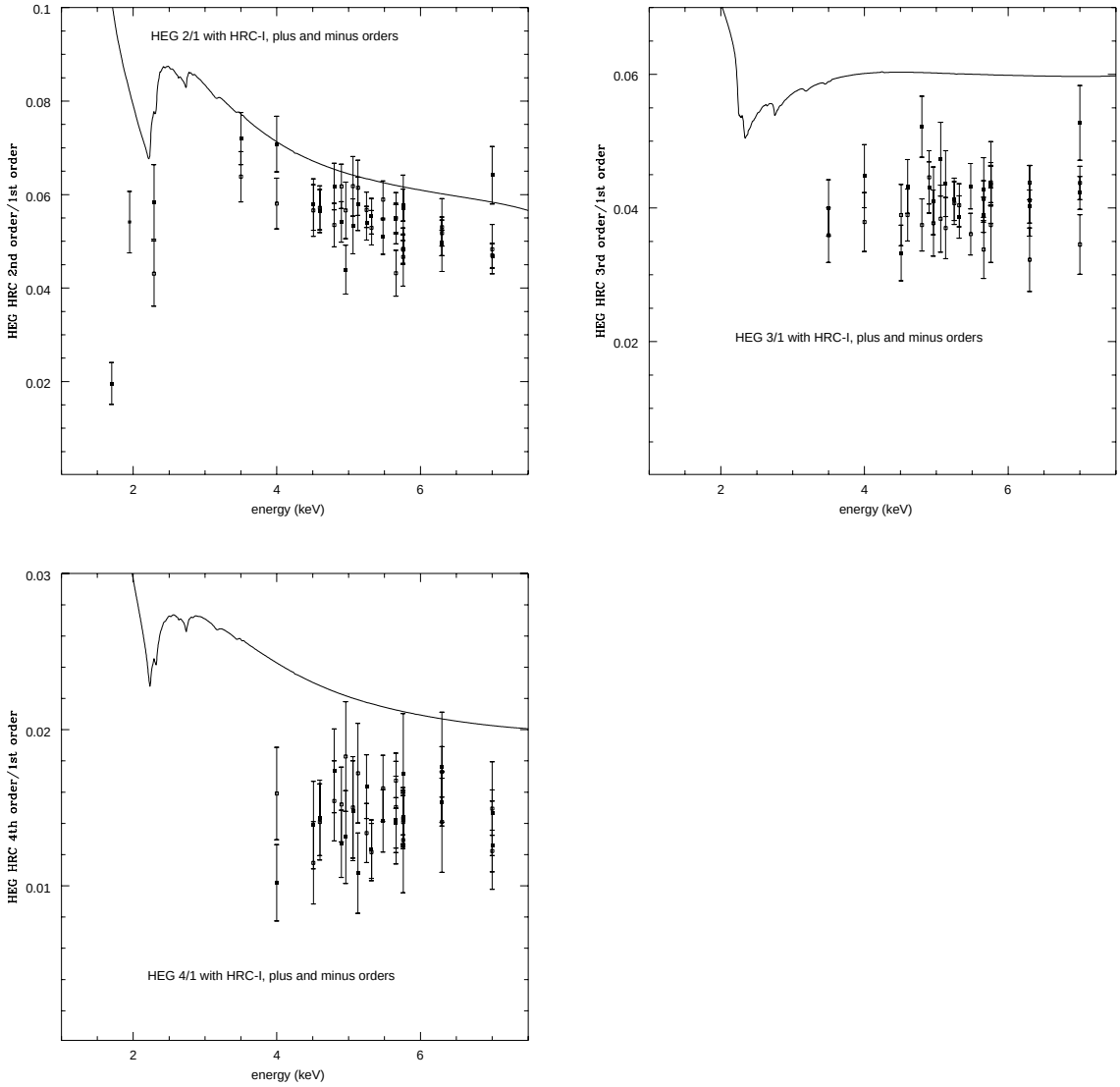

Figure 7.36: Measured HEG ratios for 2nd,3rd, and 4th orders with HRC-I. The solid curve represents the predicted ratios. Hollow points indicate ratios of negative orders, and solid points refer to positive orders. The error bars are due to counting statistics. The measurements systematically fall below predictions.

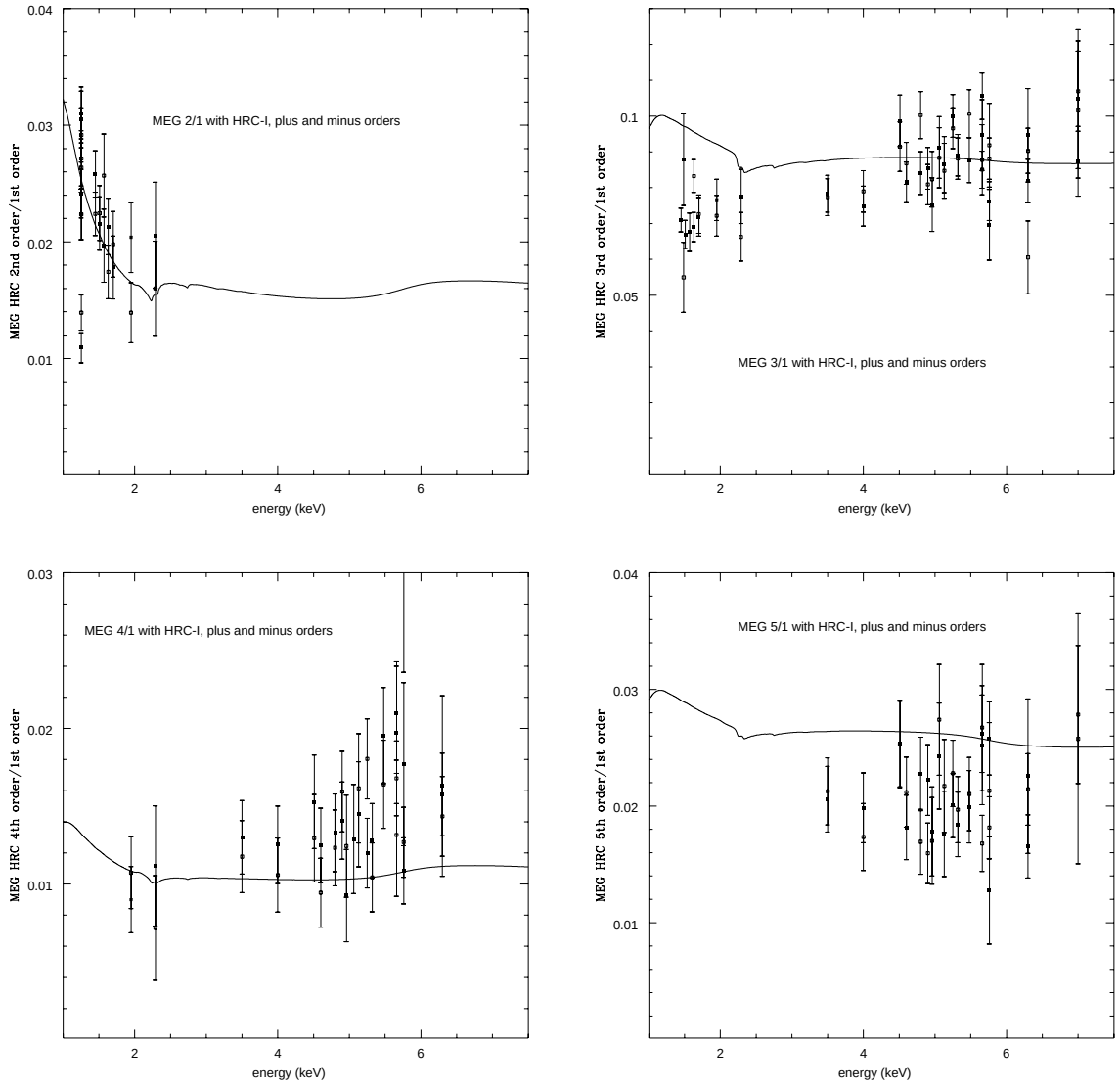

Figure 7.37: Measured MEG ratios for 2nd,3rd, 4th and 5th orders with HRC-I. The measured values agree fairly well with the predictions.

7.10.4 ACIS-S/HETG Order Ratios

Figure 7.38 shows the HEG 2nd, 3rd, 4th and 5th order ratios. Ratios between positive orders are denoted with filled boxes, whereas those between negative orders are marked by hollow boxes. In each one of these plots, there is a strong enhancement above 7 keV. Since it is common to all four order ratios, it likely arises from a supression of first order effective area. From the 2nd order ratio, it is clear that this feature is far stronger it the -2/-1 ratio (where the -1 order is captured by a FI device) than in the +2/+1 ratio (where the +1 order lands on the S3 chip, a BI device). The 3/1 ratio agrees generally with the HRC-I results over the energy range of 3 to 5 keV, but then the ratio is enhanced above 5 keV and shows other structure. In general, the HEG ratios with ACIS-S show much structure and do not reproduce the systematic reduction relative to predictions as shown with the HRC-I.

Figure 7.39 shows the MEG 3rd, 5th, 7th and 9th order ratios. The 3rd and 5th orders show enhancements above 5 keV, but there appear to be some smooth regions (2.5 to 4.5 keV) which agree reasonably well with predictions.

The features that have been noted can be traced to detector effects which will be discussed below.

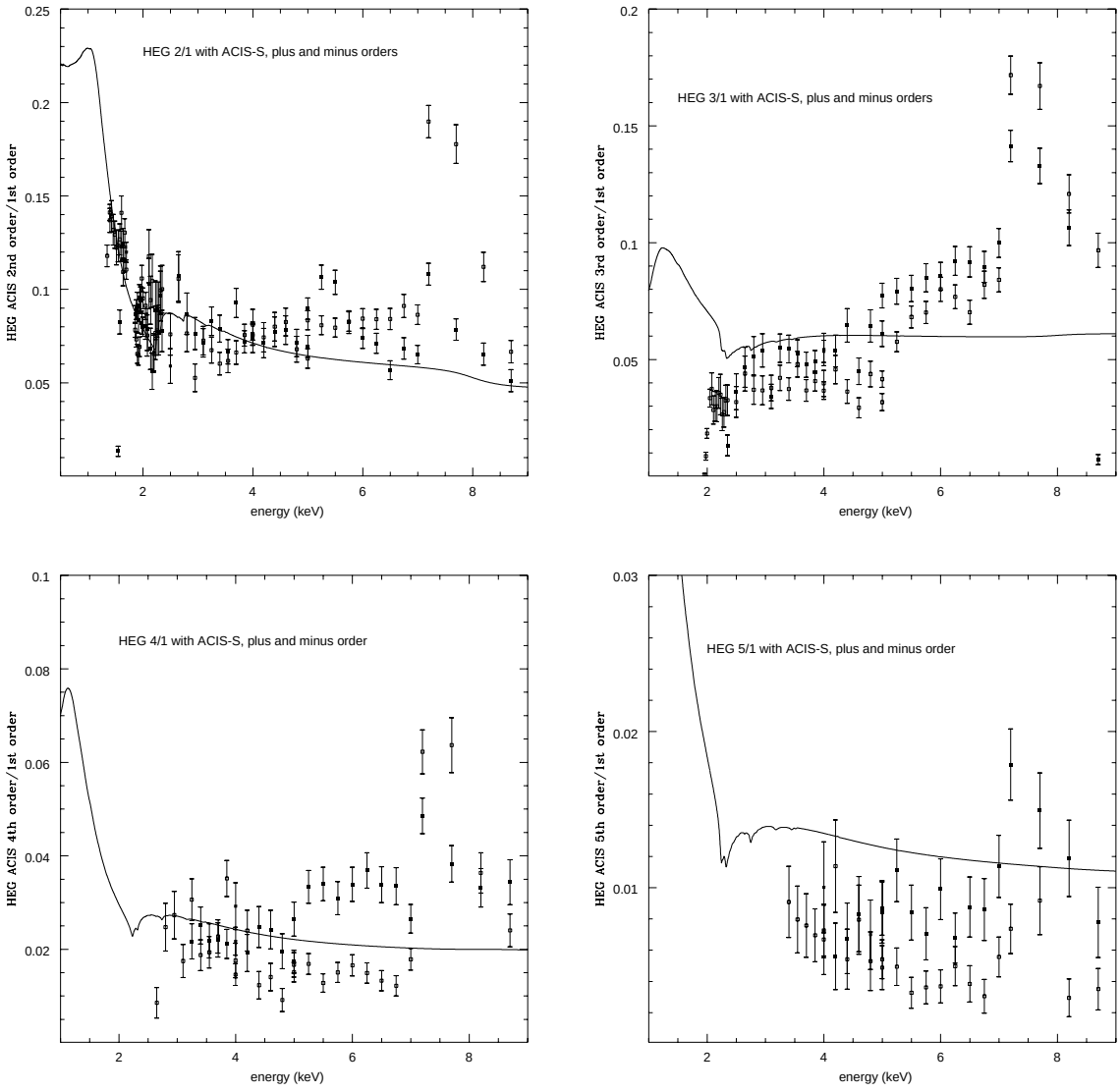

Figure 7.38: Measured HEG ratios for 2nd, 3rd, 4th and 5th orders with ACIS-S.

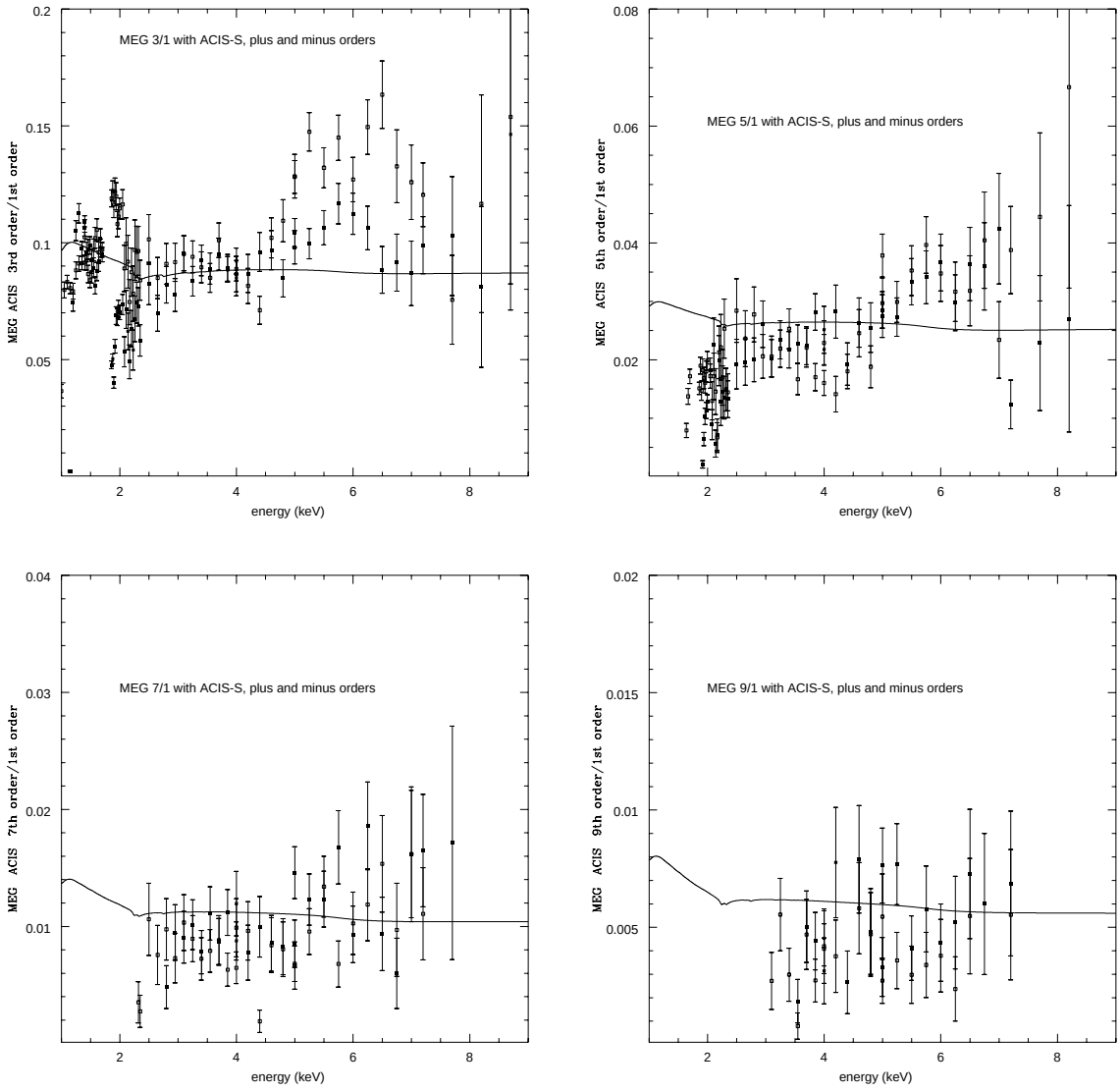

Figure 7.39: Measured MEG ratios for 3rd, 5th, 7th, and 9th orders with ACIS-S.

7.10.5 Discussion of ACIS-S/HETG Order Ratios

The absolute effective areas derived in Section 7.7 in general agree with the expected effective area function to quite a high degree. However, there are significant local deficiencies that remain. The most prominent is an apparent drop of effective area for HEG +1 and -1 orders below the expected curve at energies above 5 keV, Figure 7.21.

One possible explanation is a local non-uniformity effect in the beam to which the HEG, because of its smaller aperture, would be more susceptible than the MEG. (In the MEG such a drop is not significantly visible in the data.) However, the observed drop in HEG area sometimes exceeds 10%, which would need a quite strong local non-unifomity in the beam. This is unlikely since the DCM beam at higher energies has been measured to be very uniform overall. In addition, if beam nonuniformities were the cause, the 2nd order effective area would also show this deficiency, but it does not. Also none of the beam uniformity meaurements ever performened at that energy ever showed any significant deviations. Therefore a local beam uniformity effeect can be ruled out.

A more plausible explanation, which is currently under investigation, are deficiencies in the CCD quantum efficiencies caused by grade migration and lost charge effects at high energies and high fluences (see Section 7.7.3). The HEG is more susceptible to these effects since the fluence in the HEG image at XRCF is generally higher than in the MEG image (recall that the HEG mirror shells are of smaller diameter). A quantitative assessment of these effects is still under way.

During subassembly testing of the ACIS instrument, fluences were low and grade migration and lost charge effects were not observed[5]. Although the focused beam at XRCF increases the fluence, the higher order grating efficiencies are low enough that fluences in these orders drop below those of subassembly testing. Thus, grade migration and lost charge effects should not be noticed in any order other than 1st (see also Section 7.7). Key indicators for grade migration and charge loss effects are the ratios of the lower orders to the first orders. (Higher order ratios will have poor counting statistics and large uncertainties.) Figures 7a and 8a show the HEG 2nd to 1st order ratio and the MEG 3rd to 1st order ratio. The solid line indicates the prediction. Clearly, in both figures the ratios start to deviate from the prediction above 5 keV, suggesting a deficiency in the 1st order effective area. Here the HEG, as expected, shows the strongest deviations. Above 5 keV we probably see the effects of grade migration, and above 7 keV the additional effect of charge loss. The latter effect is more pronounced in the negative order ratio (empty squares) where the 1st order appears on a FI device, as compared to the positive ratio (filled squares), where the 1st order appears on a BI device. This is consistent with the related effect of 'blooming' caused by high energy events in FI devices; it is not seen in BI devices[75]. The effects are also observed in the HEG 3rd and MEG 5th order ratios. At higher orders, the ratios follow the predictions nicely, however the data show significant scatter due to poor counting statistics.

We can rule out the possibility that these effects are caused by the grating itself, because they are not observed in analogous measurements with the HRC-I. As discussed earlier, the near-perfect symmetry of the +1 and -1 orders (to within 5%) of the HEG with HRC-I exclude the grating as a contributor to these effects.

7.10.6 Conclusions

We have examined the ratios of higher grating orders with respect to the first order for Phase 2 tests of HETG with the flight instruments, HRC-I and ACIS-S. We found that:

- The symmetry of the +1 and -1 orders of HEG with HRC-I lead to the conclusion that detector nonuniformity, grating asymmetry and bias angle effects were small.
- HRC measurements show suppressed higher grating orders for HEG relative to predictions. Measurements of the MEG orders agree well with predictions.
- ACIS-S shows strong detector effects, compatible with grade migration and charge loss, especially in the HEG 1st orders.

Several items remain for future work. These include:

- Investigate the relation between saturation and count rate density in HRC-I.
- Quantitative analysis of grade migration and charge loss in ACIS-S.
- Incorporate synchrotron high order measurements.
- Examine Phase 1 measurements for high orders and asymmetry.
- Analyze EIPS sources with both detectors and the monochromator scan with HRC-I.

Part III

Calibration Data, Software, and Products

Section 8

Calibration Archive Organization

We have created and provide an archive of files as a companion to this Report which contains the data, software, and products described in this report. The specific directory structure of this archive are referred to in this Report so that items can be conveniently found. This chapter provides a general overview to the types of files in the archive and their organization, the next chapters provide specific information on the various data, software, and the resulting HETG and HETGS products themselves.

Directory structure... Environment variables...

Main subdirectory types...

Calibration Data are all the raw data acquired that has information to constrain the instrument models; these are the basis of a calibration.

Calibration Measurement Products are the specific results from specific manipulations of the Calibration Data and cover many levels of complexity. They represent the results when the raw data have been "analyzed" to create something, *e.g.*, "counts per second in the Al-K BND bump", "ACIS-I 5 arc min Mo-L off-axis encircled-energy curve", or "witness flat reflectivity at 8.04 keV". There are lots of these! And their meaning and organization and synthesis can require a lot of human knowledge. Many results may be ammenable to database storage, others may require memos to describe and define them. Error estimates are produced for each measurement result as well.

Fundamental Calibration Products are the most detailed "encoding" of the calibration activity into detailed (complex) models, *e.g.*, SAOSAC as a model of the HRMA. This requires a synthesizing by calibrationists of the various Calibration Measurement Products and model expectations.

Calibration Interface Products are specific, well-defined, useful parameters, tables, models which describe the essence of the instrument to sufficient accuracy to be useful yet in a more accessible form than the Fundamental Calibration Products. (The distinction is blurred and need not be too strict. For example the ACIS pixel size is about as Fundamental as can be yet it is also a very useful CIP value.) These CIPs are the main interface between the calibration activity and the rest of the system.

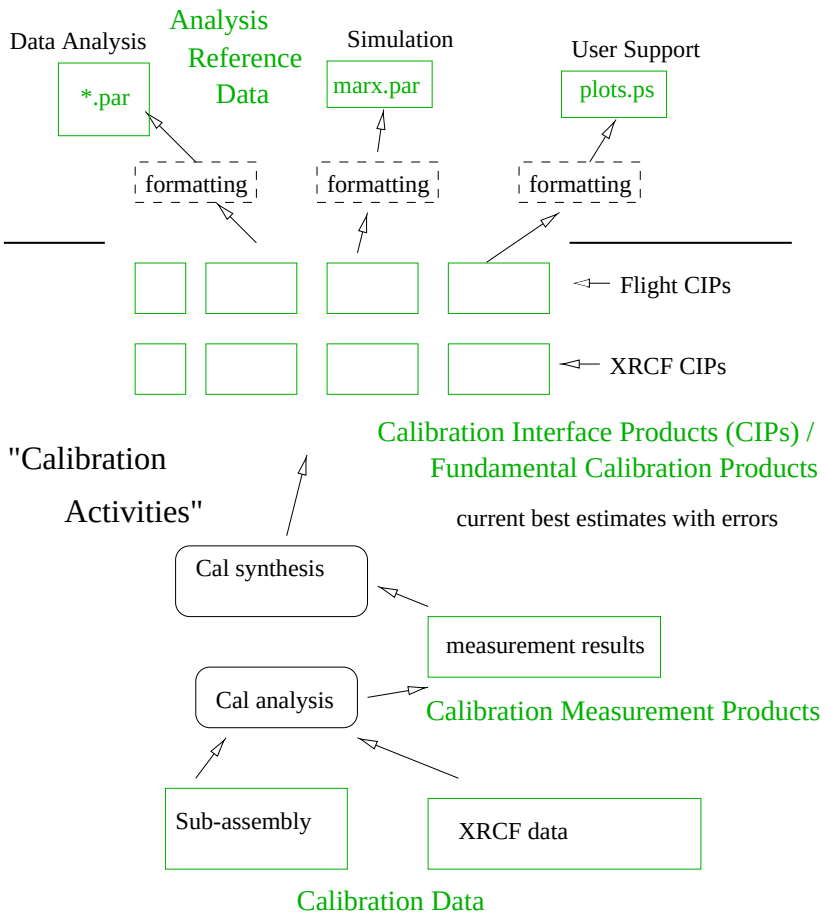

Figure 8.1: Schematic Diagram of the Types of Calibration Products

Analysis Reference Data is used to explicitly identify those data that are needed and used by, *e.g.*, the ASC Data System for simulation and data analysis. The formats are dictated by the analysis algorithms and software architecture; often these data may be simply reformatted versions of the CIPs. The **MARX** parameters, Section 11.3.5, are a good example of Analysis Reference Data.

The relationship of these products is schematically shown in Figure 8.1.

Section 9

Calibration Data

9.1 Synchrotron Data

The synchrotron data are archived in directory `/nfs/wiwaxia/d4/ASC/data/SYNCHROTRON` at MIT. The table below lists the archive subdirectories for the different data sets. The directory structure is such that the synchrotron runs are categorized by date and facility. The synchrotron facility is denoted by daresbury, bnl (the National Synchrotron Light Source at Brookhaven National Labs), als (Advanced Light Source) or BESSY (Physikalisch–Technische Bundesanstalt at BESSY).

The data have been collected and analyzed over the years by many individuals who are no longer available for consultation, so the archive directories contain notes, software and working files that may be useful. In each case there will be a subdirectory, RAW_DATA, which houses the unrefined data. The subdirectory NOTES contains publications, email correspondance, memos and pertinent information. A write-up of the results, if available, will be placed here. Finally, if the data are reanalyzed, this will be reflected in a subdirectory (i.e., `BESSY_95oct/KAF_ANALYSIS_98oct`). These archived directories will be updated as appropriate.

Table 9.1: Summary of HETG synchrotron radiation tests and archive of data

Date	Facility	Sample	Energy	Comments	Archive
July '93	NSLS	HX101	2.03 - 4	preliminary tests	
Nov '93	Daresbury	HX101	8.442	period variations (UL)	daresbury_nov93
Jan. '94	NSLS	HX101	0.7 - 6	first tests	bnl_94jan
Feb. '94	NSLS	1Au	2.03 - 6.04	new gold optical constants	bnl_94feb
Jun. '94	NSLS	HA04	2.03 - 6		bnl_94jun
"	"	HX101	2 - 3.5		"
"	"	MA12	0.7 - 5	± 1 order assymetry	"
Feb. '95	NSLS	HX220	0.5 - 6.4	X-GEF reference grating	bnl_95feb
"	"	MX078	0.5 - 3.5	X-GEF reference grating	"
May '95	NSLS	HX220	1.05 - 1.95	X-GEF reference grating	bnl_95may
"	"	poly	0.4 - 1.83	poly transmission	"
Oct. '95	NSLS	HA2021	2.03 - 6.5	flight lot 2, dense 0&1 orders	bnl_95oct
"	"	MA1047	2.1 - 5.0	flight lot 3, dense 0&1 orders	"
Oct. '95	PTB	HA2021	0.4 - 1.9	flight lot 2	BESSY_95oct
"	"	MA1047	0.4 - 1.5	flight lot 3	"
"	"	HA2049	0.2 - 1.5	polyimide sample, flight lot 2	"
"	"	MA1066	0.2 - 1.5	polyimide sample, flight lot 3	"
"	"	HX507	0.05 - 1.9	gold foil transmission	"
Mar. '96	NSLS	HD2338	2.0 - 6.4	flight lot 4; ± 1, higher orders	bnl_96mar
"	"	MB1148	2.1 - 4.9	flight lot 9; ± 1, higher orders	"
Aug. '96	ALS	poly	0.06 - .940	poly transmission, R. Blake	als_96aug
Nov. '96	NSLS	1Au	2.01 - 7.0	gold transmission, R. Blake	bnl_96nov

9.2 HETG Facet Data

9.3 LR Data

9.4 X-GEF Data

9.5 HESS Design and Metrology Data

9.6 Alignment Data

9.7 XRCF Data

Section 10

Calibration Software

Subassembly and XRCF analysis was carried out by several people using a variety of s/w. The directory `$CALDBhetgcal/software` contains subdirectories of HETG/MIT unique software that produced the analyses reported here.

10.1 dd's IDL S/W

10.2 sct's IDL S/W

10.3 hlm's IDL S/W

10.4 Efficiency S/W

Section 11

Calibration Products

11.1 Overview of Products

This section provides a general overview to the types of calibration products, the next sections provide the HETG and HETGS products themselves.

Fundamental Calibration Products are the most detailed "encoding" of the calibration activity into detailed (complex) models, *e.g.*, SAOSAC as a model of the HRMA. This requires a synthesizing by calibrationists of the various Calibration Measurement Products and model expectations.

Calibration Interface Products are specific, well-defined, useful parameters, tables, models which describe the essence of the instrument to sufficient accuracy to be useful yet in a more accessible form than the Fundamental Calibration Products. (The distinction is blurred and need not be too strict. For example the ACIS pixel size is about as Fundamental as can be yet it is also a very useful CIP value.) These CIPs are the main interface between the calibration activity and the rest of the system.

Analysis Reference Data is used to explicitly identify those data that are needed and used by, *e.g.*, the ASC Data System for simulation and data analysis. The formats are dictated by the analysis algorithms and software architecture; often these data may be simply reformatted versions of the CIPs. The **MARX** parameters, Section 11.3.5, are a good example of Analysis Reference Data.

The relationship of these products was schematically shown in Figure 8.1.

11.2 Fundamental Calibration Products for HETG

As we have seen, the LRF functions depend not only on shell-level quantities but on grating-level data, *e.g.*, grating mis-alignment angles[60]. For this reason, *the fundamental HETG calibration or model is at the grating facet level.*

For each grating facet, $f = 1$ to 336, we have a diffraction efficiency $g_f(E, m)$, period map in facet coordinates $p_f(x, y)$, and alignment distribution $\Gamma_f(\phi_{\rm roll})$ as well as mechanical parameters. These fundamental data can be combined with other information to produce, *e.g.*, ν_s, $G_s(E, m)$, $SEA(E, m, \dots)$, and $LRF(E, m, \dots)$.

11.3 HETG Calibration Interface Products

A discussion of and values for the HETG CIPs are presented here; data files, discussions, and updates are available at `http://space.mit.edu/HETG/xrcf.html` under "Calibration Products".

11.3.1 Basic Parameters

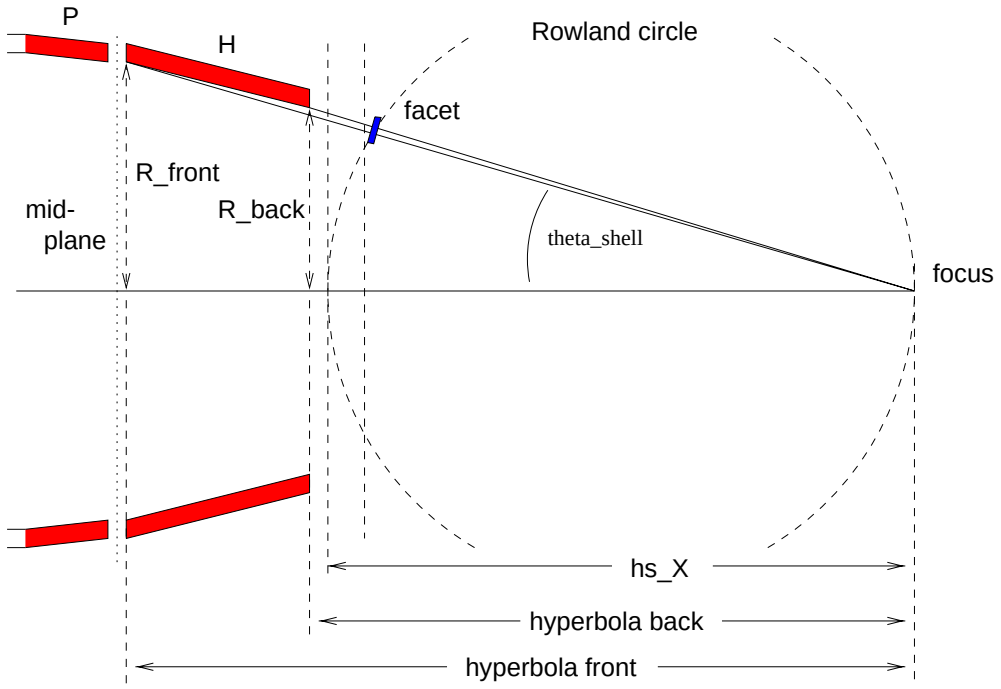

Figure 11.1: Basic Geometry for HETG Facet Location

Basic parameters of the HETG design are tabulated in the file `HETGbasic.rdb` for computer input and reproduced here in Table 11.1. The HETG radii given here are really a method to record the angle of the central ray through the shell's facets, "theta_shell" in Figure 11.1:

$$\tan\theta_s \;=\; \mathrm{HETGrad}_s \;/\; \mathrm{HETGrd} \tag{11.1}$$

To-do:
Produce and include reference to 3-D facet location information.

name	value	error	unit
HETGrd	8633.69	0.1	mm
HETGrad1	521.66	0.1	mm
HETGrad3	419.90	0.1	mm
HETGrad4	370.66	0.1	mm
HETGrad6	275.44	0.1	mm
HETGvign1	0.937	0.01	none
HETGvign3	0.940	0.01	none
HETGvign4	0.931	0.01	none
HETGvign6	0.936	0.01	none

Table 11.1: Basic HETG Design Parameters, from `HETGbasic.rdb`.

11.3.2 Periods, Angles, and Spacing

Periods

Lab measurements were made on the flight gratings for HETG as well as on the TOGA gratings used in XRCF rehearsal. These laboratory measurements were corrected based on NIST-measured reference samples (Section 4.1.2) resulting in our best estimate "LR-NIST" periods.

The current CIP adopted periods (in Å) are the sub-assembly values because XRCF measurements are not accurate enough to require a change. In particular a spacing discrepancy still exists, Section 6.2. The period errors are all taken as the sub-assembly values, again because (with an HETG displacement assumption) XRCF measurements are in agreement and do not provide any smaller error bounds.

Angles

The mean dispersion angles have been measured at XRCF and the HETG opening angle should be the same for XRCF and flight. The flight clocking and grating angles have been modified slightly from the XRCF values by the as-installed +46 arc second HETG roll.

Spacing

The HEG/MEG period difference seen between sub-assembly (HeCd,HeNe) and XRCF-AL-K (assuming a spacing of 8788.04 mm) of about 500 ppm is assumed to be due to an inaccurate value for the HETG Rowland spacing at XRCF, Section 5.2.1. Thus, for now the HETG position at XRCF is set to be 8782.8 mm to have reasonable agreement between XRCF and sub-assembly periods (and hence calculated line energies). The cause for the (alleged) displacement has not been determined.

For flight spacing, Scott Texter reports that EK measures (mechanical means) the as-installed HETG to be 0.009 inches closer to the HRMA than designed, so expected flight spacing is 8633.69+0.009*25.4 = 8633.92 mm. The error on this is probably 0.2 mm or less (HRMA-grating spacing). However the HRMA-focus spacing may still have error of order 0.5 mm.

name	value	error	unit
HEGp	2000.81	0.05	Angstrom
MEGp	4001.41	0.10	Angstrom
HETGrsX	8782.8	0.50	mm
HETGrsF	8633.92	0.50	mm
HETGopenX	9.934	0.008	degrees
HETGopenF	9.934	0.008	degrees
HETGclockX	-0.225	0.05	degrees
HETGclockF	-0.215	0.05	degrees
HEGangleX	-5.19	0.05	degrees
MEGangleX	4.74	0.05	degrees
HEGangleF	-5.18	0.05	degrees
MEGangleF	4.75	0.05	degrees

Table 11.2: HETG Period, Angle, and Spacing Parameters, from `HETGperiod.rdb`.

11.3.3 Period and Roll Variation Parameters

A coarse characterization of the gratings LRF effect is with the period and roll variations, listed as dp/p and γ in the error budget of Table 2.2. These values are measured in the laboratory by the LR and Alignment setups. Confirmation of these laboratory values at XRCF with the XRCF LRF Core analysis has only begun, Section 6.3.

The MEG mis-aligned gratings have pointed out a mechanism whereby the alignment measurement differs from the actual grating bar orientations. It is likely that the same effect operating at a lower and randomized level will lead to an increase in the actual γ value over the alignment system determined one. A simple analysis of one XRCF data set suggests that γ may be between 1 or 2 arc minutes rms, hence a value of 1.5 arc minutes (with a large 0.5 arc minute error) is being adopted preliminarily.

As for the period variations, the LR predictions of 127 ppm and 106 ppm, Figures 4.4 and 4.5, are a lower limit to these variations. Again the limited XRCF analysis has not produced a precise value but suggests $dp/p < 300$ ppm. Unlike the alignment effect, there is currently no expectation that the dp/p measured by the LR is in error, so the proposed baseline values are the LR values increased by rss'ing them with 100 ppm to account for any mounting induced distortions.

name	value	error	unit
HEGdpop	146.	50.	ppm
MEGdpop	162.	50.	ppm
HEGroll	1.5	0.5	arc minutes
MEGroll	1.5	0.5	arc minutes

Table 11.3: Parameters Effecting the HETG LRF Core, from `HETGcore.rdb`.

11.3.4 Efficiency Products

Table 11.4 lists the available files that contain the current best estimates of the HETG diffraction efficiency, $G_s(E, m)$, for $m = -11, \ldots, +11$; note that error files are available as well. These files have equal plus and minus orders and include the shell vignetting ν_s factor. Samples of this data are plotted in Figures 11.2 and 11.3.

Shell	Data File	Error File
1	HETG_shell1_effic.rdb.gz	HETG_shell1_effic_err.rdb.gz
3	HETG_shell3_effic.rdb.gz	HETG_shell1_effic_err.rdb.gz
4	HETG_shell4_effic.rdb.gz	HETG_shell1_effic_err.rdb.gz
6	HETG_shell6_effic.rdb.gz	HETG_shell1_effic_err.rdb.gz
MEG	MEG_effic.rdb.gz	MEG_effic_err.rdb.gz
HEG	HEG_effic.rdb.gz	HEG_effic_err.rdb.gz
HETG	HETG_effic.rdb.gz	HETG_effic_err.rdb.gz

Table 11.4: CIP Efficiency Files for the HETG, available from
`http://space.mit.edu/HETG/cal_prods.html/#HETG_CIP`

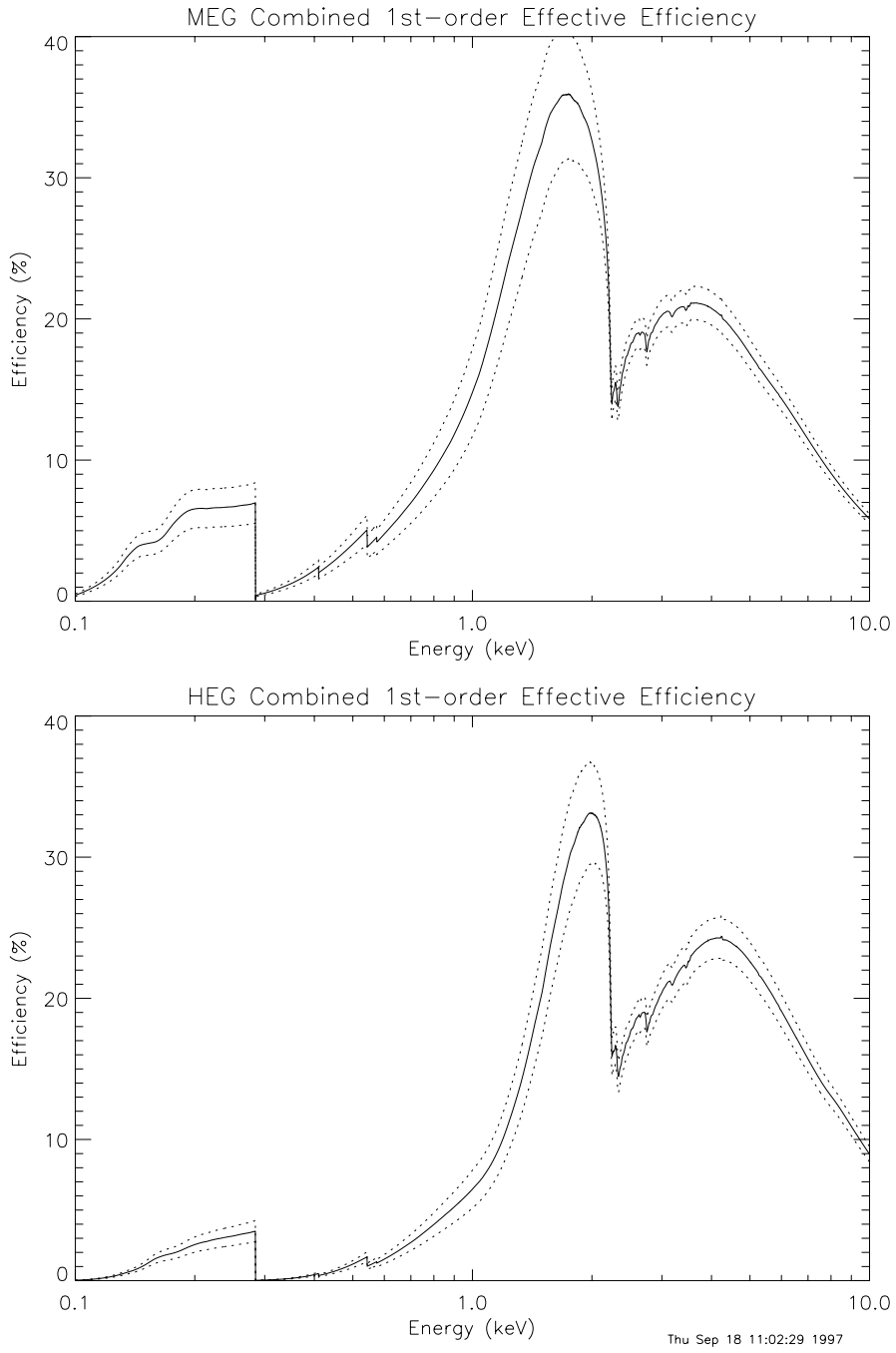

Figure 11.2: Effective Efficiency for First-order MEG and HEG. These efficiencies are the mirror weighted average of the shell-by-shell efficiencies for the appropriate pair of shells. Plus and minus orders have been combined. The dotted lines are the "2-sigma" errors of the shell efficiencies with additional error due to uncertainties in the relative area (weighting) of the HRMA shells.

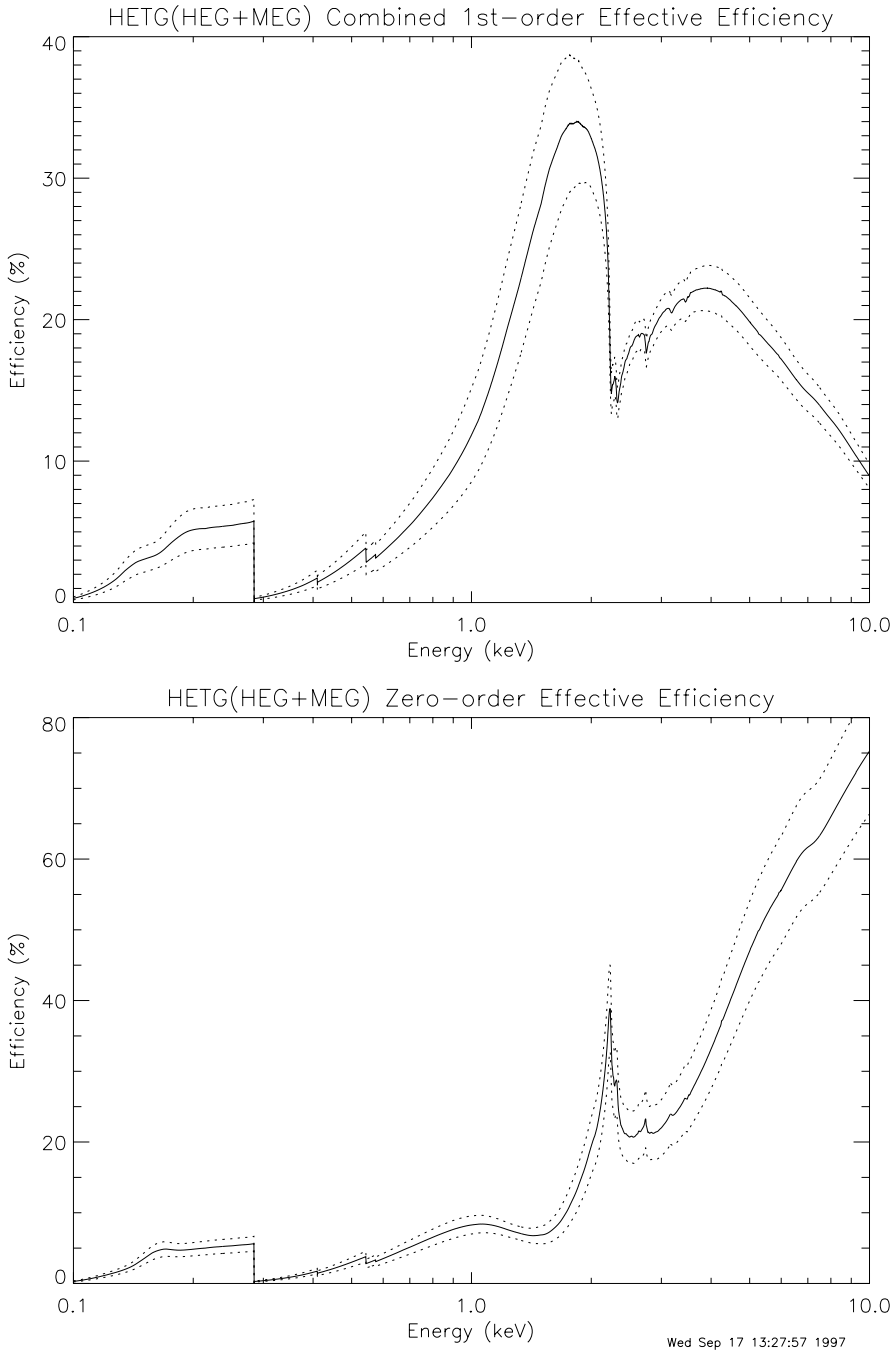

Figure 11.3: Effective Efficiency for HETG 1st and 0 orders. These efficiencies are the mirror weighted average of the shell-by-shell efficiencies. The first-order efficiency is for combined plus and minus orders for HEG and MEG. The dotted lines are the "2-sigma" errors of the shell efficiencies with additional error due to uncertainties in the relative area (weighting) of the HRMA shells.

11.3.5 MARX Parameters

The **MARX** ray-trace package, Section 2.3, provides a high fidelity model of the HETGS. To define the HETG in **MARX** there are parameters and data files to be specified. It is the HETG and ASC calibration groups domain, working with the **MARX** developers, to provide accurate values for these **MARX** inputs.

The **MARX** inputs can be divided into those directly related to the LRF and those that govern diffraction efficiency. These are presented in the following sections.

11.3.5.1 MARX HETG LRF Parameters

The LRF parameters bascially encode the Rowland design and some aspects of its real-life construction. The values presented in Table 11.5 are all taken directly from the corresponding values determined in the CIP Sections 11.3.1 through 11.3.3. Note that the MEG mis-aligned gratings and the HEG scatter are not currently included in **MARX** simulations.

Table 11.5: Flight HETG LRF parameters for use in **MARX**.

Parameter	Value	Unit
RowlandDiameter	8633.75	mm
hegTheta	-5.18	degrees
megTheta	4.75	degrees
HETG_Shell1_Theta	4.75	degrees
HETG_Shell3_Theta	4.75	degrees
HETG_Shell4_Theta	-5.18	degrees
HETG_Shell6_Theta	-5.18	degrees
hegdTheta	1.5	arc minutes rms
megdTheta	1.5	arc minutes rms
HETG_Shell1_dTheta	1.5	arc minutes rms
HETG_Shell3_dTheta	1.5	arc minutes rms
HETG_Shell4_dTheta	1.5	arc minutes rms
HETG_Shell6_dTheta	1.5	arc minutes rms
hegPeriod	0.200081	microns
megPeriod	0.400141	microns
HETG_Shell1_Period	0.400141	microns
HETG_Shell3_Period	0.400141	microns
HETG_Shell4_Period	0.200081	microns
HETG_Shell6_Period	0.200081	microns
hegdPoverP	146.e-6	rms
megdPoverP	162.e-6	rms
HETG_Shell1_dPoverP	162.e-6	rms
HETG_Shell3_dPoverP	162.e-6	rms
HETG_Shell4_dPoverP	146.e-6	rms
HETG_Shell6_dPoverP	146.e-6	rms

11.3.5.2 MARX Rectangular Efficiency Parameters

MARX offers two ways to specify a gratings diffraction efficiency. The old standby is a rectangular grating model in which a few parameters are used to specify a rectangular model and the diffraction efficiency $G_{\rm config}(E, m)$ is calculated from these parameters. The second method is to use a set of look up tables for the efficiency, described in the next section.

Although the HETG gratings are not rectangular and also vary in their properties, it is possible to select a set of rectangular parameters that comes close to approximating the effective efficiencies of Section 11.3.4. Figures 11.4–11.7 present comparisons of these rectangular efficiencies and the current best CIP values. The first-order effective efficiencies are modeled to better than 10% over the relevant ranges; orders $m = 0, 2, 3$ are largely within 20% . The rectangular parameters used in these plots are presented in Table 11.6.

Table 11.6: **MARX** Parameters for Rectangular approximation to HETG efficiency. These (non-physical) parameters provide a reasonable approximation to the HETG diffraction efficiency including higher-order contributions.

Parameter	Value	Unit
GratingOptConsts	"optical-constants.dat"	
UseGratingEffFiles	"'no"	
HEG grating		
HEGVig	0.93	
hegGold	0.0444	microns
hegChromium	0.0111	microns
hegNickel	0.0	microns
hegPolyimide	0.978	microns
hegBarHeight	0.4896	microns
hegBarWidth	0.1177	microns
MEG grating		
MEGVig	0.93	
megGold	0.0228	microns
megChromium	0.0057	microns
megNickel	0.0	microns
megPolyimide	0.543	microns
megBarHeight	0.3780	microns
megBarWidth	0.2161	microns

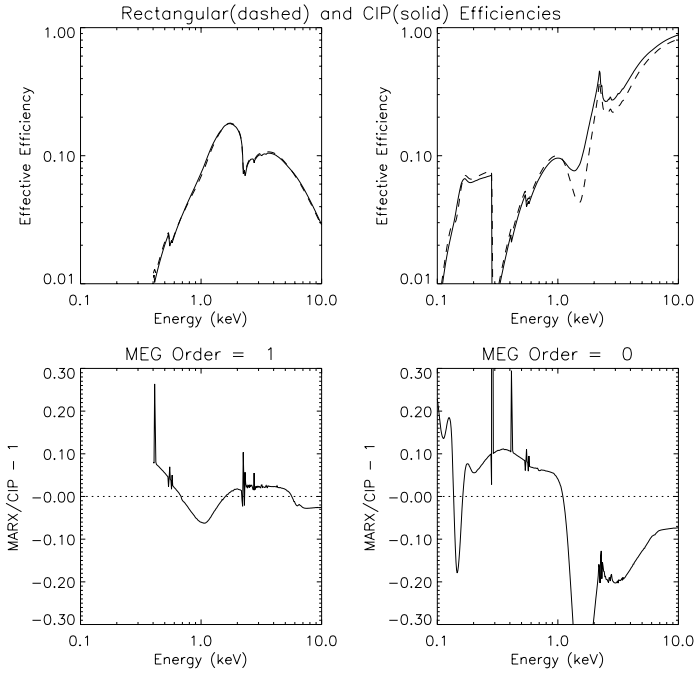

Figure 11.4: Comparing MEG Rectangular and CIP Efficiencies (orders 1, 0).

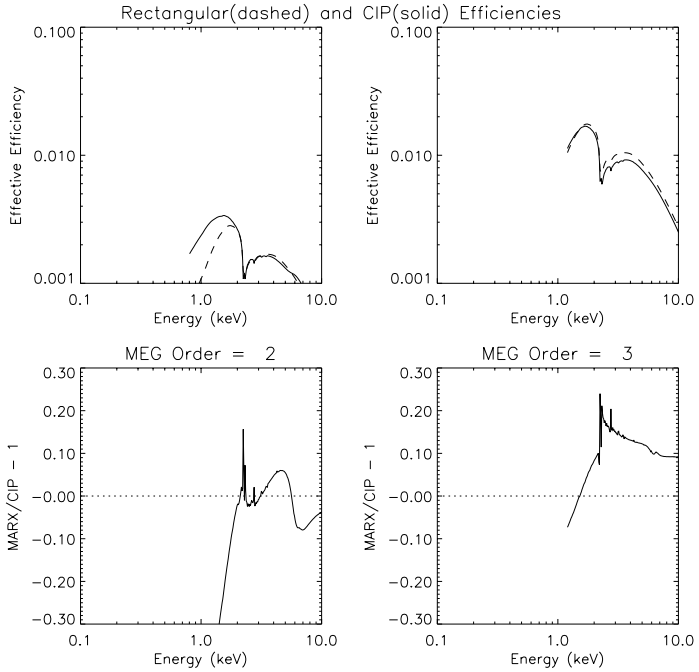

Figure 11.5: Comparing MEG Rectangular and CIP Efficiencies (orders 2, 3).

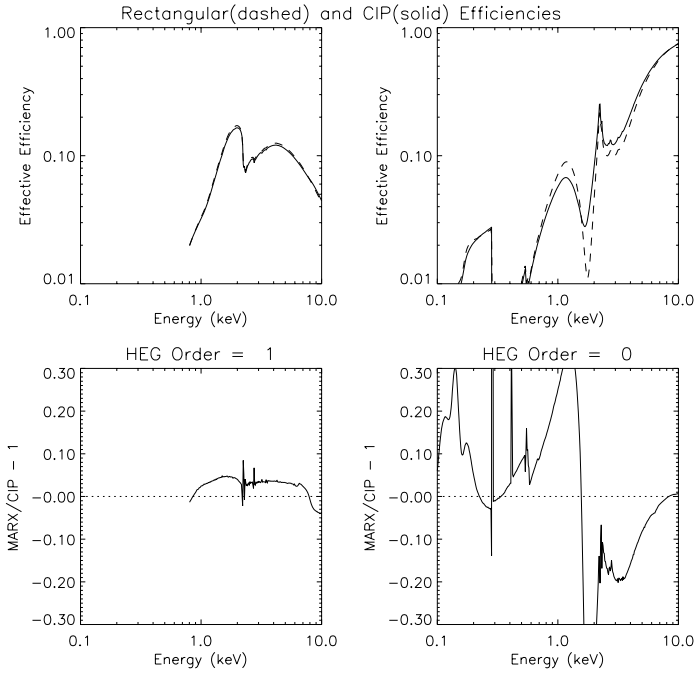

Figure 11.6: Comparing HEG Rectangular and CIP Efficiencies (orders 1, 0).

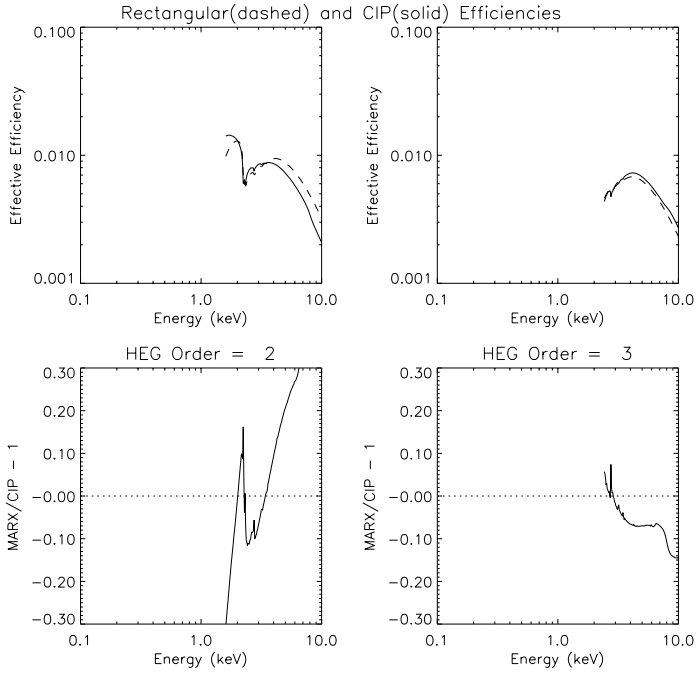

Figure 11.7: Comparing HEG Rectangular and CIP Efficiencies (orders 2, 3).

11.3.5.3 MARX Efficiency Files

MARX will soon allow the option of providing grating efficiecies as a set of lookup tables, one file for each shell. The efficiencies are tabulated on a fine energy grid and for a range of orders, currently $m = \ -11, \ldots, +11$. These tables of $G_s(E, m)$ include the shell vignetting factors (ν_s) and so the grating vignetting terms in **MARX** are set to 1.0. Table 11.7 presents the set of parameters that need to be set to implement the table lookup HETG efficiencies.

Table 11.7: **MARX** Parameters for Table-lookup HETG Efficiencies. These parameter selections allow efficiency tables encoding $G_s(E, m)$ to be read in and used by **MARX** for accurate simulations.

Parameter	Value	Unit
UseGratingEffFiles	"'yes"	
HETG_Shell1_File	"HETG_shell1_effic.dat"	
HETG_Shell3_File	"HETG_shell3_effic.dat"	
HETG_Shell4_File	"HETG_shell4_effic.dat"	
HETG_Shell6_File	"HETG_shell6_effic.dat"	
HETG_Shell1_Vig	1.0	
HETG_Shell3_Vig	1.0	
HETG_Shell4_Vig	1.0	
HETG_Shell6_Vig	1.0	

11.4 HETGS Calibration Interface Products

11.4.1 Resolving Power

Using the resolving power error budget described in Section 2.2, estimates of the flight HETGS resolving power have been made, Figure 2.3. The "optimistic" and "conservative" E/dE curves are available in rdb format in the files:

```
MEG_res_opt.rdb
HEG_res_opt.rdb
MEG_res_con.rdb
HEG_res_con.rdb
```

11.4.2 Effective Area

In order to compute the HETGS effective area, the HRMA effective area, $A_s(E)$, and the ACIS-S quantum efficiencies, $QE_{\rm ACIS}(E, \text{grade set})$, are needed. Values for these are plotted in Section 7.1 and the HETGS combined effective area is presented in plots in Section 7.7.

11.4.3 XSPEC Response Matrices

Please see `http://space.mit.edu/HETG/xspec/xspec.html` for a discussion of HETG and XSPEC.

Acronyms

	Sec.	
ACIS	1.1	Advanced CCD Imaging Spectrometer
ACIS-I		ACIS Imaging array
ACIS-S		ACIS Spectroscopic array
ACIS-2C	5.1.6	ACIS "2-chip" detector
ARD	11.1	Analysis Reference Data
ARM		Alignment Reference Mirror
ASC		AXAF Science Center (now CXC)
AXAF		Advanced X-Ray Astrophysics Facility
BESSY	??	Berlin Synchrotron Facility
BNDs	5.1.3	Beam Normalization Detectors
CCD		Charge Coupled Device
CEI	2.2	Contract End Item (specifications)
CIP	11.1	Calibration Interface Product
CMDB	5.3	Calibration Measurement Database
CXC		Chandra X-Ray Oservatory Center
CXO		Chandra X-Ray Oservatory
DCM	5.1.1	Double Crystal Spectrometer
EA	5.3.2	Effective Area
EE	6.2	Encircled Energy
FC	6.3	Focus Check
FCP	11.1	Fundamental Calibration Product
FITS		Flexible Image Transport System
FPC	5.1.5.3	Flow Proportional Counter
FWHM	1.4.3	Full Width at Half Maximum
HEG	1.2	High Energy Grating
HESS	1.2	HETG Element Support Structure
HETG	1.1	High Energy Transmission Grating
HETGS	1.4	High Energy Transmission Grating Spectrometer
HIREFS	5.1.1	High-Resolution Erect Field Spectrometer
HRMA	1.1	High Resolution Mirror Assembly
HRC	1.1	High Resolution Camera
HRC-I		HRC Imaging array
HRC-S		HRC Spectroscopic array
HSI	5.1.5.2	High Speed Imager
HXDS	5.1.5	HRMA X-Ray Detection System
LEG	1.1	Low Energy Grating
LETG	1.1	Low Energy Transmission Grating
LR	4.1	Laser Reflection setup at MIT
LRF	1.4.3	Line Response Function
MARX	2.3	Model of AXAF Response to X-rays
MC	7.8	Molecular Contamination

	Sec.	
MEG	1.2	Medium Energy Grating
MIT		Massachusetts Institute of Technology
MST		Mission Support Team at SAO
NSLS	3.2	National Synchrotron Light Source (Brookhaven)
PIGS	5.1.1	Penning Ionization Gas-discharge Source
PSF	1.4.3	Point Spread Function
PSPC	4.2	Position Sensitive Proportional Counter (in X-GEF)
rms		(square)root of the mean of the squares
rss		(square)root of sum of squares
SAO		Smithsonian Astrophysical Observatory
SF	6.3	Shutter Focus
SML	1.2	Space Microstructures Laboratory, at MIT
SPIE		Society of Photooptical Instrumentation Engineers
SSD	4.2	Solid State Detector, X-GEF
SSD	5.1.5.3	Solid State Detector, XRCF
TOGA	5	TMA Objective Grating Assembly
TMA	5	Technology Mirror Article
X-GEF	4.2	X-Ray Grating Evaluation Facility at MIT
XMM		X-Ray Multimirror Mission
XRCF	5	X-Ray Calibration Facility
XSPEC	7.8	X-Ray Spectral Fitting Package
XSS	5.1.1	X-Ray Source System

Mathematical Symbols

Symbol	Equation	Description
β	1.1	diffraction angle
m	1.1	diffraction order
λ	1.1	X-ray wavelength
p	1.1	grating period
HETGS response$(E, \dots)$	1.2	
E	1.2	X-ray energy
$SEA(E, m, \dots)$	1.2	system effective area
$PSF(E, m, \dots)$	1.2	2-d normalized point spread function
s	1.3	shell (1,3,4,6) of HRMA or grating
$A_s(E, \dots)$	1.3	HRMA effective area
$G_s(E, m)$	1.3	grating shell average efficiency
$QE(E, \dots)$	1.3	detector quantum efficiency
ν_s	1.4	average grating vignetting on shell s
N_s	1.4	number of facets in shell s
f	1.4	grating facet identifier
$g_f(E, m)$	1.4	grating facet average efficiency
$G_{\rm config}(E, m)$	1.5	grating effective efficiency for config
config	1.5	config = set of shells: HEG, MEG, HETG
$\rho(y, z)$	1.6	2-D PSF, normalized distribution
y, z	1.6	detector coordinates
$L(y'),\ L(\lambda)$	1.7	1-D LRF, normalized distribution
y', z'	1.7	grating dispersion coordinates
$R(E, m)$	1.8	resolving power
$dE,\ dy'$	1.8	FWHM of $l(E),\ l(y')$
$\Delta X_{\rm Rowland}$	2.2	detector offset to Rowland circle
$X_{\rm RS}$	2.2	Rowland spacing
R_0	2.3	perpendicular distance of grating ring
σ_H	2.7	effective HRMA rms blur
dx	2.13	detector defocus
γ	2.16	grating rms roll variation
a	2.10	aspect blur rms diameter
F	2.10	HRMA focal length
$R_{\rm dither}$	2.12	dither rate per frame time
t_D	2.12	detector quantization time
$L_{\rm pix}$	2.11	detector pixel size

(to be continued. . .)

Bibliography

[1] S. Abdali, F.E. Christensen, H.W. Schnopper, T.H. Markert, D. Dewey, and C.S. Nelson, "High Resolution X-Ray Studies of an AXAF High Energy Transmission Grating", *Multilayer and Grazing Incidence X-Ray/EUV Optics II*, Proc. SPIE, Vol. 2011, pp. 2–11, July 1993.

[2] Agarwal, B.K., *X-Ray Spectroscopy, Second Ed.*, pp. 108., Springer-Verlag, Berlin, 1991.

[3] C.L. Allen, P.P. Plucinsky, B.R. McNamara, R.J. Edgar, N.S. Schulz, and and J.W. Woo, "Analysis of the AXAF HRMA+ACIS effective area measurments from the XRCF" *X-Ray Optics, Instruments, and Missions*, Proc. SPIE, Vol. **3444** (this volume), (1998).

[4] E.H. Anderson, A.M. Levine, and M.L. Schattenburg, "Transmission X-ray Diffraction Grating Alignment using a Photoelastic Modulator", *Applied Optics*, Vol. **27**, pp. 3522-3525 (1988).

[5] Bautz, M.W., Nousek, J., Garmire, G., and the ACIS instrument team, "Science Instrument Calibration Report for the AXAF CCD Imaging Spectrometer (ACIS)", available at `wwwastro.msfc.nasa.gov/xray/axafps.html`, 1997.

[6] M.W. Bautz, F. Baganoff, T. Isobe, S.E. Jones, S.E. Kissel, B. LaMarr, H.L. Manning, M. Pivovaroff, G.Y. Prigozhin, J.A. Nousek, C.E. Grant, K. Nishikida, F. Scholze, R. Thornagel, and G. Ulm, "X-Ray CCD Calibration for the AXAF CCD Imaging Spectrometer", *X-Ray Optics, Instruments, and Missions*, Proc. SPIE, Vol. **3444**, (1998).

[7] J. van Beek, R. C. Fleming, P. S. Hindle, J. D. Prentiss, S. Ritzau, and M. L. Schattenburg 1998, *J. Vac. Sci. Technol. B*, 16, 3911–3916 (1998).

[8] Beuermann, K.P., Bräuniger, H., and Trümper, J., "Aberrations of a facet-type transmission grating for cosmic x-ray and XUV spectroscopy," *Applied Optics* Vol. **17**, No. 15, 2304 (1978).

[9] Bevington, P.R., and Robinson, D.K, *Data Reduction and Error Analysis for the Physical Sciences*, Second Edition, McGraw-Hill, 1992.

[10] R.L. Blake, J.C. Davis, D.E. Graessle, T.H. Burbine, and E.M. Gullikson, "Optical Constants and Scattering Factors from Reflectivity Measurements: 50 eV to 5 keV", *Journal of X-ray Science and Technology*, in press.

[11] M. Born and E. Wolf, *Principles of Optics, Sixth Ed.*, pp. 401-414., Pergamon, New York, 1980.

[12] previous citation, p.703.

[13] A.C. Brinkman, J. J. van Rooijen, J.A.M. Bleeker, J.H. Dijkstra, J. Heise, P.A.J. de Korte, R. Mewe, and F. Paerels, "Low energy X-ray transmission grating spectrometer for AXAF", in *X-ray Instrumentation in Astronomy, Proc. SPIE*, vol. 597, pp. 232-240, 1985.

[14] A.C. Brinkman, *et al., Astro. Lett. and Communications*, Vol. 26, p. 73, 1987.

[15] A.C. Brinkman, C.J.Th. Gunsing, J.S. Kaastra, H. Bräuninger, G. Hartner, P. Predehl, J.J. Drake, J.Z. Juda, M. Juda, D. Dewey, K.A. Flanagan, and H.L. Marshall, "Preliminary Test Results on Spectral Resolution of the Low Energy Transmission Grating Spectrometer on board of AXAF", *Grazing Incidence and Multilayer X-Ray Optical Systems*, Proc. SPIE, Vol. **3113** (1997).

[16] A.C. Brinkman, C.J.T. Gunsing, J.S. Kaastra, *et al.*, ApJ **530**, L111 (2000).

[17] Canizares, C.R., Schattenburg, M.L., and Smith, H.I., "The High Energy Transmission grating Spectrometer for AXAF", in *X-ray Instrumentation in Astronomy, Proc. SPIE*, Vol. **597**, 253–260 (1985).

[18] C.R. Canizares, *et al.*, *Astro. Lett. and Communications*, Vol. 26, p. 87, 1987.

[19] C.R. Canizares, "High Resolution X-Ray Spectroscopy of Thermal Plasmas" in Imaging X-Ray Astronomy, M. Elvis (ed.), Cambridge University Press, 1990.

[20] C.R. Canizares, D.P. Huenemoerder, D.S. Davis, D. Dewey, K.A. Flanagan, J. Houck, T.H. Markert, H.L. Marshall, M.L. Schattenburg, N.S. Schulz, M. Wise, J.J. Drake, N.S. Brickhouse, "High-Resolution X-Ray Spectra of Capella: Initial Results from the Chandra High-Energy Transmission Grating Spectrometer", ApJ, **539**, L41-44 (2000).

[21] J.E. Davis, H.L. Marshall, M.L. Schattenburg, and D. Dewey, "Analysis and Modeling of Anomalous Scattering in the AXAF HETGS", *X-Ray Optics, Instruments, and Missions*, Proc. SPIE, Vol. **3444**, 76–92 (1998).

[22] D.Dewey, D.N. Humpheries, G.Y. McLean and D.A. Moschella, "Laboratory Calibration of X-ray Transmission Diffraction Gratings", *EUX, X-Ray, and Gamma-Ray Instrumentation for Astronomy V*, Proc. SPIE, Vol. **2280**, 257–271 (1994).

[23] D. Dewey, H.L. Marshall, K.A. Flanagan, C. Baluta, C.R. Canizares, D.S. Davis, J.E. Davis, T.T. Fang, D.P. Huenemoerder, J.H. Kastner, N.S. Schulz, M.W. Wise, J.J. Drake, J.Z. Juda, M. Juda, A.C. Brinkman, T. Gunsing, J. Kaastra, G. Hartner and P. Predehl, "Towards the Callibration of the HETG Effective Area", *Grazing Incidence and Multilayer X-Ray Optical Systems*, Proc. SPIE, Vol. **3113**, 144–159 (1997).

[24] D. Dewey, J.J. Drake, R.J. Edgar, K. Michaud, and P. Ratzlaff, "AXAF Grating Efficiency Measurements with Calibrated, Non-imaging Detectors", *X-Ray Optics, Instruments, and Missions*, Proc. SPIE, Vol. **3444**, (1998).

[25] R.J. Edgar, E.Y. Tsiang, A. Tennant, S. Vitek, and D. Swartz, "Spectral Fitting in AXAF Calibration Detectors", *Grazing Incidence and Multilayer X-Ray Optical Systems, Proc. SPIE*, Vol. **3113**, (1997).

[26] I.N. Evans, E.M. Kellogg, W.C. McDermott, M.P. Ordway, J.M. Rosenberg, and B.J. Wargelin, "High Speed Imager AXAF Calibration Microchannel Plate Detector", *Grazing Incidence and Multilayer X-Ray Optical Systems, Proc. SPIE*, Vol. **3113**, (1997).

[27] Feynman, R.P., and Hibbs, A.R., *Quantum Mechanics and Path Integrals*, McGraw-Hill, New York, 1965

[28] K.F. Fischbach, A.M. Levine, M.L. Schattenburg, D. Dewey, R.L. Renshaw, J. Dalcanton, R. Newman, and W. Fissell, "Performance of High Spatial Frequency X-Ray Transmission Gratings", *X-Ray Instrumentation in Astronomy II*, Proc. SPIE, Vol. 982, pp. 273–282, July 1988.

[29] K.A. Flanagan, D. Dewey, L. Bordzol, "Calibration and Characterization of HETG grating elements at the MIT X-ray Grating Evaluation Facility", *SPIE Proceedings* **2518**, 438–456 (1995).

[30] K.A. Flanagan, T.T. Fang, C. Baluta, J.E. Davis, D. Dewey, T.H. Markert, D.E. Graessle, J. Drake, J.E. Fitch, J.Z. Juda, J. Woo, S. Kraft, P. Bulicke, R. Fliegauf, F. Scholze, and G. Ulm, "Modeling the Diffraction Efficiencies of the AXAF High Energy Transmission Gratings: II", *EUX, X-Ray, and Gamma-Ray Instrumentation for Astronomy VII*, Proc. SPIE, Vol. **2808**, 650–676 (1996).

[31] K.A. Flanagan, N.S. Schulz, S.S. Murray, G.D. Hartner, and P. Predehl, "HETG High-order Diffraction Efficiency" *X-Ray Optics, Instruments, and Missions*, Proc. SPIE, Vol. **3444**, 106–126 (1998).

[32] K.A. Flanagan, T.H. Markert, J.E. Davis, M.L. Schattenburg, R.L. Blake, F. Scholze, P. Bulicke, R. Fleigauf, S. Kraft, G. Ulm, E.M. Gullikson, "Modeling the Chandra High Energy Transmission Gratings below 2 keV" *X-Ray Optics, Instruments, and Missions*, Proc. SPIE, Vol. **4140**, (2000).

[33] A. E. Franke, M. L. Schattenburg, E. M. Gullikson, J. Cottam, S. M. Kahn, and A. Rasmussen 1997, *J. Vac. Sci. Technol. B*, 15, 2940-2945 (1997).

[34] G.W. Fraser, X-ray detectors in astronomy, Cambridge University Press, Cambridge, 1989.

[35] G.P. Garmire, *et al.*, "The AXAF CCD Imaging Spectrometer", in *X-ray Instrumentation in Astronomy, Proc. SPIE*, vol. 597, pp. 261-266, 1985.

[36] G. Garmire, G. Chartas, L. Townsley, A.B. Garmire, and M. Bautz, "Optical Flux limits for observing with the ACIS Instrument on AXAF", AAS 192, 1404G, 1998.

[37] G.P. Garmire, "Early Science Results from the ACIS on Board the Chandra X-ray Observatory", AAS Meeting 195.9603G (1999).

[38] P. Gorenstein and M. Zombeck, *High Resolution X-ray Spectroscopy of Cosmic Plasmas*, Cambridge University Press, Cambridge, 1990.

[39] D. Graessle, A.M. Clark, J.J. Fitch, B. Harris, D.A. Schwartz, R.L. Blake, "Reflectance calibrations of AXAF Witness Mirrors Using Synchrtron Radiation, 2-12 keV", *SPIE Proceedings* **2805**, 18 (1996)

[40] Graessle, D.E., Burek, A.J., Fitch, J.J., Harris, B., Schwartz, D.A., and Blake, R.L., "Optical constants from synchrotron reflectance measurements of AXAF witness mirrors - 2 to 12 keV, " in Grazing Incidence and Multilayer X-ray Optical Systems, Proc. SPIE, vol 3113, pp 52-64, 1997.

[41] Graessle, D.E., Blake, R.L., Burek, A.J., Dyson, S.E., Fitch, J.J., Schwartz, D.A., and Soufli, R., "Modeling of synchrotron reflectance calibrations of AXAF iridium-coated witness mirrors over 2-12 keV, " in X-ray Optics, Instruments, and Missions, Proc. SPIE, vol 3444, 1997.

[42] HRC Calibration web page: `hea-www.harvard.edu/HRC/calib/calib.html` (1998).

[43] B.L. Henke, E.M. Gullikson, and J.C. Davis, "X-ray Interactions: Photoabsorption, Scattering, Transmission, and Reflection at E = 50–30,000 eV, A = 1–92", *Atomic Data and Nuclear Data Tables*, Vol. 54, No. 2, July 1993.

[44] B.L. Henke, P. Lee, T.J. Tanaka, R.L. Shimabukuro and B.K. Fujikawa, "Low-Energy X-ray Interaction Coefficients: Photoabsorption, Scattering, and Reflection, E = 100–2,000 eV, Z = 1–94", *Atomic Data and Nuclear Data Tables*, Vol. 27, No. 1, January 1982.

[45] H. Henneken, F. Scholze, and G. Ulm, "Lack of proportionality of total electron yield and soft x-ray absorption coefficient", *J. Appl. Phys.*, Vol. **87**, No. 1, 257–268, 2000.

[46] J.C. Houck and L.A. DeNicola, "ISIS: An Interactive Spectral Interpretation System for High Resolution X-Ray Spectroscopy", in ASP Conf. Ser., Astronomical Data Analysis Software and Systems IX, (San Francisco: ASP), in press. (1999).

[47] H. Inoue, H. Okamoto, and Y. Hiraoka, "Effect of Chemical Structure of Acid Dianhydride in the Skeleton on the Thermal Property and Radiation Resistance of Polyimide", *Radiat. Phys. Chem.*, Vol. 29, p.283, 1987.

[48] Kameritsch, P., "Calibration of Transmission Diffraction Gratings for the AXAF X-ray Satellite", thesis at the Ludwig Maximilians University, Munich, 1995.

[49] M. Keller, K. Shumate, Software Specification and Design : a Disciplined Approach for Real-Time Systems, John Wiley & Sons, Inc., New York, 1992.

[50] E. Kellogg, "Kα Line-to-continuum ratio for electron impact x-ray sources", internal memo to AXAF Calibration Task Team, October 5, 1992.

[51] E.M. Kellogg *et al.*, "Absolute calibration of the AXAF telescope effective area", *Grazing Incidence and Multilayer X-Ray Optical Systems, Proc. SPIE*, Vol. **3113**, (1997).

[52] A. Kenter, J.H. Chappell, R.P. Kraft, G.R. Meehan, S.S. Murray, M.V. Zombeck, *SPIE Proceedings* **2808**, 626 (1996).

[53] A.T. Kenter, J.H. Chappell, K. Kobayashi, R.P. Kraft, G.R. Meehan, S.S. Murray, M.V. Zombeck, G.W. Fraser, J.F. Pearson, J.F. Lees, A.N. Brunton, S.E. Pearce, M. Barbera, A. Collura, S. Serio, *SPIE Proceedings* **3114**, 26 (1997).

[54] J.J. Kolodziejczak, R.A. Austin, R.F. Elsner, M.K. Joy, M. Sulkanen, E.M. Kellogg, and B.J. Wargelin, "X-Ray Source System at the MSFC X-Ray Calibration Facility", *X-Ray and Extreme Ultraviolet Optics*, Proc. SPIE, Vol. **2515**, 420–435 (1995).

[55] Kolodziejczak, J.J., et al., "Uses of continuum radiation in the AXAF calibration, ", in Grazing Incidence and Multilayer X-ray Optical Systems, Proc. SPIE, vol 3113, pp 65-76, 1997.

[56] C.J. Borkowski and M. Kopp, "Design and properties of position-sensitive proportional counters using resistance-capacitance position encoding", Rev. Sci. Instrum., Vol. 46, No. 8, August 1975.

[57] T.H. Markert, "Dispersive Spectroscopy on AXAF", in *High-Resolution X-ray Spectroscopy of Cosmic Plasmas, IAU Colloquium No. 115*, P. Gorenstein and M. Zombeck, eds., pp. 339-344, Cambridge University Press, Cambridge, 1990.

[58] T.H. Markert, C.R. Canizares, D. Dewey, M. McGuirk, C. Pak, and M.L. Schattenburg, "The High Energy Transmission Grating Spectrometer for AXAF", *EUX, X-Ray, and Gamma-Ray Instrumentation for Astronomy V*, Proc. SPIE, Vol. **2280**, 168–180 (1994).

[59] T.H. Markert, D. Dewey, J.E. Davis, K.A. Flanagan, D.E. Graessle, J.M. Bauer, C.S. Nelson, "Modeling the Diffraction Efficiencies of the AXAF High Energy Transmission Gratings", *SPIE Proceedings* **2518**, 424–437 (1995).

[60] H.L. Marshall, D. Dewey, K.A. Flanagan, C. Baluta, C.R. Canizares, D.S. Davis, J.E. Davis, T.T. Fang, D.P. Huenemoerder, J.H. Kastner, H.L. Marshall, N.S. Schulz, M.W. Wise, J.J. Drake, J.Z. Juda, M. Juda, A.C. Brinkman, C.J.Th. Gunsing, and J.S. Kaastra, G. Hartner and P. Predehl, "Towards the Calibration of the HETGS Line Response Function", *Grazing Incidence and Multilayer X-Ray Optical Systems*, Proc. SPIE, Vol. **3113**, 160–171 (1997).

[61] H.L. Marshall, D. Dewey, N.S. Schulz, and K.A. Flanagan, "Spectral Features in the AXAF HETGS Effective Area using High-signal Continuum Tests", *X-Ray Optics, Instruments, and Missions*, Proc. SPIE, Vol. **3444**, (1998).

[62] AXAF Science Center, `asc.harvard.edu`, "MARX 2.0 User Guide, Rev 1.0", ASC TD. 404, October 1997.

[63] M.W. Wise, J.E. Davis, D.P. Huenemoerder, J.C. Houck, and D. Dewey, "MARX 3.0 Technical Manual", MIT Center for Space Research (2000).

[64] W.C. McDermott, E.M. Kellogg, B.J. Wargelin, I.N. Evans, S.A. Vitek, E. Tsiang, D.A. Schwartz, R.J. Edgar, S. Kraft, F. Scholze, R. Thornagel, G. Ulm, M.C. Weisskopf, S.L. O'Dell, A.F. Tennant, J. Kolodziejczak, and G. Zirnstein, "AXAF HXDS germanium solid state detectors", *Grazing Incidence and Multilayer X-Ray Optical Systems*, Proc. SPIE, Vol. **3113**, 535–543 (1997).

[65] A.G. Michette and C.J. Buckley, Editors, *X-Ray Science and Technology*, pp. 320-321, Institute of Physics Publishing Ltd, London, 1993.

[66] S.S. Murray and J.H. Chappell, "The Advanced X-ray Astrophysics Facility High Resolution Camera", in *X-ray Instrumentation in Astronomy, Proc. SPIE*, vol. 597, pp. 274-281, 1985.

[67] S.S. Murray, *et al.*, *Astro. Lett. and Communications*, Vol. 26, p. 113, 1987.

[68] S.S. Murray, J.H. Chappell, A.T. Kenter, K. Kobayashi, R.P. Kraft, G.R. Meehan, M.V. Zombeck, G.W. Fraser, J.F. Pearson, J.E. Lees, A.N. Brunton, S.E. Pearce, M. Barbera, A. Collura, S. Serio, *SPIE Proceedings* **3114**, 11 (1997).

[69] S.S. Murray, J.H. Chappell, A.T. Kenter, R.P. Kraft, G.R. Meehan, M.V. Zombeck, "AXAF high-resolution camera (HRC): the challenge of calibration", *SPIE Proceedings* **3356**, 974 (1998).

[70] C.S. Nelson, *Synchrotron Studies of an X-ray Transmission Grating*, Bachelor's Thesis, MIT (1994)

[71] C.S. Nelson, T.H. Markert, Y.S. Song, M.L. Schattenburg, K.A. Flanagan, R.L. Blake, J. Bauer, E.M. Gullikson, "Efficiency Measurements and Modelling of AXAF High Energy Transmission Gratings", *EUX, X-Ray, and Gamma-Ray Instrumentation for Astronomy V*, Proc. SPIE, Vol. **2280**, 191–203 (1994).

[72] J.A. Nousek, G.P. Garmire, G.R. Ricker, S.A. Collins, and G.R. Reigler, *Astro. Lett. and Communications*, Vol. 26, p. 35, 1987.

[73] The AXAF Observatory Guide, Rev. 1.0, AXAF Science Center.

[74] S.L. O'Dell and M.C.Weisskopf, "Advanced X-ray Astrophysics Facility (AXAF): calibration overview", *X-Ray Optics, Instruments, and Missions*, Proc. SPIE, Vol. **3444**, 2–18 (1998).

[75] The AXAF Proposers' Guide, Rev. 1.0, AXAF Science Center.

[76] F.B.S. Paerels, J.V. Bixler, J.W. den Herder, C.J. Hailey, S.M. Kahn, and C.W. Mauche, "Modeling and Analysis of X-ray Emission Line Images Acquired with a Prototype Model of the XMM Reflection Grating Spectrometer", *X-Ray and Ultraviolet Spectroscopy and Polarimetry*, Proc. SPIE, Vol. **2283**, 107–118 (1994).

[77] C. Pak and M. McGuirk, "Computer Aided Design for the High Energy Transmission Grating (HETG) Spectrometer", paper 94-4566 presented at the *AIAA Space Programs and Technologies Conference*, Huntsville, AL (1994).

[78] G.J. Patnaude, D. Pease, H. Donnelly, M. Juda, C. Jones, S.S. Murray, M.V. Zombeck, R.P. Kraft, A.T. Kenter, G.R. Meehan, D.A. Swartz, R.F. Elsner, "Effective Area of the AXAF High-Resolution Camera (HRC)", *X-Ray Optics, Instruments, and Missions*, Proc. SPIE, Vol. **3444**, (1998).

[79] P. Predehl, H. Bräuninger, A.C. Brinkman, D. Dewey, J.J. Drake, K.A. Flanagan, C.J.Th. Gunsing, G. Hartner, J.Z. Juda, M. Juda, J. Kaastra, H.L. Marshall, and D. Swartz, "X-Ray Calibration of the AXAF Low Energy Transmission Grating Spectrometer: Effective Area",*Grazing Incidence and Multilayer X-Ray Optical Systems, Proc. SPIE*, Vol. **3113**,(1997).

[80] SAOimage: The Next Generation, SAOtng home page: `hea-www.harvard.edu/RD/` (1998).

[81] T. Savas, M. L. Schattenburg, J. M. Carter, and H. I. Smith, 1996, *J. Vac. Sci. Technol. B*, 14, 4167-4170 (1996).

[82] M.L. Schattenburg, *et al.*, Optical Engineering,vol. 30, p. 1590, 1991.

[83] M.L. Schattenburg, R.J. Aucoin, R.C. Fleming, I. Plotnik, J. Porter, and H.I. Smith, "Fabrication of High Energy X-ray Transmission Gratings for AXAF", *EUX, X-Ray, and Gamma-Ray Instrumentation for Astronomy V*, Proc. SPIE, Vol. **2280**, 181–190 (1994).

[84] M.L. Schattenburg, R. J. Aucoin, and R. C. Fleming 1995, *J. Vac. Sci. Technol. B*, 13, 3007–3011 (1995).

[85] M. L. Schattenburg, R. I. Fuentes, G. Czernienko, R. C. Fleming, and J. Porter 1995, it Thin Films: Stresses and Mechanical Properties V (*Materials Research Society Symposium Proceedings* **356**), eds. S.P. Baker, P. Burgensen, P. H. Townsend, C. A. Ross, and C. A. Volkert (MRS, Pittsburgh, PA), 615–620 (1995).

[86] M.L. Schattenburg, "From nanometers to gigaparsecs: the role of nanostructures in unraveling the mysteries of the cosmos", J. Vac. Sci. and Tech. B, proceedings of the 45^{th} *International Conference on Electron, Ion and Photon Beam Technology and Nanofabrication*, Washington, D.C. (2001).

[87] H.W. Schnopper, *et al.*, "Diffraction Grating Transmission Efficiencies for XUV and Soft X-rays", *Appl. Optics*, Vol. 16, p. 1088 (1977).

[88] F. Scholze, M. Krumrey, P. Müller, and D. Fuchs, "(PTB monochromator purity)", *Rev. Sci. Instrum.* **65**, 3229 (1994)

[89] Daniel J. Schroeder, *Astronomical Optics*, Chapter 14, Academic Press, San Diego, 1987.

[90] N.S. Schulz, D. Dewey, H.L. Marshall, "Absolute Effective Areas of HETG", *X-Ray Optics, Instruments, and Missions*, Proc. SPIE, Vol. **3444**, (1998).

[91] M.D. Stage and D. Dewey, "Verifying the HETG Spectrometer Rowland Design", *X-Ray Optics, Instruments, and Missions*, Proc. SPIE, Vol. **3444**, (1998).

[92] Stratonovich, R.L., *Topics in the Theory of Random Noise*, Volume 1, Gordon and Breach, 1963

[93] D.A. Swartz, R.F. Elsner, J.J. Kolodziejczak, S.L. O'Dell, A.F. Tennant, M.E. Sulkanen, M.C. Weisskopf, and R.J. Edgar, "Use of Monochromators for the Calibration of AXAF", *X-Ray Optics, Instruments, and Missions*, Proc. SPIE, Vol. **3444**, (1998).

[94] E.Y. Tsiang, R.E. Edgar, S. Vitek, and A. Tennant, "JMKMOD, a Software Suite within XSPEC for the Ground Calibration of AXAF", *Grazing Incidence and Multilayer X-Ray Optical Systems*, Proc. SPIE, Vol. **3113**, 132–141 (1997). `hea-www.harvard.edu/MST/simul/xrcf/XSPEC/jmkmod.html`

[95] G. Ulm, B. Wende, "(PTB Synchrotron)", *Rev. Sci. Instrum.* **66**, 2244-2247 (1995).

[96] B.J. Wargelin, E.M. Kellogg, W.C. McDermott, I.N. Evans, and S.A. Vitek, "AXAF Calibration: The HXDS Flow Proportional Counters", *Grazing Incidence and Multilayer X-Ray Optical Systems, Proc. SPIE*, Vol. **3113**, (1997).

[97] Warren, B.E., *X-Ray Diffraction*, Dover Publications, 1990

[98] M.C.Weisskopf and S.L. O'Dell, "Calibration of the AXAF observatory: overview", *Grazing Incidence and Multilayer X-Ray Optical Systems*, Proc. SPIE, Vol. **3113**, 2–17 (1997).

[99] M. Weisskopf, R.F. Elsner, S.L. 0'Dell and the AXAF Project Science team, "Calibration of the Advanced X-ray Astrophysics Facility: Project Science analyses" available at `wwwastro.msfc.nasa.gov/xray/axafps.html` (1997)

[100] M.C.Weisskopf, H.D. Tananbaum, L.P. Van Speybroeck, and S.L. O'Dell, "Chandra X-Ray Observatory (CXO): Overview", in *X-Ray Optics, Instruments, and Missions*, J. Truemper and B. Aschenbach, eds., Proc. SPIE, Vol. **4012** (2000).

[101] M.C. Weisskopf et al., PASP in press (2001).

[102] K.A. Arnaud, *et al.*, "XSPEC, An X-Ray Spectral Fitting Package", part of the XANADU software from NASA Goddard Space Flight Center, `legacy.gsfc.nasa.gov/`